# 83rd ARFTG Microwave Measurement Conference

# Microwave Measurements for Emerging Technologies

June 6, 2014
Tamp Marriott Waterside Hotel & Marina
Tampa, Florida

IEEE Catalog Number: CFP14ARF-USB
ISBN: 978-1-4799-4425-5

Copyright and Reprint Permission: Abstracting is permitted with credit to the source. Libraries are permitted to photocopy beyond the limit of U.S. copyright law for private use of patrons those articles in this volume that carry a code at the bottom of the first page, provided the per-copy fee indicated in the code is paid through Copyright Clearance Center, 222 Rosewood Drive, Danvers, MA 01923. For reprint or republication permission, email to IEEE Copyrights Manager at pubs-permissions@ieee.org. All rights reserved. Copyright ©2014 by IEEE.

# 83rd ARFTG Conference Organizers

| | |
|---|---|
| *General Chair* | **Mohamed Sayed** |
| *Technical Program Chair* | **Jon Martins** |

# 83rd ARFTG Technical Program Committee

**Peter Aaen,** *University of Surrey*

**Loren Betts,** *Agilent Technologies*

**Dave Blackham,** *Agilent Technologies*

**Slim Boumaiza,** *University of Waterloo*

**Juan-Mari Collantes,** *UPV/EHU*

**Gayle Collins,** *MaXentric Technologies*

**Leonard Hayden,** *Teledyne LeCroy*

**Joe Gering,** *RFMD*

**Ron Ginley,** *NIST*

**Jon Martens,** *Anritsu*

**Basim Noori,** *Freescale Semiconductor*

**J. Apolinar Reynoso-Hernandez,** *CICESE*

**Nick Ridler,** *NPL*

**Patrick Roblin,** *Ohio State University*

**Andrej Rumiantsev,** *Brandenburg University of Technology Cottbus*

**Mohamed Sayed,** *MMS Consulting*

**Dominique Schreurs,** *KU Leuven*

**Mitch Wallis,** *NIST*

**Ken Wong,** *Agilent Technologies*

**John Wood,** *Maxim Integrated*

# The 2014 ARFTG Executive Committee (ExCom)

| | |
|---|---|
| *President* | **Mohamed Sayed**, MMS |
| *Vice President* | **Jon Martens,** Anritsu |
| *Secretary & Nominations* | **Dominique Schreurs**, K.U.Leuven |
| *Treasurer & Standards* | **Ronald Ginley**, NIST |
| *Exhibits* | **Rusty Myers**, Maury Microwave |
| *Membership & Standards* | **Ken Wong**, Agilent Technologies |
| *Technical Coordination and Planning:Spring* | **Nick Ridler**, NPL |
| *Publications* | **David Blackham**, Agilent Technologies |
| *Education & Workshops* | **Patrick Roblin**, Ohio State University |
| *Nonlinear Network Analyzers & Publicity* | **Jean-Pierre Teyssier**, University of Limoges XLIM |
| *MTT-S Liaison and Awards* | **Leonard Hayden**, Teledyne LeCroy |
| *Sponsorship* | **Joe Gering**, RFMD |
| *Technical Coordination and Planning:Fall* | **John Wood,** Maxim Integrated |
| *Electronic Communications* | **Mitch Wallis**, NIST |
| *Electronic Publicity* | **Peter Aaen**, University of Surrey |

# Ex-Officio

| | |
|---|---|
| *Executive Secretary* | **John Cable** |

**Session: A**

## Evolving Nonlinear Measurements

*Chair:* *Jon Martens*

**A-1** **INVITED: Instrumentation in Mixed-signal and mixed-domain emerging technologies**

N. B. Carvalho, Instituto de Telecomunicacoes - University of Aveiro, Aveiro, Portugal

**A-2** **AM/AM AM/PM Estimation on IEEE 802.11a Packet with OFDM Demodulator**

O. Hsu, H. Jian, Broadcom Corp, San Diego, United States

**A-3** **Nonlinear System Behavioral Modeling Using Reduced Transmitter Observation Receiver Bandwidth**

F. Mkadem, S. Boumaiza, University of Waterloo, Waterloo, Canada

**A-4** **Sensitivity of AM/AM linearizer to AM/PM distortion in devices.**

F. L. Ogboi[1], P. Tasker[1], Z. Mohkti[1], J. Lees[1], J. Benedikt[1], S. Bensmida[2,2], K. Morris[2,2], M. Beach[2,2], J. McGeehan[2,2], [1]Cardiff University, Cardiff, United Kingdom, [2]University of Bristol, Bristol, United Kingdom

**Session: B**

## Calibration and Verification

*Chair:* *Nick Ridler*

**B-1** **Enhanced Vector Calibration of Load-pull Measurement Systems**

A. S. Aldoumani[1], T. Williams[2], J. Lees[1], P. Tasker[1], [1]Cardiff University, Cardiff, United Kingdom, [2]Mesuro Limited, Pencoed, United Kingdom

**B-2** **Estimation of Complex Residual Errors of Calibrated Two-Port Vector Network Analyzer**

A. A. Savin[1], V. G. Guba[2], A. Rumiantsev[3], B. D. Maxson[4], [1]Tomsk State University of Control Systems and Radioelectronics, Tomsk, Russian Federation, [2]NPK TAIR, a subsidiary of Copper Mountain Technologies, Tomsk, Russian Federation, [3]Brandenburg University of Technology (BTU), Cottbus, Germany, [4]Copper Mountain Technologies, Indianapolis, United States

**B-3** **Design of Two-port Verification Devices for Reflection Measurement in Waveguide Vector Network Analyzers at Millimeter and Sub-millimeter Wave Frequencies**

M. Horibe, R. Kishikawa, AIST, Tsukuba, Japan

**B-4** **Evaluation of CMOS Differential Transmission Lines as Two-Port Networks with On-Chip Baluns in Millimeter-Wave Band**

K. Takano, M. Motoyoshi, T. Yoshida, K. Katayama, S. Amakawa, M. Fujishima, Hiroshima University, Higashi-Hiroshima, Japan

**Session: C**

## Measurements in Complex/Challenging Environments

*Chair:* *Dave Blackham*

**C-1** **INVITED: Microwave measurements for biological materials analysis**

K. Grenier, LAAS cnrs, Toulouse, France

**C-2** **Study of Calibration Standards for Extreme Impedances Measurement**

M. Haase, K. Hoffmann, Czech Technical University in Prague, Prague, Czech Republic

**C-3** **Characterizing a Noninsertable Directional Device Using the NIST Uncertainty Framework**

J. A. Jargon, D. F. Williams, P. D. Hale, M. D. Janezic, NIST, Boulder, United States

**C-4** **Method for Estimating Probe-Dependent Residual Errors of Wafer-Level TRL Calibration**

A. Rumiantsev[1], R. Doerner[2], [1]Brandenburg University of Technology (BTU) Cottbus-Senftenberg, Cottbus, Germany, [2]Ferdinand-Braun-Institut (FBH), Leibniz-Institut fuer Hoechstfrequenztechnik, Berlin, Germany

**Session: D**

## Nonlinear and Mixed-Signal Measurements

*Chair:* *Joe Gering*

**D-1** **Characterization and modeling scheme for harmonics at power amplifier output**

M. Rawat[1], P. Roblin[1], C. Quindroit[1], N. Naraharisetti[1], R. Pond[1], K. Salam[2], C. Xie[2], [1]The Ohio State University, Columbus, United States, [2]Rockwell collins, Cedar Rapids, United States

**D-2** **Active Harmonic Source-/Load-Pull Measurements of AlGaN/GaN HEMTs at X-Band Frequencies**

T. Maier, V. Carrubba, R. Quay, F. van Raay, O. Ambacher, Fraunhofer Institute for Applied Solid State Physics (IAF), Freiburg, Germany

**D-3** **Two-Stage Correction for Wideband Wireless Signal Generators with Time-Interleaved Digital-to-Analog-Converters**

Y. Park[1], K. A. Remley[2], [1]Hankuk Univ. of Foreign Studies, Yongin-si, Republic of Korea, [2]National Institute of Standards and Technology, Boulder, United States

**D-4** **Measurements for Microwave Differential and IQ Devices**

J. P. Dunsmore, X. Chen, Agilent Technologies, Santa Rosa, United States

**Session: P**

# ARFTG Interactive Forum

*Chair:* *Ron Ginley*

**P-01** **Method for Calibration Vector signal analyzer based on Baseband waveform Design**

F. Zhou[1], R. Zhang[1], D. Mu[1,2], K. Cheng[1], Y. Xu[1], Y. Gao[2], [1]China Academy of telecommunication Research of MIIT, Beijing, China, [2]Beijing University of Posts and Telecommunications, Beijing, China

**P-02** **Analyzing and Improvement of the Thermopile Output Signal Noise Ratio of a Calorimeter**

Y. Li, X. Cui, X. Gao, W. Sun, National Institute of Metroloy, Beijing, China

**P-03** **Further Investigations into Connection Repeatability of Waveguide Devices at Frequencies from 750 GHz to 1.1 THz**

N. M. Ridler[1], R. G. Clarke[2], [1]NPL, Teddington, United Kingdom, [2]University of Leeds, Leeds, United Kingdom

**P-04** **An Improved Measurement Technique for Retrieval of Effective Constitutive Properties of Thin Dielectric/Magnetic and Metamaterial Samples**

H. B. Baskey, . Akhtar, Indian Institute of Technology, Kanpur, India

**P-05** **Using Electromagnetic Modeling to Evaluate Uncertainty in a Millimetre-wave Cross-guide Verification Standard**

H. Huang[1], N. Ridler[2], M. Salter[3], [1]National Institute of Metrology, Beijing, China, [2]National Physical Laboratory, Teddington, United Kingdom, [3]National Physical Laboratory, Teddington, United Kingdom

**P-06** **Observations on the sensitivity of on-wafer cascode cell S-parameter measurements due to probing uncertainities**

P. Shinghal[1], R. Sloan[1], C. I. Duff[1], S. Cochran[2], [1]The University of Manchester, Manchester, United Kingdom, [2]Agilent Technologies, Santa Rosa, United States

**P-07** **Characterizing Calibration Standards Using One Airline as a Transfer Standard**

T. Roberts, J. Martens, Anritsu Company, Morgan Hill, United States

**P-08** **Global Dynamic FET Model for GaN Transistors: DynaFET Model validation and comparison to locally tuned models**

J. Xu[1], S. Halder[2], F. Kharabi[2], J. McMacken[2], J. Gering[2], D. E. Root[1], [1]Agilent Technologies, Inc., Santa Rosa, United States, [2]RFMD, Greensboro, United States

**P-09** **A Digital, PXI-Based Active Load-Pull Tuner to Maximize Throughput of a Load-Pull Test Bench**

T. Williams[1], B. Wee[2], R. Saini[1], S. Mathias[1], M. V. Bossche[2], [1]Mesuro Ltd., Pencoed, United Kingdom, [2]National Instruments , Zaventem, Belgium

**P-10** **A Novel Half Space Time-Domain Measurement Technique for One-Dimensional Microwave Imaging**

S. L. Gupta, Z. A. Siddiqui, M. Bhaskar, M. J. Akhtar, Indian Institute of Technology Kanpur, Kanpur, India

**P-11** **A Method for De-Embedding Cable Flexure Errors in S-parameter Measurements**

F. A. Mubarak[1], G. Rietveld[1], M. Spirito[2], [1]VSL, Delft, Netherlands, [2]Delft University of Technology, Delft, Netherlands

**P-12** **Calibration of EM Simulator on Substrate Complex Permittivity**

V. Sokol[1], J. Eichler[1,2], M. Rütschlin[1], [1]Computer Simulation Technology, Darmstadt, Germany, [2]Czech Technical University in Prague, Prague, Czech Republic

**P-13** **HFTools - An open source python package for microwave engineering**

J. Stenarson[1,2], [1]SP Technical Research Institute of Sweden, Boras, Sweden, [2]GHz Centre, Gothenburg, Sweden

**P-14** **Microwave Substrate Loss Tangent Extraction from Coplanar Waveguide Measurements up to 125 GHz**

U. Arz, PTB, Braunschweig, Germany

**P-15** **Noise Diode Calibration Using Receiver Noise Parameters**

R. C. Aarons, M. H. Weatherspoon, Florida A&M University-Florida State University, Tallahassee, United States

**P-16** **A Novel CPW- Fed Polarization Reconfigurable Microstrip Antenna**

V. Zarei[2], H. Hamid Boudaghi[2], S. Abazari Aghdam[1], [1]Florida Atlantic University, Boca Raton, United States, [2]Microelectronics Research Laboratory Urmia University, Urmia, Iran

**P-17** **Correlation Analysis between a VNA-based Passive Load Pull System and an Oscilloscope-based Active Load Pull System: A Case Study**

Z. A. Mokhti, J. Lees, P. J. Tasker, Cardiff University, Cardiff, United Kingdom

**P-18** **A New Method for the Determination of the Reflection and Transmission characteristics of Dielectric Materials**

J. Kim, J. Kang, J. Park, T. Kang, Korea Research Institute of Standards and Science , Daejeon, Republic of Korea

# AM/AM AM/PM Estimation on IEEE 802.11a Packet with OFDM Demodulator

Oliver (Chun-Hao) Hsu[#1] , Henry (Heng-Yu) Jian[#2]
[#]*Broadcom Corporation*
*16340 West Bernardo Dr., San Diego, CA 92127*
[1]olhsu@broadcom.com, [2]henryj@broadcom.com

*Abstract*—**nowadays, accurately characterizing linearity of power amplifier (PA) becomes difficult in system-on-chip (SoCs) solutions because the PA input is not accessible. This paper introduces a methodology to characterize AM-AM/AM-PM distortion on 802.11a OFDM packets without knowing input signals or synchronizing device under test (DUT) Xtal to reference clock of equipment. Reference samples for AM-AM/AM-PM calculation are derived from captured samples with channel response added for cancellation. Frequency and timing offset are compensated on captured samples. Measured AM-AM/AM-PM results are correlated to EVM of the DUT.**

## I. INTRODUCTION

Orthogonal Frequency Division Multiplexing (OFDM) has become the most popular modulation scheme in wideband digital communications systems, such as WiFi and LTE, due to its simple implementation of channel equalization. However, summation of multiple subcarriers results in a high crest factor, which requires a highly linear RF power amplifier (PA). To operate at a more linear region, the PA needs to be biased closer to a class-A type and back off more from its saturation region. This bias results in low efficiency and short battery time for handheld devices. An alternative is to use linearization techniques, such as digital pre-distortion (DPD) to correct nonlinearity of the PA. To characterize this nonlinearity, amplitude and phase distortion can be measured with respect to the input amplitude, or AM-AM and AM-PM distortion.

For an external PA, a CW power sweep with a network analyzer can measure AM-AM and AM-PM distortion [1], but this method would not capture dynamic behavior of the circuit when envelope-modulated signals are applied. To characterize a PA with non-constant envelope signals, a training signal at RF frequency can be injected by a vector signal generator (VSG) at the PA input, and IQ samples can be captured by a vector signal analyzer (VSA) at the PA output. By simply overlapping and normalizing input and output time domain IQ samples, AM-AM and AM-PM curves can be calculated [2]. The captured samples can still suffer from frequency-selective channel response or inter-symbol interference from baseband antialiasing filter, as well as carrier frequency error (CFO) of local oscillators (LO) and symbol timing offset (STO) of sample clocks between VSG and VSA. These effects can be eliminated if we can synchronize reference clocks between VSG and VSA, and compare the captured samples at the PA input and output [3][4]. However, this technique does not work for a PA integrated into a transmitter in SoCs solutions. SoCs usually have no access to PA input and cannot either provide a reference clock to equipment or lock to an external clock.

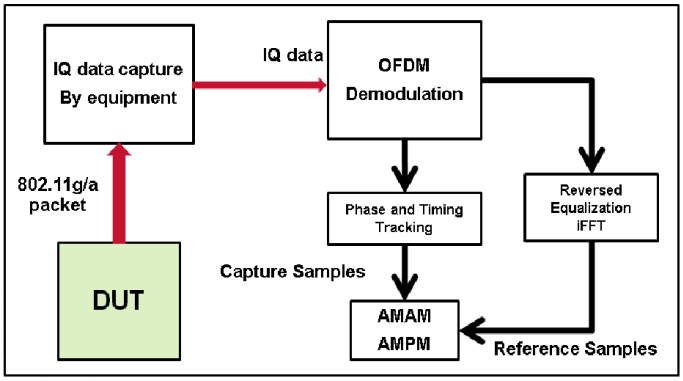


Figure 1: AM-AM/AM-PM analysis block diagram

In this paper, a method is proposed to measure PA nonlinearity with OFDM signals that does not require knowledge of transmitting signals in advance. It is extremely helpful for checking effectiveness of the DPD and for measuring packets with real data payload. Block diagram in Fig. 1 shows samples collected by equipment going through demodulation process for OFDM packets. The reference time domain samples can be obtained by running inverse fast Fourier transform (IFFT) on demodulated frequency domain symbols. Frequency-selective channel response can be cancelled by reversing the applied equalization on the reference samples.

CFO and STO can also be resolved by phase and timing tracking in part of the OFDM demodulator. As a result, the time domain samples at the PA output can be adjusted to remove these impairments. By comparing the recovered reference samples and the adjusted captured samples, AM-AM and AM-PM distortion can be calculated. However, the distortion also creates spectral regrowth. Receiver baseband antialiasing filter in the demodulator results in loss of information due to its rejection of leakage power in adjacent channels. This paper proposes to remove the receiver baseband filter to preserve information in time domain. Sampling clock of two or three times symbol clock can be used for better CFO and STO estimation accuracy. The paper is organized as follows: Section II models the OFDM signals to derive AM-AM/AM-PM distortion, section III discusses the recovery of reference samples, section IV explains the adjustment of capture samples and section V provides the measurement setup and results.

978-1-4799-4423-1/14/$31.00 ©2014 IEEE

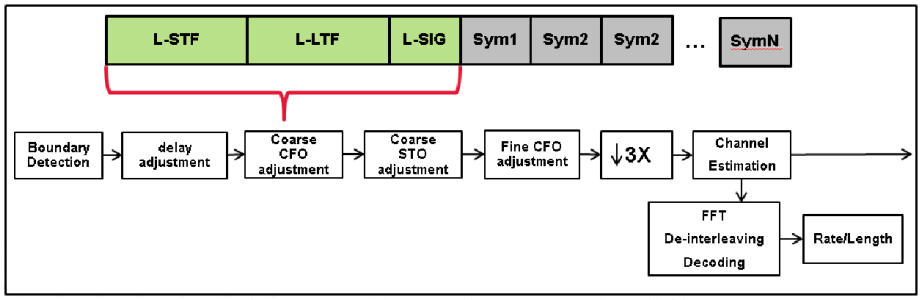


Figure 2: Correction steps in STF, LTF and SIG field

## II. OFDM SIGNAL MODLE TO CHARACTERIZE AM-AM/AM-PM DISTORTION

OFDM signals can be expressed as IFFTs of data symbols, $a_{l,k}$ where $l$ is the OFDM symbol time index and $k$ is the subcarrier frequency index. Preceded by a guard interval, $T_g$, to avoid ISI, the complex baseband symbols can be written as shown in equation (1), per reference[5].

$$s_{l,k}(n) = a_{l,k} \cdot e^{j2\pi\left(\frac{k}{NT}\right)(nT - T_g - lT_s)} \quad (1)$$

where $T$ *and* $T_s$ denote sampling time and OFDM symbol time, respectively, and $N$ denotes the FFT size. After the digital-to-analog converter (DAC), the spectrum of the OFDM signals is shaped by the transmitter baseband filter with impulse response, $h(t)$. The filtered complex baseband symbols become

$$s_{l,k}(t) = \sum_i h_i(t) a_{l,k} \cdot e^{j2\pi\left(\frac{k}{NT}\right)(t - T_g - lT_s - \tau_i)} \cdot u(t - lT_s - \tau_i)$$

$$u(t) = \begin{cases} 1, & 0 \le t \le T_s \\ 0, & else \end{cases} \quad (2)$$

This signal is up-converted to RF frequency by the LO. Assume $f_c$ is the LO frequency, the RF signal of the $l^{th}$ OFDM symbol at input of the PA can be written as

$$T_l(t) = \mathcal{R}e\left( e^{j2\pi f_c t} \cdot \sum_{k=-\frac{N}{2}}^{\frac{N}{2}} s_{l,k}(t) \right) = A(t) \cdot cos(2\pi f_c t + \phi(t)) \quad (3)$$

The nonlinearity of the PA distorts $T_{l,k}(t)$ to $T'_{l,k}(t)$:

$$T'_l(t) = \mathcal{R}e\left( e^{j2\pi f_c t} \cdot \sum_{k=-N/2}^{N/2} s'_{l,k}(t) \right)$$

$$= A'(A(t)) \cdot cos\left(2\pi f_c t + \phi'(A(t))\right) \quad (4)$$

$A'(A(t))$ and $\phi'(A(t))$ are the desired AM-AM and AM-PM functions. They can also be derived from the equivalent baseband signals of the $l^{th}$ OFDM $\sum_{k=-N/2}^{N/2} s_{l,k}(t)$ *and* $\sum_{k=-N/2}^{N/2} s'_{l,k}(t)$,where $s'_{l,k}$ are the distorted baseband symbols.

The PA output signal is then down-converted and sampled by the equipment, with LO running at a different frequency and captured with analog-to-digital converters (ADCs) clocking at different rates. With CFO of $\Delta f$ and STO of $\zeta=(T'-T)/T$, the captured complex baseband symbols can be derived as shown in equation (5), per reference[6].

$$\gamma_{l,k}(n) = \left(e^{j2\pi\Delta f n(1+\zeta)T}\right)\left(\sum_l \sum_k s'_{l,k}(n(1+\zeta))\right) \quad (5)$$

To accurately characterize power amplifier performance, impairments which are not related to the power amplifier needs to be removed from the captured IQ data. Using the proposed technique, one can obtain $s'_{l,k}$ from $\gamma_{l,k}$ and calculate the AM-AM and AM-PM curves from $\sum_{k=-N/2}^{N/2} s_{l,k}(t)$ and $\sum_{k=-N/2}^{N/2} s'_{l,k}(t)$

## III. THE REFERENCE SAMPLES RECOVERY

The idea to recover the reference samples from the captured samples relies on a standard OFDM demodulator. IEEE 802.11a signal contains 16μs preamble. The first 8μs is a short training field (STF). This period is used for delay adjustment, coarse CFO, and coarse STO adjustment. The second 8μs period, called long training field (LTF), is used for fine CFO correction and channel estimation. A one-tap equalizer is used for OFDM signal to equalize channel response of transmitter baseband filter.

The 4μs period after LTF is called SIG field. This field is interleaved and convolutional-coded. By decoding this field after FFT, code rate and packet length can be obtained. This information is needed to recover the input samples. Fig. 2 shows the correction steps on STF, LTF, and SIG fields.

Blue path in Fig. 3 shows the flow to recover reference samples in payload. After the SIG field, there are payload symbols; each symbol is 4μs long with 52 active subcarriers. Subcarriers numbered −21, −7, +7 and +21 are pilot subcarriers. Pilot-based synchronization is used in this paper. Known BPSK data in the pilot subcarriers can be used to perform residual CFO and STO correction. If FFT window drift is small enough not to create ISI, and if STO is small enough not to cause inter-carrier interference (ICI), equation (5) can be simplified to the following equation for $n$ inside the FFT window.

$$\gamma_{l,k}(n) = \left(e^{j2\pi\Delta f n(1+\zeta)T}\right) s'_{l,k}(n(1+\zeta))$$

$$= \left(e^{j2\pi n(\Delta f(1+\zeta)T + \frac{k}{N}\zeta)}\right) s'_{l,k}(n) \quad (6)$$

The phase error on pilot subcarriers can be expressed as $\Theta = 2\pi n(\Delta f(1+\zeta)T + \frac{k}{N}\zeta)$. CFO and STO can be obtained by $\partial\Theta/\partial n$ and $\partial\Theta/\partial k$, respectively. The CFO can be corrected by rotating the time domain samples, and the STO can be corrected by fractional delay filtering in each OFDM symbol. By running FFT on time domain samples, frequency domain data ( $a'_{l,k}$) can be recovered. Assuming the bit error rate (BER) is 0%, the original data $a_{l,k}$ can be fully restored by subcarrier demodulation mapping. The phase and amplitude error caused by PA nonlinearity is removed by this process. This method requires 0% BER for proper reference sample recovery. If the BER is not 0%, lower modulation index can be chosen to lower the SNR requirement.

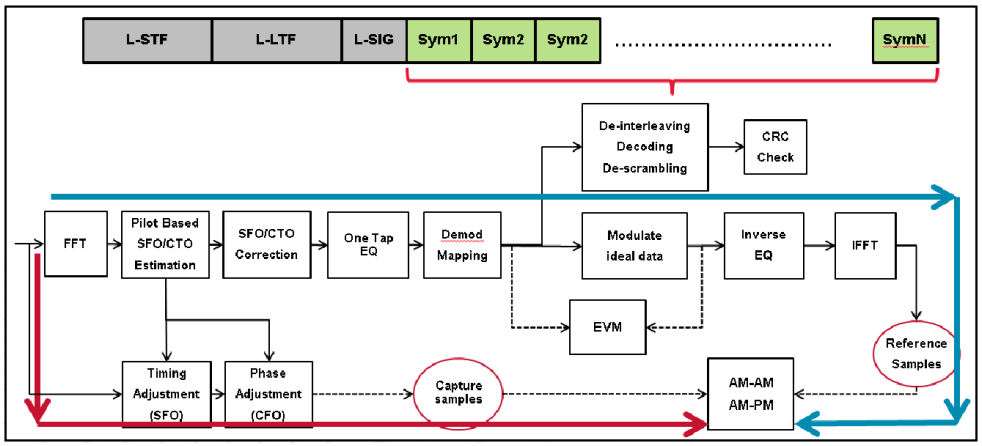


Figure 3: Reference samples recovery flow (blue) and captured samples adjustment flow (red)

To reconstruct the filtered baseband samples $\sum_{k=-N/2}^{N/2} s_{l,k}(n)$, the channel response estimated in the LTF is applied to the recovered frequency domain symbols, which is later converted to time domain samples with IFFT.

## IV. THE CAPTURE SAMPLES ADJUSTEMENT

With gain compression and phase distortion from the PA, the signal power can expand as wide as the 2nd adjacent channel. A conventional method is capturing at least three times the signal bandwidth for 5th order distortion to preserve all information in time domain. Since the proposed demodulator is running on the symbol clock frequency, the comparison between the capture samples and reference samples can be done only at the same frequency. For example, in 20MHz bandwidth mode, the symbol is clocked at 20MHz. Thus a down-sampler is required to down-sample the captured data to 20MHz. However, the rejection of the expanded data bandwidth further distorts the time domain signal.

To circumvent this issue, the antialiasing filter before down-sampler needs to be widened to capture the expanded analog signals. In this paper, IQ digitizer sampling clock is set to three times the symbol clock for CFO and STO estimation accuracy. After the coarse CFO and STO adjustment, the captured data is down-sampled by a factor of 3 before going to the OFDM demodulator, as shown in Fig. 2. It is noted that the antialiasing filter is completely removed to avoid cutting off the expanded spectrum, which is why we cannot directly use signal constellations in the state-of-the-art VSA to measure AM-AM/AM-PM distortion.

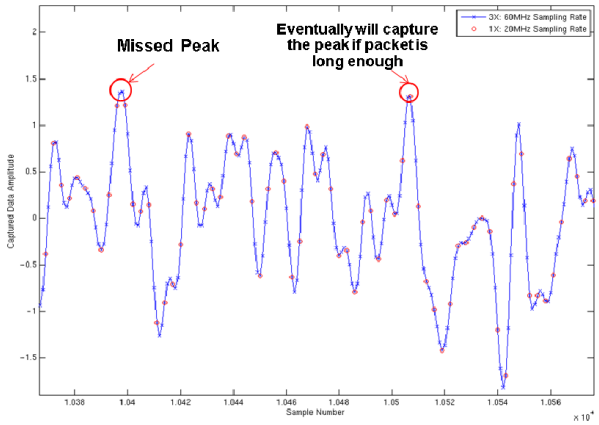


Figure 4: Subsampling eventually capture the peak if packet is long and random.

Since the down-sampling is done without the baseband antialiasing filter, the leakage power from spectrum regrowth creates aliasing in the frequency domain. However, AM-AM and AM-PM curves are meant to measure the amplitude and phase information statistically in the time domain. Such aliasing would not affect the measurement accuracy. As shown in Fig. 4, performing subsampling on the signal which is higher than the Nyquist rate misses some samples, especially the peak. However, subsampling eventually captures the peaks, which 3x sampling speed would have captured, as long as the packet is long and random.

After down-sampling, the red path in Fig. 3 shows the flow to adjust the captured samples on payload data. Since the pilot-based CFO and STO estimation are done in section III, they can be used to adjust residue frequency and timing errors in the time domain samples. This process converts measured samples of $\gamma_{l,k}$ to $s'_{l,k}$. We can obtain the adjusted time domain samples of $\sum_{k=-N/2}^{N/2} s'_{l,k}(n)$ to compare with the recovered reference time domain samples of $\sum_{k=-N/2}^{N/2} s_{l,k}(n)$ for AM-AM/AM-PM calculation.

## V. MEASUREMENT SETUP AND RESULTS

DUT in this paper is an integrated PA SoC solution with DPD enabled. Equipment used to capture IQ data is a spectrum analyzer. IQ digitizer function in the spectrum analyzer is used to capture IQ data at RF frequency. IQ data is processed by MATLAB for demodulation, CFO and STO recovery, and AMAM/AMPM analysis.

### A. *Vector signal generator as DUT*

This test uses an Agilent VSG as DUT. VSG and spectrum analyzer are not synchronized, and VSG sends a 0dBm 802.11g signal with pseudorandom payload data. After correcting frequency and timing on capture IQ data and recovering reference data by a demodulation-modulation process, we can scatter plot the input and output IQ data. Sixth-order polynomial regression is applied to get averaged AM-AM/AM-PM, which is demonstrated as red curve in Fig. 5. Result shows flat AM-AM and AM-PM. At the low-power region, the AM-PM data shows wider spread. It is because when amplitude is small, a slight amplitude change is misinterpreted as phase change.

### B. *Residue AMAM/AMPM analysis with proper DPD*

The second test demonstrates the capability of this method on analyzing PA nonlinearity after DPD, with real packet

transmission and without knowledge of input data. Fig. 6 shows the normalized AM-AM/AM-PM in magnitude. Fig. 7 shows the AM-AM/AM-PM versus output power. EVM of this signal is −33dB. The result clearly shows the AM-AM is not fully compensated. The maximum residue AM-AM is around −0.5dB, and the maximum residue AM-PM is around −0.5deg. Because there are only a few data points at high power, the polynomial regression does not fit properly at the end of the averaged AMPM curve.

### *C. Residue AMAM/AMPM analysis with improper DPD*

In this test, we intentionally applied an offset on DPD compensation. Fig. 8 shows 1.5deg degradation on maximum AMPM. The EVM of this signal is −26.56dB. Incorrect DPD compensation results in higher residue AM-PM, thus degrading EVM performance.

## VI. CONCLUSION

This paper has proposed a methodology to measure AM-AM/AM-PM curves of integrated PA nonlinearity on SoCs, using any equipment capable of sampling IQ data. The proposed method does not require a training sequence or clock synchronization. It may find applications in debugging packets or adaptive DPD calibration. Data processing of this work utilizes a standard OFDM demodulator with baseband antialiasing filter removed. Since most hardware already exists in receivers of today's SoCs, the proposed method can be easily adopted on-chip to characterize PA nonlinearity in real-time for adaptive DPD calibration.

## VII. REFERENCES


[1] S.-W Chen, W. Panton and Robert Gilmore, , "Effects of nonlinear distortion on CDMA communication systems," *Microwave Theory and Techniques, IEEE Transactions on* , vol.44, no.12, pp.2743,2750, Dec 1996

[2] Michael S. Heutmaker, E. Wu, Chauncey Herring and John R. Welch, "Using Digitally-Modulated Signals to Measure the Gain Compression and Phase Distortion of a Radio Frequency Amplifier," *ARFTG Conference Digest-Fall, 46th* , vol.28, pp.56,63, Nov. 1995

[3] Michael S. Heutmaker, "The error vector and power amplifier distortion," *Wireless Communications Conference, 1997., Proceedings* ,pp.100,104, 11-13 Aug 1997

[4] J. Ibanez-Diaz, C. Pantaleon, I. Santamaria, T. Fernandez and D. Martinez, "Nonlinearity estimation in power amplifiers based on subsampled temporal data," *Instrumentation and Measurement, IEEE Transactions on* , vol.50, no.4, pp.882,887, Aug 2001

[5] M. Speth, S. Fechtel, G. Fock, and H. Meyr, "Optimum receiver design for broadband systems using OFDM-part I," IEEE Trans. Commun., Vol. 47, pp. 1668-1677, Nov. 1999.

[6] Dah-Chung Chang, "Analysis and Compensation of Channel Correction in Pilot-Aided OFDM Systems With Symbol Timing Offset," *Electro/information Technology, 2006 IEEE International Conference on* , pp.324,329, 7-10 May 2006


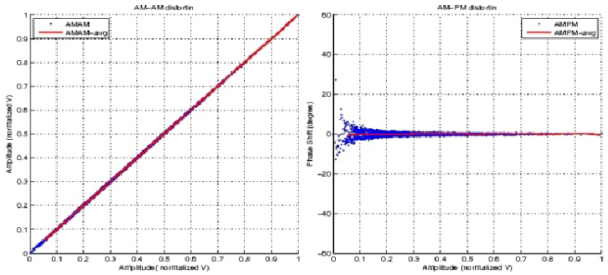

Figure 5: Normalized AMAM/AMPM with VSG as DUT

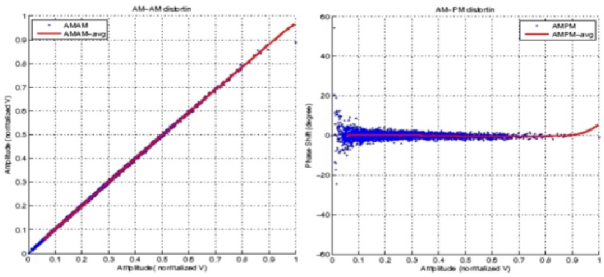

Figure 6: Normalized AMAM/AMPM with SoC as DUT

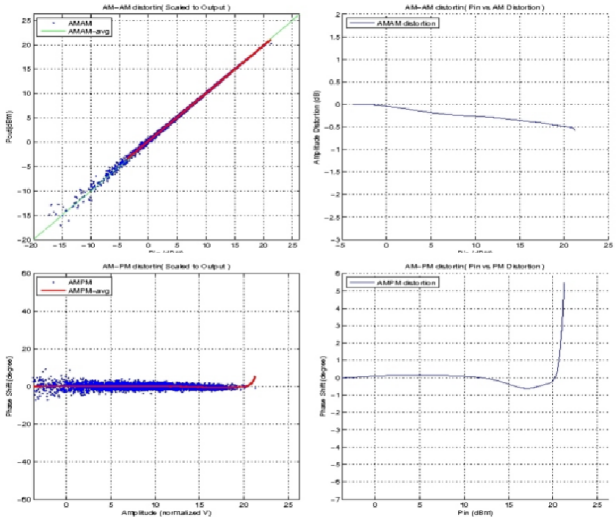

Figure 7: AMAM/AMPM versus output power on SoC with DPD compensation

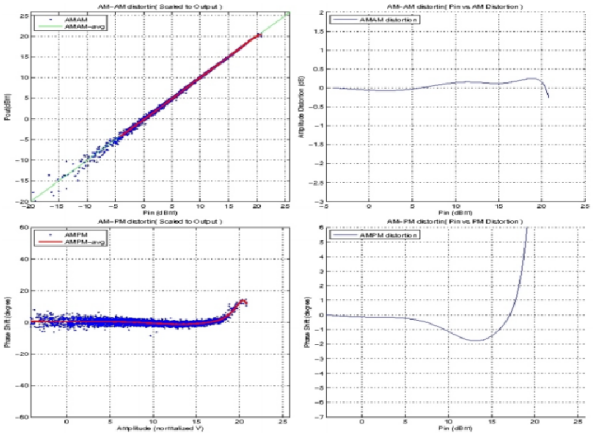

Figure 8: AMAM/AMPM versus output power on SoC with offseted DPD compensation

# Nonlinear System Behavioral Modeling Using Reduced Transmitter Observation Receiver Bandwidth

*Farouk Mkadem and Slim Boumaiza*

*Emerging Radio Systems Group, University of Waterloo, Waterloo, ON, N2L 3G1, Canada*

**Abstract — A new approach for modeling wideband power amplifiers (PAs) using a reduced transmitter observation receiver (TOR) bandwidth is proposed. The general sampling theorem (GST) was used to lower the bandwidth requirement of the TOR. This approach highlighted that linearization should be carried out prior to the application of GST; two digital predistortion approaches using reduced TOR bandwidth were used for this purpose. Measurements were conducted using a 250-W Doherty PA driven with a 20 MHz WCDMA input signal. Good agreement between the modeled and the measured output spectrum was found across 100 MHz when the TOR bandwidth was reduced as low as 27.65 MHz.**

**Index Terms — Behavioral Modeling, Complexity Reduction, Volterra series, Wideband Power Amplifier.**

## I. Introduction

Traditionally, radio frequency (RF) building blocks have been designed and optimized separately before integrating them in a radio system. Unfortunately, their performances often vary noticeably when operating as part of a system. To minimize the performance degradation, generally inter-stage networks are added and the building block parameters are adjusted so that the overall system's figures of merit are optimized. This step is increasingly vital given the current design trend towards RF systems with a high level of integration. However, given the high level of complexity involved, the analysis and optimization of an RF system can no longer be conducted on the test bench. These tasks are accomplished more efficiently using computer aided design (CAD) tools through which optimum performance is more likely to be achieved. This requires a priori modeling of the behavior of the building blocks to accurately predict their responses when part of the system. The power amplifier (PA) is a critical block in an RF system as it dominates the sources of nonlinearity and power consumption. CAD analysis of the PA effects on overall system performance can be completed by replacing the PA with its schematic along with the transistor's compact model or with its behavioral model. Compact models tend to be very computationally demanding and inaccurate in predicting the behavior of the PA when driven with wideband modulated signals. For fast and accurate system level analysis, behavioral models are more suitable since they can accurately reproduce the output of the PA under specific conditions. Behavioral models can be constructed to mimic the behavior of an RF integrated circuit (RFIC) PA based on its schematic, or on a real PA demonstrator.

Low Pass Equivalent (LPE) Volterra series [1] is a general framework for predicting the dynamic nonlinear behavior of a PA. Identification of the LPE Volterra series kernels is carried out using samples of the input and output envelopes collected when the PA under test is stimulated with a realistic modulated signal. Modeling a PA demonstrator driven with a broadband signal, in order to analyze the performance of the system (efficiency and linearity), can be very challenging. Vector signal analyzers (VSA) are used to emulate the transmitter observation receiver (TOR) which captures the PA output signal. However, as bandwidth requirements for future radio systems increase, VSA will fall short. It calls for the development of new approaches to constructing accurate LPE Volterra series behavioral models for wideband PAs using a VSA or a TOR with reduced bandwidth.

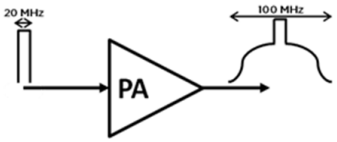


Fig. 1. Signal representation of a nonlinear PA

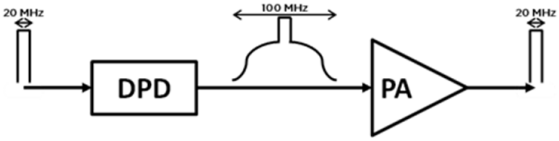


Fig. 2. Signal representation of a nonlinear PA with an exact DPD

In this paper, a new approach is introduced to enable the application of the generalized sampling theorem (GST) [2] for the construction of a behavioral model using a VSA or a TOR with reduced bandwidth. This approach highlighted the fact that linearization should be carried out prior to the application of the GST. The proposed approach can be used for any building block in a radio system that exhibits nonlinearities. Section II details the proposed approach and its theoretical roots. Section III provides measurement results for validation. Conclusions will be given in Section IV. Note that, both the VSA and the TOR will be generically referred to hereafter as TOR.

## II. Proposed Approach

Traditionally, to construct a PA behavioral model, the PA is first driven with a modulated signal while a TOR is used to capture the output signal. Then, an LPE Volterra series behavioral model is identified to describe the input to output relationship. This model can then be used with CAD tools to predict both the response of the PA and its impact on overall system performance. To illustrate, Fig. 1 shows a typical nonlinear PA driven with a 20 MHz input signal. Since the PA is a nonlinear system, its output signal has a bandwidth that is

978-1-4799-4423-1/14/$31.00 ©2014 IEEE

TABLE I
NMSE AND PSDE BETWEEN THE MODELED AND THE MEASURED OUTPUT SPECTRUM

| Output Captured Bandwidth (MHz) | Without DPD | | W/ DPD with Reduced TOR Bandwidth | | W/ Band-limited DPD | | W/ Modified DPD with Reduced TOR Bandwidth | |
|---|---|---|---|---|---|---|---|---|
| | NMSE | PSDE | NMSE | PSDE | NMSE | PSDE | NMSE | PSDE |
| 27.65 | -31.3 | -39.9 | -39.5 | -48.1 | -30.4 | -39.0 | -43.8 | -52.6 |
| 36.86 | -35.3 | -43.8 | -40.8 | -49.5 | -33.8 | -42.4 | -44.1 | -52.9 |
| 55.30 | -44.5 | -53.3 | -43.5 | -52.2 | -42.4 | -51.1 | -43.5 | -52.3 |
| 92.16 | -45.3 | -54.0 | -43.2 | -52.0 | -43.2 | -52.0 | -43.2 | -52.0 |

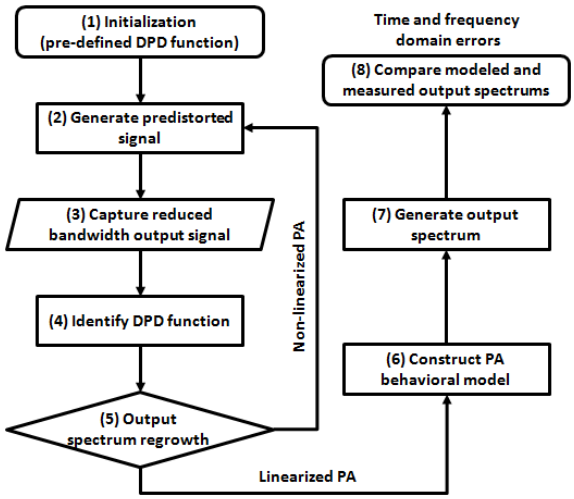

Fig. 3. Behavioral model identification approach

typically 5 times that of the input signal (i.e., 100 MHz). Therefore, in order to construct the corresponding LPE Volterra series model, the TOR is required to have a bandwidth equal to at least 100 MHz. This requirement is more stringent when deploying wider bandwidth signals. For example, to accurately model the PA when using advanced-LTE (where the modulation bandwidth can reach 100 MHz), a TOR with a bandwidth equal to at least 500 MHz would be required. Not only would this result in a frequency dispersive receiver across the signal bandwidth, the cost and power consumption of the TOR would be excessive and not feasible for certain applications.

### A. General Sampling Theorem

The GST [2] proposed a solution for capturing the output signal of a nonlinear system (e.g., PA), with a receiver that has a bandwidth less than the output signal bandwidth. The GST stipulates that for an arbitrary function *f(t)*, with no required limit on the bandwidth of its output signal, if a one-to-one mapping function *g(t)* can be found such that *g(f(t))* is band limited, then *f(t)* can be fully recovered by sampling at the points $t_n=nT_s$ as in:

$$f(t)=g^{-1}\left\{\sum_{-\infty}^{\infty} g\left[f(t_n)\right]\frac{\sin\left[w_0(t-nT_s)\right]}{w_0(t-nT_s)}\right\} \quad (1)$$

The GST can be explained using Fig. 2, where the PA and the exact digital predistortion (DPD; i.e., the PA inverse) correspond to the functions *f(t)* and *g(t)* in (1), respectively. In this case, it is clear that the output signal bandwidth is compressed back to 20 MHz from 100 MHz. Therefore, a TOR with a bandwidth less than 100 MHz can accurately recover the output signal using (1), and consequently enables the identification of an LPE Volterra series behavioral model.

### B. Behavioral Modeling Approach Using the Generalized Sampling Theorem

In previous works, results of the GST have been used incorrectly; it was claimed the DPD could be identified using the GST. However, to correctly apply the GST, a priori knowledge of the DPD function is required as given by (1) and explained in [2]. Often, the GST has been confused with under-sampling where a TOR with reduced bandwidth was applied to capture the output of the PA without a priori identification of the function *g(.)* (i.e., the DPD). In this paper, the DPD is identified first using a TOR with reduced bandwidth which enables the application of the GST. This is illustrated in Fig. 3. Two DPD schemes were used in this paper, namely the band-limited Volterra series [3] and a reduced TOR bandwidth LPE Volterra series pruned using G-functionals [4].

The band-limited Volterra series [3] guarantees the linearization and modeling of the PA output signal within the observed bandwidth. Authors in [3] introduced a band-limiting function to control the bandwidth expansion when the input signal passes each nonlinear Volterra series operator. Conversely, using a DPD with a reduced TOR bandwidth allowed linearization within and outside the observed band by using a pre-defined nonlinear function to enable estimation of the spectrum regrowth outside of the TOR bandwidth. In other words, the DPD with reduced TOR bandwidth proved that a fraction of the PA output signal was sufficient to linearize all of the spectrum regrowth of the PA's output signal. An LPE Volterra series pruned with G-Functionals [4] was used as the DPD engine with reduced TOR bandwidth which was further modified by applying the band-limited functions introduced in [3] when identifying the behavioral model (step 7 in Fig. 3). This enabled the application of the GST after linearizing the PA using the DPD with reduced TOR bandwidth.

## III. MEASUREMENT RESULTS

A 250 W LDMOS Doherty PA was used as the device under test. The PA was driven with a 20 MHz 4C WCDMA

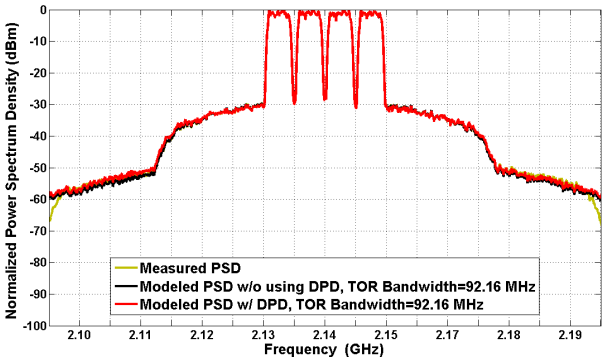


Fig. 4. Power spectrum density comparison between the measured and modeled output spectrums without using DPD and when using DPD with TOR bandwidth of 92.16 MHz

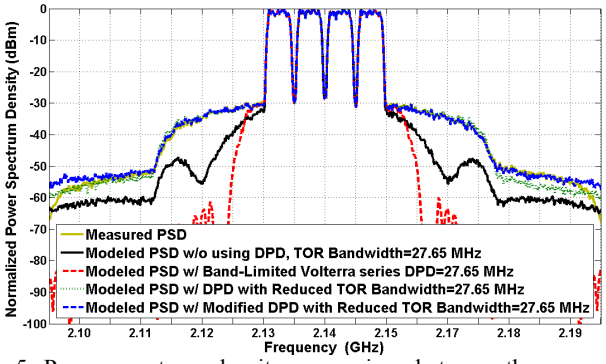


Fig. 5. Power spectrum density comparison between the measured and modeled output spectrums without using DPD and when using DPD with reduced TOR bandwidth of 27.65 MHz

input signal into compression resulting in an output signal with a bandwidth of about 92.16 MHz. An N9030A PXA signal analyzer was used to capture the output signal with the analysis bandwidth set to 27.65, 36.86, 55.30, and 92.16 MHz.

The TOR bandwidth was first set to 92.16 MHz to prove the validity of the LPE Volterra series model in predicting the output spectrum. It is clear from Table I that the normalized mean square error (NMSE) and the power spectrum density error (PSDE) showed excellent modeling capability. Fig. 4 also demonstrates good agreement between the modeled and measured output spectrum. However, as the TOR bandwidth decreased, the modeling of the PA response became inaccurate and the modeled spectrum was far from the actual spectrum, especially outside of the observed band. For example, Table I shows an NMSE of -31 dB and a PSDE of -40 dB when the TOR bandwidth was set to 27.65 MHz. This phenomenon is even more apparent in Figs. 5 and 6, where the modeled output spectrum fails to mimic the measured output spectrum outside of the observed band. This proves that the GST cannot be applied unless the DPD is first identified. To support this assertion, the application of (1) will guarantee an accurate recovery of the output spectrum shown hereafter.

When applying the band-limited Volterra series DPD, no enhancements in the NMSE or PSDE were observed. In fact, the band-limited Volterra series only guaranteed modeling within the observed band. This is more apparent from Figs. 5 and 6, where the dashed red lines show empty spectrums outside of the TOR bandwidth. Again, the GST cannot be

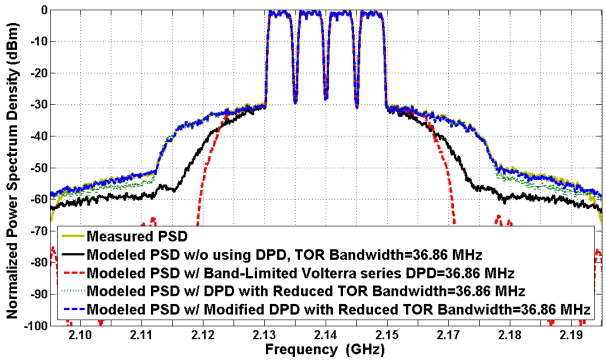


Fig. 6. Power spectrum density comparison between the measured and modeled output spectrums without using DPD and when using DPD with reduced TOR bandwidth of 36.86 MHz

applied because full linearization of the PA was not achieved (i.e., the PA did not converge to the configuration in Fig. 2).

Conversely, when applying the proposed approach of Fig. 3, and using the DPD with reduced TOR bandwidth, the NMSE and PSDE were considerably enhanced and approached the case where the TOR bandwidth was set to 92.16 MHz, as given in Table I. This was more pronounced when the band-limited Volterra function was applied during the identification of the behavioral model (Step 7 of Fig. 3). Indeed, Table I shows an NMSE of about -44 dB and a PSDE of -53 dB when the TOR bandwidth was set to only 27.65 MHz. Figs. 5 and 6 show that the proposed DPD allowed the application of the GST to recover the output spectrum even outside of the observed band. This was possible due to the initial identification of the function *g(.)*.

## IV. Conclusion

A new approach to enable the application of the GST when predicting the wideband output spectrum of a nonlinear PA using a TOR with reduced bandwidth has been presented. A DPD with reduced TOR bandwidth was first applied to compress the output spectrum of the PA. Good agreement was observed between the modeled and measured output spectrums of the PA across a 100 MHz bandwidth when the TOR bandwidth was set as low as 27.65 MHz.

## References

[1] M. Isaksson, D. Wisell, and D. Ronnow, "A comparative analysis of behavioral models for RF power amplifiers," *IEEE Trans. Microw. Theory Tech.*, vol. 54, pp. 348-359, Jan. 2006.

[2] Y. M. Zhu, "Generalized sampling theorem," *IEEE Trans. Circuits and Systems II: Analog and Digital Signal Processing,* vol. 39, no. 8, pp. 587-588, Aug. 1992.

[3] C. Yu, L. Guan, E. Zhu, and A. Zhu, "Band-Limited Volterra Series-Based Digital Predistortion for Wideband RF Power Amplifiers," *IEEE Trans. Microw. Theory and Tech.* pp. 4198-4208, vol. 60, no. 12, Dec. 2012

[4] F. Mkadem, D. Y. Wu, and S. Boumaiza, "Wiener G-Functionals for Nonlinear Power Amplifier Digital Predistortion," 2012 *IEEE MTT-S 2012 International Microwave Symposium*, Montreal, QC, Canada

# †Sensitivity of AM/AM linearizer to AM/PM distortion in devices.

F.L. Ogboi†, P. Tasker†, Z. Mohkti†, J. Lees†, J. Benedikt†, S. Bensmida*, K. Morris*, M. Beach*, J. McGeehan*

†Centre for High Frequency Engineering, Cardiff University, The Parade, Cardiff, CF24 3AA, UK

*Centre for Communications Research, University of Bristol, Woodland Road, Bristol, BS8 1UB, UK

†Tel: +44 7531951316, †Email: ogboifl2@Cardiff.ac.uk

**Abstract — Baseband injection is a technique that can provide a cost-effective linearizing solution that can be combined with supply modulation techniques such as envelope tracking (ET), to minimize AM/AM distortion and potentially simplify the DSP linearization requirement and associated cost. Recently [8], a new approach for computing the baseband injection stimulus, formulated in the envelope domain, was introduced. The concept was originally demonstrated using a 10W Cree GaN-on-SiC HFET device. In this work its robustness with respect to alternative device technology is investigated using 25W Nitronex NPTB00025 GaN-on-SiC HEMT depletion-mode and a 10W, high-voltage LD-MOS, enhancement-mode devices. Its effectiveness in dealing with AM/AM distortion is confirmed.**

**Index Terms — Distortion, Modulation, Multi-tone, Power amplifiers, signal.**

## I. Introduction

Active devices and amplifiers used in the wireless communication industry exhibit non-linear behavior, leading to distortion and reduced linearity [1]-[2]. Typically the power amplifier (PA) is designed targeting the RF power and efficiency specifications while Digital Signal Pre-distortion (DSP) addresses the linearity requirement. However, because of the relatively high power consumption of DSP systems in small-cell architectures, this architecture may be viable in future systems where the trend is increasing modulation bandwidths coupled with the scaling back of RF output power. Baseband injection is a technique that could provide a cost-effective aid by minimizing power amplifier AM/AM distortion, thus simplifying DSP linearization requirement, complexity [3]-[7] and hence power consumption. It can also be combined with supply modulation techniques such as envelope tracking (ET). Recently, a baseband linearization formulation, generalized in the envelope domain, was demonstrated [8]. The beauty of the approach lies in its scalability to different modulated excitations and applicability to different device technologies. It is the latter that is studied in this paper.

## II. Baseband Signal Formulation

Consider the behavior of a non-linear power transistor subjected to a modulated RF carrier stimulus at its input.

$$V_{1,rf}(t) = \frac{\hat{V}_{1,rf}(t)e^{j\omega_c t} + \hat{V}_{1,rf}(t)^* e^{-j\omega_c t}}{2}. \quad (1)$$

where $\hat{V}_{1,\mathrm{rf}}(t)$ is the input carrier voltage envelope and $\omega_c$ is the RF carrier frequency.

The RF output carrier current response of the device is given as follows:

$$I_{2,rf}(t) = \frac{\hat{I}_{2,rf}(t)e^{j\omega_c t} + \hat{I}_{2,rf}(t)^* e^{-j\omega_c t}}{2}. \quad (2)$$

Assuming that the transistor is a memory-less non-linear system the envelope transfer characteristic can be modeled as follows:

$$\hat{I}_{2,rf}(t) = \sum_{n=0}^{m} \alpha_{2n+1} \left|\hat{V}_{1,rf}(t)\right|^{2n} \hat{V}_{1,rf}(t). \quad (3)$$

where $\alpha_1$ represents the linear gain of the system, $\alpha_3$ quantifies the level of third order intermodulation distortion, $\alpha_5$ quantifies the level of fifth order intermodulation distortion, and so on, up to the desired maximum order m.

In [8], an envelope formulation for the output baseband voltage envelope signal $\hat{V}_{2,\mathrm{bb}}(t)$ was introduced, as follows:

$$\hat{V}_{2,bb}(t) = \sum_{p=1}^{q} \beta_{2p} \left|\hat{V}_{1,rf}(t)\right|^{2p}. \quad (4)$$

where $\beta_{2p}$ are the even order voltage component scaling coefficients and $q$ specifies the selected maximum range; bandwidth. The motivation for using this formulation lies in the fact that only cancelling odd-order intermodulation terms will be added to the RF output current envelope response. Hence, only the coefficients in (3) will be modified such that

$$\alpha_{2n+1}|_{n=1}^{m} = f\left(\beta_2, \beta_4, \ldots \beta_{2p}, \ldots \beta_{2q}\right). \quad (5)$$

Optimizing baseband linearization requires the determination of the coefficients $\beta_{2p}$ that set $\alpha_{2n+1}|_{n=1}^{m} = 0$, independent of signal complexity and device technology.

## III. Measurement System

In this paper we will confine analysis to addressing systems with intermodulation distortion up to fifth order (m=2). The baseband linearization range will now be restricted to forth order (q=2), hence equating to determining the values of $\beta_2$ and $\beta_4$ that can simultaneously set $\alpha_3 = 0$ and $\alpha_5 = 0$. This was performed using the measurements system shown in Fig.

978-1-4799-4423-1/14/$31.00 ©2014 IEEE

1, a fully vector-error corrected modulated LSNA-based measurement system integrated with both RF fundamental and harmonic load-pull and baseband signal injection.

All the measurements are calibrated to the device package plane using a custom built 50 Ω TRL test fixture. The calibration extended over a wide bandwidth, precisely 50MHz baseband bandwidth and 100MHz RF bandwidth for each of the first three harmonics. A modulated 3-tone excitation centered at 2 GHz, with 2MHz tone spacing and PAPR of 4.77dB was used with fundamental and all harmonic frequencies terminated into a passive 50Ω load environment.

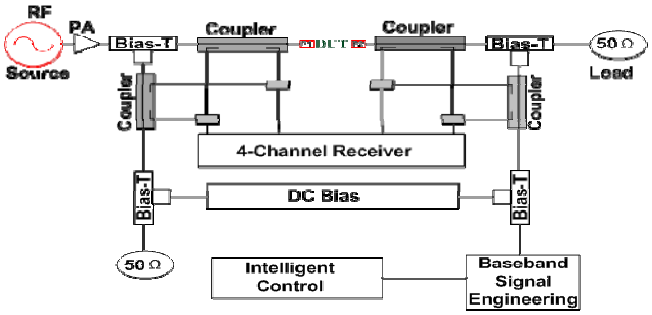


Fig. 1. Baseband waveform engineering and modulated RF measurement system

## IV. Technology Nonlinear Behaviour

Two device technologies were investigated; a 25W Nitronex NPTB00025 GaN-on-SiC HFET depletion-mode device, and a 10W, high-voltage LD-MOS, enhancement-mode device. The Nitronex device was biased at a drain voltage of +28V and a gate voltage of -1.3V, and the LDMOS device was biased at +32V drain voltage and +2.8V gate voltage targeting class AB operation on both devices and giving a quiescent current of 12% of $I_{DSmax}$. They were then both driven into 2.4dB compression, with the output terminated into passive 50 Ohms. The LDMOS device giving a peak envelope power (PEP) of approximately 33dBm and the 25W GaN-on-SiC HFET device, a peak envelope power PEP of 40dBm. Reference conditions were established with baseband output voltage set to zero (reference baseband short circuit state) and are shown in Fig. 2 and 3. Results indicate a non-well behaved AM/PM (green curve) distortion in the 10W LDMOS device and 7th order distortion. A well behaved AM/PM (green curve) distortion in the 25W GaN-on-SiC HFET with only 5th order distortion present.

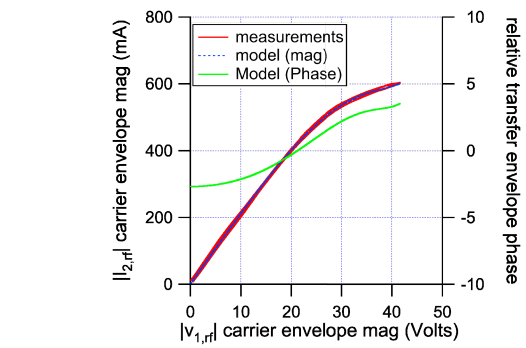


(a)

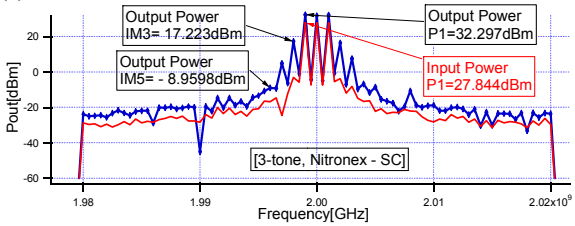


(b)

Fig. 2 25W GaN-on-SiC HFET Device: Measured reference baseband short circuit state. (a) Dynamic transfer characteristic and (b) Power Spectra.

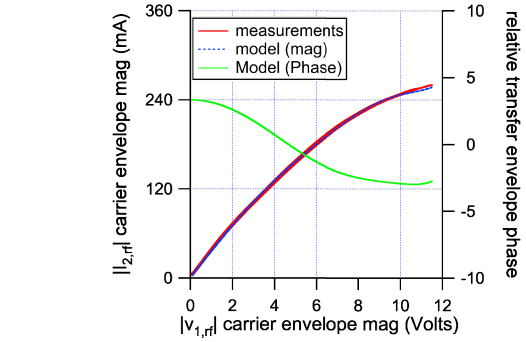


(a)

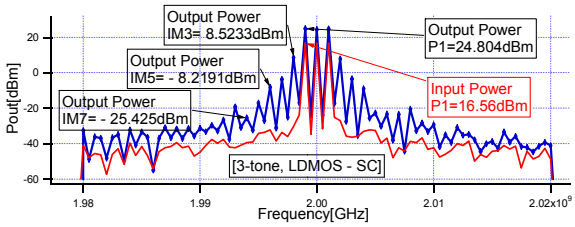


(b)

Fig. 3. LDMOS device: Measured reference baseband short circuit state. (a) Dynamic transfer characteristic and (b) Power Spectra.

## V. Linearization Results Analysis

The optimized baseband injection signal was determined by adjusting the values of $\beta_2$ and $\beta_4$ in order to simultaneously

minimize $\alpha_3$ and $\alpha_5$. The results achieved are shown in Fig. 2 to 5. In the case of the 25W GaN-on-SiC HFET the results clearly show that this device was successfully linearized with respect to AM/AM. This is shown by the red (AM/AM) and blue (model defined by $\beta_2$ and $\beta_4$) curve on the dynamic transfer characteristic of Fig.4a, a considerable agreement. The green curve on the same figure, show the strong presence but a very well behaved AP/PM distortion. A result similar to that previously reported on the 10W GaN-on SiC HFET device [8]. However, in this case only modest overall linearity improvement of 13.62dBc in IM3 with the IM5 2.56dBc from the noise-floor were achieved. We believe that this level of AM/PM distortion, insensitive to baseband injection, observed in this device explains this limited overall improvement in linearity.

In the case of the 10W LDMOS, elimination of the AM/AM distortion was not completely possible. Hence, only an improvement of 10dBc was achieved in IM3 and none on IM5 on this device. This is because this device exhibited a non-well behaved AM/PM distortion, shown by the green curve on the dynamic transfer characteristics of Fig. 3a and 5a. Also a strong presence of the 7$^{th}$, order term, shown in Fig.3b and 5b respectively. These cannot be addressed using only two $\beta_{2p}$ even order voltage component scaling coefficients (meant for 3$^{rd}$ and 5$^{th}$ order term) nor AM/AM distortion canceller. However, the model defined by the coefficients and the AM/AM curve in these figures all agree, confirming AM/AM distortion mitigation effectiveness.

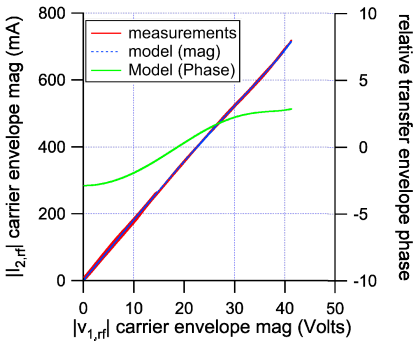


(a)

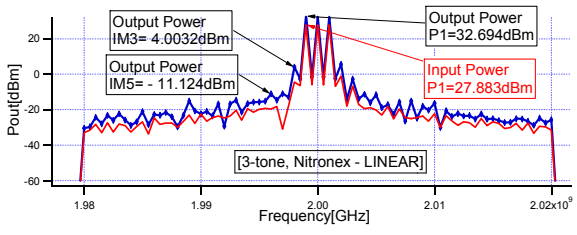


(b)

Fig. 4 25W GaN-on-SiC HFET Device: Measured linear state. (a) Dynamic transfer characteristic and (b) Power Spectra.

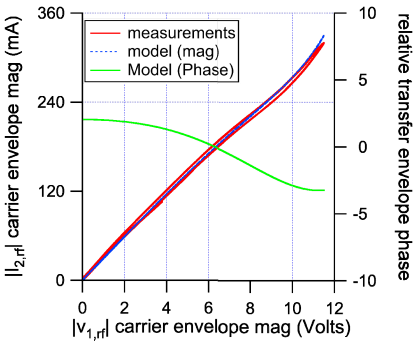


(a)

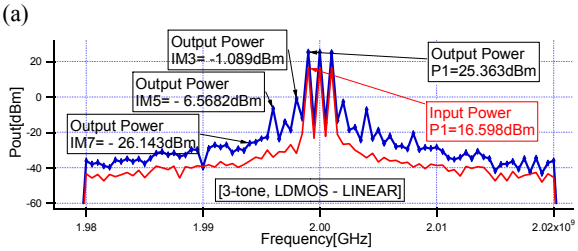


(b)

Fig. 5. LDMOS device: Measured linear state. (a) Dynamic transfer characteristic and (b) Power Spectra.

## VI. Conclusion

The robustness with respect to device technology of an envelope domain formulation which describes the baseband injection signal required to minimize the AM/AM distortion has been investigated. In both device technology investigated the formulation was able to minimize AM/AM distortion, hence confirming it would be a useful tool to use in conjunction with DSP. However, the need to use a more complex signal for higher than 5$^{th}$ order distortion was shown. Also, as expected, baseband injection has no impact on AM/PM distortion.

Importantly, this experiment confirmed [8] AM/AM efficacy, in the presence of severe AM/PM distortion.

New work on [8] is now planned to cost effectively suppress AM/AM, AM/PM distortions and also improve device efficiency.


## Acknowledgement

This work has been carried out as part of EPSRC grant EP/F033702/1. The authors would also like to thank CREE for supporting this activity and supplying the devices; specifically Ray Pengelly and Mr. Simon Wood.


## References


[1] Andrei Grebennikov, "RF and Microwave Power Amplifier Design". McGraw-Hill ISBN 0-07-144493-9

[2] John Wood, David E. Root, "Fundamentals of nonlinear behavioral modeling for RF and microwave design". Artech House, 2005.S Int. Microwave Symp. Dig., vol. 3, pp. 1721-1724, June 2003.

[3] Boumaiza, S.; Mkadem, F.; Ben Ayed, M., "Digital predistortion challenges in the context of software defined transmitters," General Assembly and Scientific Symposium, 2011 XXXth URSI , vol., no., pp.1,4, 13-20 Aug. 2011 doi: 10.1109/URSIGASS.2011.6050519

[4] Abd-Elrady, E., "A Recursive Prediction Error algorithm for digital predistortion of FIR Wiener systems," Communication Systems, Networks and Digital Signal Processing, 2008. CNSDSP 2008. 6th International Symposium on , vol., no., pp.698,701, 25-25 July 2008 doi: 10.1109/CSNDSP.2008.4610732

[5] Salkintzis, A.K.; Hong Nie; Mathiopoulos, P.T., "ADC and DSP challenges in the development of software radio base stations," Personal Communications, IEEE , vol.6, no.4, pp.47,55, Aug 1999, doi: 10.1109/98.788215

[6] Mehendale, M., "Challenges in the design of embedded real-time DSP SoCs," VLSI Design, 2004. Proceedings. 17th International Conference on , vol., no., pp.507,511, 2004 doi: 10.1109/ICVD.2004.1260971

[7] Mitra, B., "Consumer digitization: accelerating DSP applications, growing VLSI design challenges," Design Automation Conference, 2002. Proceedings of ASP-DAC 2002. 7th Asia and South Pacific and the 15th International Conference on VLSI Design. Proceedings. , vol., no., pp.3,4, 2002, doi: 10.1109/ASPDAC.2002.994869

[8] Ogboi, F.L.; Tasker, P.J.; Akmal, M.; Lees, J.; Benedikt, J.; Bensmida, S.; Morris, K.; Beach, M.; McGeehan, J., "A LSNA configured to perform baseband engineering for device linearity investigations under modulated excitations," Microwave Conference (EuMC), 2013 European , vol., no., pp.684,687, 6-10 Oct. 2013

# Enhanced Vector Calibration of Load-pull Measurement Systems

A.Aldoumani*, Tudor Williams**, J. Lees* and P. J. Tasker*,
* School of Engineering, Cardiff University, Cardiff, UK, CF24 3TF Tel +44 2920 75938
** Mesuro Limited, Pen coed Technology Park, Pencoed, CF35 5HZ
aldoumainia@cardiff.ac.uk

***Abstract*—This paper presents an alternative approach to improving the vector measurement accuracy, especially near the edge of the Smith Chart, of load-pull measurement systems. Improved measurement accuracy, after vector calibration, is achieved by exploiting the load-pull capability during calibration to minimize the impact of measurement errors on the raw data of the calibration standards before it is utilized in the traditionally implemented LRL/TRL calibration algorithm. This approach eliminates the need to utilize complex optimization algorithms post calibration. The proposed method has been tested and applied to actual measurement data.**

***Index Terms*—Load-pull system, TRL calibration, NMSE.**

## I. INTRODUCTION

Waveform engineering measurement systems consist of a vector measurement component, Large Signal Vector Network analyzer (LSNA), integrated with source/load-pull capability [1], as shown in fig. 1. The LSNA measurement component is typically either sampler based or Vector Network Analyzed (VNA) based, having a minimum of four channels. The source/load-pull component can be either passive, mechanical tuners, or active, employing phase locked RF sources. Its main purpose is to vary, or engineer, the source and load impedance environment presented to the device during large signal operation.

To achieve accurate measurements the LSNA must be vector error corrected using an error model [1-3]. Vector calibration, determination of the error model coefficients, involves the measurement of a set of calibration standards. The measurement systems accuracy during this process will, unfortunately, limit the quality of the determined error coefficients; hence the accuracy of all subsequent error corrected s-parameter measurements. Previous investigations have shown that this affect is most noticeable when performing large signal measurements with source/load impedances near the edge of the Smith Chart [4-6].

In [4] it was shown that this measurement inaccuracy could be reduced by post processing a set of load-pull measurements, performed when the Device Under Test (DUT) was a thru or a line, to modify the error model coefficients using a global optimization approach.

In this paper an alternative, more systematic, approach is presented. In this case the load-pull capability of the measurements system is exploited during the Line-Reflect-Line (LRL)/Thru-Reflect-Line (TRL) calibration process to minimize the uncertainties in determining the raw, *un-corrected s-parameters*, of the thru and line standards. Determination of the calibration error model can thus still be undertaken using the standard, un-modified, LRL/TRL calibration algorithm. It will be shown that the error model coefficients determined in this case provide accurate error corrected s-parameter measurements, even at the edge of the Smith Chart.

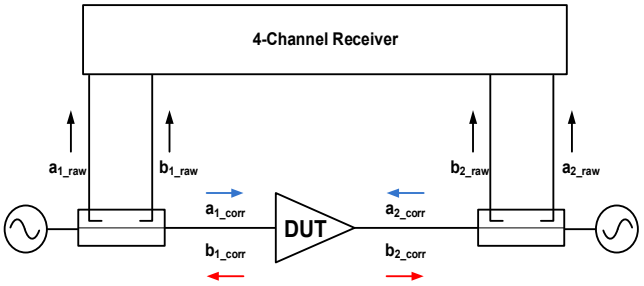


Fig. 1. A generic Two Port LSNA RF architecture with integrated active load-pull.

## II. LSNA CALIBRATION AND VERIFICATION

The LSNA error model has two elements [1-3], see (1). One is identical to that used to vector correct VNA system's 7-term error model *($\alpha_1(f)$, $\beta_{1,2}(f)$, $\gamma_{1,2}(f)$ and $\delta_{1,2}(f)$)* and it ensures that the system can perform vector corrected ratio, s-parameter, measurements. The other component, *K(f)*, scales all the measurements to allow for the measurement of power flow and phase aligns the harmonics to allow for the measurement of waveforms.

The coefficients of the 7-term error model are determined from a set of *un-corrected s-parameters*, measured on a set of calibration standards. In this case, we will use the Line-Reflect-Line (LRL)/Thru-Reflect-Line (TRL) calibration procedure. It is the determination of these error coefficients that is the focus of this paper.

$$\begin{vmatrix} a_1(f) \\ b_1(f) \\ a_2(f) \\ b_2(f) \end{vmatrix} = K(f) \begin{vmatrix} 1 & \beta_1(f) & 0 & 0 \\ \gamma_1(f) & \delta_1(f) & 0 & 0 \\ 0 & 0 & \alpha_1(f) & \beta_1(f) \\ 0 & 0 & \gamma_2(f) & \delta_2(f) \end{vmatrix} \cdot \begin{vmatrix} a_{0Raw} \\ b_{0Raw} \\ a_{3Raw} \\ b_{3Raw} \end{vmatrix}$$

Eq. (1)

The process of calibration consists of connecting the thru and the line standards between port 1 and port 2 and measuring the raw, *un-corrected two-port s-parameters*, for each frequency on a defined frequency grid. The calibration process is completed by measuring the, raw, *un-corrected one-port s-parameters* of an unknown reflect standard, or identical

978-1-4799-4423-1/14/$31.00 ©2014 IEEE

standards, connected to port 1 and port 2. Typically this reflect standard is an Open or Short.

This procedure provides just sufficient measurements to determine the 7-term error model coefficients, the reflection coefficient of the unknown reflect standard and the transmission coefficient of the line standard. The accuracy of the determined error model coefficients is, therefore, directly related to the accuracy of the measured *un-corrected s-parameters*.

Typically a verification process is used to investigate the quality of the **corrected s-parameters** determined after vector correcting raw measurement data. In this case the active load-pull systems was used to perform this investigation. The **corrected s-parameters** of the thru and line standards were measured into different load impedance for one of the frequencies in the measurement grid. A typical set of load impedances used is shown in fig 2.

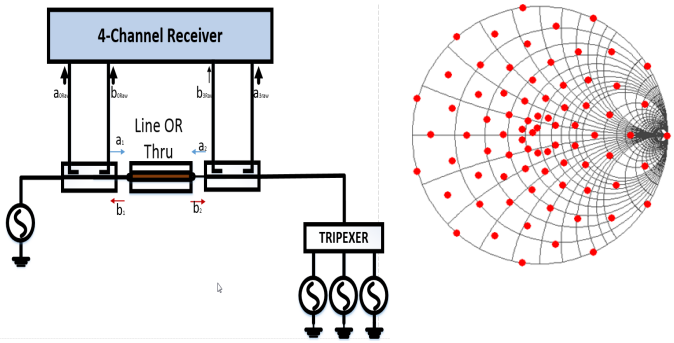


Fig. 2. The calibration accuracy is verified by measuring the thru and line calibration standards under different load conditions. Note that during calibration the load is set to the nominal reference value (50 ohms).

Irrespective of the load impedance the measured **corrected s-parameters** of the thru or line should be invariant. Hence, for example, the ratio $20\log(b_2/a_1)$ should be invariant and equal to zero. Figures 3 and 4 show, as contours, the results achieved on the thru and line standards respectively. They indicate a variation of around 0.06 dB, which results from inaccuracies in the determined error model coefficients. This error, increasing for load impedances near the edge of the Smith Chart.

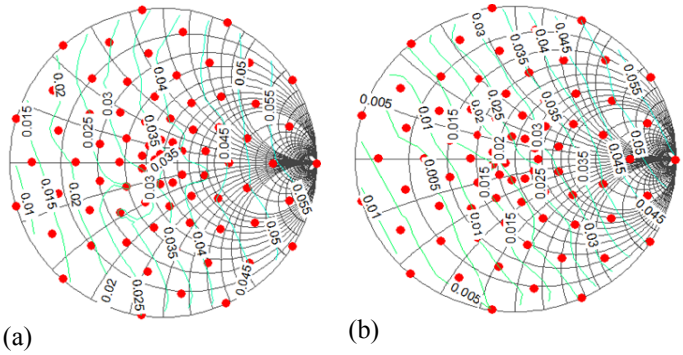

(a) (b)

Fig. 3. Gain $20\log(b_2/a_1)$ variations observed on the corrected s-parameters obtained from measuring (a) the Line and (b) the thru while varying the load impedance. After performing a standard TRL calibration procedure.

In previous work [4] such load-pull measurements were used to modify the error model coefficients using a global optimization approach aimed a minimizing this variation.

## III. Modified Calibration

In this paper an alternative, more systematic, approach is used to improve the accuracy of the determined error coefficients. In this case the load-pull measurements are used directly during calibration. The aim is to use the increased number of measurements performed on the thru and line standards to pre-process the data; minimize the impact of measurement uncertainties, random error, during determination of their *un-correct s-parameters* before executing the standard LRM/TRM calibration algorithm. Fig 4 shows the proposed calibration procedure.

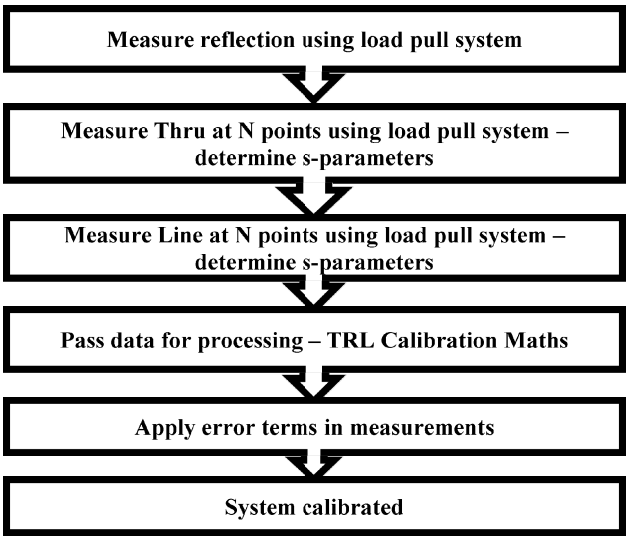


Fig. 4. Procedure for new calibration method.

The key steps are as follows:-

1. Replace the two measurements (forward and reverse) for determining the *un-correct s-parameters* of the thru and line with multiple measurements at different load impedances (target the complete coverage of the Smith Chart)
2. Utilize a least squares minimization technique to process the thru and line multiple measurements (raw data without any correction) to determination a more accurate measure of their, raw, *un-corrected s-parameters* respectively.
3. These thru and line *un-corrected s-parameters* along with the reflection standard measurements can be used directly, without modification, by the standard LRM/TRM calibration algorithm to obtain 7-term error model coefficients.

This process can be repeated for all frequencies required in the measurement grid or just at selected frequencies where the need for unproved accuracy is essential. At the other frequencies the *un-corrected s-parameters* determined from the forward and reverse measurements can be used as normal.

## IV. Experimental Validation

Consider first the validity and accuracy of determining of the *un-corrected s-parameters* of the thru and line standards using multiple measurements at different load impedances. Since the device under test is invariant during these measurements they can all be described by the following equation;

$$\begin{bmatrix} b_0^i \\ b_3^i \end{bmatrix} = \begin{bmatrix} s_{11}^{RAW} & s_{12}^{RAW} \\ s_{21}^{RAW} & s_{22}^{RAW} \end{bmatrix} \begin{bmatrix} a_0^i \\ a_3^i \end{bmatrix} \qquad \text{Eq. (2)}$$

The raw s-parameters can be computed using the least squares fitting technique. Key to providing a more accurate calibration is the requirement of determined raw un-corrected s-parameters to model accurately the measured variation of the raw $b_{0,3}^i$ waves to variations in the measured raw $a_{0,3}^i$ waves over the whole Smith Chart. This is successfully demonstrated in fig. 4.

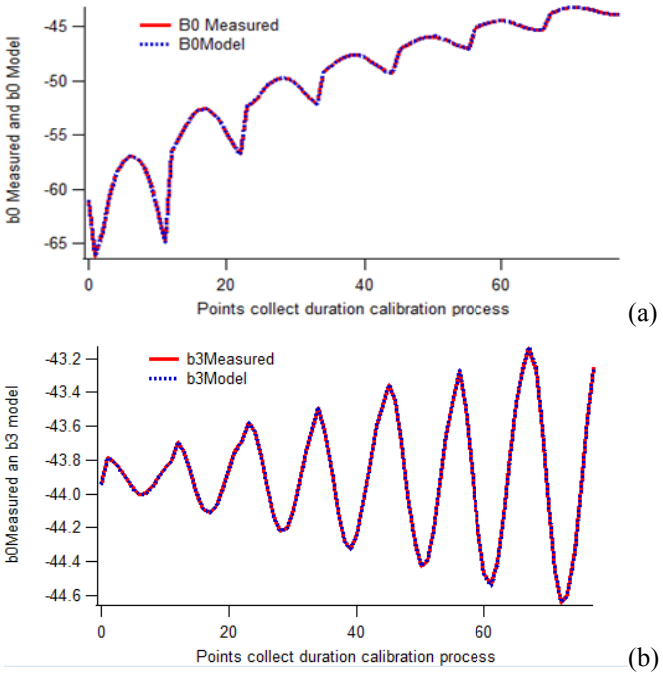


Fig. 4. Comparison between measured and modeled, using the determined raw s-parameters, of the values of (a) $b_0^i$ and (b) $b_3^i$. In this case the DUT is the Thru.

The quality of this fitting process can be quantified by computing the normalized mean square error (NMSE) for both $b_{0,3}$ waves [7].

$$NMSE_{0,3} = \frac{\sum |b_{0,3}^{meas} - b_{0,3}^{mod}|^2}{\sum |b_{0,3}^{meas}|^2} \qquad \text{Eq. (3)}$$

This was investigated as a function of the number of load impedance points used and the area of the Smith Chart covered. It was observed, see fig. 5 that the accuracy improved if higher reflection coefficient load impedances were used, in fact values greater than unity can be used in the case of an active load-pull system. Also, as shown in fig. 5, greater than 40 points were required to minimize the impact of measurement uncertainties, random error, on the computed, raw *un-corrected s-parameters*.

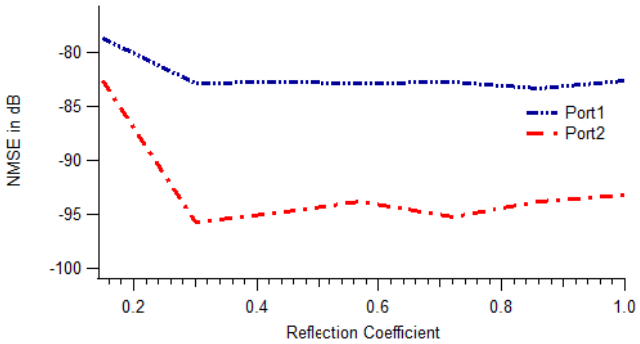


Fig 5. Sensitivity of the calculated NMSE to the maximum reflection coefficient of load-pull points

## V. System Verification

The ability of the 7-term error model coefficients computed using the more accurate raw, *un-corrected s-parameters*, of the thru and the line to provide more accurate measurements is demonstrated using the previously discussed verification approach. The results obtained in this case are shown in fig. 6, contours of gain variation computed as a function of load impedance from the **corrected s-parameters**.

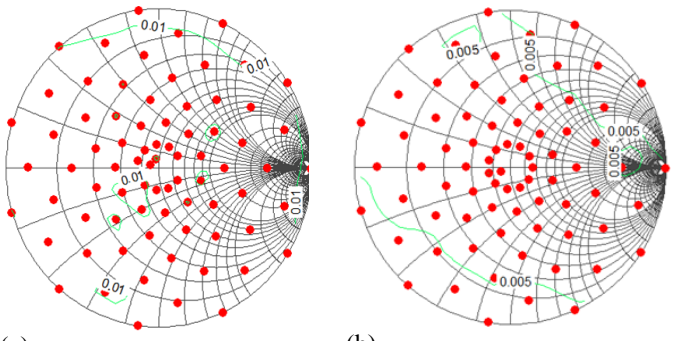


Fig. 6. Gain $20\log(b_2/a_1)$ variations observed on the corrected s-parameters obtained from measuring (a) the Line and (b) the thru while varying the load impedance. After performing a enhanced TRL calibration procedure.

In this case only a variation of around 0.006 dB, an order of magnitude improvement, is observed. This accuracy is maintained up to the edge of the Smith Chart. This is also highlighted in figures 7 and 8. The higher point numbers correspond to higher reflection coefficient magnitudes.

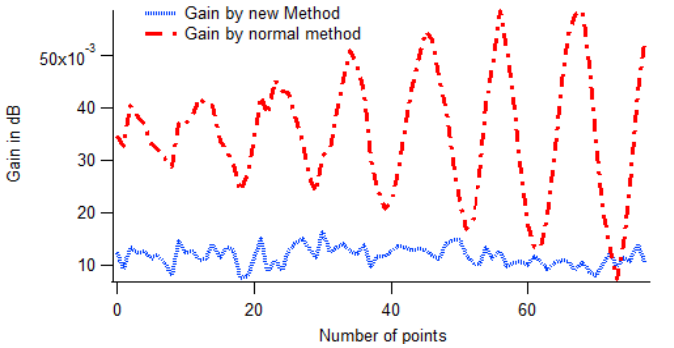

Fig. 7. Comparison between gain calculated by using normal method and gain calculated by using load pull system for Line.

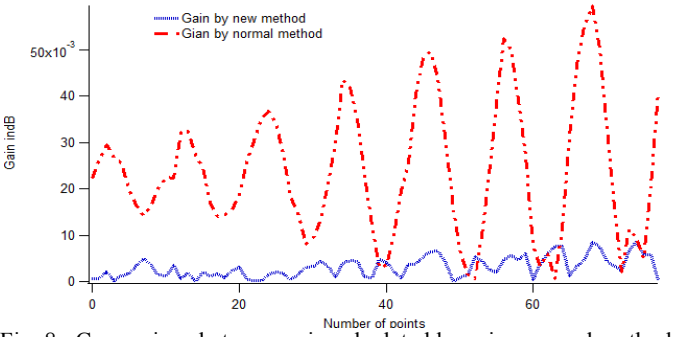

Fig. 8. Comparison between gain calculated by using normal method and gain calculated by using load pull system for Thru.

It is important to recognize that in this case this is not a "true" verification procedure since the measurements used for verification were also utilized during calibration.

An alternative approach is to compute the consistency of the measured raw, *un-corrected s-parameter data* of the thru and line standards for use in the LRL/TRL calibration algorithm.

This can be quantified by the following figure of merit X, computed from the *un-corrected s-parameter data* of the thru and line standards;

$$X = (T_{LM} \quad T_{TM}^{-1}) \qquad \text{Eq.(4)}$$

Since the error model states that the *un-corrected s-parameter data* of the thru and line must satisfy the following mathematical description;

$$[T_{TM}] = [T_A][T_T][T_B] \qquad \text{Eq.(5)}$$

$$[T_{LM}] = [T_A][T_L][T_B] \qquad \text{Eq.(6)}$$

It can be shown that the Det(X) should be equal to one.

$$X_{11}X_{22} - X_{12}X_{21} = 1 \qquad \text{Eq.(7)}$$

For the *un-corrected s-parameter data* obtained from the forward/reverse measured Det(X)= 1.00227+0.02143i while for those obtained from the multiple load-pull measurements Det(X)= 1.00014-0.00405i. The calibration validity is improved because we are now using higher quality raw data [8].

## VII. Conclusion

An alternative, systematic, approach for enhancing the calibration accuracy of LSNA (and VNA) systems exploiting load-pull has been developed and demonstrated. Since this approach is based on the pre-processing of multiple measurements it does not require any modification of the LRM/TRM calibration algorithm.

An order of magnitude improvement in the quality of the corrected s-parameters was demonstrated. This improvement can be quantified directly during calibration using a figure of merit which measures the consistency of the measured raw, *un-corrected s-parameter data* of the thru and line standards to satisfy a mathematical constraint implicit in the LRL/TRL algorithm.

## Acknowledgements

This work is part funded EPSRC iCase.

## References

[1] Tasker, P.J., "Practical waveform engineering," Microwave Magazine, IEEE , vol.10, no.7, pp.65,76, Dec. 2009.

[2] Benedikt, J.; Gaddi, R.; Tasker, P.J.; Goss, M.; , "High-power time-domain measurement system with active harmonic load-pull for high-efficiency base-station amplifier design," Microwave Theory and Techniques, IEEE Transactions on , vol.48, no.12, pp.2617-2624, Dec 2000.

[3] Van den Broeck, T.; Verspecht, J.; , "Calibrated vectorial nonlinear-network analyzers," Microwave Symposium Digest, 1994., IEEE MTT-S International , vol., no., pp.1069-1072 vol.2, 23-27 May 1994.

[4] Teppati, V.; Ferrero, A.; Parena, D.; Pisani, U., "Accuracy Improvement of Real-Time Load-Pull Measurements," *Instrumentation and Measurement, IEEE Transactions on* , vol.56, no.2, pp.610,613, April 2007 doi: 10.1109/TIM.2007.891049 .

[5] Pisani, U.; Ferrero, A., "A unified calibration algorithm for scattering and load pull measurement," Instrumentation and Measurement Technology Conference, 1996. IMTC-96. Conference Proceedings. Quality Measurements: The Indispensable Bridge between Theory and Reality., IEEE , vol.2, no., pp.1250,1253 vol.2, 1996 doi: 10.1109/IMTC.1996.507571.

[6] Teppati, V.; Pinarello, S.; Ferrero, A.; Mueller, J.-E., "An unconventional VNA-based time-domain waveform load-pull test bench," Microwave Conference Proceedings (APMC), 2010 Asia-Pacific , vol., no., pp.1893,1896, 7-10 Dec. 2010.

[7] A. Bevilacqua, D. Bollini"A new approach to image reconstruction in positron emission tomography using artificial neural networks", Online http://citeseerx.ist.psu.edu/viewdoc/download?doi=10.1.1.13.5829&rep=rep1&type=pdf, [Accessed:02-05-2014]

[8] California Esatern Laboratories; "Designing And Characterizing TRL fixture calibration standards for device modelling" Application Note AN1041,Online http:// http://www.cel.com/pdf/appnotes/an1041.pdf [Accessed 04_02-2014].

# Estimation of Complex Residual Errors of Calibrated Two-Port Vector Network Analyzer

Aleksandr A. Savin[1)], Vladimir G. Guba[2)], Andrej Rumiantsev[3)], and Benjamin D. Maxson[4)]

[1)]Tomsk State University of Control Systems and Radioelectronics, 634050, Tomsk, Russia
[2)]NPK TAIR, a subsidiary of Copper Mountain Technologies, 634041, Tomsk, Russia
[3)]Brandenburg University of Technology (BTU), 03046, Cottbus, Germany
[4)]Copper Mountain Technologies, 46268, Indianapolis, USA

***Abstract* — This article presents a new method for verification of the residual errors of calibrated two-port vector network analyzers based on a special time-domain technique. The method requires two devices under test including a high-precision air line. Calibration residual errors are extracted from a distance-frequency system model and special estimation algorithm based on the quasi-optimal unscented Kalman filter. Experimental studies were conducted in coaxial measurement environments and at the wafer level. Suitable applications of the proposed verification method are discussed.**

***Index Terms* — S-parameters, vector network analyzer (VNA), verification, residual error-box, unscented Kalman filter (UKF).**

## I. Introduction

Vector network analyzer (VNA) measurement uncertainties depend on several factors, including the type of calibration method and the accuracy of the calibration standards used. Estimation of calibration residual errors ensures measurement accuracy of the calibrated system. Conventional methods for measurement of residual errors require standards with known frequency characteristics (e.g. [1]–[5]). An alternative approach for reflection measurements was described in [6]. The residual error model of a one-port VNA consists of three unknown components. Therefore, verification of such a VNA nominally requires at least three independent measurement conditions (devices). The alternative algorithm described in [6] calculates three residual errors from the reflection coefficient of a single device under test (DUT), such as an air line, terminated with a short.

The residual error model of a two-port non-leaky VNA consists of ten unknown components. In this article, we extend the algorithm from [6] to the two-port VNA. Ten residual errors are calculated from six measurements of two DUTs: two reflection coefficients of the first DUT (e.g. an air line terminated with a short) measured on both ports of the VNA, and the full S-parameter matrix of the second DUT (e.g. an air line) connected to both VNA ports.

## II. System Error Model and Observed Signals

We denote the residual directivity as $D$, the residual source match as $S$, the residual reflection tracking as $R$, the residual load match as $L$, and the residual transmission tracking as $T$. Indexes $F$ (Forward: from port 1 to port 2) and $R$ (Reverse: from port 2 to port 1) will be used to indicate the measurement direction. Fig. 1 shows a calibrated two-port VNA and corresponding error-boxes when performing measurements in both the forward and reverse directions.

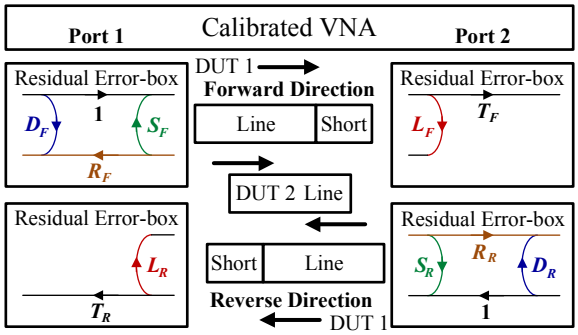


Fig. 1. The model of a two-port calibrated measurement system.

We described the calibration residual error model of the VNA in the time domain as a set of ten networks, so-called "reflectors". Each reflector has known distance (time delay) and unknown frequency characteristics. We denote the length of the air line as $l$ and the propagation velocity constant of the air line as $\gamma$. Fig. 2 shows the set of samples for $A$ (reference values $A_1$, $A_2$, $A_3$) and $B$ (reference values $B_1$, $B_2$, $B_3$) reflectors in the distance-frequency plane.

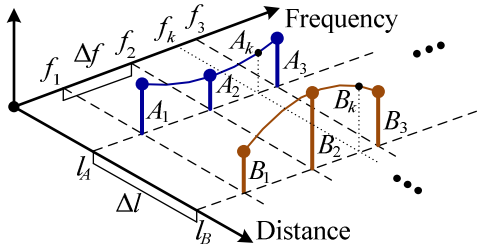


Fig. 2. Distance-frequency model of the measurement system.

In Fig. 2, $f_1$ is the start frequency, while $f_2$ and $f_3$ are other reference frequencies, $\Delta f$ is the frequency step between samples, $l_A$ the distance of $A$ from the reference plane of VNA, $l_B$ the distance of $B$, and $\Delta l$ is the distance step between reflectors depending on the length of the air line. The value of $\Delta f$ was chosen to provide a phase step of $2\pi$ for double $\Delta l$.

978-1-4799-4423-1/14/$31.00 ©2014 IEEE

For this example, the VNA signal $M$ at a particular frequency point $\omega_k$ can be described as the sum of two components:

$$M_k = A_k \cdot \exp(-\gamma_k \cdot l_A) + B_k \cdot \exp(-\gamma_k \cdot l_B). \quad (1)$$

We used cubic splines to interpolate the frequency characteristics of the reflectors and to calculate $A_k$ and $B_k$. The number of reference frequency points $N$ for each reflector depends on the frequency range and the frequency step $\Delta f$. So, the vector of the residual directivity consists of $N$ unknown complex constants:

$$\mathbf{D} = [D_1 \quad D_2 \quad \ldots \quad D_N]^{\mathrm{T}}. \quad (2)$$

Similarly, **S**, **R**, **L** and **T** in both the forward and reverse directions can be defined. The total number of unknown variables is $10 \cdot N$. Estimates of the unknown variables can be made from measurements of the verification DUTs. By processing the VNA measurements, the estimate of **D** improves sequentially for each $k$=1,2,.. ($\omega_1$, $\omega_2$,..). The following equation defines the system state vector:

$$\mathbf{x} = \left[\mathbf{D}_F^{\mathrm{T}} \quad \mathbf{S}_F^{\mathrm{T}} \quad \mathbf{R}_F^{\mathrm{T}} \quad \mathbf{L}_F^{\mathrm{T}} \quad \mathbf{T}_F^{\mathrm{T}} \quad \mathbf{D}_R^{\mathrm{T}} \quad \mathbf{S}_R^{\mathrm{T}} \quad \mathbf{R}_R^{\mathrm{T}} \quad \mathbf{L}_R^{\mathrm{T}} \quad \mathbf{T}_R^{\mathrm{T}}\right]^{\mathrm{T}}$$

$$\mathbf{x}(k) = \mathbf{x}(k-1). \quad (3)$$

Equation (3) is valid for true values of the error terms, but estimates of these values vary with the arrival of new measurements. Final estimates of the residual parameters are obtained once measurements are processed from all frequencies.

On the $k$-th step, dependence of observations **z** on the state vector **x** can be written as:

$$\mathbf{z}(k) = \mathbf{h}[\mathbf{x}, k] + \mathbf{n}(k). \quad (4)$$

The observed signals are related to the state vector by the complex nonlinear expression $\mathbf{h}[\mathbf{x},k]$. Sampling measurement inaccuracies are represented by the vector of noise $\mathbf{n}(k)$. The measured signal can be determined using a flow-graph analysis. The first DUT is an air line terminated with a short. The short has a reflection parameter $\Gamma_S$. The second DUT is an air line connected to both VNA ports with response $\delta=\exp(-\gamma \cdot l)$. For simplicity, we will omit the index $k$ in the equations that follow. The reflection coefficient of the first DUT measured on the first VNA port is:

$$\Gamma_1 \approx D_F + R_F \cdot (\delta^2 \cdot \Gamma_S) + S_F \cdot R_F \cdot (\delta^2 \cdot \Gamma_S)^2. \quad (5)$$

$S_F$ can be derived from the product of $S_F$ and $R_F$ for known $R_F$. The $S$-parameters of the second DUT in the forward direction:

$$S_{11} \approx D_F + L_F \cdot R_F \cdot \delta^2. \quad (6)$$

$$S_{21} \approx T_F \cdot \delta + L_F \cdot S_F \cdot T_F \cdot \delta^3. \quad (7)$$

The second term of (7) is usually close to 0.

The parameters $\gamma$ and $l$ of the transmission line and of the reflection coefficient of the short ($\Gamma_S$) must be known and should not affect the estimate of residual factors. Expressions for the reverse direction for $\Gamma_2$, $S_{22}$ and $S_{12}$ can be obtained from (5)-(7) replacing the index $F$ by $R$. The observed signal is $\mathbf{h}[\mathbf{x},k]=[\Gamma_1 \ \Gamma_2 \ S_{11} \ S_{21} \ S_{12} \ S_{22}]^{\mathrm{T}}$. Then, the first DUT is measured on the second VNA port; calculations are processed in the same way.

## III. Algorithm

The algorithm for estimating the frequency characteristics of ten reflectors was developed using the Markov theory of the nonlinear filtering [8], [9]. The algorithm is based on the unscented transformation [10], and is also known as UKF (Unscented Kalman Filter) [11].

The UKF algorithm involves a definition of the initial conditions to evaluate the status of $\mathbf{x}(0)$, as well as the covariance matrix of the estimate error $\mathbf{V_x}(0)$, based on a priori information. Prior to iteration, the $R$ and $T$ coordinates of the state vector should be set to 1, and the rest to 0. Dispersions of all initial estimates can be set to $0.1^2$. The covariance matrix is diagonal. A number of operations are performed sequentially for each measurement, i.e. in a sequence for each $k$=1,2,..

The first step includes the calculation of a set of "sigma-points" in the state space. The next step is forecasting of average values of the state and observation vectors (marked further by the superscript "–"). Forecasted values of "sigma-points" and their corresponding observations are calculated from the state equations (3) and observation equations (4)-(7). Weighted summation is used to produce final forecast values of the state vector, the observation vector and the covariance matrices. The final stage of filtration includes calculation of the gain ratio, estimation and the covariance matrix of estimation errors. The filter gain ratio is:

$$\mathbf{K}(k) = \mathbf{V}_{\mathbf{xz}}^{-}(k) \cdot [\mathbf{V}_{\mathbf{z}}^{-}(k)]^{-1}, \quad (8)$$

where $\mathbf{V_z}$ is the covariance matrix of observations, $\mathbf{V_{xz}}$ is the cross-covariance matrix of **x** and **z**. Both are calculated using the "sigma-point". The $k$-th estimate depends on the $k$-th count of incoming signal $\mathbf{z}(k)$ and is determined by:

$$\hat{\mathbf{x}}(k) = \hat{\mathbf{x}}^{-}(k) + \mathbf{K}(k) \cdot [\mathbf{z}(k) - \hat{\mathbf{z}}^{-}(k)]. \quad (9)$$

The covariance matrix of estimation errors required for calculations on the following ($k$+1)-th step is:

$$\mathbf{V_x}(k) = \mathbf{V_x}^{-}(k) - \mathbf{K}(k) \cdot \mathbf{V_z}(k) \cdot \mathbf{K}^{\mathrm{T}}(k). \quad (10)$$

## IV. Experimental Results and Discussion

Experimental studies of the algorithm were performed verifying the measurement accuracy of the VNA calibrated using a full two-port Short-Open-Load-Thru method. Experiments were conducted in a 3.5 mm connector coaxial

waveguide environment over a frequency range from 10 MHz to 32 GHz (in 10 MHz steps). Measurements were performed with an Agilent E8364B VNA with IFBW=1 kHz and output power of Pout=-15 dBm. Verification DUT1 and DUT2 were combined from the 9.5 mm long offset short and a 75 mm long air line ($\Delta f$=2 GHz), Fig 1. The system was calibrated using coaxial calibration kit model 85052D from Agilent Technologies [12]. The frequency responses of the DUTs are shown in Fig. 3 and Fig. 4.

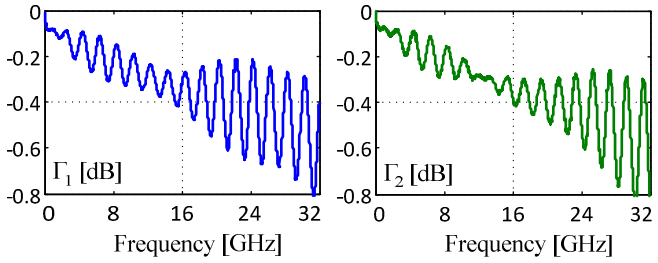


Fig. 3. The measured reflection coefficients of a coaxial line terminated with the short at VNA port 1 (left) and port 2 (right).

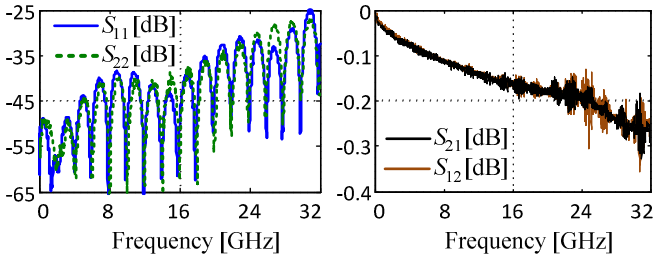


Fig. 4. The measured S-paremeters of a coaxial line connected to both VNA ports.

Transformation into the time domain was performed using fast Fourier transform ($F^{-1}\{\bullet\}$ operator). Results, shown in Fig. 5, reveal several local reflectors. The frequency parameters of the reflections contain information about residual errors of the VNA.

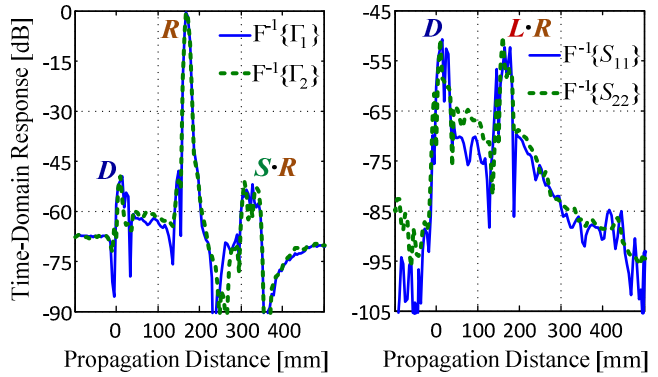


Fig. 5. Time domain diagram of DUT1 and DUT2.

The algorithm was applied to process the verification measurements. Results are given in Fig. 6 to Fig 8. The estimates of the residuals were obtained from 3200 frequency samples and are within the factory specification limits.

Fig. 6-8 also show estimated calibration residual errors of the experimental system measured by the conventional ripple-test method. Residual directivity $D$ and source match $S$ were measured using a verification line terminated with a mismatch load (VSWR 2.0) and a short, respectively. The three-point method used for processing the measured results yielded amplitude values only.

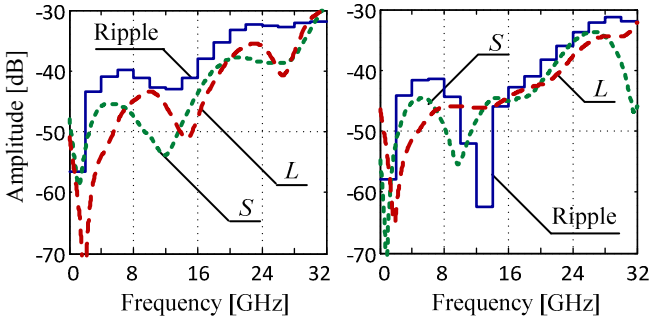


Fig. 6. Amplitude of the residual source match ($S$) and the residual load match ($L$) in forward (left) and reverse (right) directions. Resuts of conventional ripple-test (solid line) are obtained from measurements of a verification line terminated with a short.

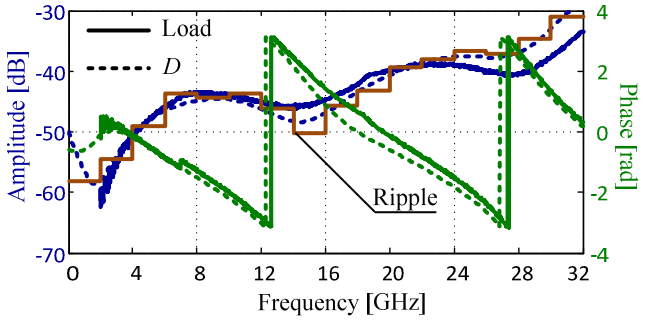


Fig. 7. Comparison of the amplitude (blue lines) and the phase (green lines) of estimates of the residual directivity $D$ (dotted lines) and the reflection coefficient of the 85052D load match (solid lines). The reflection coefficient of the load was shifted in phase by $\pi$. Results of a conventional ripple-test (brown solid line) were obtanied from measurement of a verification line terminated with a mismatched load.

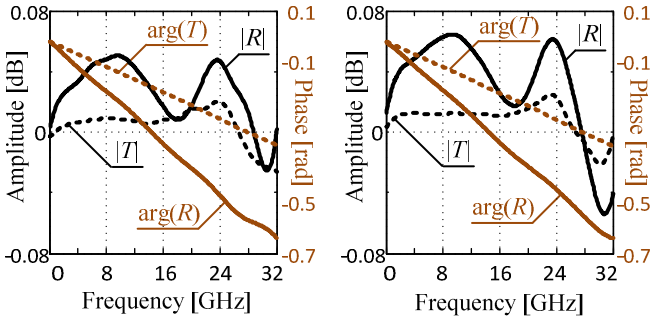


Fig. 8. Amplitude (left axis) and phase (right axis) of the residual reflection ($R$) and transmission ($T$) tracking in forward (left figure) and in reverse (right figure) directions.

It is important to note that the residual directivity $D$ affects the estimate of $S$ when measured using the ripple test. As the magnitude of $D$ is relatively small, its impact is usually negligible. However, as shown in Fig. 6, such is not the case for the experimental system. More accurate estimation of the residual source match $S$ from the ripple test requires additional data processing methods, such as are presented in [6]. Results for the residual directivity $D$ calculated by the proposed method and by a conventional ripple test are in good agreement (Fig. 7).

The reflection coefficient of the 85052D load match corrected by precision two-port Thru-Reflect-Line calibration is shown in Fig 7. It is in close agreement with the estimated $D$ in both amplitude and phase. It is important to note that the reflection coefficient of the 85052D load was assumed to be zero for the SOLT calibration step. The reflection and transmission tracking are correlated.

Finally, the proposed algorithm was evaluated for wafer-level applications up to 110 GHz. The experimental setup included an Agilent PNA 110 GHz VNA, a manual probe station PM8 and 110 GHz ACP-L GSG wafer probes from Cascade Microtech. The system was calibrated using the two-port multiline TRL method from [13] and a custom calibration substrate of coplanar waveguide (CPW) design. The substrate also included offset short verification elements. A qualitative verification was performed of the method using the 8.25 mm long CPW line (frequency steps of $\Delta f = 8$ GHz) and the offset short. Fig. 9 shows the amplitude of the residual directivity ($D$), residual source match ($S$), and residual load match ($L$) calculated for the forward measurement direction.

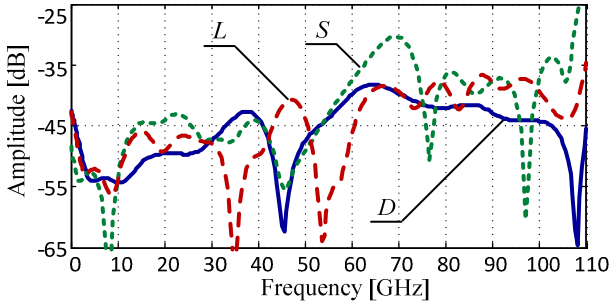


Fig. 9. Results of the qualitative verification of the proposed method at the wafer-level.

## V. Conclusion

In this paper we presented an algorithm for estimation of complex residual errors of a calibrated two-port VNA requiring only two verification elements. The algorithm significantly reduces both the measurement time and the cost of the verification procedure. Experimental results proved suitability of the new method for application in coaxial and wafer-level environment. Further improvements to the estimation accuracy can be achieved through use of a verification line and termination with fully known electrical characteristics.

The method measures complex residual errors of a calibrated VNA. Therefore, it can also be considered as an additional error correction step, for instance for the enhancement of the S-parameter measurement accuracy of a calibrated system.

## Acknowledgments

The authors thank Sergey Zaostrovnykh, and Alex Goloschokin from Copper Mountain Technologies, Indiana, USA for support of this work and for their helpful discussions. Ralf Doerner from Ferdinand-Braun-Institut (FBH), Berlin, Germany is acknowledged for his great help with the on-wafer measurements.

The work was supported by Russian Foundation for Basic Research RFBR Project 14-07-31312.

## References

[1] D.K. Rytting, "An analysis of vector measurement accuracy enhacement technique," *presented at the RF and Microwave Symp. Exhibition*, 1980.

[2] D.K. Rytting, "Network analyzer accuracy overview," *ARFTG Conference Digest-Fall, 58th*, vol. 40, pp. 1-13, Nov. 2001.

[3] B. Oldfield, "VNA S11 uncertainty measurement a comparison of three techniques," *ARFTG Conf. Digest-Spring, 39th*, vol. 21, pp. 86-105, June 1992.

[4] D.F. Williams, R.B. Marks, and A. Devidson, "Comparison of on-wafer calibration," *38th ARFTG Conf. Dig.*, pp. 68-81, Dec. 1991.

[5] G. Wübbeler, C. Elster, T. Reichel, and R. Judaschke, "Determination of the Complex Residual Error Parameters of a Calibrated One-Port Vector Network Analyzer," *IEEE Transactions on Instrumentation and Measurement*, vol. 58, no. 9. September 2009, pp. 3238-3244.

[6] A.A. Savin, "A Novel Factor Verification Technique for One-Port Vector Network Analyzer," *Proceedings of the 43rd European Microwave Conference*, 7-10 Oct 2013, Nuremberg, Germany, pp. 60-63.

[7] A.A. Savin, V.G. Guba, and B.D. Maxson , "Residual Errors Determinations for Vector Network Analyzer at a Low Resolution in the Time Domain," *82nd ARFTG Microwave Measurement Conference*, 18-22 Nov 2013, Columbus, Ohio, USA, pp. 15-19.

[8] A. P. Sage, and J.L. Melsa, "Estimation theory with application to communication and control," *McGraw-Hill*, New-York, p. 529, 1971.

[9] R.E. Kalman, "A new approach to linear filtering and prediction problems," *Trans. ASME, J. Basic Eng.*, vol. 82D, pp. 34-45, March 1960.

[10] S. Julier, J. Uhlmann, and H.F. Durrant-White, "A new method for the nonlinear transformation of means and covariances in filters and estimators," *IEEE Trans. on Automatic Control*, vol. 45, no. 3, March 2000, pp. 477-482.

[11] S.J. Julier and J.K. Uhlmann, "Unscented Filtering and Nonlinear Estimation," *Proceedings of the IEEE*, vol. 92, no. 3. March 2004, pp. 401-422.

[12] "PNA Series Network Analyzers E8362B/C, E8363B/C, and E8364B/C," Technical Specifications E8364-90031, Agilent Technologies, Inc., Santa Rosa, CA, USA.

[13] R.B. Marks, "A multi-line method of network analyzer calibration," *IEEE Trans. Microwave Theory Tech.*, vol. 39, no. 7, pp. 1205-1215, Jan. 1991.

# Design of Two-port Verification Devices for Reflection Measurement in Waveguide Vector Network Analyzers at Millimeter and Sub-millimeter Wave Frequencies

Masahiro Horibe, and Ryoko Kishikawa
National Metrology Institute of Japan, Advanced Industrial Science and Technology,
1-1-1 Umezono, Tsukuba Ibaraki, 305-8563, Japan

***Abstract* –Confidence of vector network analyzer (VNA) measurement can be established by verification process of measurements. The design role of waveguide verification devices has been developed for use at millimeter and sub-millimeter wave frequencies, up to 1.1 THz. Other research groups have also been studied the two port mismatch device for VNA system verification [1-3]. This paper describes design role of verification devices, and then both theoretical estimation and simulation results of verification device characteristics is explained. Furthermore, the measurement results of verification devices are shown in the WM-1651 (WR-6, 110 GHz – 170 GHz) frequency band.**

***Index terms* – Verification, Waveguide vector network analyzer, Reflection characteristics, Aperture dimensions, Flat frequency response of reflection characteristics**

## I. Introduction

In the millimeter-wave and sub-millimeter-wave frequency regions, science, electronic applications and instruments has accelerated in recent years, and operation frequency in the commercial waveguide vector network analyzers (VNA) reaches now up to 1100 GHz. Therefore this occasion provides improving the measurement accuracy of VNA, and then importance of the system level verification and verification device are increased. The national metrology institutes (NMIs) are challenging to develop an S-parameter national measurement system and standards [4-8]. However, waveguide verification kits are only readily available for frequencies up to 110 GHz [9-10]. In the commercial verification kits, four specific devices, i.e. two different attenuators, a straight section of waveguide, a stepped impedance waveguide, with known characteristics are provided for system level verification for calibrated VNA. Further commercial verification device, i.e. two port mismatch waveguide, has already been available for reflection characteristic measurements [1]. However, in the case of verification using above verification devices, magnitude of reflection coefficient has frequency dependence and reduction of reflection characteristics is produced at the both frequency band-edges.

In this paper, we proposed the two-port mismatch standard based on design rule of waveguide aperture dimensions, then electromagnetic theoretical calculation and subsequently simulation were applied to calculate the reflection characteristics and estimate the uncertainty of device characteristics propagated from dimensional measurement results. Furthermore, we show the measurement results for four verification devices with different return loss, i.e. -6 dB, -10 dB, -20 dB and -30 dB, shown in Fig. 1. Finally, we discuss the VNA measurement results comparing to designed characteristics and dimensionally-derived reflection characteristics.

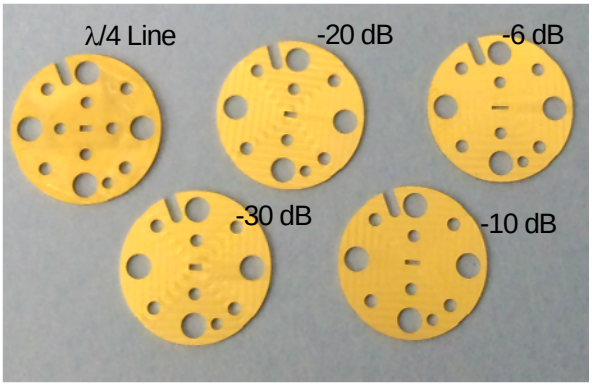


Fig. 1 Photographs of two-port mismatch waveguide section and TRL lines.

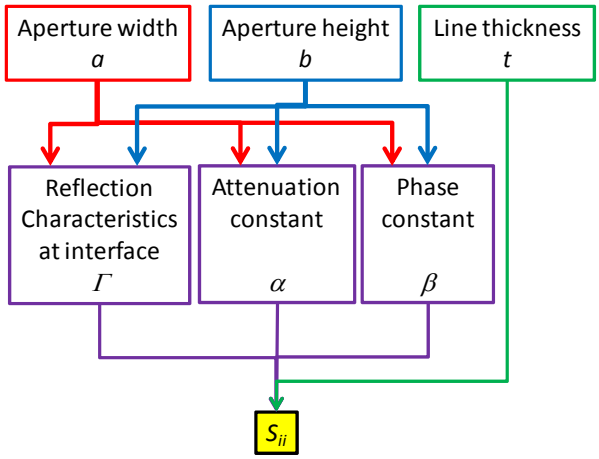


Fig. 2 Design concept of two-port verification device for return loss measurements

978-1-4799-4423-1/14/$31.00 ©2014 IEEE

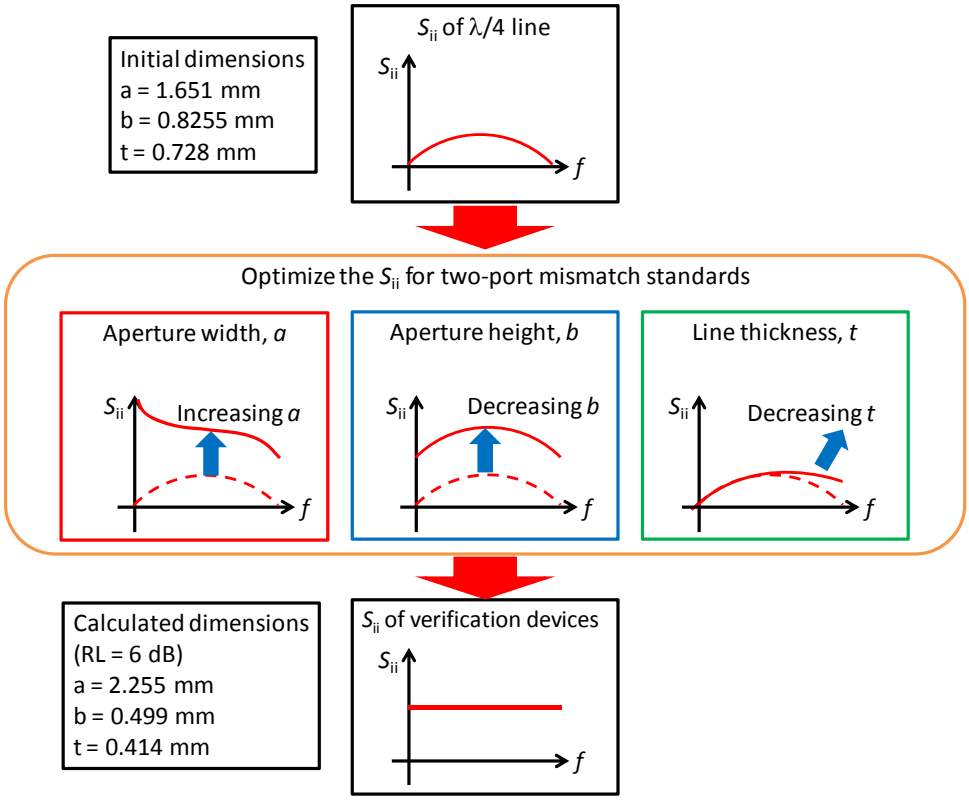


Fig. 3 Design process flow of two-port verification device for return loss measurements

Table 1 Dimensional design of aperture size and thickness for return loss verification device (Unit: mm)

| Return loss | *a* | *b* | *t* |
|---|---|---|---|
| -30 dB | 1.669 | 0.803 | 0.525 |
| -20 dB | 1.709 | 0.758 | 0.514 |
| -10 dB | 1.938 | 0.619 | 0.444 |
| -6 dB | 2.255 | 0.499 | 0.414 |
| *λ/4 line* | *1.651* | *0.8255* | *0.728* |

## II. Verification device for waveguide VNA at millimeter wave and above

In a coaxial line system, several accuracy verification methods of VNA measurement have been investigated by using an air line as a precision reference standard. The conventional ripple testing method can provide one of solution of system verification as benchmarking system conditions, however it cannot be considered as a good candidate for a practical application. Furthermore, in the waveguide VNA system over 110 GHz (up to 1.1 THz) technical skill and knowledge for waveguide connection and VNA system are required for verification operation and understanding the result of verification. Other solution of verification method for a VNA measurement system is usage of verification devices. However, no commercial verification device is derived. For transmission characteristics, system accuracy is commonly tested by fixed attenuators or variable attenuator, even if operation frequency is over 110 GHz [7]. However, the precision reflection devices are required for reflection characteristic measurement in VNA. In the coaxial line system, mismatch terminations are designed and established by the different values of resistance. However, it is difficult to design and adjust the reflection characteristics by the resistance value over 110 GHz. Then, two-port mismatch lines have been proposed. Over 110 GHz (perhaps terahertz frequency), reflection characteristics strongly depends on frequency, then, it is difficult to design the high reflection characteristics (high return loss) at the both edge of frequency band [1]. We propose the design concept of two-port mismatch devices as verification device with frequency-independent return loss by controlling the three parameters, i.e. thickness of line, and width and height of aperture (Fig. 2).

## III. Design concept of two-port mismatch standard with flat frequency response

Design process of two-port mismatch verification device is shown in Fig. 3. The initial dimensions of aperture and thickness are providing scattering parameters (S-parameter) of quarter wave length line at the mid frequency of the waveguide band, i.e. 140 GHz in the WM-1651 waveguide band. The return loss value is, first, set a preferred value for verification of reflection characteristics. Then, waveguide aperture height, *b*, is reduced to adjust the target value of return loss. Next, by changing values of the both aperture width, *a*, and line thickness, *t*, frequency dependence of return loss can be

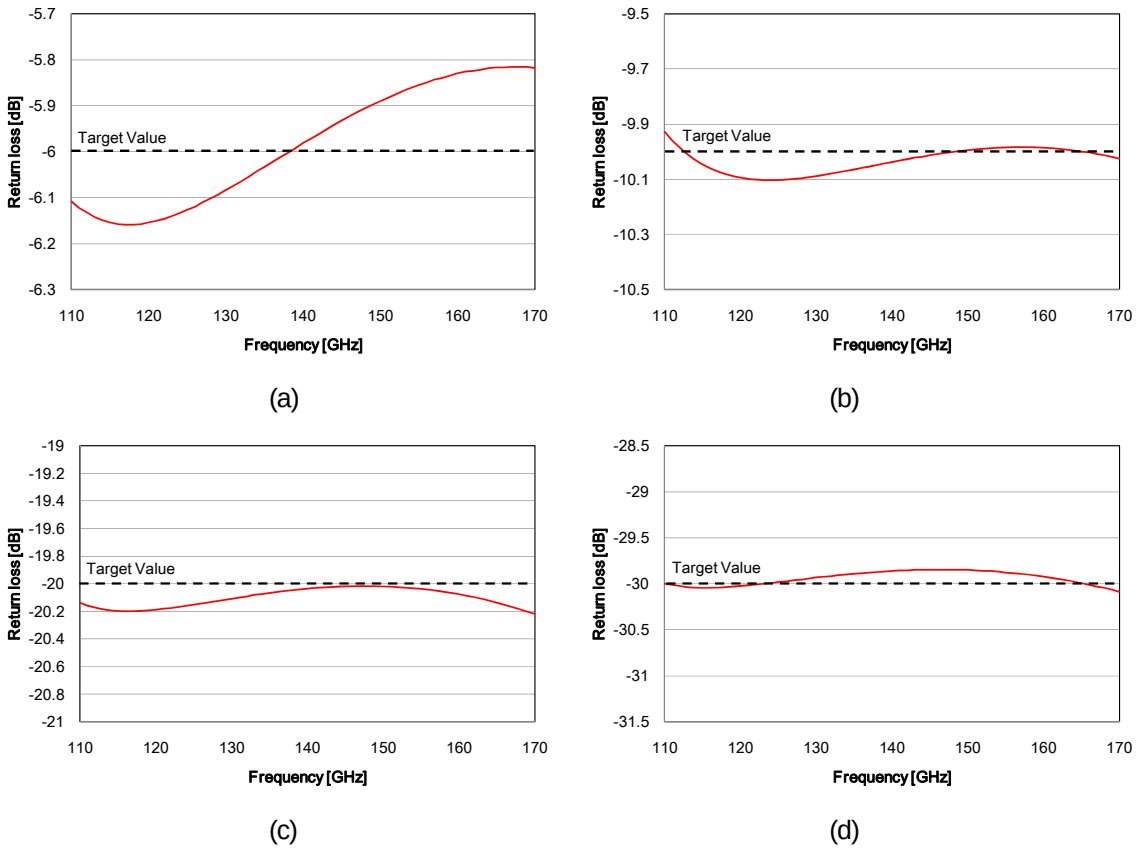


Fig. 4 Results of electromagnetic theoretical analysis for two-port verification devices with return loss of (a) -6 dB, (b) -10 dB, (c) -20 dB and (d) -30 dB for WM-1651 (WR-6) waveguide VNA measurement system.

Table 2 Dimensional measurement results of aperture size and thickness for return loss verification device (Unit: mm)

| Return loss | *a* | U(*a*) | *b* | U(*b*) | *t* | U(*t*) |
|---|---|---|---|---|---|---|
| -30 dB | 1.6758 | 0.0025 | 0.8088 | 0.0032 | 0.5285 | 0.0025 |
| -20 dB | 1.7150 | 0.0017 | 0.7642 | 0.0032 | 0.5175 | 0.0025 |
| -10 dB | 1.9448 | 0.0034 | 0.6245 | 0.0055 | 0.4460 | 0.0024 |
| -6 dB | 2.2609 | 0.0023 | 0.5043 | 0.0036 | 0.4218 | 0.0025 |

extinguished. If flatness of frequency dependence is over 5 % entire operation frequency range, value of *b* is re-adjusted, then values of *a* and *t* are also changed. Calculated values of dimensional parameters are listed in Table 1. Four different values of return loss, i.e. -6dB, -10 dB, -20 dB and -30 dB, were designed. From the table, the flat rectangular-like shape, i.e. aperture with wider width and thinner height, provides high return loss characteristics.

Figures 4 show return loss calculation results of electromagnetic theoretical analysis. The return loss, derived from $S_{ii}$ of S-parameter, was estimated from the aperture size and line thickness of the WM-1651 rectangular waveguide when it was connected in accordance with IEEE standards. The S-parameter was derived from a series expansion of the field in eigen-modes [8]. This method takes into account the influence of evanescent fields and power transmission due to higher order modes. Computer simulation software (Ansoft HFSS) was then used to validate the mathematical analysis results. Return values were distributed within ±5% of target value at all frequencies (110 GHz to 170 GHz).

## IV. Dimensional measurement and Simulation of two-port mismatch device characteristics

Two-port mismatch lines as verification devices was designed to fit the newly designed waveguide flanges [11, 12] and fabricated on a CNC milling machine for flange interfaces. Before estimations and measurements of device characteristics, aperture dimensions were measured by dimensional measurement system based on three-dimensional coordinate measuring machine (3DCMM) [8]. To establish repeatability this measurement was made 5 times by setting and removing the lines as a device under test on the 3DCMM stage. Reproducibility error of the measurement was less than 0.5 μm with a standard uncertainty of 0.23 μm. Therefore

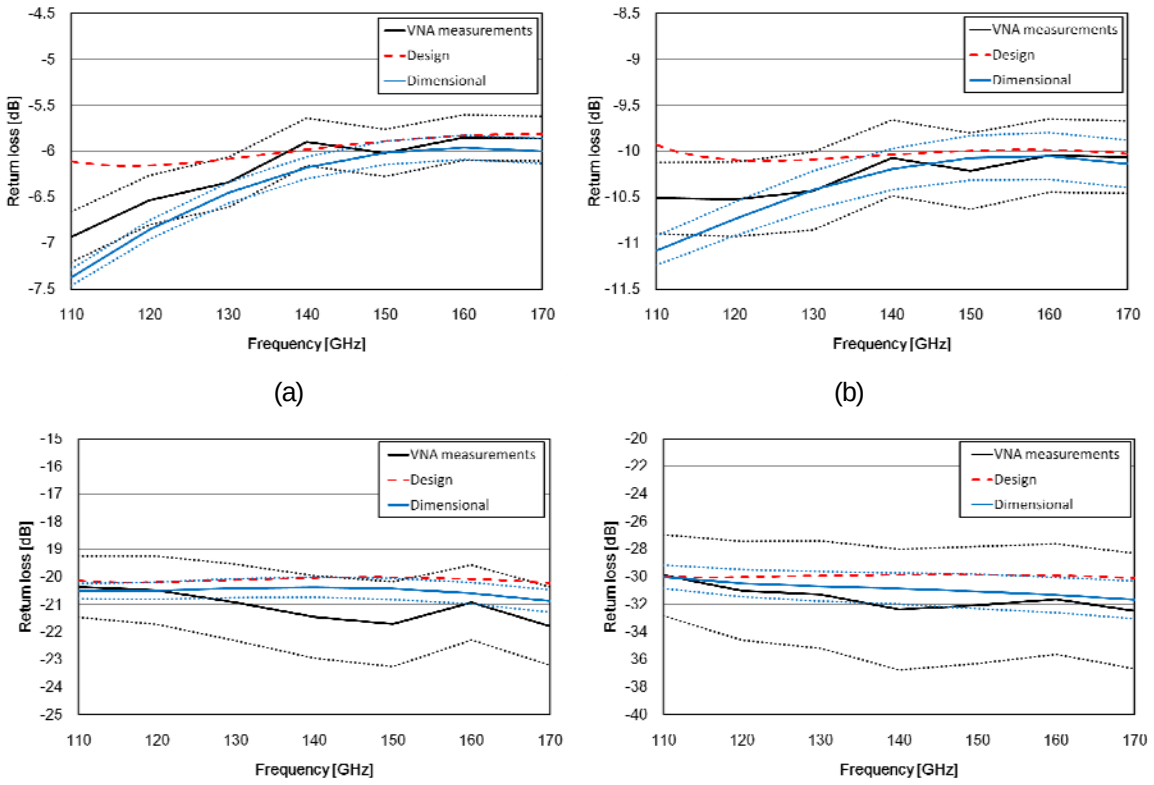


Fig. 5 Measurement results of two-port verification devices for return loss of (a) -6 dB, (b) -10 dB, (c) -20 dB and (d) -30 dB for WM-1651 (WR-6) waveguide VNA measurement system. Read broken line indicates designed characteristics. The dimensionally-derived return loss values and its uncertainty limits ($k$=2) are shown by blue solid and dotted lines, respectively. Then, Black solid and broken lines indicate measured values and its uncertainty limits ($k$=2) by VNA.

Table 3 Dimensional deviation of measured values form designed values for return loss verification device (Unit: mm)

| Return loss | *a* | *b* | *t* |
|---|---|---|---|
| -30 dB | 0.0071 | 0.0055 | 0.0034 |
| -20 dB | 0.0062 | 0.0064 | 0.0037 |
| -10 dB | 0.0066 | 0.0052 | 0.0021 |
| -6 dB | 0.0058 | 0.0056 | 0.0078 |

the systematic standard uncertainty due to the 3DCMM error and the uncertainty of the block gauge reference was approximately 0.45 μm. The resulting expanded uncertainty (k=2, 95% level of confidence) contribution from the measurement system was approximately 1.0 μm for small aperture waveguide. Dimensional measurement results are summarized in Table 2 together with measurement uncertainty. The measurements for the aperture width at varying positions along the aperture height for the aperture height at varying positions along the aperture width are made at varying depths (line thicknesses). The uncertainty listed in Table 2 contains the both systematic uncertainty and non-uniformity of aperture dimensions.

This uncertainty estimation of return loss, derived from $S_{ii}$, reflects dimensional parameters listed in Table 2.

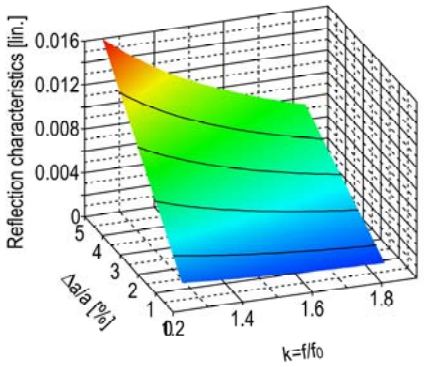


Fig. 6 Effect of width dimension difference from aperture width of test-port waveguides on the reflection characteristics with frequency dependence.

The uncertainty of permittivity was calculated at the standard laboratory air condition (temperature of 23 ºC ± 1 ºC, relative humidity of 50% ± 10%, atmospheric pressure of 1013.25 hPa±100 hPa). The S-parameters and their associated uncertainties were estimated from a series expansion of the field in eigenmodes [11] by a Monte Carlo simulation involving 100,000 trials. This uncertainty evaluation does not include misalignment uncertainty contributions due to misalignment which effect measurement reproducibility and can be treated as

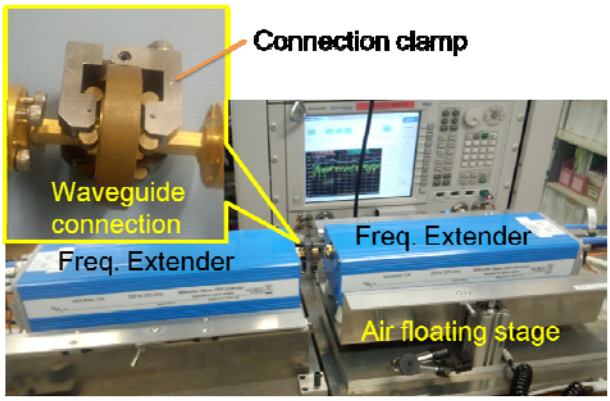


Fig. 7 Measurement set-up for verification of VNA system. Connection clamp and air floating stage can provide high throughput measurements with precise connections for waveguide [13, 14].

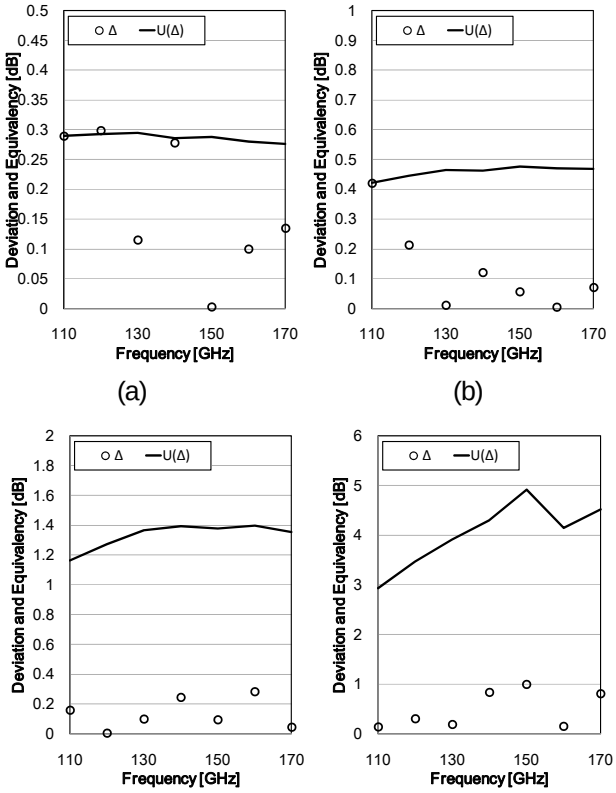


Fig. 8 Comparison results between electrical measurements and dimensionally-derived calculation for return loss of (a) -6 dB, (b) -10 dB, (c) -20 dB and (d) -30 dB for WM-1651 (WR-6) waveguide.

deviations in the actual VNA measurements.

Real and imaginary values of reflection characteristics, derived from $S_{11}$, for four mismatch lines with their associated uncertainties are shown in Fig. 5 together with designed characteristics. Estimated return loss values of verification devices providing -6 dB and -10 dB return loss are lower than designed value near lower edge of band frequency in the WM-1651 waveguide. This is because measured values of verification devices of aperture width and thickness are several μm larger than designed values (Table 3). For high return loss device, reflection characteristics are much more sensitive to dimensions, *a* (Fig. 6) and *t*.

## V. System verification for vector network analyzer

### A. Measurement system set-up

Using two-port verification device achieves system verification for a VNA from Agilent Technologies and a WR-6 (WM-1651) frequency extension module from Oleson Microwave Laboratory Inc. (OML). All results presented in this paper have been taken with IF bandwidth 10 Hz and averaging factor 1. The clamps and air floating stage on the connection table shown in Fig. 7 are used to connect verification devices quickly rather than the usual connection scheme of waveguides using four screws. Using the clamp, tightening one screw produces easily managed mating force on the flange plane. This way reduces measurement time and obtains a repeatable result in VNA measurements.

### B. Experimental results

First, VNA was calibrated by Thru-Reflect-Line (TRL) calibration. TRL line standard has been dimensionally calibrated and its associated uncertainty has been estimated by the Monte Carlo simulation [8]. Measurement uncertainty of waveguide VNA in the WM-1651 waveguide has already been calculated by uncertainty propagation from line standard and systematic uncertainty evaluation, i.e. linearity and noise floor, etc. [14].

The 10 disconnection/reconnection was made the measurement of four verification devices. Systematic stability was as well as less than 90 dB during measurement for approximately 30 minutes. The complex reflection coefficients representing aperture dimensions and line thickness of verification devices were obtained. Averaged values of return loss of verification devices are plotted together with its associated uncertainty in Fig. 5.

To verify the both VNA measurement and verification device characteristics, we compared two different values from VNA measurement and dimensionally-derived calculation results of return loss. Figs. 8 show the both values, Δ, and equivalency $U(\Delta)$, i.e. uncertainty of difference Δ [15], in the comparison of return loss measurement results. The differences Δ between both values of return loss were almost less than equivalency $U(\Delta)$for all verification device, however, Δ is larger than equivalency $U(\Delta)$ at some of measured frequency points. Our uncertainty calculation slightly underestimated the actual error in the measurement at

some frequency points, due to movement of cable between frequency extender modules to VNA.

## VI. Summary

This paper has presented design of two-port mismatch device as verification device providing frequency-independent return loss for VNA measurement. The return loss derived from S-parameter of two-port mismatch devices was estimated by the Monte Carlo simulations and electromagnetic simulations using dimensional measurement results. Then, VNA measurement capability was verified by the comparison between the both results of simulation and VNA measurement of verification devices. The measurement results of return loss were slightly larger than dimensional-derived values. This might be caused by excess reflection characteristics coming from misalignment and center offset of aperture at the mated interface of waveguide and systematic error, i.e. cabling between VNA and extenders, etc..

**Acknowledgement**

The work described in this paper was supported by Support for Ventures Involved in Innovation and Practical Application in 2013 from New Energy and Industrial Technology Development Organization (NEDO) of Japan.

**References**

[1] R. W. Beatty, "Calculated and measured S11, S21, and Group Delay for Simple Types of Caxial and Rectangular Waveguide 2-Port Standards," *NBS Technical Note* 657, Dec. 1974.

[2] N M Ridler and M J Salter, "Cross-connected Waveguide Lines as Standards for Millimeter- and Submillimeter-wave Vector Network Analyzers," *81st ARFTG Microwave Measurement Conference Digests*, pp.1 – 7, June 2013

[3] Stergios Papantonis, Nick M. Ridler, and Stepan Lucyszyn, "A New Technique for Vector Network Analyzer Calibration Verification Using a Single Reconfigurable Device," *82th ARFTG Microwave Measurement Conference Digests*, pp.1 – 3, Nov. 2013

[4] D. F. Williams, "500 GHz – 750 GHz Rectangular-Waveguide Vector-Network-Analyzer Calibrations," IEEE Trans. *THz Sci. Technol*., vol. 1, no. 2, pp. 364-377, Nov 2011.

[5] D. F. Williams, "Comparison of Sub-Millimeter-Wave Scattering-Parameter Calibrations with Imperfect Electrical Ports," *IEEE Trans. THz Sci. Technol*., vol. 2 no. 1, pp. 144-152, Jan 2012.

[6] N. M. Ridler, R. G. Clarke, M. J. Salter, and A. Wilson, "Traceability to National Standards for Sparameter Measurements in Waveguide at Frequencies from 140 GHz to 220 GHz," *76th ARFTG Microwave Measurement Conference digests*, pp. 1-7 Dec. 2010.

[7] T. Schrader, K. Kuhlmann, R. Dickhoff, J. Dittmer, and M. Heibel, "Verification of scattering parameter measurements in waveguides up to 325 GHz including highly-reflecting devices, *Adv. Radio Sci*., vol. 9, pp. 9-17, 2011.

[8] M Horibe, R Kishikawa and M Shida, "Complete characterization of rectangular waveguide measurement standards for vector network analyzer in the range of millimeter and sub-millimeter wave frequencies", *76th ARFTG Microwave Measurement Conference digests*, pp 1-15, , 2-3 December 2010.

[9] Maury Microwave, "Two-port Standard Sets", Technical Data Sheet 3A-322A, Apr. 1998. http://maurymw.com/pdf/datasheets/3A-322A.pdf

[10] Agilent Technologies, "11645A R, Q, U, V, W Waveguide Verification Kits User's and Service Guide", Part Number 11645-90013, Nov. 2004.

[11] M. Horibe, and K. Noda, "Modification of Waveguide Flange Design for Millimeter and Sub-millimeter-wave measurements," *77th ARFTG Conference Digest*, pp. 1-7, June. 2011.

[12] M. Horibe, and R. Kishikawa, "Performance of New Design of Waveguide Flange for Measurements at Frequencies from 800 GHz to 1.05 THz," *81th ARFTG Conference Digest*, pp. 1-6, June. 2013.

[13] M. Horibe K. Shimaoka, K. Fujii, A. Widarta, H. Iida, and R. Kishikawa, "Standards Research in Japan: Latest Development of Millimeter-Wave and Submillimeter-Wave Measurements", *IEEE Microwave Magazine*, Vol 14, No 7, pp 59-66, November/December 2013.

[14] M. Horibe and R. Kishikawa, "Metrological Traceability in Waveguide S-parameter Measurements at 1.0 THz Band," *IEEE Trans. Instrum. Meas.*, vol. 62, no. 6, pp. 1814 – 1820, June 2013.

[15] M. G. Cox, "*The evaluation of key comparison data*," Metrologia Vol. 39, pp. 589-595, 2002.

# Evaluation of CMOS Differential Transmission Lines as Two-Port Networks with On-Chip Baluns in Millimeter-Wave Band

Kyoya Takano, Mizuki Motoyoshi, Takeshi Yoshida, Kosuke Katayama, Shuhei Amakawa, and Minoru Fujishima

Graduate School of Advanced Sciences of Matter, Hiroshima University
1-3-1 Kagamiyama, Higashi-Hiroshima, Hiroshima 739-8530, Japan

**Abstract — It is difficult to evaluate four-port on-chip CMOS devices in the millimeter-wave (MMW) band using four-port vector network analyzer. To obtain the differential-mode characteristics, we proposed the technique of evaluating four-port networks as two-port networks using on-chip baluns, and applied the technique to the evaluation of differential transmission lines in the MMW band. As a result, it was shown that the propagation constant of the differential mode obtained by this technique was in the good agreement with one obtained by the EM simulation at the frequency band from 47 GHz to 110 GHz. By using this technique, it is expected that on-chip CMOS differential devices in the MMW band can be evaluated more easily.**

**Index Terms —Differential transmission line, millimeter-wave, on-chip balun, S-parameters, two-port measurement.**

## I. Introduction

Differential topology has many advantages such as better gain, second-order linearity, superior spurious response performance, and noise immunity [1]. Therefore, it is used to improve the performances of millimeter-wave (MMW) integrated circuits [2]. To design differential circuits, the characteristics of differential devices are required. They are usually characterized with four-port scattering parameters (S-parameters) which are obtained by measuring device under tests (DUTs) as four-port networks shown in Fig. 1(a). The four-port S-parameters are measured by four-port vector network analyzer (VNA). However, it is difficult to measure four-port S-parameters in the MMW band because the measurement systems and calibration are more complicated [3]. In the past, the method of characterizing differential networks using two-port VNA was proposed [4]. However, this method is not suitable for on-chip CMOS devices in the MMW band because 50Ω terminations used in the method are not accurate in the MMW band.

Four-port S-parameters can be converted to mixed-mode S-parameters [5]. The pure differential mode is the main characteristics of differential devices. Therefore, it is important to know the pure differential-mode characteristics. To obtain them without measuring four-port S-parameters, off-chip baluns are used [6]. However, connecting of off-chip buluns to a chip with high accuracy is difficult in the MMW band. Therefore, we propose the technique of evaluating on-chip CMOS differential devices as two-port networks with on-chip baluns shown in Fig. 1(b) in the MMW band. In this paper, we consider a differential transmission line as a differential device because it is the important and simple device. In the following sections, the technique using two-port network with baluns for the evaluation is called "two-port technique", and the technique using four-port network is called "four-port technique".

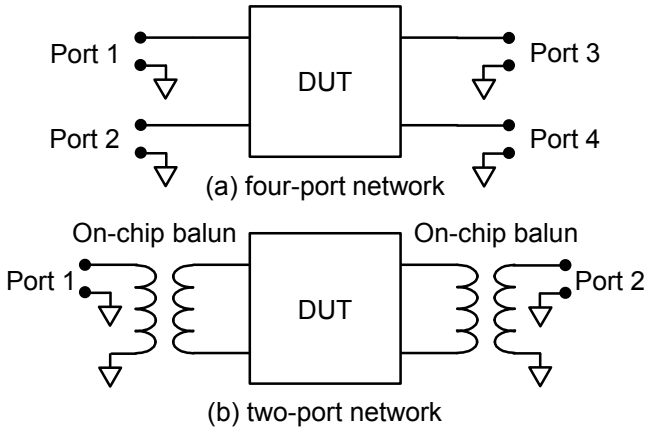


Fig. 1. Networks of test structures for a four-port device as (a) a four-port network and as (b) a two-port network with on-chip baluns.

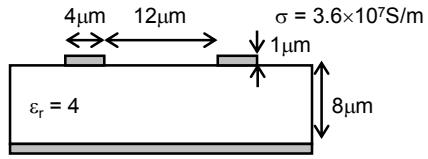


Fig. 2. Cross-section of a differential transmission line used for the estimation of the impact of the amplitude and phase imbalances of baluns.

## II. Procedure of Two-Port Technique and Impact of Amplitude and Phase Imbalances of Baluns

The pure differential-mode characteristics are derived from the S-parameters of two-port networks with baluns. Baluns convert a four-port network to a two-port network. Furthermore, ideal baluns convert the four-port S-parameters to the differential-mode S-parameters [5]. Therefore, the differential-mode S-parameters of the DUT can be obtained by

978-1-4799-4423-1/14/$31.00 ©2014 IEEE

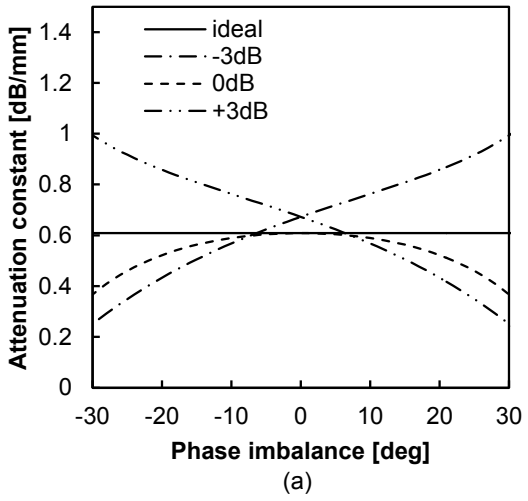


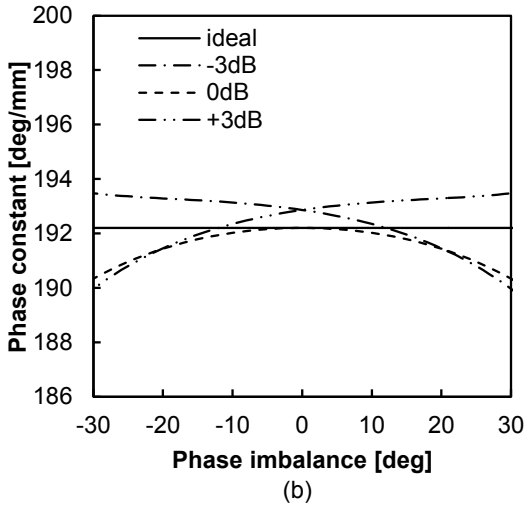


Fig. 3. (a) Attenuation constant and (b) phase constant as a function of the phase imbalance changing the amplitude imbalance at 100 GHz.

de-embedding them from the S-parameters of the test structures including baluns [7]. As a result, we can evaluate the differential-mode S-parameters of four-port devices using same procedure as two-port device evaluation.

Next, we consider the errors caused in the measurement results of the differential-mode S-parameters when baluns have the amplitude and phase imbalances in the balanced port signals. To clarify the impact of the imbalances to the differential-mode propagation constant of a differential transmission line in the MMW band, the differential-mode S-parameters including the errors were calculated using a transmission line of which characteristics are known a priori. The structure of the transmission line is shown in Fig. 2. Moreover, the S-parameters of a balun which has the amplitude imbalance $\Delta$ and phase imbalance $\theta$ is assumed as

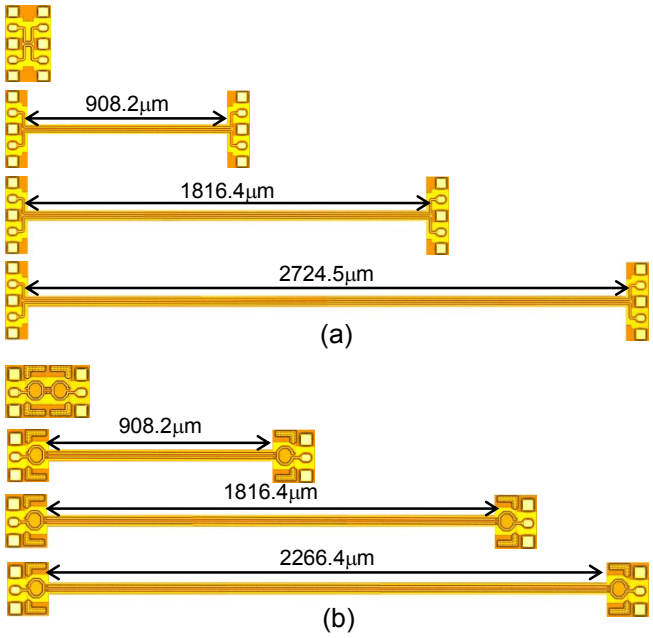


Fig. 4. Microscopy images of the test structures (a) for the two-port technique and (b) for the four-port technique.

$$\mathbf{S}_{\mathrm{BAL}} = \begin{bmatrix} 0 & \frac{1}{\sqrt{2}} & -\frac{\Delta e^{j\theta}}{\sqrt{2}} \\ \frac{1}{\sqrt{2}} & 0 & \frac{1}{3} \\ -\frac{\Delta e^{j\theta}}{\sqrt{2}} & \frac{1}{3} & 0 \end{bmatrix}. \quad (1)$$

The S-parameters of the test structures including baluns were derived from the expression (1) and the S-parameters of the differential transmission lines of which lengths were 0, 1, 2 and 3 mm at 100 GHz. The amplitude imbalance $\Delta$ was changed to -3, 0 and +3dB. The phase imbalance $\theta$ was changed from -30 to 30°. The propagation constant of the differential transmission line was derived by multiline thru-reflect-line method [8] using the S-parameters of those test structures. Figure 3 shows the attenuation constant and phase constant as a function of the phase imbalance changing the amplitude imbalance. The solid line shows the differential-mode propagation constant calculated from the four-port S-parameters of the transmission line only. As shown in Fig. 3, although the amplitude and phase imbalances affect the propagation constant, if the absolute value of the phase imbalance can be made below 5° with the amplitude imbalance of ±3dB, the attenuation constant and phase constant become below about 0.1dB/mm and 1°/mm at 100 GHz, respectively. Therefore, the differential-mode propagation constant can be evaluated correctly by making baluns with low imbalances at the MMW band.

## III. Comparisons using Measurement Results

To verify the two-port technique at the MMW band, it is compared with the four-port technique and the EM simulation.

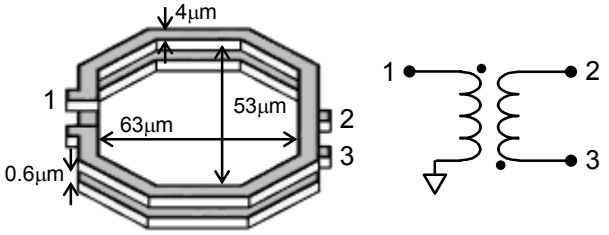


Fig. 5. Structure and circuit of the on-chip transformer balun with one-turn windings used for measurements.

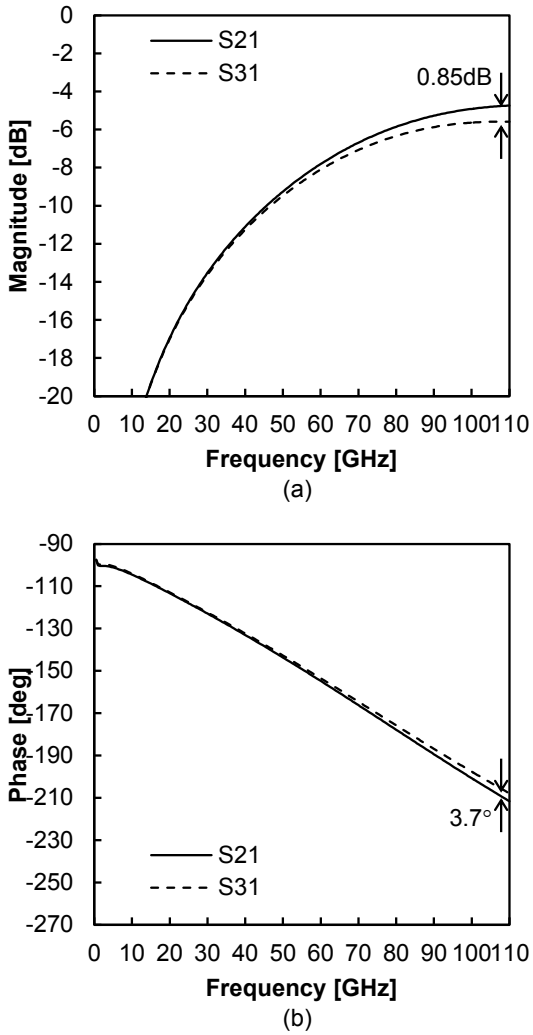


Fig. 6. EM simulation results of the (a) magnitude and (b) phase of $S_{21}$ and $S_{31}$.

We fabricated the test structures using the 40nm CMOS process. The microscopy images of the test structures are shown in Fig. 4. The structure of the on-chip balun is shown in Fig. 5. Transformer balun with one-turn windings were used. Figure 6 shows the EM simulation results of the magnitude and phase of $S_{21}$ and $S_{31}$. The EM simulator is Agilent Technologies Momentum. As shown in Fig. 6, the amplitude and phase imbalances were 0.85dB and 3.7° at 110 GHz,

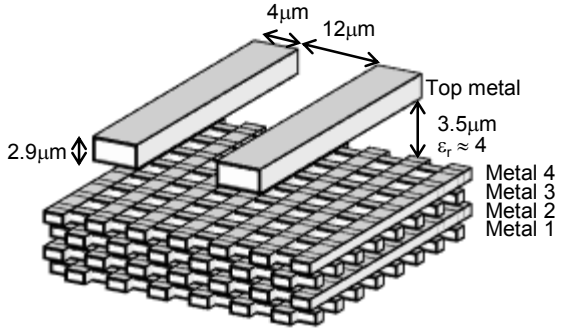


Fig. 7. Structure of the differential transmission line used for measurements.

respectively. The structure of the differential transmission line is shown in Fig. 7. A top metal layer was used for signal lines and lower four metal layers were used for ground lines. Figure 8 shows the differential-mode and common-mode propagation constants of the differential transmission lines obtained by the four-port technique up to 65 GHz. The upper frequency was limited by the four-port VNA. The four-port VNA was calibrated by a short-open-load-thru (SOLT) probe-tip reference calibration. To derive the propagation constant from the measured four-port S-parameters, the multimode TRL technique [7] was used. Figure 9 shows the propagation constant obtained by the two-port technique up to 110GHz. The two-port VNA was calibrated by a line-reflect-reflect-match (LRRM) probe-tip reference calibration. To derive the propagation constant from the measured two-port S-parameters, the multiline TRL method [8] was used. The propagation constant cannot be evaluated in the frequency range from DC to about 47 GHz because the baluns cut the signals in the lower frequency. The comparison of the propagation constants obtained by two-port and four-port techniques and the EM simulation are shown in Fig. 10. As shown in Fig. 10, the differential-mode propagation constant obtained by two-port technique is in the good agreement with one obtained by the EM simulation. From these result, it is considered that the differential-mode propagation constant of the transmission line could be obtained correctly by the two-port technique with on-chip baluns from 47 to 110 GHz.

## IV. Conclusion

The technique to evaluate four-port networks as two-port networks using on-chip baluns for the MMW band for on-chip CMOS differential devices was proposed and it applied to differential transmission lines. As a result, it was shown that the propagation constant of the differential mode obtained by two-port measurements was in the good agreement with one obtained by the EM simulation at the frequency band from 47 to 110 GHz. By using this technique, it is expected that on-chip CMOS differential devices in the MMW band can be evaluated more easily.

ACKNOWLEDGEMENT

This study was supported by the Ministry of Internal Affairs and Communications of Japan.

REFERENCES

[1] S. Belkin, "Differential Circuit Characterization with Two-Port S-Parameters," *IEEE Microwave Magazine*, vol. 7, no. 6, pp. 86-98, Dec. 2006.

[2] C. Weyers, P. Mayr, J. W. Kunze, and U. Langmann, "A 22.3 dB voltage gain 6.1 dB NF 60 GHz LNA in 65 nm CMOS with differential output," in *ISSCC Dig. Tech. Papers*, pp. 192–193, Feb. 2008.

[3] Cascade Microtech, Inc., "Making Accurate and Reliable 4-Port On-Wafer Measurements," *Application Note*, 2009.

[4] D. E. Bockelman and W. R. Eisenstadt, "Combined differential and common-mode scattering parameters: Theory and simulation," *IEEE Trans. Microwave Theory Tech.*, vol. 43, no. 11, pp. 1530–1539, July 1995.

[5] K. M. Ho, K. Vaz, and M. Caggiano, "Scattering parameter characterization of differential four-port networks using a two-port vector network analyzer," in *Proc. Electron. Components Technol. Conf.*, pp. 1846–1853, June 2005.

[6] C. R. Curry, "How to calibrate through balun transformers to accurately measure balanced systems," *IEEE Trans. Microwave Theory Tech.*, vol. 51, no. 3, pp. 961–965, Mar 2003.

[7] M. Wojnowski, V. Issakov, G. Sommer and R. Weigel, "Multimode TRL Calibration Technique for Characterization of Differential Devices," *IEEE Trans. Microwave Theory Tech.*, vol. 60, no. 7, pp. 2220–2247, July 2012

[8] R. B. Marks, "A Multiline Method of Network Analyzer Calibration," *IEEE Trans. Microwave Theory Tech.*, vol. 39, no. 7, pp. 1205–1215, July 1991.

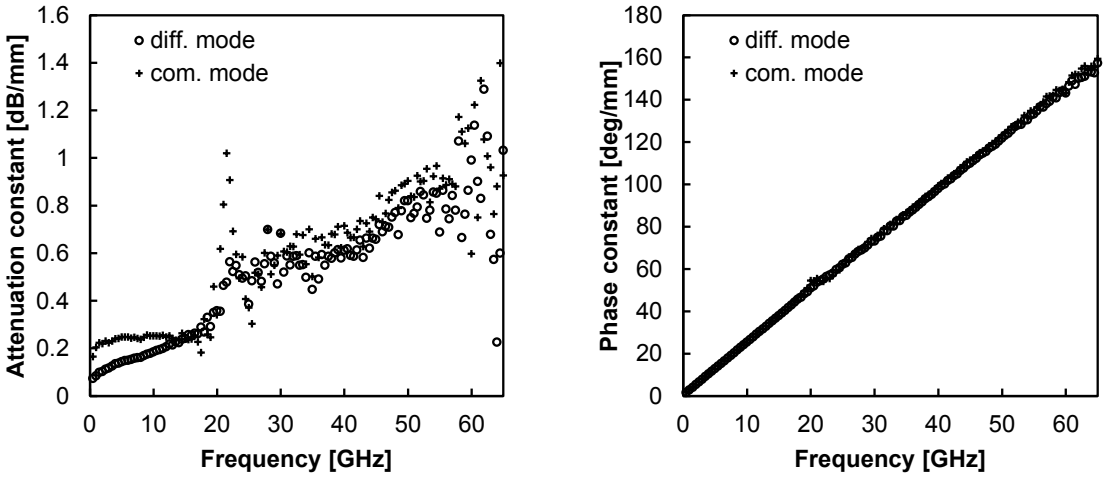


Fig. 8. Measured differential-mode and common-mode propagation constants of the differential transmission lines obtained by the four-port technique.

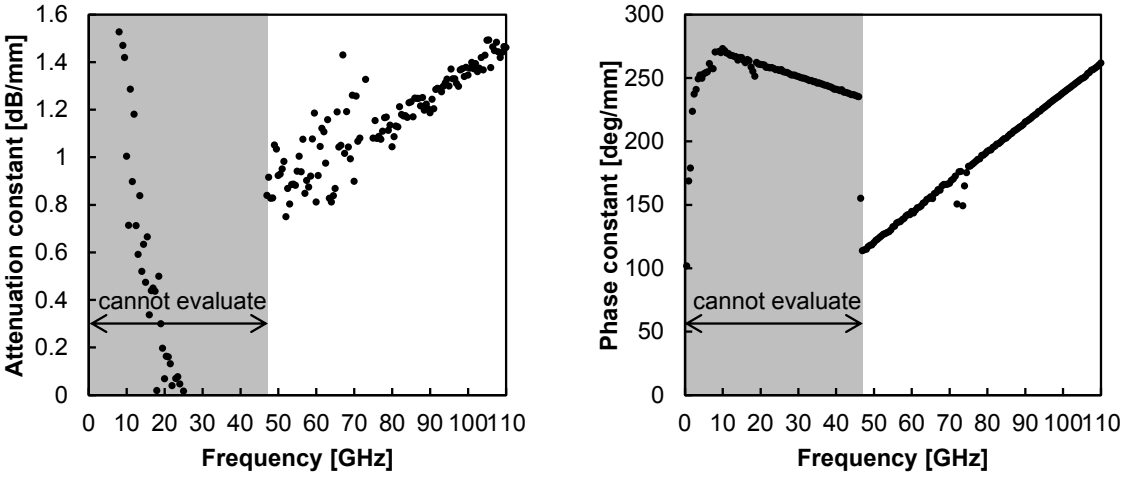


Fig. 9. Measured propagation constant obtained by the two-port technique.

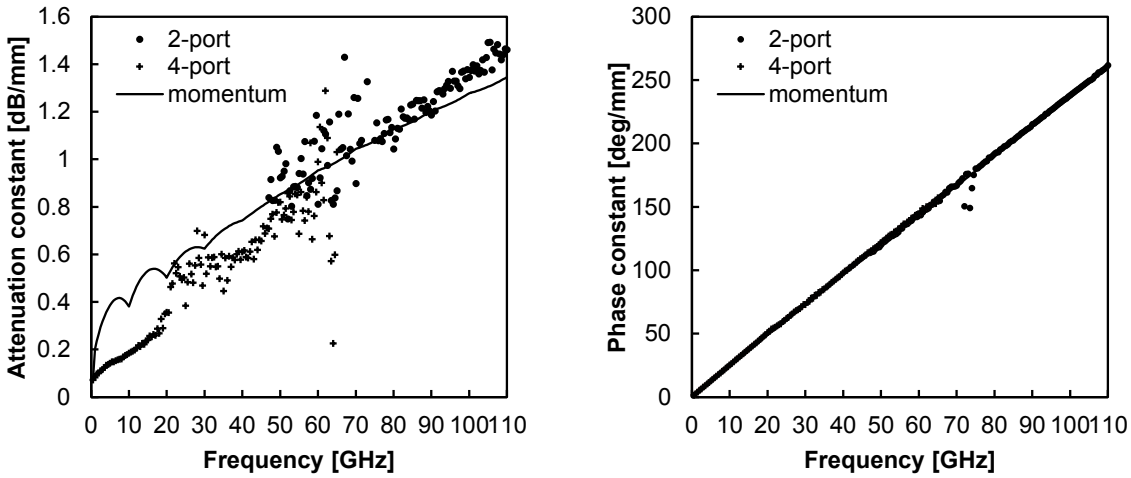


Fig. 10. Comparison of the measured propagation constants obtained by two-port and four-port techniques and the EM simulation.

# Study of Calibration Standards for Extreme Impedances Measurement

*Martin HAASE, Karel HOFFMANN*

*Czech Technical University in Prague, Faculty of Electrical Engineering, Dept. Of Electromagnetic Field*
*Technická 2, 166 27, Praha, Czech Republic, haasema1@fel.cvut.cz, hoffmann@fel.cvut.cz*

**Abstract — The paper describes first results of pioneering research in the field of calibration standards for the measurement of extreme impedances. It is a necessary step for the measurement of extreme impedances since the method has been developed. The proposed calibration standards are based on coaxial microwave connector APC-7 and were extensively analyzed in CST Microwave Studio at the frequency range from 0.1 GHz to 18 GHz. Some of the analyzed structures seem to be promising for measurements of tiny very high impedance structures like carbon nanotubes or atto-farad varactors.**

**Index Terms — Calibration standard, CST Microwave Studio, microwave measurement, APC-7, impedance measurement.**

## I. Introduction

Extreme impedances are often mentioned in connection with the RF and microwave measurement of nanoscale devices [1]-[3] – carbon nanotubes and nanowires – since their DC resistance is of the order of kΩ. According to [3] a single walled carbon nanotube has the resistance per unit of length approximately 6 kΩ/µm. At present, the measurement of extreme impedances with common measurement equipment in RF and microwave technique is seriously a great challenge due to the significant impedance mismatch.

A simple method for measurement of extreme impedances has been introduced in [4]. This method substantially increases sensitivity and accuracy of the measurement since it can suppress the influence of the noise and the instability of a vector network analyzer (VNA). Afterwards, this method was extended to directly measure the impedance [5]. Authors proposed a suitable error model and a calibration process for real measurements. The process needs at least three full known calibration standards. The basic problems of these calibrations and measurements were mentioned in [6]. These are the absence of well-defined calibration standards and low mounting reproducibility of standards and a device under test (DUT).

The main purpose of this paper is to discover the basic problems and to present the first simulated results of the design of precise calibration standards for measurement of extremely high impedances. The closed coaxial structure compatible with APC-7 connectors was chosen for future realizations of these standards to eliminate any radiation problems and to get good mounting reproducibility. The studied structures were analyzed using CST Microwave Studio electromagnetic simulator at the frequency band up to 18 GHz. Calibration standards with different values in the impedance range from 25 kΩ to infinite were simulated.

## II. Methodology

The values of calibration standards were chosen similarly to [6] – two resistors and OPEN. Since calibration standards have values of the order of kΩ a special attention must be paid on the setting of the electromagnetic simulator to get an appropriate accuracy of the frequency solver in CST. For instance, to distinguish the value 100 kΩ from the OPEN the accuracy of the order of $10^{-4}$ is needed at least, see Fig. 1.

| $Z_0$ (Ω) | $Z_L$ (kΩ) | $\Gamma_L$ (-) |
|---|---|---|
| 50 | 5 | 0.980198 |
| 50 | 10 | 0.990050 |
| 50 | 25 | 0.996008 |
| 50 | 50 | 0.998002 |
| 50 | 100 | 0.999000 |
| 50 | OPEN | 0.9999…. |

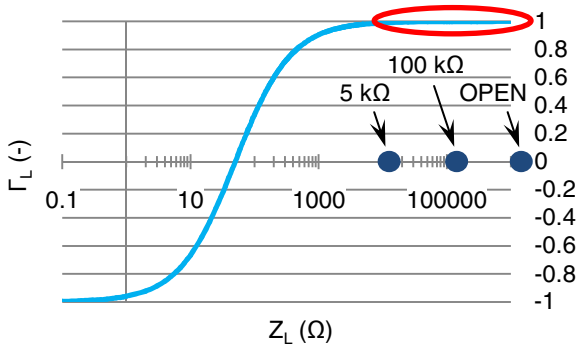


Fig. 1. Illustration of extreme high impedance area and corresponding reflection coefficient $\Gamma_L$.

Calibration standards were simulated in CST Microwave Studio as a close form structures. Frequency solver, tetrahedral mesh and adaptive mesh refinement were used. In order to ensure the desired accuracy the criterion S-parameter (delta S) was adjusted to the value $1 \cdot 10^{-4}$. It means that the difference between two or more last s-parameter calculations has to be smaller than the adjusted value to stop refining the mesh density.

978-1-4799-4423-1/14/$31.00 ©2014 IEEE

Loss free materials except resistive parts were considered in all simulations because of simplicity. Then the behavior of the calibration standard for different configurations can be more easily determined since it is clear that the changes in properties are not caused by losses in metals and dielectrics.

Well known demand on an identical electromagnetic field distribution around the calibration standards and DUT was taken into account. The requirements for a simple technological fabrication and good mechanical properties were supposed. Therefore, the fused silica as a dielectric and a carrier for CrNi resistive material and DUT respectively was considered. Fused silica has low permittivity 3.8 [7], high homogeneity and good mechanical and chemical properties compatible with CrNi thin layer technology.

The connector APC-7 was chosen due to its good mechanical properties and its suitable dimensions. The connector can be easily disassembled and some new parts can be added to create a new calibration standard. This minimizes requirements for calibration standard fabrication. The connector dimensions, however, result in relatively low upper frequency of application. It was not considered as a serious problem in this study.

## III. Simulated Structures

Different mechanical arrangements of resistive calibration standards on the glass carrier placed in 7 mm air coaxial line were analyzed.

### *A. Standard with glass disk*

The first idea was to use a glass substrate in the shape of a disk placed inside the 7 mm air coaxial line, see Fig. 2. The disk carries a resistive strip creating the calibration standard. Behind the disk there is only the outer conductor of APC-7 connector as a cylindrical waveguide below the cutoff. Fig. 2 depicts the real appearance of calibration standard. Further, for simulation purposes the structures were drawn "inversely". It means that the prefect electric conductor (PEC) was used as a background material in contrast to the structure from Fig. 2

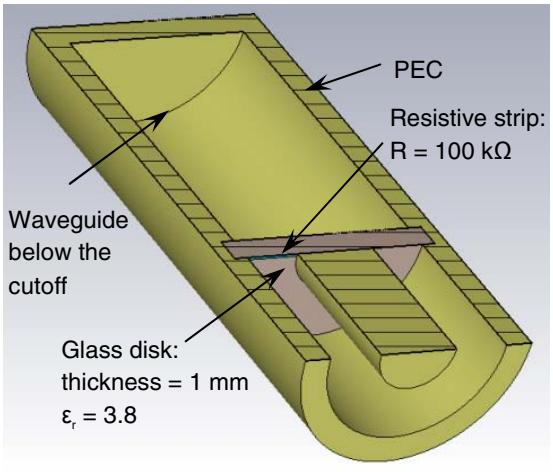


Fig. 2. Real appearance of the calibration standard.

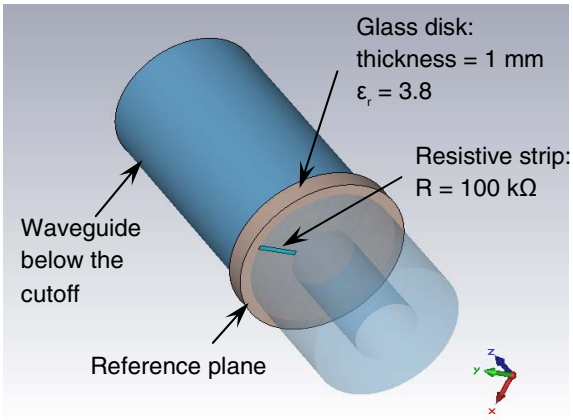


Fig. 3. Simulated structure ("inversely" drawn) with 1 mm thick glass disk, resistive strip and cylindrical waveguide below the cutoff in CST Microwave studio.

where vacuum was used. Therefore, only dielectrics, metallic strips and resistive strips are depicted in following figures. Fig. 3 shows simulated structure which is identical to the structure in Fig. 2. The resistive material with the resistance 10 kΩ/□ and length 2 mm was simulated as infinitely thin layer and was placed on the glass substrate between inner and outer conductor of coaxial line. This technology was considered since it was supposed to be achievable. The value of a calibration standard depends on the width of the resistive strip. The waveguide below the cutoff was used to eliminate any problems with radiation mentioned above. The s-parameter $S_{11}$ of the structure is depicted in Fig. 4.

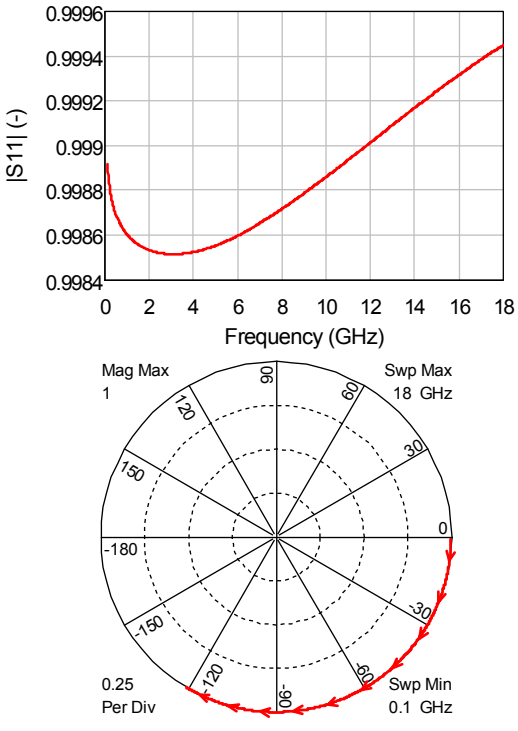


Fig. 4. S-parameter $S_{11}$ of the 100 kΩ calibration standard with 1 mm thick glass disk.

This structure suffers from high fringing capacity at the reference plane of the resistive strip. This high fringing capacity causes the electromagnetic field to avoid the resistive strip since there is a parallel combination of a resistor and a capacitor. The higher fringing capacity is the smaller difference in reflection coefficients between two calibration standards with different resistive value can be achieved. The problem is more serious at higher frequencies and for thicker glass disk. Calibration standards with the same configuration but different value of resistor were considered in order to illustrate the fringing capacity problem, see Fig. 5.

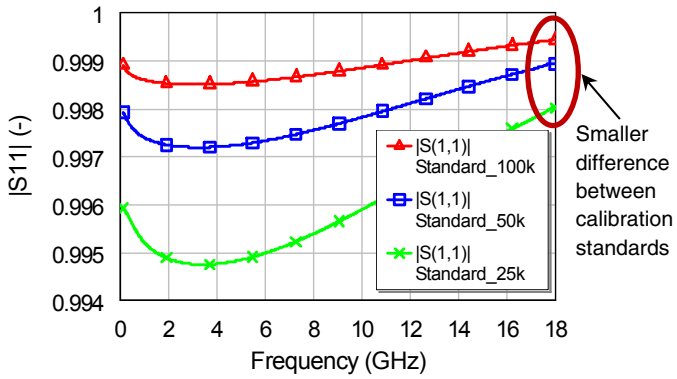


Fig. 5. $|S_{11}|$ dependence of three calibration standards with identical structure but with different value of resistor – 25 kΩ, 50 kΩ and 100 kΩ.

*B. Standard with glass coaxial line*

To suppress the above mentioned problems a new concept of calibration standard was proposed, see Fig. 6. This structure uses a glass coaxial line terminated with the cylindrical waveguide below the cutoff and sufficiently suppresses undesirable fringing capacity, see Fig 7. In order to determine the fringing capacity at the end of the glass line the air coaxial line was not used.

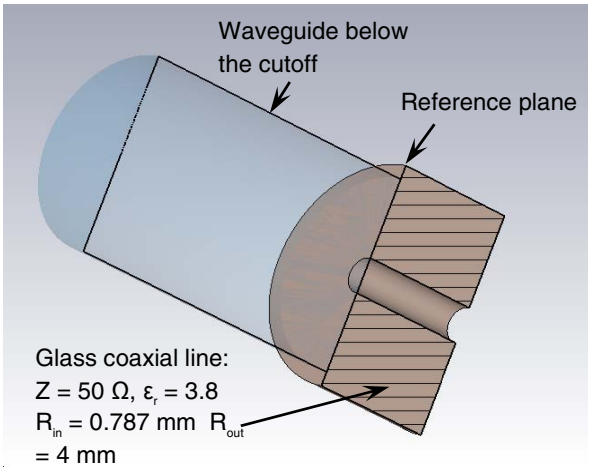


Fig. 6. Simple structure composed of a 50 Ω glass coaxial line and cylindrical waveguide bellow the cutoff for determining the fringing capacity.

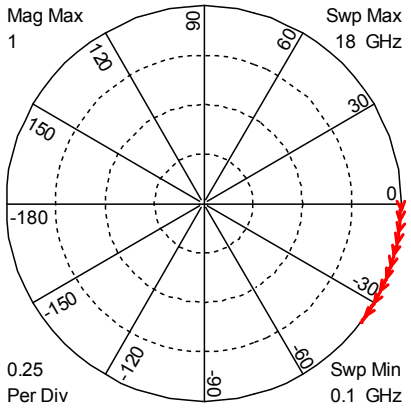


Fig. 7. $S_{11}$ of the fringing capacity of the structure in Fig. 6 at the reference plane.

Subsequently, the resistive strips were placed at the end of the glass coaxial line and additional metallic parts simulated as infinitely thin perfect conductors were added

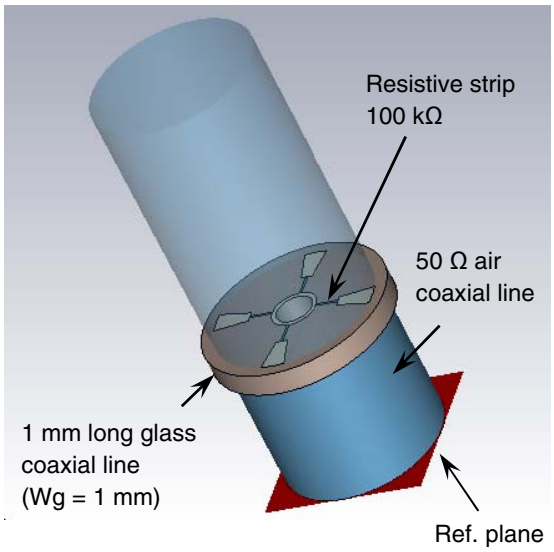


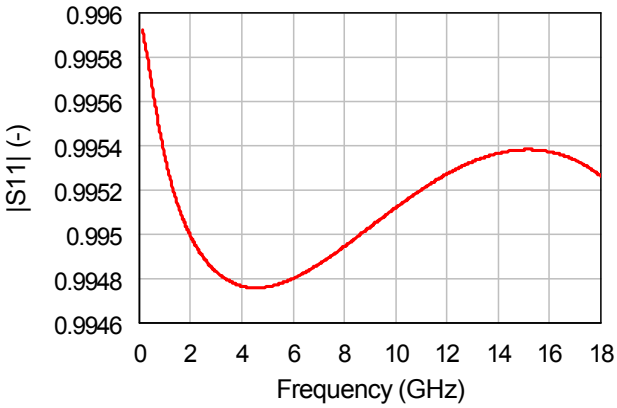


Fig. 8. Four-strip 25 kΩ calibration standard with 1 mm long glass coaxial line and its frequency dependence of $|S_{11}|$.

because of technological reasons. Fig. 8 shows the new structure and its properties.

Sharp frequency dependence is evident from achieved results. A deep analysis clarified the effect. There are two reasons for these properties. Firstly, for short glass coaxial lines a capacity coupling between the inner conductor of the air coaxial line and the resistive strips causes a sharp decrease of reflection coefficient $|S_{11}|$ below 3 GHz. Secondly, multiple reflections at both ends of the glass coaxial line cause frequency dependence at higher frequencies. In Fig. 9 there are depicted s-parameters for different lengths of the glass coaxial line.

If a very short length of the glass line is considered (0.2 mm) a strong capacity coupling can be observed, see Figs. 10a and 10b. Figures show two simulations for different frequencies. It is apparent that the electric field distribution along the resistive strip changes significantly with frequency. Effectively only small part of resistive strip is connected to the circuit, therefore the effective value of resistor is smaller which results in a smaller reflection coefficient. The problem is surprisingly significant even at relatively low frequencies.

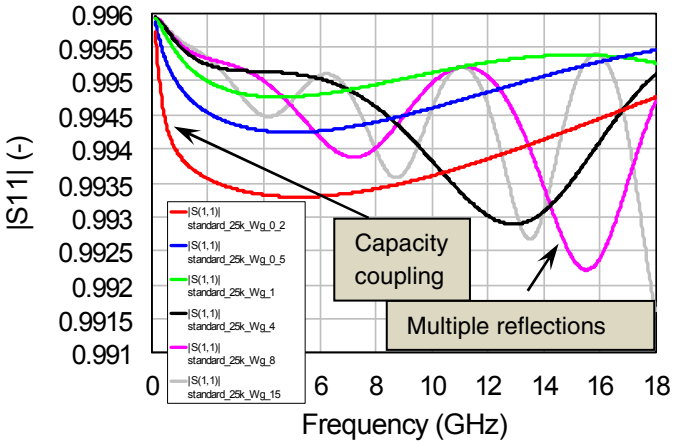


Fig. 9. |S11| of the 25 kΩ calibration standard for different lengths Wg of glass coaxial line (0.2 ÷ 15 mm).

In order to suppress the parasitic coupling the glass coaxial length must be longer. In Figs. 10c and 10d there are depicted simulations at the same frequencies but the length of the glass coaxial line is 4 mm. It is clearly seen that the frequency

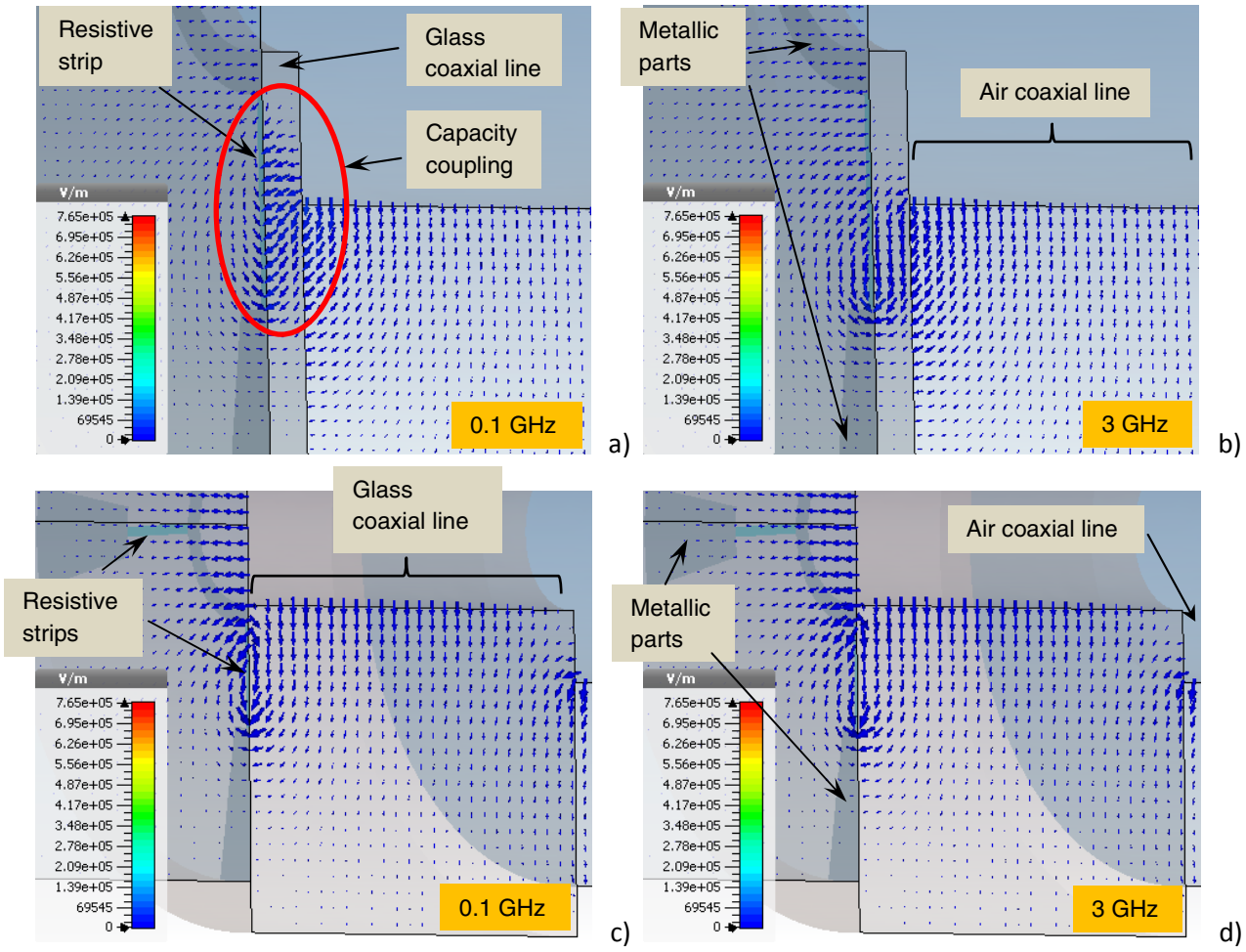


Fig. 10. The effect of capacity coupling between inner conductor of air coaxial line and resistive strip – 0.2 mm long glass coaxial line at frequencies 0.1 GHz (a) and 3 GHz (b), 4 mm long glass coaxial line at frequencies 0.1 GHz(c) and 3 GHz (d).

dependence of the electric field distribution along the resistive strip is now significantly reduced.

A bit strange increase of reflection coefficient around 14 GHz in Fig. 8 and ripple traces in Fig. 9 corresponding to longer glass line lengths can be explained by multiple reflections and possible presence of higher order modes since the glass substrate has permittivity 3.8. The cutoff frequency of the first waveguide mode in glass coaxial line is around 11 GHz, therefore the higher order mode(s) can propagate in the structure above that frequency. The ripples, however, do not represent any serious problem. They can be eliminated by the measurement method itself if the reference impedance, see [5], [6], is realized similarly like the calibration standards.

### *C. Simulation in glass coaxial line structure*

As it was explained above the influence of multiple reflections can be eliminated. Therefore, calibration standards can be simulated without air coaxial line. This makes possible to shift the reference plane to the location of resistive strips where their behavior can be directly analyzed.

Two realization versions of coaxial standards depicted in Fig. 11 were studied. The left one consists of four symmetrical radial resistive strips, the right one is created by the only one radial resistive strip. Simulated results of the frequency

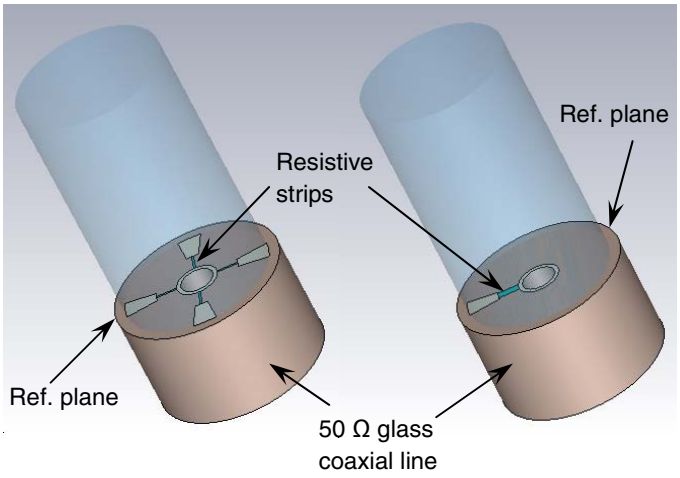


Fig. 11. One-strip and four-strip calibration standards composed of 50 Ω glass coaxial line, resistive material and cylindrical waveguide bellow the cutoff.

dependence of reflection coefficients are depicted in Fig. 12. The four resistive strip standard shows smooth trace of the reflection coefficient decreasing with frequency. On the other hand a completely different behavior of the one-strip calibration standard can be seen. The reason results from a higher order mode. The one-strip non-symmetrical configuration can better excite the higher order mode compared to the four-strip configuration. It can be clearly seen that reflection coefficients of both standards smoothly decrease with frequency. It should be emphasized that the standards are supposed to be pure resistive elements. The reason why the reflection coefficients are still frequency dependent remains in this moment unclear and will need more effort to be understood.

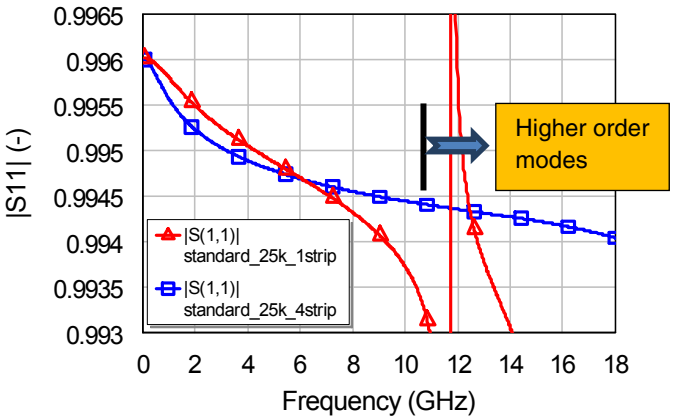


Fig. 12. Comparison of one- and four-strip configurations of final structure with 50 Ω glass coaxial line and waveguide bellow the cutoff – 25 kΩ standards.

## IV. Conclusion

Different mechanical arrangements were analyzed to map basic problems connected with the design of calibration standards for the measurement of very high impedances compatible with APC-7 connectors at frequencies up to 18 GHz. CST Microwave studio frequency solver was applied for all simulations. The fused silica was supposed as a dielectric carrier of the resistive calibration standards or a DUT.

One- or four-strip calibration standards placed at the end of the coaxial line with fused silica dielectric seem to be promising for the calibration and measurement up to about 10 GHz. The one-strip calibration standards can be potentially used for measurements of very tiny high impedance nanoscale elements. This configuration is more practical from the measurement point of view since the DUT can be placed instead of resistive strip and the impedance of the DUT can be directly measured. The four resistive elements standards can be potentially used for measurement of very low capacitance varactors. The DUT position is supposed to be on the inner conductor of the glass coaxial line and four bonding wires replace four resistive calibration strips maintaining the symmetry.

There are still some problems which have not been sufficiently clarified namely the weak frequency dependence of pure resistive calibration standard. The authors believe to be well on the way to explain it in near future. Verification of final simulations on an independent electromagnetic simulator HFSS and final realization of the standards using an accessible technology are future tasks, too.

## Acknowledgement

This work was funded through the European Metrology Research Programme (EMRP) Project SIB62 'Metrology for

New Electrical Measurement Quantities in High-frequency Circuits'. The EMRP is jointly funded by the EMRP participating countries within EURAMET and the European Union.

This work has been supported also by the Czech Technical University in Prague under project No. SGS13/198/OHK3/3T/13.

## REFERENCES

[1] P.J. Burke, Z. YU, S. Li, and C. Rutherglen, "Nanotube technology for microwave applications," *IEEE MTT-S International, Microwave Symposium Digest,* pp. 897-900, June 2005

[2] P.J. Burke, and C. Rutherglen, "RF measurements of nanoscale devices: Challenges and opportunities," *Precision Electromagnetic Measurements Digest,* Broomfield, CO, pp. 494-495, June 2008

[3] P.J. Burke, Z. YU, and C. Rutherglen, "Carbon nanotubes for RF and microwaves," *Gallium Arsenide and Other Semiconductor Application Symposium,* Paris, pp. 1-4, Oct. 2005

[4] M. Randus, and K. Hoffman, "A simple method for extreme impedances measurement," *72nd Digest of 2007 ARFTG Int. Conference*, Dec. 2007

[5] M. Randus, and K. Hoffman, "A method for direct impedance measurement in microwave and millimeter-wave bands," *IEEE Transactions on Microwave Theory and Techniques,* vol. 59, no. 8, pp. 2123-2130, Aug. 2011

[6] M. Randus, and K. Hoffman, "A simple method for extreme impedances measurement – Experimental testing," *72nd ARFTG Microwave Measurement Symposium,* Portland, OR, pp. 40-44, Dec. 2008

[7] H.E. Bussey, J.E. Gray, E.C. Bamberger, E. Rushton, G. Russell, B.W. Petley, and D. Morris, "International *Comparison of Dielectric Measurements ,"IEEE Transactions on Instrumentation and Measurement,* pp. 305-311, Dec. 1964

# Characterizing a Noninsertable Directional Device Using the NIST Uncertainty Framework

Jeffrey A. Jargon, Dylan F. Williams, Paul D. Hale, and Michael D. Janezic

National Institute of Standards and Technology, Boulder, CO 80305 USA
Tel.: +1.303.497.4961, Email: jeffrey.jargon@nist.gov

**Abstract — We characterize and provide uncertainties for a noninsertable, directional device over a frequency range of 90 to 100 GHz using the NIST Microwave Uncertainty Framework in conjunction with a commercial vector network analyzer. Our device consists of a chain of components, including a coaxial-to-waveguide adapter, a waveguide band-pass filter, a waveguide low-noise amplifier, a waveguide isolator, and a waveguide taper. With the aforementioned directional components, the well-known adapter removal technique is not adequate on its own for characterizing our device. In this paper, we describe and implement our method, and propagate the uncertainties from the two required calibrations to the characterized device.**

**Index Terms — Characterize, coaxial, directional, noninsertable, rectangular waveguide, uncertainty, vector network analyzer.**

## I. Introduction

Noninsertable devices, such as adapters with the same-sex or different-size coaxial connectors, and microwave probes with one port typically coaxial or rectangular waveguide and the other coplanar waveguide, are commonly encountered in high-frequency applications. Characterizing these devices poses a challenge since they cannot be characterized by use of a single vector network analyzer (VNA) calibration. Several methods [1–5], including the well-known adapter-removal technique [6], have been developed over the years for characterizing noninsertable adapters and probes. However, none of them are adequate on their own when the noninsertable device transmits power in one direction only, such as an isolator or amplifier. In this case, if the device is comprised of a noninsertable adapter connected to an insertable directional component, the adapter can be characterized by use of the adapter removal technique or one of its variants, the insertable directional component can be characterized using a single VNA calibration, and then the overall device may be characterized by cascading the two resultant *S*-parameter matrices.

Here, we implement this multi-step approach utilizing the NIST Uncertainty Framework [7–9] to propagate uncertainties. The Framework is based on a covariance-matrix description that enables us to capture all of the *S*-parameter measurement uncertainties and statistical correlations between them [10]. By identifying and modeling the physical error mechanisms in the calibration standards, we can determine the statistical correlations between uncertainties at different frequencies. These covariance-based uncertainties can then be propagated into the uncertainties of the *S*-parameters of the noninsertable, directional device. This is particularly valuable when transforming from the frequency domain to the time domain.

In the following sections, we describe our measurement methodology and error mechanisms, and present our results.

## II. Methodology

Our device under test consisted of a chain of components, including a 1 mm coaxial-to-WR-10 waveguide adapter, a WR-8 waveguide band-pass filter (BPF), a WR-8 waveguide low-noise amplifier, a WR-8 waveguide isolator, and a WR-8-to-WR-10 waveguide taper, as shown in Figure 1. This device will be used in conjunction with a characterized photodiode and sampling oscilloscope [11] to calibrate a down-converter.

Because our device is comprised of a noninsertable adapter connected to additional components, two of which are directional, we first characterize the adapter by use of a technique that determines the *S*-parameters of the adapter from two one-tier calibrations [7]. The first calibration is performed at a reference plane to the left of the adapter (in our case, WR-10 rectangular waveguide) with the adapter connected to port 2, and the second calibration is performed at a reference plane to the right of the adapter (in our case, 1 mm coax) with the adapter connected to port 1, as illustrated in Figure 1. The first estimate for the adapter *S*-parameters comes from the difference of the left calibration's port 1 error box (port 1 VNA terms only) and the right calibration's port 1 error box (port 1 VNA terms and adapter). The second estimate for the adapter *S*-parameters comes from the difference of the left calibration's port 2 error box (adapter and port 1 VNA terms) and the right calibration's port 2 error box (port 2 VNA terms only). The two estimates are then averaged.

During the left calibration (in WR-10 rectangular waveguide), we also measure our device chain without the adapter. Using the WR-10 calibration, we can characterize this portion of our device. Then, once the adapter is characterized using the two calibrations, we characterize the overall device by cascading the two resultant *S*-parameter matrices.

Our WR-10 calibration kit consisted of a flush short, a thru connection, and three delay lines of differing lengths. Using these measurements, along with their respective definitions (i.e., lengths, widths, etc.) and associated uncertainties, listed

U.S. Government work not protected by U.S. copyright

in Table I, we calibrated the VNA utilizing the NIST Microwave Uncertainty Framework, which resulted in a set of calibration coefficients along with uncertainties. The Uncertainty Framework [7–9] was employed to construct models for the calibration standards, and was used for propagating the uncertainties to the calibrated DUTs in conjunction with the calibration engine, StatistiCAL™ [12–13], which accommodates most coaxial, waveguide, and on-wafer standards. For our WR-10 calibration, we assumed the thru and flush short to be ideal, while the delay lines were modeled using closed-form expressions for waveguides with finite metal conductivity [14].

Our 1 mm coaxial calibration kit consisted of four offset shorts of differing lengths, an open, a load, and a thru connection. The offset short standards were modeled using closed-form expressions for coaxial lines with finite metal conductivity [15]. Table II lists the offset lengths and associated uncertainties for the short standards, and Table III lists the other sources of uncertainty. Our values and distributions of the uncertainties come from a variety of sources, including previous publications [15], manufacturers' specifications, and an IEEE standard [16]. We assumed the thru to be ideal, while the load and open models were derived from DC measurements and an offset-short calibration above 20 GHz. The model for the load standard consisted of a rational function, while the model for the open was comprised of a short transmission line terminated with a capacitor. Both models were fit to measured data using a nonlinear least squares procedure [17]. Uncertainties for the load and open models were estimated from the uncertainties in the measurements from which they were derived.

## III. Results

Utilizing the NIST Microwave Uncertainty Framework, we were able to characterize our noninsertable, directional device and provide uncertainties that have been propagated through from both calibrations. Figure 2 plots the magnitudes of the calibrated *S*-parameters of the device over the measured frequency range of 90 to 100 GHz. As expected, the values of the $S_{21}$ transmission terms are very low, while the values of $S_{12}$ are as high as 15.32 dB due to port 2 being on the input side of the amplifier and isolator. Although the amplifier is specified to have a gain of approximately 22 dB, the loss of the other components lowers the overall gain of the device. The values of $S_{12}$ taper off at the lower and higher frequencies due to the bandpass filter, which has a center frequency of 94 GHz. Likewise, the reflection terms on port 2 ($S_{22}$) are very high at the lower and higher frequencies because of the filter.

Figures 3 and 4 display the magnitudes and 95 % confidence intervals of $S_{12}$ and $S_{22}$, respectively, from 93 to 96 GHz. Over the entire frequency range, the mean confidence intervals are ± 0.038 dB for $S_{12}$ and ± 0.599 dB for $S_{22}$. The physical error mechanisms that contribute most to the overall uncertainties are those of the WR-10 line lengths.

TABLE I
PHYSICAL ERROR MECHANISMS FOR THE WR-10 STANDARDS

| Mechanism (units) | Value ± Uncertainty (Distribution) |
|---|---|
| Thru Length (mm) | 0.000 ± 0.005 (Rectangular) |
| Line 1 Length (mm) | 2.105 ± 0.005 (Rectangular) |
| Line 2 Length (mm) | 3.157 ± 0.005 (Rectangular) |
| Line 3 Length (mm) | 4.209 ± 0.005 (Rectangular) |
| Width (mm) | 2.540 ± 0.005 (Rectangular) |
| Height (mm) | 1.270 ± 0.005 (Rectangular) |
| Metal Resistivity Relative to Cu | 2 ± 1 (Rectangular) |

TABLE II
LENGTHS AND UNCERTAINTIES OF 1 MM OFFSET SHORT STANDARDS

| Offset Short Designation | Female Connector Length (mm) ± Uncert. (Distribution) | Male Connector Length (mm) ± Uncert. (Distribution) |
|---|---|---|
| Short 1 | 1.2869 ± 0.008 (Rect.) | 1.2883 ± 0.008 (Rect.) |
| Short 2 | 1.8119 ± 0.008 (Rect.) | 1.8133 ± 0.008 (Rect.) |
| Short 3 | 2.4369 ± 0.008 (Rect.) | 2.4383 ± 0.008 (Rect.) |
| Short 4 | 2.9869 ± 0.008 (Rect.) | 2.9883 ± 0.008 (Rect.) |

TABLE III
PHYSICAL ERROR MECHANISMS FOR THE 1MM OFFSET SHORTS

| Mechanism (units) | Value ± Uncertainty (Distribution) |
|---|---|
| Inner Conductor Diameter (mm) | 0.434 ± 0.003 (Rectangular) |
| Outer Conductor Diameter (mm) | 1.000 ± 0.005 (Rectangular) |
| Pin Diameter (mm) | 0.250 ± 0.005 (Rectangular) |
| Pin Length (mm) | 0.005 ± 0.005 (Rectangular) |
| Metal Conductivity (S/m) | $7.3\times10^6 \pm 1.7\times10^6$ (Rectangular) |
| Relative Dielectric Constant | 1 ± 0 (Rectangular) |
| Dielectric Loss Tangent | 0 ± 0 (Rectangular) |

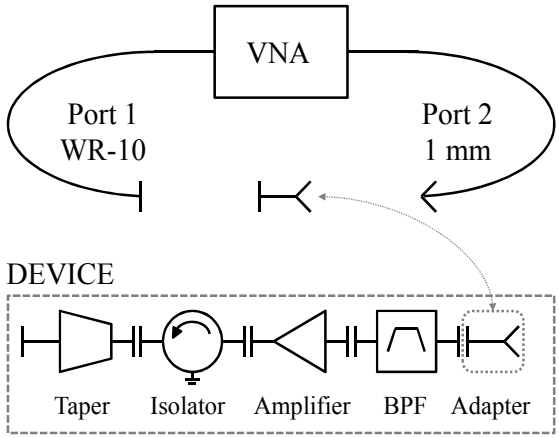


Fig. 1. Measurement set-up for characterizing a noninsertable directional device that consists of a 1 mm coaxial-to-WR-10 waveguide adapter, a WR-8 waveguide band-pass filter, a WR-8 waveguide low-noise amplifier, a WR-8 waveguide isolator, and a WR-8-to-WR-10 waveguide taper.

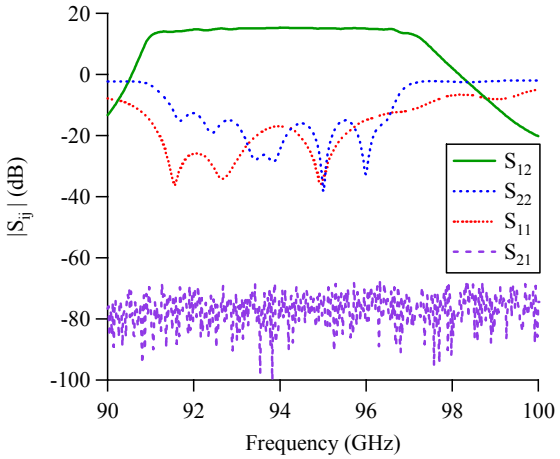


Fig. 2. Magnitudes of the scattering parameters for the noninsertable directional device.

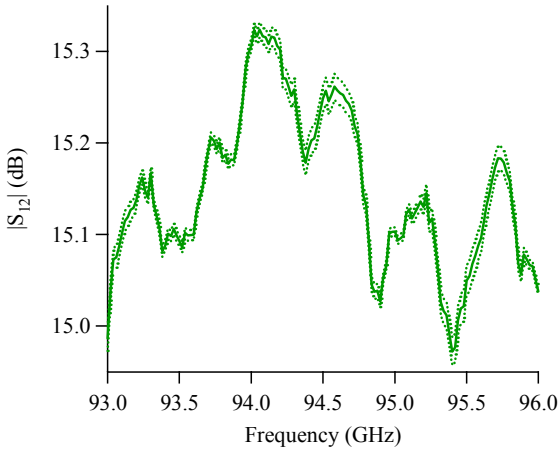


Fig. 3. Magnitude of $S_{12}$ for the device along with 95 % confidence intervals.

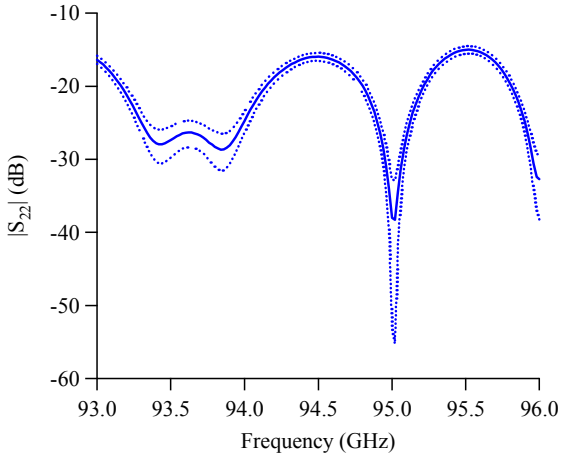


Fig. 4. Magnitude of $S_{22}$ for the device along with 95 % confidence intervals.

## IV. Conclusion

We have characterized and provided uncertainties for a noninsertable, directional device from 90 to 100 GHz by use of the NIST Microwave Uncertainty Framework. Although other sources of uncertainty may be included in a final uncertainty analysis, we believe these minor additions will not significantly increase the overall uncertainty.

## Acknowledgement

This work was supported by the U.S. Department of Commerce, and is not subject to U.S. copyright.

## References

[1] R. F. Bauer and P. Penfield, Jr., "De-Embedding and Unterminating," *IEEE Trans. Microwave Theory Tech.*, vol. MTT-22, no. 3, pp. 282-288, Mar. 1974.

[2] J. Randa, W. Wiatr, and R. L. Billinger, "Comparison of Adapter Characterization Methods," *IEEE Trans. Microwave Theory Tech.*, vol. 47, no. 12, pp. 2613-2620, Dec. 1999.

[3] J. Martens, "Common Adapter/Fixture Extraction Techniques: Sensitivities to Calibration Anomalies," 74th ARFTG Microwave Measurements Conference, Dec. 2009, Broomfield, CO.

[4] U. Arz and D. Schubert, "Coplanar Microwave Probe Characterization: Caveats and Pitfalls," 67th ARFTG Microwave Measurements Conference, pp. 214-218, June 2006, San Francisco, CA.

[5] U. Arz, H. C. Reader, P. Kabos, and D. F. Williams, "Wideband Frequency-Domain Characterization of High Impedance Probes," 58th ARFTG Microwave Measurements Conference, pp. 214-218, Nov. 2011, San Diego, CA.

[6] "Measuring Noninsertable Devices," Hewlett-Packard Company, Santa Rosa, CA, Product Note 8510-13, Aug. 1988.

[7] NIST Microwave Uncertainty Framework, Beta Version, D. F. Williams, http://www.nist.gov/pml/electromagnetics/related-software.cfm, 2012.

[8] J. A. Jargon, D. F. Williams, T. M. Wallis, D. X. LeGolvan, and P. D. Hale, "Establishing Traceability of an Electronic Calibration Unit Using the NIST Microwave Uncertainty Framework," 79th ARFTG Microwave Measurement Conference, pp. 32-36, Montreal, CANADA, Jun. 2012.

[9] J. A. Jargon, U. Arz, and D. F. Williams, "Characterizing WR-8 Waveguide-to-CPW Probes Using Two Methods Implemented within the NIST Uncertainty Framework," 80th ARFTG Microwave Measurement Conference, pp. 16-320, San Diego, CA, Nov. 2012.

[10] A. Lewandowski, D. F. Williams, P. D. Hale, C. M. Wang, and A. Dienstfrey, "Covariance-Matrix-Based Vector-Network-Analyzer Uncertainty Analysis for Time-and Frequency-Domain Measurements," *IEEE Trans. Microwave Theory Tech.*, vol. 58, no. 7, pp. 1877-1886, July 2010.

[11] T.S. Clement, P.D. Hale, D.F. Williams, C. M. Wang, A. Dienstfrey, and D.A. Keenan, "Calibration of Sampling Oscilloscopes with High-Speed Photodiodes," *IEEE Trans. Microwave Theory Tech.*, vol. 54, no. 8, pp. 3173 - 3181, Aug. 2006.

[12] StatistiCAL VNA Calibration Software Package, D. F. Williams, http://www.nist.gov/pml/electromagnetics/related-software.cfm, 2012.

[13] D.F. Williams, C.M. Wang, and U. Arz, "An Optimal Vector-Network-Analyzer Calibration Algorithm," *IEEE Trans. Microwave Theory and Tech.*, vol. 51, no. 12, pp. 2391 2401, Dec. 2003.

[14] R. E. Collin, Foundations for Microwave Engineering, Second Edition, IEEE Press, 2001.

[15] A. Lewandowski, "Multi-Frequency Approach to Vector-Network Analyzer Scattering-Parameter Measurements," Ph.D. Thesis, Warsaw University of Technology, 2010.

[16] IEEE Standard 287-2007 - Standard for Precision Coaxial Connectors (DC to 110 GHz).

[17] Personal Communication with Dr. Arkadiusz Lewandowski, Institute of Electronic Systems, Warsaw University of Technology, Nov. 27, 2013.

# Method for Estimating Probe-Dependent Residual Errors of Wafer-Level TRL Calibration

*Andrej Rumiantsev*[*] *and Ralf Doerner*[**]

[*]*Brandenburg University of Technology (BTU) Cottbus-Senftenberg, Cottbus, Germany*
[**]*Ferdinand-Braun-Institut (FBH), Leibniz-Institut fuer Hoechstfrequenztechnik, Berlin, Germany*

**Abstract — We present a method for estimating the probe-dependent residual errors of wafer-level TRL calibration. The method does not require additional measurement steps. It was verified experimentally for four industry standard RF probe types. The proposed method can be used, e.g., for confident cross-laboratory data sharing and comparison.**

**Index Terms — S-parameters on-wafer calibration, wafer-level measurements, calibration residual errors, RF probes.**

## I. Introduction

Estimation of calibration residual errors is a crucial step in any cross-laboratory comparison of measurement data and system precision. Traditionally, the efforts in analyzing accuracy of the RF calibration and, more general, traceability of measurements have been focusing on calibration methods and standards inaccuracies. In this work, we show that RF probes also contribute to calibration residual errors. Therefore, the type of the wafer probes should be taken into account when sharing and analyzing the measurement data obtained from different setups. We present a simple method for estimation of this probe-type-dependent residual errors for [1]TRL calibration performed with a given set of calibration standards.

The coupling of RF probes into adjacent resonant structures during the calibration at relatively low frequencies was identified already in the early 90s [1]. Much later, similar effects were reported at mm-wave frequencies [2]. However, methods for measurement and analysis of the probe-dependent calibration residual errors are still underway, as the nature of these effects is still not completely understood. Different phenomena can contribute to these errors, such as coupling between probes, radiation losses as well as possible propagation of higher-order modes in the probe-substrate environment. The impact of the probe-dependent calibration residual errors on the measurement accuracy increases with frequency. That is why estimation of these errors becomes essential especially when dealing with mm-wave data.

We selected the TRL calibration method as the analysis tool because of the following reasons:

1) It requires only information about the physical length of lines and a rough estimate for the phase of the reflection coefficient of the reflect standard. All these parameters do not depend on the design of the RF probe-tip.
2) The TRL self-calibration step determines the propagation constant γ of the line standard [3].

The next chapter describes the main steps of the proposed method. The experimental results and an example for application of the method are given in the chapters III and IV. The conclusions discuss possibilities for further improvement of the proposed method.

## II. Measurement Method

### A. Measurement of the Self-Calibration Parameters

The systematic measurement errors of a two-port double-reflectometer VNA can be described by the seven-term error model given by Fig. 1, where $m_i$ denote the wave quantities measured by an ideal $i-$th VNA receiver; $[A]$ and $[B]$ are the 2x2 matrices of error terms; $a_k$ and $b_k$ are the wave quantities at the $k-$th port of the DUT, and $[T_X]$ is the $T$-parameter matrix of the DUT [4]. Self-calibration algorithms can be used to calculate $[A]$ and $[B]$ from measurement data of partly-known calibration standards, such as the line and the reflect for the TRL method. The propagation constant γ of the line and the reflection coefficient $r$ of the reflect are extracted by the TRL self-calibration step from the redundancy in the measured data [5]. We use this TRL feature to determine γ and $r$ of a specific calibration substrate in combination with different RF probes. Thereby, we can quantify the impact of RF probe design on the measurement results.

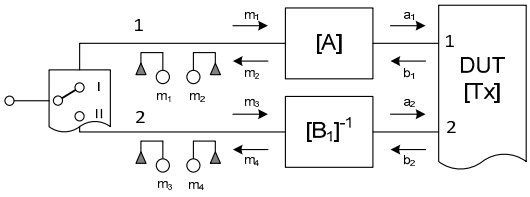


Fig. 1. The seven-term systematic error model of a two-port double reflectometer VNA.

Calculation of the propagation constant $\gamma$ of the line is performed according to the following procedure. The relationship between the actual and measured $T$-parameters of the DUT is given by:

$$[M_X] = [A][T_X][B]^{-1}, \qquad (1)$$

where $[M_X]$ is the measurement matrix:

[1] Thru-Reflect-Line

978-1-4799-4423-1/14/$31.00 ©2014 IEEE

$$[M_X] = \begin{bmatrix} m_1' & m_1'' \\ m_2' & m_2'' \end{bmatrix} \begin{bmatrix} m_3' & m_3'' \\ m_4' & m_4'' \end{bmatrix} = [m_a][m_b]^{-1}. \quad (2)$$

Prime and double-prime $m_i$ stand for results measured in forward and reverse direction, respectively. For the first (thru) standard, we have:

$$[T_{X1}] = \begin{bmatrix} 1 & 0 \\ 0 & 1 \end{bmatrix}, \text{ and therefore: } [M_1] = [A][B]^{-1}. \quad (3)$$

The robust TRL solution from [6] proposes to derive $[M]$ for the second (line) and the third (reflect) standards as:

$$[M] = \frac{1}{m_3' m_4'' - m_3'' m_4'} \begin{bmatrix} m_1' & m_1'' \\ m_2' & m_2'' \end{bmatrix} \widetilde{\begin{bmatrix} m_3' & m_3'' \\ m_4' & m_4'' \end{bmatrix}}^T =$$

$$= \frac{1}{m_X}[M']. \quad (4)$$

Consequently, for the second (line) standard the (1) gives:

$$[M_2] = [A][T_{X2}'][B]^{-1}, \text{ with } [T_{X2}'] = \begin{bmatrix} t_r & 0 \\ 0 & \frac{1}{t_f} \end{bmatrix}, \quad (5)$$

where:

$$t_r = S_{X2,12} m_{2X} \text{ and } t_f = \frac{S_{X2,21}}{m_{2X}}. \quad (6)$$

$S_{X2,12}$ and $S_{X2,21}$ are the actual $S$-parameters of the line. Finally, the propagation constant $\gamma$ of the line is extracted from:

$$\gamma = -\ln(\frac{t_r}{m_{2X}})/l_L, \quad (7)$$

where $l_L$ denotes the physical length of the line. $t_r$ can be calculated from the measurement matrices $[M_1]$ and $[M_2']$ using

$$t_r = \frac{\beta_1}{2} \pm \sqrt{\frac{\beta_1^2}{4} - \beta_2}, \quad (8)$$

$$\beta_1 = trace[M_2'][M_1]^{-1}, \beta_1 = trace[M_2'][M_1]^{-1}. \quad (9)$$

The right solution for the root in (8) can be taken from a rough estimate of the phase of $S_{X2,12}$. In a similar way, the reflection coefficient $r$ of the reflect is extracted from manipulation of matrices $[M_1]$, $[M_2']$, and $[M_3']$ [6].

### *B. Calculation of Residual Errors*

The propagation constant $\gamma$ of the line and the reflection coefficient $r$ of the reflect are properties of a specific calibration substrate. Thus, possible variations of $\gamma$ and $r$ when measured by different RF probes (*i.e.* on the reference and the test system configurations) can be attributed to the probe-dependent residual errors. We assume that all probes are of the same pitch and that the possible small difference of the phase of $r$ can be neglected for simplification reasons. Here, we propose to calculate these errors of the TRL algorithm as follows:

1) Extract line $\gamma_{REF}$ and $r_{REF}$ from data measured on the reference system configuration.
2) Extract line $\gamma_{TEST}$ and $r_{TEST}$ from measurement of the same standards on the test system configuration.
3) Calculate TRL error terms set $[A]_{TEST}$, $[B]_{TEST}$ for the test system using extracted $\gamma_{TEST}$ and $r_{TEST}$.
4) Calculate TRL error terms set $[A]_{TEST-REF}$ , $[B]_{TEST-REF}$ for the test system using $\gamma_{REF}$ and $r_{REF}$.
5) Calculate error bounds $\Delta S_{XY_{TEST-REF}}$ for 3) and 4) using the calibration comparison method from [7].

Often, the reference and the test setups are located in different laboratories. In such cases, the proposed method can be used for calculation of the cross-laboratory measurement error budgets increasing confidence of data sharing:

1) Perform calibration $TRL_{REF}$ on the reference setup. Extract $\gamma_{REF}$ and $r_{REF}$.
2) Obtain reference data $DUT_{REF}$ from the raw data $DUT_{RAW.REF}$ corrected by $TRL_{REF}$.
3) Perform calibration $TRL_{TEST}$ on the test setup.
4) Obtain test data $DUT_{TEST}$ from raw data $DUT_{RAW.TEST}$ of the identical DUT measured on the test setup and corrected by $TRL_{REF}$.
5) Calculate $TRL_{TEST-REF}$ from the raw data of $TRL_{TEST}$, $\gamma_{REF}$ and $r_{REF}$.
6) Calculate $\Delta S_{XY_{TEST-REF}}$ from $TRL_{TEST-REF}$ and $TRL_{TEST}$ using the calibration comparison
7) Calculate error bounds for each $S$-parameter of the DUT from $\Delta S_{XY_{TEST-REF}}$, $DUT_{REF}$ and $DUT_{TEST}$.

## III. Experimental Results

### *A. Measurement Setup*

The experimental setup included an Agilent PNA 110 GHz VNA, a manual wafer probe station PM8 and the calibration substrate ISS model 104-783A from Cascade Microtech. The calibration substrate was positioned on a thick ceramic holder to suppress possible propagation of higher-order modes. The uncalibrated $S$-parameters were obtained in a sequence for the same ISS using four different RF probe types of the same pitch: Infinity Probe (setup 'I'), ACP (setup 'A'), both from Cascade Microtech, Picoprobe (setup 'P') from GGB Industries, and Allstron (setup 'AL') (Fig. 2, Table I). We used proprietary Matlab scripts for extraction and calibration algorithms and the Verify program from NIST (Boulder, CO, USA) for calibration comparison.

The 150 µm and 1750 µm long CPW lines were used as thru and line, respectively, and the short as the reflect for extraction of $\gamma$, $r$ and for the TRL calibration step. The calibration reference impedance was set to the characteristic impedance of the line and the reference plane was kept at the

center of the thru. The proposed calculation algorithm does not require the conversion of the reference impedance to 50 Ω and the transformation of the reference plane.

The chosen combination of the thru and the line lengths results in TRL singularities below 5 GHz and around 40 GHz and 82 GHz. This is why we selected the frequency band from 5 GHz to 35 GHz for verifying the proposed method.

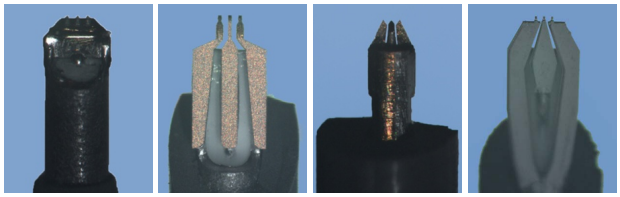

Fig. 2. Probe tips of (from left to right) Infinity Probe, ACP, Picoprobe, and Allstron used for the experiment.

### *B. Extraction Results*

First, we calculated the drift of the experimental system from two measurement series obtained for the setup 'A' within approximately two hours. These results define the bottom line of the comparison including instability of the VNA as well as the contact repeatability errors.

Next, we extracted the propagation constant $\gamma$ of the ISS 104-783A CPW line and the reflection coefficient $r$ of the reflect (short) from measurement data obtained for each configuration of the test system (Table I). Significant variation of the extracted $\gamma$ and $r$ can be observed starting from 10 GHz (Fig 3).

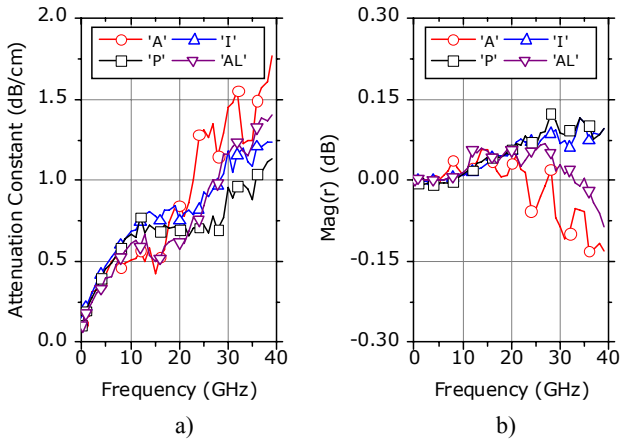


a) b)

Fig. 3. Attenuation constant $\alpha_A$, $\alpha_I$, $\alpha_P$, and $\alpha_{AL}$ of the experimental CPW line (a) and the reflection coefficients $r_A$ $r_I$, $r_P$, and $r_{AL}$ (b) of the short on ISS 104-783A measured by ACP, Infinity Probe, Picoprobe, and Allstron probes, respectively. Measurement reference plane is at the center of the thru.

The propagation constant $\gamma_I$ and the reflection coefficient $r_I$ extracted from the experimental configuration 'I' are closest to the expected trend in the frequency band of interest. Thus, we decided to use $\gamma_I$ and $r_I$ for the reference $\gamma_{REF}$ and $r_{REF}$.

TABLE I
CALIBRATION CONFIGURATIONS

| Setup | Test Calibration | | Ref. Calibration | |
|---|---|---|---|---|
| | Data | $\gamma, r$ | Data | $\gamma, r$ |
| 1. "A" | ACP | $\gamma_{(A)}, r_{(A)}$ | ACP | $\gamma_{(I)}, r_{(I)}$ |
| 2. "P" | Picoprobe | $\gamma_{(P)}, r_{(P)}$ | Picoprobe | $\gamma_{(I)}, r_{(I)}$ |
| 3. "I" | Infinity | $\gamma_{(I)}, r_{(I)}$ | N/A | N/A |
| 4. "AL" | Allstron | $\gamma_{(AL)}, r_{(AL)}$ | Allstron | $\gamma_{(I)}, r_{(I)}$ |

Now, we calculated the reference $[A]_{REF}$ and $[B]_{REF}$ from the configuration 'I' and the test $[A]_{TEST}$, $[B]_{TEST}$ from configurations 'A', 'P', and 'AL' and the maximum bound $\Delta S_{XY_{A-I}}$, $\Delta S_{XY_{P-I}}$, and $\Delta S_{XY_{AL-I}}$ respectively. Fig. 4, a presents the maximum error bound for all $S$-parameter of $\Delta S_{XY}$ for three setups and the sum of the contact repeatability error and the system drift within two hours. $S$-parameter measurement errors $\Delta S_{XY}$ are larger than the drift and the contact repeatability errors. Therefore, they should be included into the overall measurement confidence interval.

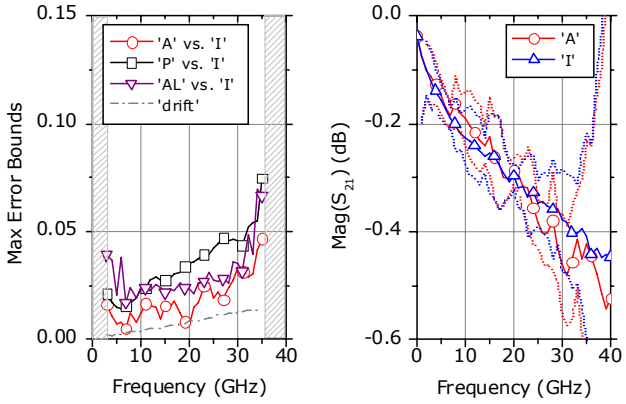


a) b)

Fig. 4. Maximum error bounds $\Delta S_{XY_{A-I}}$, $\Delta S_{XY_{P-I}}$ and $\Delta S_{XY_{AL-I}}$ for the system configuration 'A', 'P', and 'AL' (a) and magnitude of $S_{21}$ of the experimental 3450 µm long CPW line on ISS 104-783A (b) measured on the system configuration 'A' (red solid line) and 'I' (blue solid line). The added maximum error bounds 'plus' and 'minus' were calculated from $\Delta S_{21_{A-I}}$ for the configuration 'A' (red dotted line) and configuration 'I' (blue dotted line). $\Delta S_{XY}$ rapidly increase below 5 GHz and above 35 GHz due to the TRL calculation singularity for the phase of the thru and the line standards used.

## IV. APPLICATION FOR DUT

As discussed above, the electrical characteristics of the ISS CPW lines are insensitive to the type and the design of RF probes. Therefore, we used the 3450 µm long CPW line to demonstrate the application of the proposed method. The $S_{21}$ of the DUT obtained for system configurations 'A' and 'I' are given in Fig. 4, b (solid red and solid blue lines, respectively). The confidence interval for the cross-comparison of the setup 'A' and 'I' was calculated from the $\Delta S_{21_{A-I}}$ (dotted red and

blue lines, respectively). System drift and the contact repeatability errors are excluded from error bounds. The DUT data for both system configurations are within the confidence interval, as expected. Note, that we excluded drift and the contact repeatability errors from this experimental data to simplify the comparison. Therefore, it is a conservative estimate.

Finally, we calculate the maximum and minimum worst-case cross-estimates for all four setups as: $\Delta S_{MIN} = min(\Delta S_{XY_{i-j}})$ and $\Delta S_{MAX} = max(\Delta S_{XY_{i-j}})$. Fig. 5 shows the application of $\Delta S_{MIN}$ and $\Delta S_{MAX}$ for comparing the magnitude of $S_{21}$ of the experimental CPW line and the magnitude of $S_{11}$ of the experimental short measured on four setups.

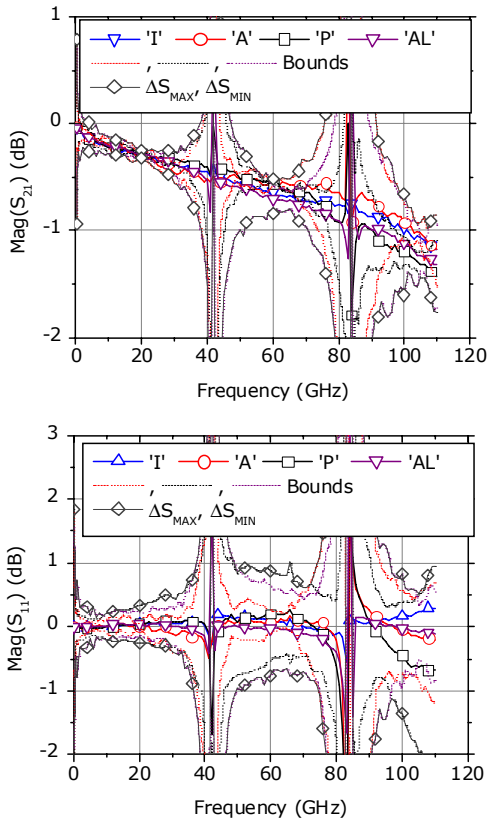


Fig. 5. Magnitude of $S_{21}$ of the experimental 3450 µm long CPW line (top) and the magnitude of $S_{11}$ of the experimental short (bottom) on ISS 104-783A measured on the four system configurations. The chosen combination of the thru and the line lengths results in TRL singularities below 5 GHz and around 40 GHz and 82 GHz.

## V. Conclusions

In this work, we present a simple method for estimating the probe-dependent residual errors of the wafer-level TRL calibration. The method does not require any reference standards (except the calibration standards themselves) or additional measurements. Instead, it utilizes the self-calibration step of the TRL algorithm and the calibration comparison technique. Thus, it is easy to be implemented into the conventional wafer-level device characterization workflow, especially for confident cross-laboratory measurement comparison and data sharing.

The experiment was carried out for three RF probe types and for the robust TRL solution. Capabilities of the method were demonstrated for the frequency range from 5 GHz to 35 GHz. We expect that the reliability of the proposed method can be improved and the valid frequency range can be extended by implementing the multiline solution, similar to the one used by the multiline TRL from [8].

## References


[1] T. H. Miers, A. Cangellaris, D. Williams, et al., "Anomalies observed in wafer level microwave testing," in Microwave Symposium Digest, 1991., IEEE MTT-S International, 1991, pp. 1121-1124.

[2] A. Rumiantsev, R. Doerner, and E. M. Godshalk, "The influence of calibration substrate boundary conditions on CPW characteristics and calibration accuracy at mm-wave frequencies," ARFTG Microwave Measurements Conference-Fall, 72nd, pp. 168-173, 2008.

[3] R. B. Marks and D. F. Williams, "Characteristic impedance determination using propagation constant measurement," IEEE Microwave and Guided Wave Letters, vol. 1, pp. 141-143, June 1991.

[4] H. J. Eul and B. Schiek, "A generalized theory and new calibration procedures for network analyzer self-calibration," Microwave Theory and Techniques, IEEE Transactions on, vol. 39, pp. 724-731, 1991.

[5] G. F. Engen and C. A. Hoer, "Thru-Reflect-Line: an improved technique for calibrating the dual six-port automatic network analyzer," Microwave Theory and Techniques, IEEE Transactions on, vol. 27, pp. 987-993, 1979.

[6] H. Heuermann and B. Schiek, "Robust algorithms for Txx network analyzer self-calibration procedures," Instrumentation and Measurement, IEEE Transactions on, vol. 43, pp. 18-23, 1994.

[7] D. F. Williams, R. B. Marks, and A. Davidson, "Comparison of on-wafer calibrations," in ARFTG Microwave Measurements Conference-Fall, 38th, 1991, pp. 68-81.

[8] R. B. Marks, "A multiline method of network analyzer calibration," Microwave Theory and Techniques, IEEE Transactions on, vol. 39, pp. 1205-1215, 1991.

# Characterization and modeling scheme for harmonics at power amplifier output

Meenakshi Rawat*, Patrick Roblin*, Christophe Quindroit*, Naveen Naraharisetti*, Robert Pond*,
Khan Salam†, Chenggang Xie †
*Ohio State University, Department of Electrical & Computer Engineering, Columbus, Ohio, 43210.
†Rockwell Collins, Advanced Technology Center, Cedar Rapids, IA, 52498.

***Abstract*—With upcoming trends of multiband, broadband and ultrawideband transmitters, there is a need for understanding and representing nonlinear transmitter behavior at system level at frequencies other than transmitter frequency, which might fall within the working range of ultra wideband power amplifier (PA) or other PAs. This paper presents characterization setup, data time-alignment technique and modeling scheme to model second harmonic at the output of PA. The method can easily be extended to higher harmonics. The modeling performance is reported in terms of time domain as well as frequency domain validation. Normalized mean square error is used as quantitative measure of performance.**

***Index Terms*—Dual Band, modelling, harmonics, power amplifiers, polynomials.**

## I. Introduction

Recently, frequency spectrum has been refered to as consumable resource due to increasing number of users and applications. Therefore, there is a strong motivation towards broadband and ultra wideband communication schemes as well as circuit designs [1]. Such innovation on system level requires accurate representation of the measurement system in the simulation environment. Behavioral modeling is a simple and popular method where digital models extracted from actual measurement data can be used in a system level simulation.

There is a rich literature on power amplifier (PA) / Transmitter (Tx) behavioral modeling while considering frequency band under operation [2]-[3]. As an advancement over single-band case, behavioral modeling considering concurrent operation of dual-band [4]-[5] and tri-band [6] PA has been studied and reported with application. However, such models represent nonlinearity within the frequency band of transmitted signals and generation of harmonics due to PA nonlinearity has not been studied. This work focuses on characterization scheme, time alignment method and behavioral modeling of harmonics generated by PA to accurately represent such harmonics in system level simulations. An example case of second harmonic is demonstrated in this paper.

The remainder of this paper is organized as follows. Section II explains the measurement setup capable of capturing PA output at fundamental as well harmonic frequency. Section III describes time alignment scheme for second harmonic and the harmonic memory polynomial (HMP)model for behavioral modeling of captured data. Section IV reports the modeling performance of proposed models in terms of normalized mean squared error (NMSE) as well graphical evaluation in terms of time domain, frequency domain, voltage variation plots with respect to input signal.

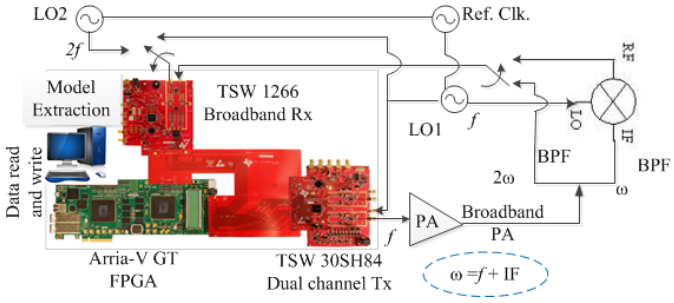


Fig. 1. Measurement setup to capture harmonic and fundamental.

## II. Measurement setup for harmonic and fundamental signal capturing

Measurement setup used for behavioral modeling of PA at fundamental and harmonic frequencies is shown in Fig.1. The input data is stored in the pre-allocated FPGA memories using MATLAB and Quartus Softwares. The data is modulated, IF and RF frequency upconverted and transmitted via one of the channels available in TSW30SH84 dual-channel transmitter from Texas Instruments. The data from Arria-V (GT series) FPGA can be sent to TSW30SH84 board at the sampling rate of 307.2 MHz. The DAC in the transmit path is programmed with a sampling frequency of 1228.8 MHz i.e. with an interpolation factor of 4. The signal is upconverted using TRF3705 quadrature modulator within TSW30SH84 board and sent to the ultrawideband 1W PA (ZX60-14012L from Minicircuits). Output of the PA is downconverted and demodulated using 500 MHz bandwidth TSW1266 receiver board from Texas Instruments with sampling rate of 614.4 MHz. A reference clock (Ref. clk) as shown in Fig 1 is used for synchronization between the receiver and transmitter boards. The signal is down-converted, digitized and stored in the FPGA memory.

PA is driven with 10 MHz WCDMA signal with peak to average power ratio of 9.5 dB at 988.4 MHz (950 MHz + 38.4 IF shift). Receiver board accepts RF in the frequency range of 1880MHz-2390MHz, therefore PA output at fundamental frequency is directed to receiver range using broadband mixer Zx05-42MH from minicircuits. LO for mixer is also synchronized with the receiver and transmitter LOs. Second harmonic signal is captured directly at receiver. A switch is used at

978-1-4799-4423-1/14/$31.00 ©2014 IEEE

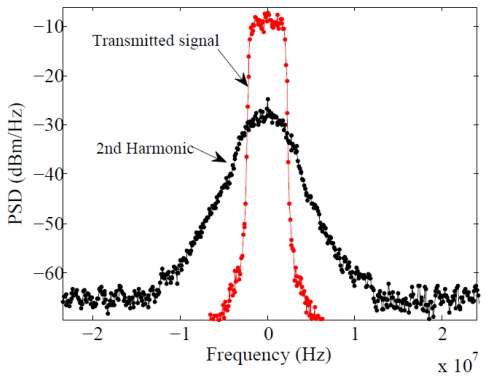


Fig. 2. Spectrum of captured harmonic signal with respect to transmitted signal .

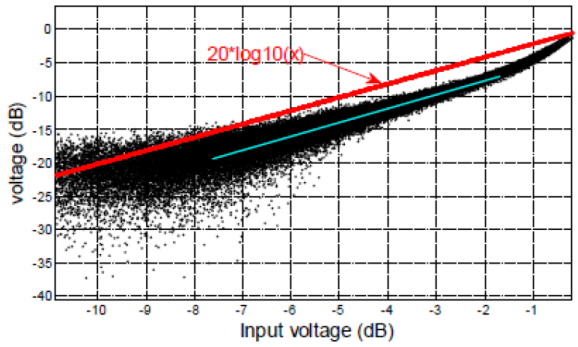


Fig. 3. Captured Harmonic signal voltage with respect to transmitted signal.

receiver to select harmonic or fundamental frequency signal.

## III. Harmonic Characterization and Modelling

### A. Time alignment between input and output signals

Fig.2 shows spectrum of captured second harmonic signal and spectrum of transmitted input signal. It can be observed that the bandwidth of the harmonic signal is almost twice to that of the original signal.Moreover, Fig.3 shows the plot of second harmonic vs. input signal. Harmonic signal shows expansion when we increase input signal strength. Figure also shows that when we plot $x^2$ with respect to input signal in logarithmic graph, harmonic signal plot is actually parallel to $x^2$ plot for most of the linear range. However, at higher power higher order terms also becomes effective. Therefore, second harmonic is linearly proportional to $x^2$ for considerable signal range and we can use it as reference signal for time alignment.

Time delay alignment is done using frequency domain cross-correlation technique given in [7]. For $p^{th}$ harmonic, the cross-correlation of $\vec{x^p}$ and $\vec{y_p}$ can be denoted as the convolution of two complex signals. In frequency domain, the cross-correlation of the two signals is given by

$$\mathcal{F}(\vec{x^p} \star \vec{y_p}) \quad = \quad \mathcal{F}(\vec{x^p})^* \cdot (\mathcal{F}(\vec{y_p})) \tag{1}$$

where $\mathcal{F}$ denotes the fourier transform. As $\vec{x^p}$ is linearly proportional to $\vec{y_p}$ for most of the range, (1) can be re-written

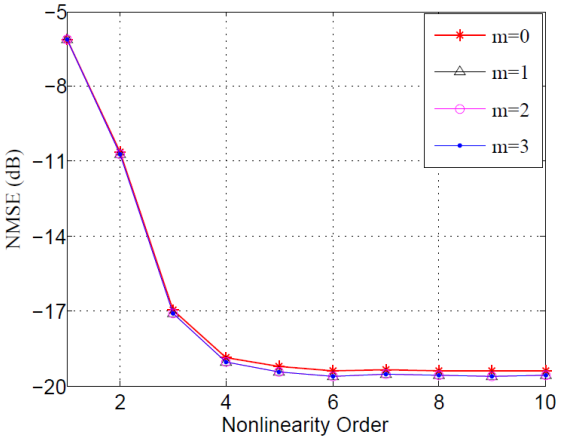


Fig. 4. NMSE curves with respect to nonlinearity order and memory depth.

as:

$$\mathcal{F}(x^p \star y_p) \quad = \quad G \cdot \mathcal{F}(x^p)^* \cdot (\mathcal{F}(x^p) e^{j(2\pi\tau+\phi_0)} \tag{2}$$

where $G$ is the gain, $\tau$ and $\phi_0$ are the time delay and phase rotation of $y_p$ with respect to reference signal $x^p$.When $\arg(\mathcal{F}(x^p \star y_p))$ is plotted with respect to frequency, $\tau$ is the slope of linear curve and $\phi_0$ is the intercept of the curve with y-axis [7]. The cross-correlation given by (2) is maximum when $(2\pi\tau+\phi_0 = 0)$, therefore time adjusted harmonic signal should be given by

$$\vec{y}_{p,adj} \quad = \quad \vec{y_p} e^{-j(2\pi\tau+\phi_0)} \tag{3}$$

For, second harmonic, time is aligned by maximizing the frequency domain cross-corrleation between $x^2$ and second harmonic of PA output.

### B. Harmonic polynomial modelling

PA model for fundamental inband modelling using memory polynomial is given by

$$y_\omega(n) \quad = \quad \sum_{j=0}^{k_1} \sum_{m_1=0}^{M_1} a_{m,j} \cdot x(n-m) \left|x(n-m)\right|^j \tag{4}$$

where $x$ is the complex baseband input signal at instance '$n$' and $a_{m,j}$ are the coefficients of the model and $M$ represents memory depth. However signal at $p^{th}$ harmonic is theoretically proportional to $x^p$ with higher power terms of $x$, therefore a harmonic memory polynomial can be obtained with following modification:

$$y_{p\omega}(n) \quad = \quad \sum_{i=0}^{k_p} \sum_{m_p=0}^{M_p} b_{m_p,i} \cdot x^p(n-m_p) \left|x(n-m_p)\right|^i \tag{5}$$

Let us define the following vector notations representing $N$ samples of the input signal:

$$\vec{x}(n) \quad = \quad [x(n), \ldots, x(N+n)] \tag{6}$$

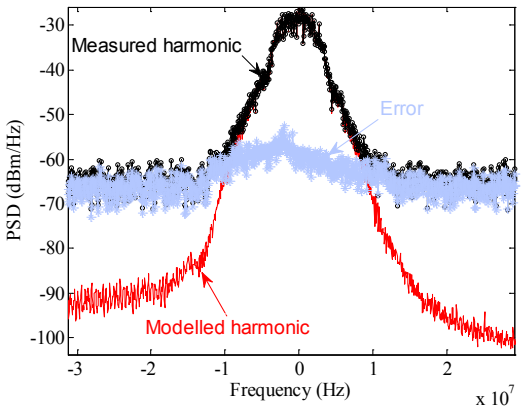


Fig. 5. Modeling performance of HRM model in frequency domain.

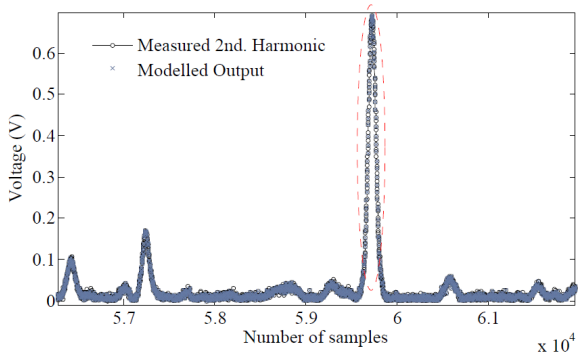


Fig. 6. Modeling performance in terms of harmonic signal in time domain.

$$\vec{\gamma}_i(n) = [\vec{x}^p(n)\cdot|\vec{x}(n)|^i, \ldots, \vec{x}^p(n-1)\cdot|\vec{x}(n-1)|^i, \ldots, \vec{x}^p(n-M_p)\cdot|\vec{x}(n-M_p)|^i \quad (7)$$

corresponding matrices $\Gamma$ for $N$ samples will be

$$\vec{\Gamma} = [\vec{\gamma}_0, \ldots, \vec{\gamma}_{k_p}] \quad (8)$$

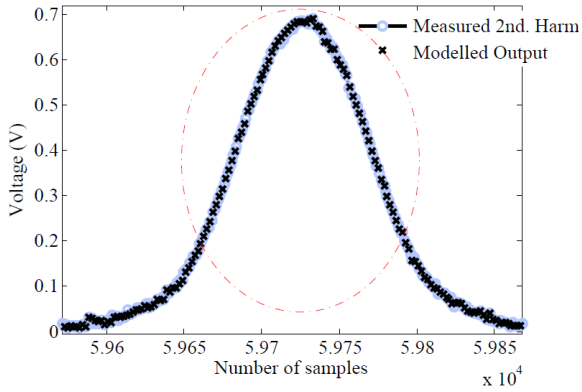


Fig. 7. Expanded view of peak data modelling performance in time domain.

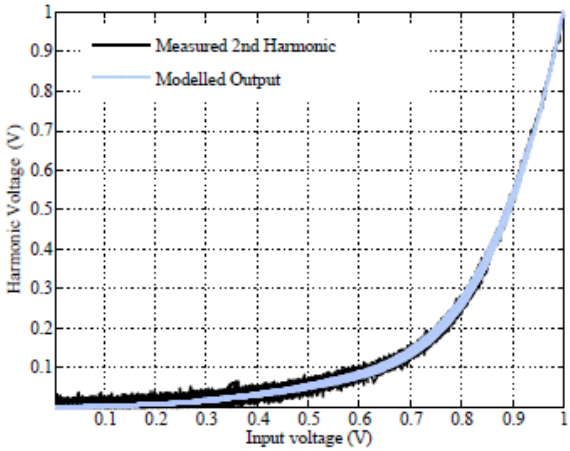


Fig. 8. Modeling performance in terms of harmonic signal Vs. input signal voltage.

$$\vec{\delta} = [b_{0,0}, \ldots, b_{K_p,M_p}]^T \quad (9)$$

Using these vector notations, (2) can be written as

$$\vec{y}_{p\omega} = \Gamma\vec{\delta} \quad (10)$$

The coefficients $b_{m_p,i}$ can be calculated using the least squares (LS) solution. In this paper LS has been implemented according to the singular value decomposition (SVD) method.

## IV. In-Band and Out-of-Band Modeling Performances

The proposed models are evaluated in terms of normalized mean squared error (NMSE) defined as:

$$NMSE = \frac{\sum_{l=0}^{l=L}|e(l)|^2}{\sum_{l=0}^{l=L}|y_{meas.}(l)|^2} \quad (11)$$

where $L$ is length of data, $e$ is error between measured output $y_{meas.}$ and modeled output for any data sample $l$.

Fig. 4 shows effect of different memory lengths on model NMSE performance. No marked improvement is observed by increasing memory depth beyond $M = 1$ and nonlinearity order beyond $k_p = 6$, which are chosen as model parameters.

Fig.5 shows power spectrum density of proposed model and measured second harmonic. It can be observed that proposed model is able to model within the harmonic signal band, however it does not model measurement noise and therefore modeled and measured signals have difference in noise floor. Fig. 6 shows time domain validation and its expanded version around peak power shown in Fig. 7. The model is able to estimate even fast variations at peak. Fig. 8 shows harmonic signal voltage vs. input signal voltage. From Figs. 5 and 8, it can be seen that model is able to provide good modeling for high power data, where most of the harmonic signal lies, however for small input signals, noise is prevalent where model does not follow noisy measurement.

## V. Conclusion

Paper proposes the characterization and behavioral modeling scheme for the harmonics generating from power amplifier. As an example case, second harmonic at the PA output is studied. The captuted harmonic is time aligned using frequency domain time alignment technique. Based on the characteristics of captured signal as compared to the fundamental signal, a harmonic memory polynomial model is proposed to model the time aligned output harmonic signal. Model performance is validated in time and frequency domain as compared to measured data and it is reported that model is able to imitate the harmonic output signal for most of the signal range. Model performance diverts only near noise levels, where measurement noise interference is excessive. The model can be used in system level simulations to study the effect and interference of the harmonic with other signals.

## Acknowledgment

This work is supported in part by the National Science Foundation (NSF) Collaborative Grant ECS-1129013. The authors would like to thank Altera Inc.,Texas Instruments Inc. and Minicircuits for the donation, respectively of the FPGA testbed, transceivers and RF power amplifier used in this work.

## References

[1] R. Wang, Y.K. Su and C.H. Liu, "3 5 GHz cascoded UWB power amplifier," *2006 IEEE Asia Pacific Conf. on circuits and systems*, pp. 367-369, Dec. 2006.

[2] F. Ghannouchi and O. Hammi, "Behavioral modeling and predistortion," *IEEE Microw. Mag.*, vol. 10, no. 7, pp. 52-64, Dec. 2009.

[3] M. Rawat and F. Ghannouchi, "Three-layered biased memory polynomial for modeling and predistortion of transmitters with memory," *IEEE Trans. Circuits Syst. I, Reg.Papers*, vol. 60, no. 3, pp. 768-777, Nov. 2013.

[4] P. Roblin, C. Quindroit, N. Naraharisetti, Shahin Gheitanchi, Mike Fitton, "Concurrent linearization: The state of the art for modeling and linearization of multiband power amplifiers," *IEEE Microw. Mag.*, vol. 14, no. 7, pp 75-91, Nov. 2013.

[5] C. Quindroit, N. Naraharisetti, P. Roblin, S. Gheitanchi, V. Mauer, M. Fitton,"FPGA implementation of orthogonal 2D digital predistortion system for concurrent dual-band power amplifiers based on time-division multiplexing," *IEEE Trans. Microw. Theory Tech.*, vol. 61, no.12, pp. 4591-4599, Dec.2013.

[6] M. Younes, A. Kwan, M. Rawat and F. Ghannouchi, "Linearization of concurrent tri-band transmitters using 3-D phase-aligned pruned Volterra model," *IEEE Trans. Microw. Theory Tech.*, vol. 61, no. 12, pp. 4569-4578, Dec. 2013.

[7] S. Boumaiza, M. Helaoui, O. Hammi, T. Liu and F. Ghannouchi, "Systematic and adaptive characterization approach for behavior modeling and correction of dynamic nonlinear transmitters," *IEEE Trans. Instrum. Meas*, vol. 56, no. 6, pp. 2203-2211, Dec. 2007.

# Active Harmonic Source-/Load-Pull Measurements of AlGaN/GaN HEMTs at X-Band Frequencies

*T. Maier, V. Carrubba, R. Quay, F. van Raay, and O. Ambacher*

Fraunhofer Institute for Applied Solid State Physics (IAF), Tullastrasse 72, 79108, Freiburg, Germany
thomas.maier@iaf.fraunhofer.de

**Abstract — Active harmonic loadpull measurements investigation for a 1-mm AlGaN/GaN HEMT power transistor at X-Band frequencies are in this paper reported. The paper highlights the transistor performances in terms of maximum PAE, $P_{OUT}$ and Gain achieved at 8.7 GHz together with the application of a systematic source-/load-pull measurement procedure including wafer-mapping capability.**

**The measurements were carried out using an active harmonic loadpull test system with four control loops. In particular, fundamental and second harmonic "loads" as well as second harmonic "source" terminations have been properly varied and optimized. The 1-mm GaN power device delivered very high efficiency of DE=71.2% and PAE=66.1%, together with high $P_{OUT}$ and power gain of 35 dBm (3.2 W) and 11.5 dB, respectively.**

**Index Terms — Active, efficiency, harmonic, loadpull, tuning.**

## I. Introduction

Nowadays more and more high-efficiency power amplifiers (PAs) are needed in order to save energy and to reduce costs e.g. for cooling systems. As the load and the source impedances seen by the transistor at harmonic frequencies significantly affect the overall performance in terms of output power, gain and efficiency [1-2] these impedances have to be valuated to be delivered by the matching networks. The PA designer needs to know the optimum terminations in order to achieve the best efficiency with low trade-off in output power and gain [2]. Furthermore the right source and load terminations obtained through loadpull measurements lead to accurate nonlinear models [3] which are then used in the simulation environments. Other than the optimum fundamental terminations, the optimum magnitudes of the higher harmonic reflection coefficients are typically near to unity with different phases depending on the PA classes, e.g. class-J [2], class-F or inverse class-F [4-5]. With passive tuner setups these high reflection conditions equal to unity cannot be set due to losses introduced by the various components such as couplers, diplexers, cables and probes. This issue becomes more pronounced when increasing the frequency, e.g. X-band frequencies. Therefore, special care needs to be taken during the high frequency measurement calibration and activity in order to avoid stability issues, to allow proper measurements with improved accuracy as well as for an improved overall power transistor performance. Because of the requirement for high gain and power-efficiency at X-band frequencies typically used for space applications as satellite or radar communication systems, the accurate measurement activity has to be accompanied with a highly performed technology. For this reason, the development of active harmonic loadpull measurement systems capable of presenting highly reflective fundamental and harmonic terminations at both the transistor input and output side [6-7] together with a systematic measurement procedure [8] needs to be accompanied with the continuous development of GaN technology capable of providing high performance at high frequency [9-10].

In this paper an in-house IAF AlGaN/GaN HEMT power transistors with gate length of 250 nm and gate width of 1 mm [9-10] together with a systematic source-/load pull measurement procedure has been investigated in order to achieve and deliver very high power-added-efficiency at X-band frequencies [11-12].

## II. Modified Test System

Figure 1 shows a simplified block diagram of the commercially available Anteverta MT2000 active harmonic loadpull system [6, 13]. The test system covers the frequency range 0.5 - 26.1 GHz and can handle 100 W of CW RF power at 2 GHz of fundamental frequency with the built-in test-set couplers and even more in pulsed mode. This power range can be extended by using external couplers when measuring for example packaged high-power devices. The test system supports up to four loops. One of these loops is needed for the input signal at fundamental frequency (1×f0) and a second one for the tuning of the output load at 1×f0. The two remaining loops can be used to control the 2nd (2×f0) and 3rd (3×f0) harmonic loads at the output or both 2nd harmonics at input and output.

The MT2000 external control software [13] option together with IAF in-house software allows automated wafer mappings combined with any loadpull configuration. RF- power amplifiers are needed for the fundamental frequency input signal and for each load which has to be tuned or set to a defined value. Diplexers or triplexers are needed in order to combine two or three harmonics to be fed into the DUT (device-under-test) ports, respectively. In order to supply sufficient RF-power to the DUT, the loop amplifiers have to deliver significantly more power than the DUT itself. Even at the input of the DUT the available power delivered from the

978-1-4799-4423-1/14/$31.00 ©2014 IEEE

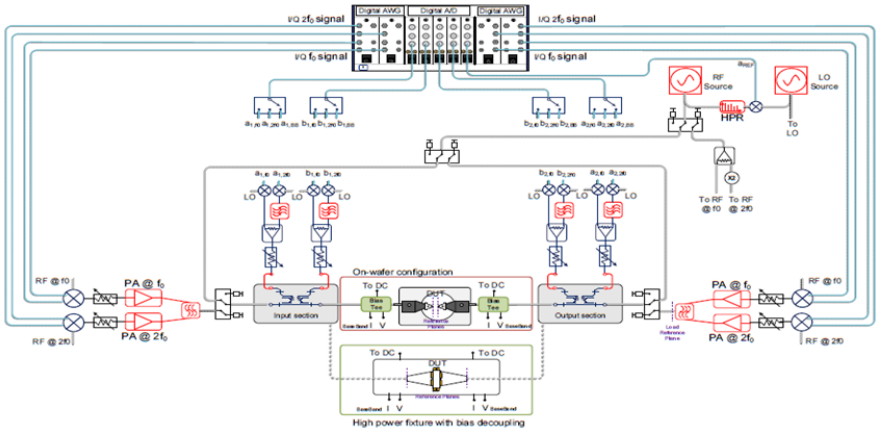


Fig. 1. Simplified block diagram of the commercially available Anteverta MT2000 mixed-signal active harmonic loadpull system [6, 13].

fundamental loop amplifier can be critical when measuring devices without matching networks at high frequency, e.g. X-band frequencies. As an example, for the 1 mm GaN power transistor used in this experiment, an input reflection magnitude of 0.94 leads to a mismatch loss of 9.3 dB. Therefore, these losses need to be compensated by the loop amplifier. Due to these aspects, the attenuation of the "high power paths" which again include probes, cables, directional couplers, diplexers, and/or triplexers and bias-tees has to be minimized. For this reason, cable lengths of both input and output were reduced by placing the external couplers as near as possible to the wafer probes. The use of external couplers as near as possible to the wafer probes also improve the calibration accuracy as well as reduce stability considerations.

## III. Measurements

The following measurements have been conducted by using two loops in the input (fundamental and second harmonic source) and two loops in the output (fundamental and second harmonic load) following a systematic measurement procedure in order to optimize the power transistor performance. The measurements have been conducted on the IAF 1 mm (8×125 µm) AlGaN/GaN power HEMT in CW (continuous wave) mode at 8.7 GHz of fundamental frequency, $V_{DS}$=30 V of drain bias voltage and an quiescent bias setting of $I_{dq}$=10 mA.

- ***Fundamental Tuning***

In the first step, only fundamental impedance 1×f0 was swept (area shown in the Smith chart of Fig. 2) in order to find the region for optimum device efficiency. In this case the 2×f0 source and load loops were set to the passive system impedance, meaning that the DUT is terminated with the impedance defined by the test setup hardware without injecting any loops signal, therefore 50 Ω. As shown in Fig. 2, the 1×f0 loadpull is combined with an input power sweep as PAE depends also on input power [2]. Despite the higher harmonics are not optimized high PAE up to 59.7% is already achieved while delivering an high output power of 36.1 dBm (4.1 W) and a power gain of 13 dB (related to the $Z_{L,F0}$=13.0+ j28.0 Ω as given by the blue cross in the Smith chart). The maximum output power of the 1 mm AlGaN/GaN HEMT device at another load reflection point ($Z_{L,F0}$=19.5+ j20.4 Ω - red cross) is 37.3 dBm (5.4 W) where lower PAE of 48.2 % is delivered with power gain decreased to 8.6 dB.

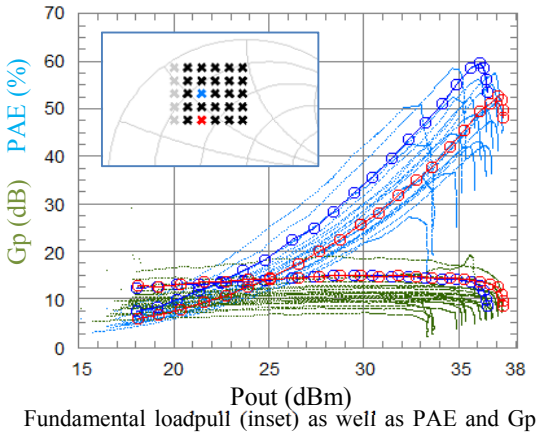


Fig. 2. Fundamental loadpull (inset) as well as PAE and Gp as a function of $P_{OUT}$. Blue markers: load reflection of PAEmax. Red markers: load reflection of $P_{OUT}$max.

- ***Second Harmonic Load Tuning***

After optimizing the 1×f0 load where keeping the higher terminations to 50 Ω, the second step is to conduct a 2×f0 loadpull sweep while the 1×f0 load is set to the $Z_{L,F0}$=13.0+ j28.0 Ω (optimum PAE) previously obtained. The 2×f0 source termination is still set to the passive 50 Ω impedance. At harmonic frequencies, reflection magnitudes near to unity deliver the best efficiencies since no energy lost occurs. This means that the only phase sweep with constant magnitude equal to one is now sufficient. Such 2×f0 load has been swept all around the Γ=1 edge of the Smith chart and a successive fine phase variation was set, as shown in the zoomed Smith chart of Fig. 3.

The power performances related to those loads are also reported in Fig. 3 where PAE and gain are function of the power sweep as well as the 2×f0 loadpull. In this case higher performance is obtained as compared to the one where only the 1×f0 load was optimized. Here the maximum PAE yields 61.3%, Pout=36.2 dBm (4.1W), and an associated power gain Gp = 13.2 dB, proving the importance of the proper setting of the 2×f0 load.

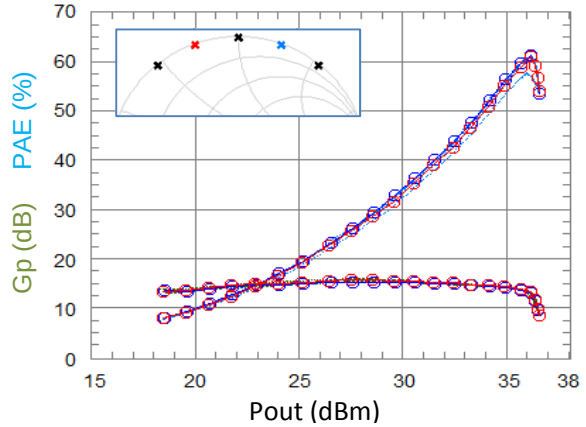


Fig. 3. Second harmonic loadpull (inset) as well as PAE and Gp as a function of $P_{OUT}$. Blue markers: load reflection of PAEmax. Red markers: load reflection of $P_{OUT}$max.

- ***Fundamental Retuning***

After optimizing the 2×f0 load while maintaining a constant optimum 1×f0 load achieved in step 1, a re-optimization of the fundamental load is needed. This is due to the fact that in non-linear power transistors, the harmonic contents are directly related to the fundamental one; therefore, being the superposition principle not valid, the variation of the 2×f0 load would inevitable vary the optimum impedance at 1×f0.

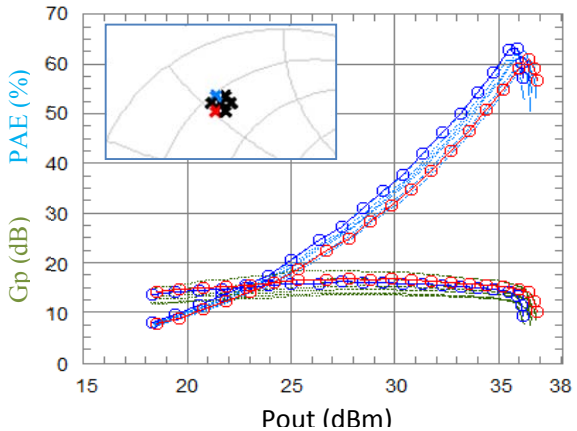


Fig. 4. Fundamental loadpull retuning (inset) as well as PAE and Gp as a function of $P_{OUT}$. Blue markers: load reflection of PAEmax. Red markers: load reflection of $P_{OUT}$max.

Therefore the 1×f0 load impedance is retuned in a small area around the optimum value found during the previous 1×f0 load sweep where the optimum PAE value is found at $Z_{F0}$=10.8+j28.5 Ω with higher PAE value equal to 63.4% as illustrated in Fig. 4.

- ***Second Harmonic Input Tuning***

Once the impedances have been optimized in the transistor output side, an optimization of the input impedance is also necessary in order to achieve the best overall output performance. In this case a 2×f0 source-pull is conducted while the 1×f0 and 2×f0 loads are set to the optimum PAE previously achieved. Fig. 5 shows the Smith chart segment where the 2×f0 source impedance has been swept and the associated output performance.

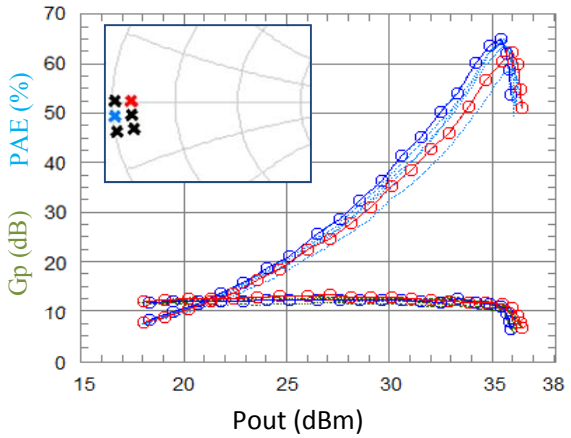


Fig. 5. Second harmonic sourcepull (inset) as well as PAE and Gp as a function of $P_{OUT}$. Blue markers: load reflection of PAEmax. Red markers: load reflection of $P_{OUT}$max.

Here, by source-pulling the 2×f0, even better performance is achieved as compared to the only output terminations optimization where in this case: PAE=65.3%, $P_{OUT}$=35.4 dBm (3.5 W) and Gp=10.9 dB. After optimizing the source 2×f0 a fundamental loadpull is again needed, as shown in Fig. 6. Final optimum performance shows very high efficiency of DE=71.2% (not displayed) and PAE=66.1% while delivering high $P_{OUT}$=35 dBm (3.2 W) and Gp=11.5 dB.

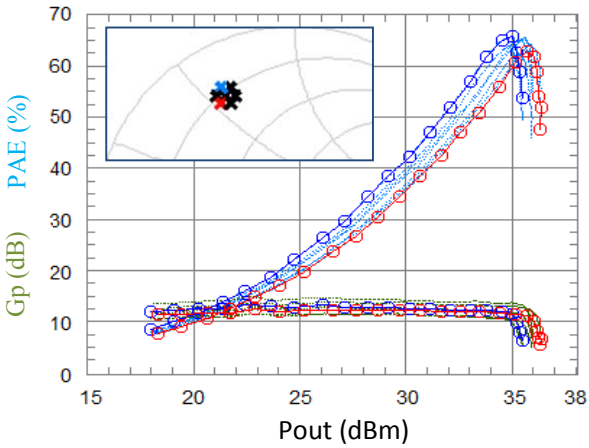


Fig. 6 Final power sweeps and fundamental impedances sweep at optimum 2×f0 source impedance. Blue trace: load set to PAEmax Red trace: load set to $P_{OUT}$max.

## IV. Wafer Mapping

The measurement procedure with the optimum impedances and results so far described, have been carried out on a few on-wafer devices. These optimum impedances are then set and used together with an IAF in-house software for the complete wafer-mapping at (in this case) X-band frequencies. Thanks to the wafer mapping measurement capability, the devices of the whole wafer can be measured in a fully automated approach. This means that at the fixed frequency, bias condition and optimum source and load terminations previously achieved, automated power sweep can be conducted on the full wafer and yield investigation with respect to maximum gain and power-efficiency can be conducted in a very time efficient process.

The distribution of the most important parameters are shown in Fig. 7 where the devices deliver the same output power and gain of > 35 dBm and > 12dB with an average PAE of 65%.

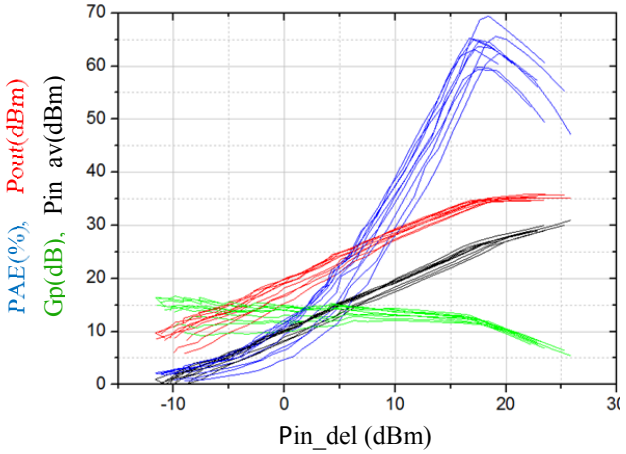


Fig. 7. PAE, Pout, Gp and Pin_available as a function of Pin_delivered traces of several wafer cells in one plot - performance variation.

## V. Conclusions

This paper has shown the measurement results of a 1 mm power HEMT in AlGaN/GaN technology delivering very high power-efficiency at X-band frequencies. By using an active harmonic loadpull system capable of performing accurate measurements at X-band frequencies together with a systematic measurement procedure for the DUT matching optimization, optimum fundamental and second harmonic output- as well as second harmonic source- terminations have been found which deliver valuable information for the design of high-efficiency RF-power amplifiers at 8.7 GHz. The step by step procedure shows the influence of the single impedances on the transistor performance and from here final tuning around the known optimum areas can be done with simultaneous load/source pull of several loops successfully. The optimization of the second harmonic terminations seen by the 1-mm GaN power transistor both at input and output increases the PAE by approximately 6% from 59.7% to 66.1% where also the 2×f0 load and source terminations were optimized.

The paper highlights the high performance of the IAF 1 mm AlGaN/GaN power transistor at X-band frequencies together with a systematic load/source pull measurement procedure for which four RF power loops have been properly varied and optimized for high power-efficiency PAs.

## References


[1] Travis A. Barbieri, Basim Noori "Improvements in High Power LDMOS Amplifier Efficiency Realized Through the Application of Mixed-Signal Active Loadpull", Microwave Measurement Conference, 2013 82nd ARFTG.

[2] Steve C. Cripps "RF Power Amplifiers for Wireless Communications", 2nd Edition, Artech House Publishers Inc., ISBN: 0-89006-989-1, 2006.

[3] M. Seelman, T. Merkle, F. van Raay, R. Quay, M. Schlechtweg, "A Systematic State-Space Approach to Large-Signal Transistor Modeling," *IEEE Transaction Microwave Theory and Techniques,* Vol. 55, No. 2, pp. 195-206, February 2007.

[4] C. Wongtanark, S. Chalermwisutkul, "Design and implementation of a 1 GHz GaN HEMT class-F power amplifier for transistor model evaluation," *Telecommunications and Information Technology (ECTI-CON)*, pp. 152-155, 2011.

[5] P. Saad, H. M. Nemati, M. Thorsell, K. Andersson, C. Fager, "An inverse class-F GaN HEMT power amplifier with 78% PAE at 3.5 GHz," *European Microwave Conference (EuMC)*, pp. 496-499, 2009.

[6] M. Marchetti, M. J. Pelk, K. Buisman, W. C. E. Neo, M. Spirito "Active harmonic loadpull with realistic wideband signals," *IEEE Transaction on Microwave Theory and Techniques*, Vol. 56, No. 12, pp. 2979-2988, December 2008.

[7] T. Williams, J. Benedikt, P. J. Tasker, "Experimental evaluation of an active envelope load-pull architecture for high speed device characterization, "*IEEE MTT-S International Microwave Symposium Digest*, pp. 1509-1512, June 2005.

[8] P. Colantonio, F. Giannini, E. Limiti, V. Teppati "An Approach to harmonic load- and source-pull measurements for high efficiency PA design," *IEEE Transaction on Microwave Theory and Techniques,* Vol. 52, Issue 1, Part 1, pp. 191-198, 2004.P.

[9] Waltereit, W. Bronner, R. Quay, M. Damman, R. Kiefer, W. Pletschen, S. Müller, R. Aidam, H. Menner, L. Kirste, K. Köhler, M. Mikulla, O. Ambacher," AlGaN/GaN epitaxy and technology," *International Journal of Microwave and Wireless Technology (IJMWT)*, pp. 3-11, 2010.

[10] Rüdiger Quay "Gallium Nitride Electronics," Springer Series in Materials Science (Berlin Heidelberg), Vol. 96, Print ISBN: 978-3-540-71890-1.

[11] W. Wohlmuth, M. H. Weng, C. K. Lin, J. H. Du, S. Y. Ho, T. Y. Chou, S. M. Li, C. Huang, W. C. Wang, W. K. Wang, K. S. Hsiang, T. Y, Shien, "AlGaN/GaN HEMT Development Targeted for X-band Applications," *Microwaves, Communications, Antennas and Electronics Systems (COMCAS)*, pp. 1-4, 2013.

[12] C. Schuberth, H. Arthaber, M. L. Mayer, G. Mageri, R. Quay, F. van Raay, "Load Pull Characterization of GaN/AlGaN HEMTs," *Integrated Nonlinear Microwave and millimeter-Wave Circuits (INMMIC)*, pp. 180-182, 2006.

[13] Anteverta-mw website: http://www.anteverta-mw.com.

# Two-Stage Correction for Wideband Wireless Signal Generators with Time-Interleaved Digital-to-Analog-Converters

*Youngcheol Park*[*], *and Kate A. Remley*[**]
[*]*Hankuk Univ. of Foreign Studies, South Korea*
[**]*National Institute of Standards and Technology, Boulder, CO 80305 .*

**Abstract — We present a correction technique for arbitrary waveform generators that utilize time-interleaved digital-to-analog converters. By correcting non-ideal responses of the digital-to-analog converters, the overall signal quality of the source can be improved. To verify this technique, the improvement in a 64-quadrature-amplitude-modulated waveform with a bandwidth of 1.25 GHz was evaluated. The error vector magnitude of the source was improved from 7.8 % to 0.7% with the proposed corrections.**

**Index Terms — Millimeter-wave wireless communications, modulated signal, signal generator, wireless systems.**

## I. Introduction

Signal sources are needed to study and implement wireless communications in the millimeter-wave regime. Sources based on arbitrary waveform generators and frequency converters have recently been reported [1],[2]. For signal generation at intermediate frequencies (IFs), high-speed arbitrary waveform generators (AWG) directly generate waveforms by utilizing time-interleaved digital-to-analog converters (DACs) [3]. This time-interleaving technique is adopted to overcome the sampling-rate limitation of the individual DACs [4],[5]. With accurate switching between outputs from the two DACs, the final waveform has a sampling rate equivalent to twice that of the individual sampling rate of each DAC. As illustrated below, the DAC outputs add below the Nyquist rate while cancelling out the image signal above the Nyquist rate.

However, because the bandwidth of signals with millimeter-wave carrier frequencies (roughly 10 % of the carrier frequency) may occupy several gigahertz, obtaining a flat frequency response with the self-calibration processes that are provided by the equipment's manufacturer is very difficult. Additionally, any amplitude or timing imbalance between the DACs associated with time interleaving creates errors both at the in-band and the image-band signals. In particular, the in-band error is critical to the error vector magnitude (EVM) of measured communication signals.

To address these issues, and to create a method to accurately calibrate AWGs that incorporate time interleaving, a two-stage correction process is proposed here. Passing waveforms through a digital de-multiplexer allows us to correct for DAC imbalance. This is followed by a system response correction to account for the nonideal frequency response of the DACs. By applying these corrections in predistortion, the AWG can generate high-quality wideband signals, as intended.

## II. Time-Interleaved Signal Generation

The time-interleaving technique is now utilized in state-of-the-art measurement equipment with sampling frequencies higher than 20 Giga-samples-per-second (Gsps) [3]. Figure 1 shows a block diagram of the time-interleaving architecture of these arbitrary waveform generators.

For a transmitted signal $x(t)$ the stored waveform, consisting of $L$ digital samples, is defined as follows:

$$x[m] = x(mT_s) = \sum_{m=1}^{L} \left( x(t)\delta(t - mT_s) \right), \qquad (1)$$

where $x[m]$ is the discrete version of $x(t)$ sampled at a period of $T_s$. This signal will be uploaded to the AWG. To perform interleaving, $x[m]$ is alternately split into separate paths, one for each DAC. The DACs each have an identical sampling period of $2\,T_s$, creating waveforms $x[2k+1]$ and $x[2k]$, which all have the Nyquist frequency of one half of $x[m]$'s.

Because DACs use a zero-order hold circuit to store and dispense electric charges with a sampling period of $T_s$, the Fourier transform of the first DAC may be expressed as follows

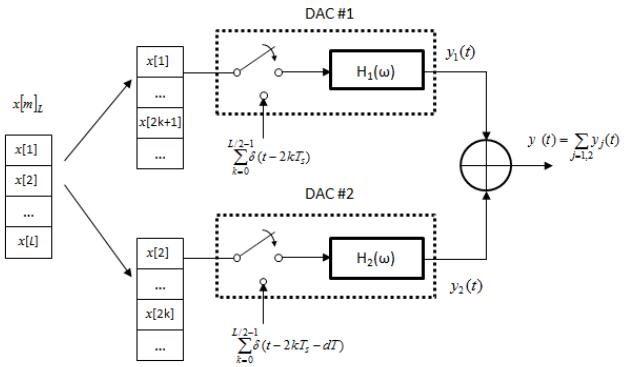


Fig. 1. Operation of time interleaving where the stored $x[m]$ is split and fed into separate DACs, one of which has a timing offset of $dT$ to cancel images at the even-numbered Nyquist zones.

U.S. Government work not protected by U.S. copyright

$$Y_1(\omega) = \sum_{n=-\infty}^{\infty} X\left(\omega - \frac{(n-1)\pi}{T_s}\right) H_1(\omega), \quad (2)$$

where $X(\omega)$ is the Fourier transform of the continuous signal $x(t)$ with the angular frequency of $\omega$, and $H_1(\omega)$ is the Fourier transform of the DAC's impulse response function $h_1(t)$.

For the second DAC, which generates the alternate samples, the sampling clock is supplied with a delay of $T_s$. Therefore, its Fourier transform $Y_2(\omega)$ would have identical $X(\omega)$ but it has its own impulse response with 180 degree phase rotation in every zone (that is, the frequency range between adjacent Nyquist frequencies). In this way, image signals created in the second zone are, ideally, cancelled, where

$$\begin{aligned} Y_2(\omega) &= \sum_{n=-\infty}^{\infty} X\left(\omega - \frac{(n-1)\pi}{T_s}\right) H_2(\omega) e^{j(n-1)\pi} \\ &= \sum_{n=-\infty}^{\infty} X\left(\omega - \frac{(n-1)\pi}{T_s}\right) [H_1(\omega) H_{imb}(\omega)] e^{j(n-1)\pi}. \end{aligned} \quad (3)$$

The Nyquist zone is defined as the frequency range between neighboring integer-multiple frequencies of the Nyquist frequency. Thus, because the sampling rate of the individual DAC is 10 Gsps, we define the first zone as the frequency range between 0 to 5 GHz (with zone number $n = 1$).

At the output of each path, signals are summed, to generate $Y(\omega)$, in which the overall frequency response is expressed by the common response ( $H_1(\omega)$ ) and the imbalance response ( $H_{imb}(\omega)$):

$$\begin{aligned} Y(\omega) &= Y_1(\omega) + Y_2(\omega) \\ &= \sum_{n=-\infty}^{\infty} X\left(\omega - \frac{(n-1)\pi}{T_s}\right) [H_1(\omega) \pm H_2(\omega)] \begin{pmatrix} +: n \text{ odd} \\ -: n \text{ even} \end{pmatrix} \\ &= \sum_{n=-\infty}^{\infty} X\left(\omega - \frac{(n-1)\pi}{T_s}\right) H_1(\omega) [1 \pm H_{imb}(\omega)]. \end{aligned} \quad (4)$$

In (4), images in zones with a negative sign (where $n$ is even) are cancelled out, resulting in the ideal Fourier transform of the original $x(t)$ sampled at a period of $T_s$.

In the implementation of the overall system, which is shown in Fig. 1, there are non-idealities such as timing errors and gain mismatches between time-interleaved paths caused by imperfect manufacturing processes. Even a small amount of mismatch adversely affects image cancellation and the signal-to-noise ratio.

## III. Identification of Nonidealities

To identify and correct DAC nonidealities, we conducted measurements with a commercially available AWG with time-interleaved DACs. The test signal was generated with a sampling rate of 20 Gsps at a center frequency of 4 GHz, representing a 64-QAM modulated signal. The signal had a data rate of 1 Gsps, with an occupied bandwidth of approximately 1.25 GHz. The signal from the AWG was captured with a high-speed sampling oscilloscope and the data were post-processed with an accurate time-base distortion correction algorithm [6],[7].

For the first step of the procedure, the frequency response of each path was identified by separately uploading the time-interleaved waveforms one at a time, while the other DAC was given all zeros. The two measured signals, when combined, represent the composite response of the ideal $X(\omega)$ and the impulse responses of the individual paths, $H_1(\omega)$ and $H_2(\omega)$:

$$Y(\omega)_{x_2=0} = Y_1(\omega) + N_o = \sum_{n=-\infty}^{\infty} X\left(\omega - \frac{(n-1)\pi}{T_s}\right) H_1(\omega) + N_o \quad (5)$$

and

$$\begin{aligned} Y(\omega)_{x_1=0} &= Y_2(\omega) + N_o \\ &= \sum_{n=-\infty}^{\infty} X\left(\omega - \frac{(n-1)\pi}{T_s}\right) H_2(\omega) e^{j(n-1)\pi} + N_o \end{aligned}, \quad (6)$$

where $N_o$ is the total random noise across the bandwidth $B$ from various noise sources such as thermal noise and quantization noise [8].

The $n^{\text{th}}$ zone frequency response of the $k^{\text{th}}$ DAC path within the signal bandwidth $B$ may be given as follows:

$$H_k(\omega)_{n^{th}-zone} = \frac{Y_k(\omega)_{n^{th}-zone}}{X\left(\omega - \frac{(n-1)\pi}{T_s}\right)}, \quad |\omega - \omega_c| \le B/2. \quad (7)$$

Figure 2 shows the first- and second-zone spectral response of the signal from the AWG with a combined sampling frequency of 20 Gsps (blue, solid line), measured after passing through a low-pass filter with a cut-off frequency of 7 GHz. In the figure, the residual image signal in the second zone (5 to 10 GHz) is quite significant because of the imbalance, despite the AWG's built-in calibration process. By taking the difference of (5) and (6), the in-band ($n$ = 1) and image-band ($n$ = 2) residual error with noise can be observed and is shown in Figure 2 as well (red, dotted line). In this particular case, we assume that the spectral components from DAC #1 have sufficient signal-to-noise ratio within the bandwidth of the signal, and, thus, the responses in the first two zones may be identified.

To obtain the imbalance information in the frequency domain, the spectral components of DAC #1 and DAC #2 are compared within a bandwidth of $B$ for the first two zones, where, again, a high signal-to-noise ratio is assumed:

$$H_{imb}(\omega)_{n^{th}-zone} = \frac{H_2(\omega - n\omega_s)}{H_1(\omega - n\omega_s)}, \quad |\omega - n\omega_s - \omega_c| \le B/2. \quad (8)$$

Figure 3(a) shows the identified magnitude response $|H_{imb}(\omega)|$ over the signal bandwidth within the first two zones.

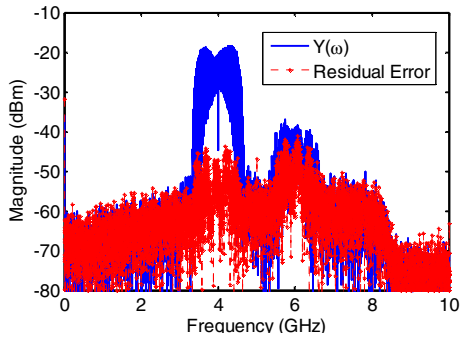


Fig. 2. Measured response (solid line) of a 1 Gsps 64-QAM signal generated with an AWG sampling frequency of 20 Gsps and the residual error due to DAC imbalance (dotted line).

This residual error corresponds to the cancellation path that is not exactly 180º over the band of interest. Additionally, Figure 3(b) shows the common frequency response $|H_1(\omega)|$ of the overall system over the same frequency range, which can be identified by (8). We see that the system obviously has highly frequency-dependent non-idealities.

To correct these non-idealities, a pre-filter that compensates for the in-band imbalance in the first zone (below the Nyquist frequency of DAC #2) is applied to the DAC #2 waveform. This filter is placed at the output of DAC #2, and has the inverse response of (8) over the desired bandwidth. In a similar manner, a pre-filter that has the inverse response of $H_1(\omega)$, the common frequency response from (7), is applied to the sum of the DAC outputs. Figure 4 shows the final block diagram. This figure shows the pre-filtering blocks for the common- and imbalance- response corrections.

The correction performance was evaluated with the EVM metric, which was 1.8 %, compared to 8.9 % without the correction. Furthermore, the value could be improved to a nominal value of 0.7 % when the correction method was incorporated with an iterative pre-distortion technique to remove additional excitation-dependent, nonlinear distortion [1].

An uncertainty analysis based on the NIST Microwave Uncertainty Framework [9, 10] included more than 640 error mechanisms. This analysis included a wide array of parameters from the pin depth of the calibration standards, to effects of cable bend, to optical parameters for the electro-optic sampling system used to calibrate the sampling oscilloscope. This analysis found an overall mean error in the EVM of approximately 1.0 % ± 0.3%, with measurement repeatability being the largest source of error.

## IV. Conclusion

We presented a correction method for use in generating multi-gigabit-per-second signals with AWGs that include time-interleaved DACs. With this method, we first identify and pre-filter the imbalance between DAC paths. We then identify and pre-filter the linear response of the system. With this proposed method, we improved the EVM from 8.9 % to 1.8 % for a 1 Gsps, 64-QAM modulated signal with a 4 GHz carrier frequency. This could be further improved to ~1.0 % by iteratively correcting complex frequency coefficients to compensate for both linear and nonlinear distortion.

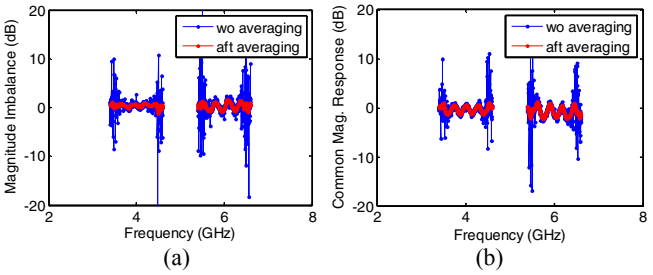


Fig. 3. Identified magnitude responses over the signal bandwidth within the first two zones: (a) Imbalance response (b) Common response.

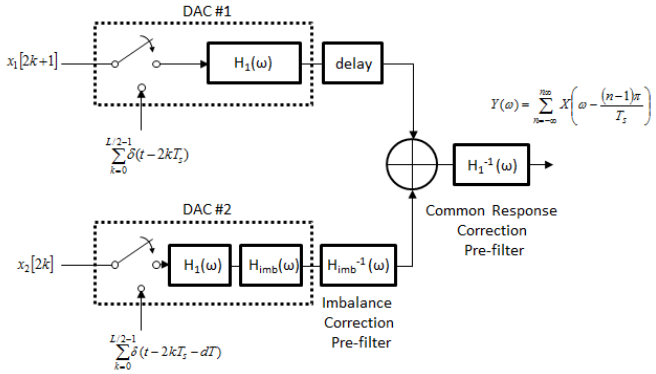


Fig. 4. Correction of frequency-dependent non-idealities by pre-filters to correct the imbalance- and common-frequency responses.

## V. Acknowledgment

The authors acknowledge NIST researchers Dylan Williams, Paul Hale, Chih-Ming Wang, and Jeff Jargon for their support of this work in the context of the NIST project "Traceability to Enable Multi-GigaBit-per-Second Mobile Wireless."

## References

[1] K. A. Remley, P. D. Hale, D. F. Williams, and C.-M. Wang, "A precision millimeter-wave modulated-signal source," *IEEE Int. Microwave Symp. Dig.,* Seattle, WA, June 2-7, 2013, Paper TH2D-3.

[2] Tomorrow Works (2013, May 13), "Samsung Announces World's First 5G mmWave Mobile Technology" *Samsung Tomorrow* [Online]. Available: http://global.samsungtomorrow.com/?p=24093

[3] *Application Note: 76W-29216-0, Understanding AWG70000A Series Frequency Response and DAC Performance*, Tektronix, Beaverton, OR, 2013.

[4] W. C. Black and D. A. Hodges, "Time interleaved converter arrays," *IEEE J. Solid-State Circuits*, vol. SC-15, no. 6, pp. 1022-1029, Dec. 1980.
[5] C. Krall, C. Vogel, and K. Witrisal,"Time-interleaved digital-to-analog converters for UWB signal generation," *IEEE Int. Conf. Ultra-Wideband,* Singapore, pp. 24-26, Sept. 2007.
[6] C.-M. Wang, P.D. Hale, J.A. Jargon, D.F. Williams, and K.A. Remley, "Sequential estimation of timebase corrections for an arbitrarily long waveform," *IEEE Trans. Inst. and Meas.*, vol. 61, no. 10, pp. 2689-2694, October, 2012.
[7] D. F. Williams, P. D. Hale, K. A. Remley, "The sampling oscilloscope as a microwave instrument," *IEEE Microwave Mag.*, vol. 8, issue 4, pp.59-68, April, 2007.
[8] J. Mitola III, *Software Ratio Architecture*, John Wiley & Sons, Inc., New York, NY, 2000.
[9] NIST Microwave Uncertainty Framework, Beta Version, D. F. Williams, http://www.nist.gov/pml/electromagnetics/related-software.cfm , 2012.
[10] J. A. Jargon, D. F. Williams, T. M. Wallis, D. X. LeGolvan, and P. D. Hale, "Establishing Traceability of an Electronic Calibration Unit Using the NIST Microwave Uncertainty Framework," *79th ARFTG Conf. Dig.*, pp. 32-36, Montreal, Canada, Jun. 2012.

# Measurements for Microwave Differential and IQ Devices

*Joel Dunsmore, Xin Chen*

*Agilent Technologies, Santa Rosa, Ca.*

**Abstract —In the past, devices that require true-mode differential drive (+-180 degree) or true-mode IQ drive (0 and 9 degree) have been difficult to measure at RF and microwave frequencies. At microwave frequencies, baluns and 90 degree hybrids have poor performance, and are very difficult to use in on-wafer test. True-mode VNAs have allowed non-linear measurements of compression, but require input and output frequencies to be the same. To date, no method has been presented that can allow measurements of differential harmonics, differential mixers, or IQ mixers without the use of baluns or hybrids at high frequency, or with high accuracy. This paper presents a new method that provides fully corrected measurements for all these cases, over swept frequency or swept power, or swept phase without the use of baluns. It is suitable for on-wafer applications and extensible to mm-wave frequencies.**

**Index Terms — Differential, IQ, Mixer, Modulator, Non-linear, Harmonics.**

## I. Introduction

Differential design and IQ modulation have in the past been limited to low-frequency devices. But with the increase in microwave and mm-wave use of complex RF integrated circuits, these low-frequency design techniques have moved into RF, microwave and even mm-wave frequencies.

Differential, or balanced, devices do not use a single coax port but rather use a pair of ports at the input and output. The output signal is the difference (in a voltage sense) of the pair of output ports. The mathematics for differential devices, expressed as mixed-mode S-parameters, has been fully developed [1], and many modern VNAs can make true-mode as well as mixed-mode measurements[2,3]. While many devices don't show any difference in measured results using either single-ended or true-mode stimulus [4], some devices require that the input drive to the device also be fully differential, and behavior of the device, especially non-linear behavior, may be quite different if between differential drive and single-ended drive; the implications of true-mode drive on amplifiers has been the subject of several papers[5-7].

However, all of the previous work has only been applied to amplifiers, and only to ratio measurements (gain and match). No work has been published on making balanced measurements of power (in most case, power is not mentioned, or output power is inferred from the source power setting and the gain). Thus no measurement of other amplifier characteristics such as harmonics has been described to date. In this paper, we describe the required mathematical corrections needed to create a true-mode or IQ RF drive, and describe a measurement system that can create a true-mode or IQ drive at one frequency and measure the output (including single-ended, differential or IQ) at a multitude of other output frequencies, as well as demonstrate correction methods for measuring differential and IQ power.

## II. System Description

In the past, devices that require true-mode differential drive (+-180 degree) or true-mode IQ drive (0 and 90 degree) have been difficult to measure at RF and microwave frequencies. At low frequency the differential or IQ drive can be created using programmable arbitrary-waveform generators, and measurements made using oscilloscopes with differential probes.

For RF and Microwave systems, a VNA with dual sources has been used in the past to create true-mode signals, but all implementations require that the device measurement be done at only the frequencies of the sources. Presumably this limitation is needed because the source control requires a measurement of the source signal to obtain the relative amplitude and phase of the drive signal. Figure 1 shows such a VNA system, but in our case, the system has been modified to allow re-tuning the receivers to any of a set of arbitrary frequencies after the sources have been aligned to the proper amplitude and phase.

In the case of measuring balanced harmonics at the output, the receiver LO is tuned first to the receiver the fundamental frequency, which is iterated until the proper amplitude and phase is measured on the a1 and a3 receivers. Then, holding the sources constant, the LO is immediately switched other the desired harmonic frequencies, and the power and relative phase of signals applied to all eight receivers is recorded. This data acquisition method ensures than the sources do not drift during the acquisition of the harmonic signals.

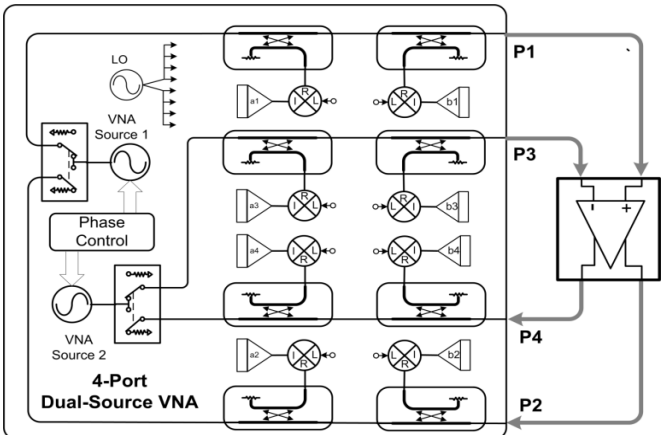


**Figure 1: Dual Source VNA used to measure power and harmonics of a differential amplifier**

978-1-4799-4423-1/14/$31.00 ©2014 IEEE

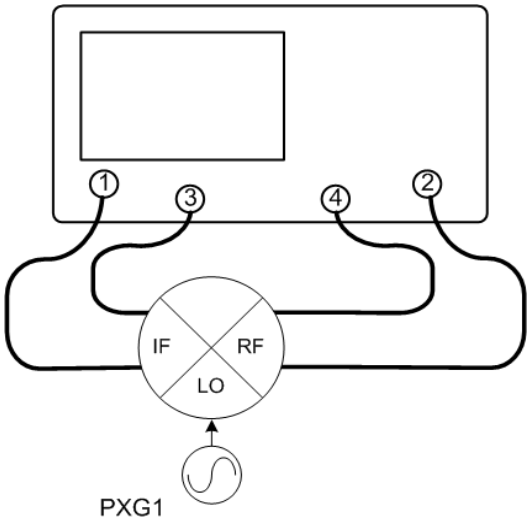


**Figure 2: Balanced Mixer Measurement**

A similar block diagram is used for measuring balanced mixers, but in this case an external source is used as the Local Oscillator (LO), unless of course the mixer, more properly called a frequency converter, has an embedded LO. Figure 2 illustrations the connection diagram for a differential mixer. Finally, for an IQ mixer, several configurations can be utilized. An example configuration is show in Figure 3.

In this type of mixer, key measurements are measuring the desired output (RF), the image signal, the LO feed through, and adjusting the I and Q magnitude and phase offset, as well as DC offsets at the I and Q inputs, to minimize the image signal and LO feed through. Performing these tests when I and Q signals are in the RF or Microwave range have been extremely difficult in the past.

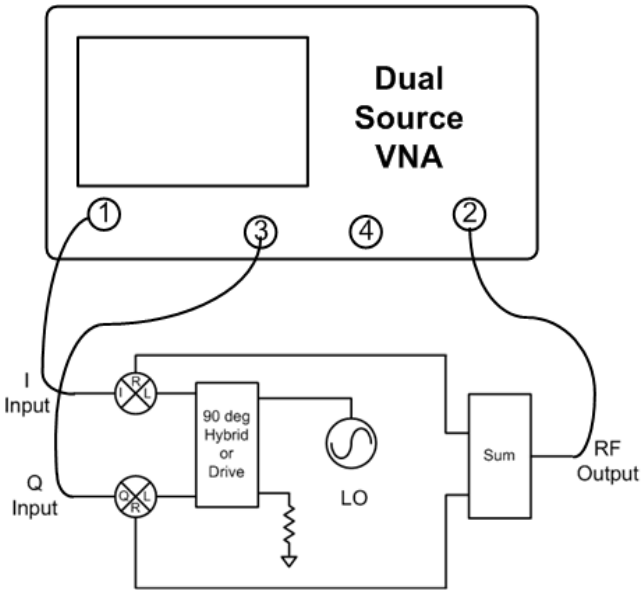


**Figure 3: IQ mixer test setup**

## III. Error Correction

Error correction is needed for both the stimulus and response portions of the measurement. In the stimulus case, the match of the DUT can interact with the source match from the VNA to distort the amplitude and phase the actual applied to the DUT. Correction of the measurement of the ratio of the input signals can found from equation 1.

$$\frac{a_1}{a_3} = \frac{\left(a_{1M}ERF_1 + b_{1M}ESF_1 - a_{1M}ESF_1 \cdot EDF_1\right)}{\left(a_{3M}ERF_3 + b_{3M}ESF_3 - a_{3M}ESF_3 \cdot EDF_3\right)} \frac{ETF_{31}}{ERF_1} \quad (1)$$

Error correction for the output signals also requires mismatch correction as well as magnitude and phase response correction. The error correction for each receiver is computed from equation 2.

$$b_{2A} = \frac{b_{2M}}{BTF} \cdot \left(1 - ELF \cdot \Gamma_2\right) \quad (2)$$

Differential power measurements can be computed from (3) where N represents the signal desired, e.g., N=1 is fundamental, N=2 is second harmonic.

$$P_d = \frac{(b_{2,N} - b_{4,N})}{\sqrt{2Z_0}} \quad (3)$$

## IV. Measurement Results

Two important questions arise as to the measurement method:

1) How well does the stimulus create a representation of the desired differential or IQ signal
2) How well does the response measure the differential output

That is, are the stability of the source and the error correction methods sufficient to give meaningful results and how might those results be verified.

Figure 4 shows the result of measuring the harmonics of a single ended amplifier. Also shown is the same amplifier driving a 180 degree hybrid. This represents what one would see from a single-ended to balanced amplifier. In such a case, the harmonic content should be nearly the same (except for the difference in loss of the hybrid between the fundamental and harmonic frequency). Clearly the results measuring as shown in equation 3, corrected by equation 2 demonstrate very good correlation.

These tests validate that the differential power measurement of the harmonic match expectations, but the DUT was not a true differential amplifier as a hybrid was used at the output to give a differential harmonic with known power. So, another test of a true-differential amplifier was performed finding differential output power and differential output harmonics.

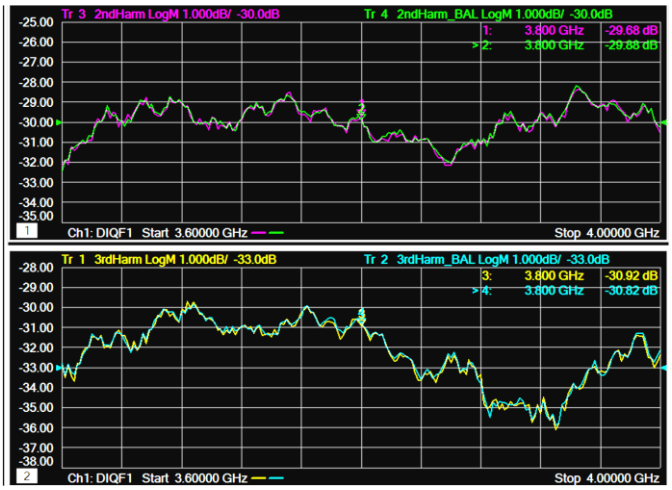


**Figure 4:Comparing Earmonics Single-Ended and through a Differential Balun**

Figure 5 shows a photo of the amplifier used in the test. Figure 6 shows the resulting differential output power and differential gain. While the amplifier was driven with a true-mode drive, it is not very sensitive to small phase errors of the source.

**Figure 5: True Differential Amplifier used for Harmonic Test**

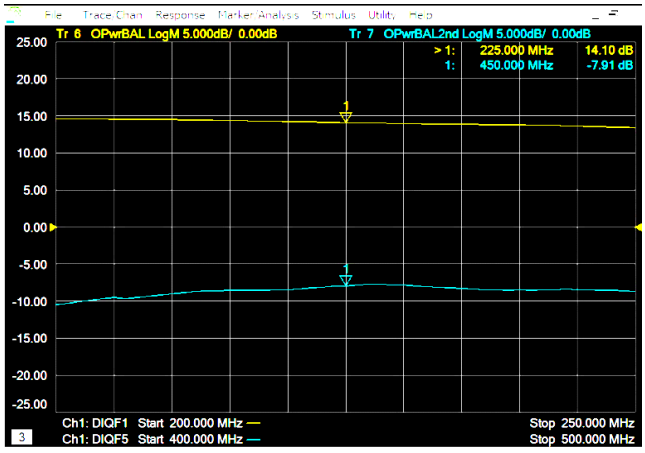


**Figure 6: Balanced Output Power and Balanced Harmonics**

A similar test is shown in Figure 7, but this time for a balanced frequency-converter as shown in Figure 2.

However other devices, such as IQ mixers, are very sensitive to phase offsets and measurement results will vary dramatically for even slight errors in phase and power. The

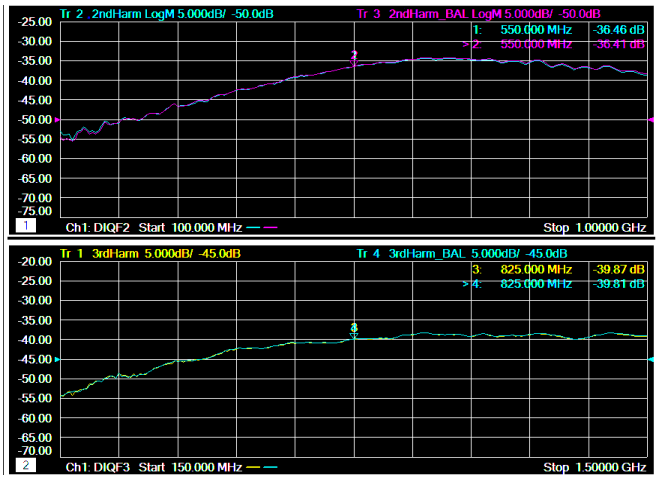


**Figure 7: Harmonic Measurement of a Balance Mixer**

next set of experiments validated the phase accuracy of the source-setting algorithm while performing frequency offset measurements of an IQ mixer.

IQ converter designs often use a 90 degree hybrid on the fixed-frequency LO port as shown in Figure 3. We use the hybrid to help validate the quality of the phase setting of the sources for the IQ mixer test. First, the 4-port S-parameters of the 90 degree hybrid were measured and the ratio of S31 to S21 was found to determine the IQ response; in this case the phase error was 91.5 degrees and the amplitude error was about 0.5 dB. Next, the Hybrid was used to validate the phase setting of the sources. The frequency of the two input signals were swept across a wide band and applied the 0 and 90 degrees input, with +90 and -90 degree offsets. The output was routed to the B-receiver and the power measured. Figure 8 shows the results of measuring the hybrid. When the sources are set to 0 and 90 degrees, a maximum is seen; when the sources are set to 0 and -90 degrees, a minimum is seen. This demonstrates good source phase control.

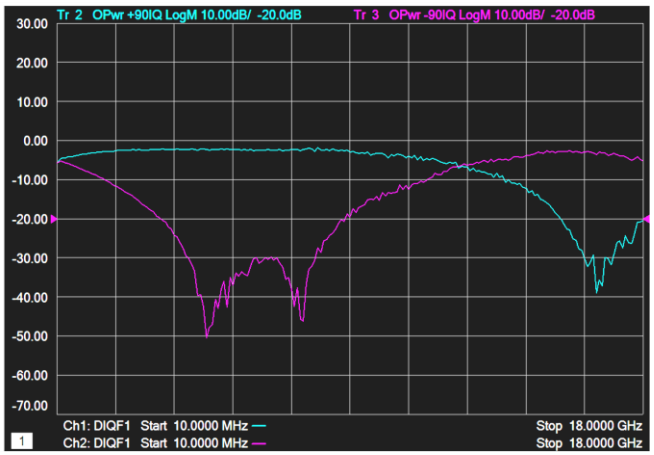


**Figure 8: Measurement of output power of a 90 degree hybrid with +90 and -90 drives.**

Finally, figure 7 shows the results of 3 measurements of a device as in figure 3: Several measurement scenarios were performed to establish the characteristics of the IQ mixer. For these devices, image rejection is a key specification, and the image rejection depends upon getting good balance between the I and Q paths. Often the individual mixers are not identical, and so the skew, or phase difference, of the IQ path is first determined mid-band to allow a fixed IQ offset. The amplitude balance is also important to achieve good image rejection. To determine the phase amplitude skew, and then measure the image rejection, the following 3 steps are performed:

1) Set the I/Q source to 90 degrees and sweep the IQ power offset, while monitoring the image and RF signal. Then record the value of offset that gives the lowest image
2) Set the amplitude offset as in 1) and then sweep the IQ phase to find the minimum image; then record the phase offset
3) Set the IQ amplitude and phase as in 1 and 2 above and sweep the frequency of the input while maintaining constant IQ phase.

Figure 9 shows the results of each of the 3 steps for the IQ converter from Figure 3.

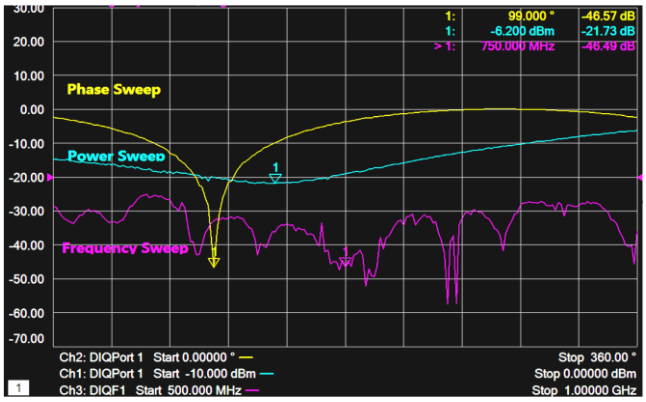


**Figure 9: IQ converter Image Reject measurements**

Once the proper skew is found for the IQ inputs, other characteristics of the converter can be measured such as conversion loss (or output power), LO feedthrough (leakage), RF isolation, and spurious or harmonic outputs. Figure 10 shows some sample measurements: Output Power, LO feedthrough, and RF Isolation. Figure 10 shows these output signals for another mixer. This represents a very complicated measurement process, which is:

1) Set the input power and initial phase of the I and Q ports, at the first frequency point.
2) Measure the Match of the DUT on the IQ ports, and compute the incident power
3) Compute and offset amplitude and phase to achieve the desired IQ signals
4) Re-set the IQ sources and re-measure the result. Continue iterating the settings until the desired IQ response is achieved.
5) Change the receiver to measure all the desired output frequencies including LO output, RF isolation, Image frequency and desired Output frequency.
6) Repeat for each frequency point.

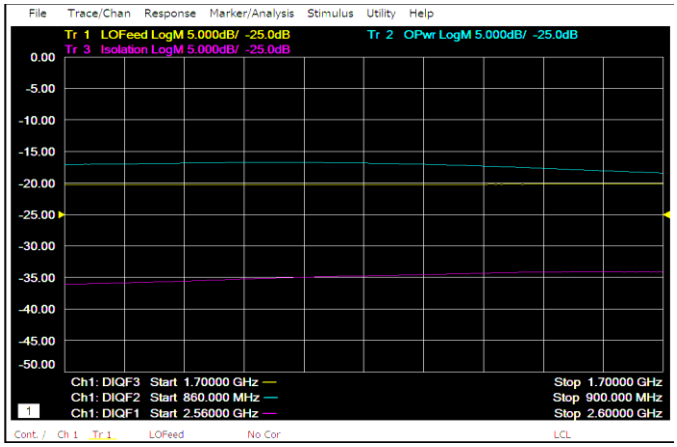


**Figure 10: Measurements of LO Feedthrough, Isolation, and Power**

## V. Conclusion

The measurement system presented shows the ability to make differential harmonic and IQ mixer measurements. This is the first time such measurement have been demonstrated in the RF and Microwave range, with fully corrected results.

## References


[1] Bockelman, D.E.; Eisenstadt, W.R., "Combined differential and common-mode scattering parameters: theory and simulation," Microwave Theory and Techniques, IEEE Transactions on , vol.43, no.7, pp.1530,1539, Jul 1995

[2] Dunsmore, Joel; Anderson, K.; Blackham, D., "Complete Pure-Mode Balanced Measurement System," *Microwave Symposium, 2007. IEEE/MTT-S International* , vol., no., pp.1485,1488, 3-8 June 2007

[3] Simon, J., "True differential stimulus gives additional insight into nonlinear device behavior," *ARFTG Conference, 2007 69th* , vol., no., pp.1,9, 8-8 June 2007

[4] Dunsmore, J., "New methods & non-linear measurements for active differential devices," *Microwave Symposium Digest, 2003 IEEE MTT-S International* , vol.3, no., pp.1655,1658 vol.3, 8-13 June 2003

[5] J. Dunsmore: "New Measurement Results and Models for Non-Linear Differential AmplifierCharacterization, Proc. 34th EuMC, Amsterdam, pp. 689-692,2004

[6] J. Dunsmore: New Modeling Results for Non-Linear Differential Amplifier Behavior, Including Two-Tone TOI Response, Proc. 35th European Microwave Conference, Paris, 2005, pp.349-352

[7] Schmitz, O.; Hampel, S.K.; Rabe, H.; Reinecke, T.; Rolfes, I., "Differential Amplifier Characterization Using Mixed-Mode Scattering Parameters Obtained From True and Virtual Differential Measurements," *Microwave Theory and Techniques, IEEE Transactions on* , vol.59, no.1, pp.132,142, Jan. 2011


.

# Method for Calibration Vector signal analyzer based on Baseband waveform Design

ZHOU Feng[1, 2], ZHANG Rui[1], MU Dan[1, 2], CHENG Kai[1], XU Yu-chou[1], GAO You-gang[2]
*1. China Academy of telecommunication Research of MIIT, Beijing 100191 China;*
*2. Beijing University of Posts and Telecommunications, Beijing 100876 China;*
Email: zhoufeng@catr.cn

Abstract

In this paper, we focus on the calibration on VSA, which consists three parts : 1. realization on the peroidic continuity of baseband waves of finite-length digital modulated signals ; 2. fundamental error setting techniques based on error symbols design ; 3. technique of full error symbol frame, which assures that each symbol is present in the measurement on equal probability. This technique will alleviate the negative effects of stochastic symbol sequences on metrology measurement, and unify the measurement model and mathematical model. Our experiements have shown that this metrology method and system can : 1. continuously adjust the values of digital modulated errors in a large range, and set the expected digital modulated error parameters; 2. exhibit strong consistency of the measured value and calculated value for such digital-modulated parameters as EVM; 3. show good repeatability on the values of digital modulated parameters, 4. be widely applied to almost all digital modulation schemes, such as 256QAM or higher rank modulation scheme.

Keywords: Calibration, VSA, EVM, Waveform, Generator

## 1.INTRODUCTION

Vector modulation signal is very important in modern communication, broadcasting and navigation systems. Digital modulation error parameters include EVM (Error Vector Magnitude) and so on [1]. Vector signal analyzer (VSA) is the instrument to measure EVM and so on. VSA needs effective calibration, however, a problem can be perceived in present calibration of VSA in the aspect of digital modulation error: the lack of error settings. When calibrating VSA, the vector modulation signal generator generates standardized modulated signals with little modulation error. For LTE-TDD wireless communication standards, maximum limit of EVM for 64QAM modulation is 8% [2]. If a VSA's range to measure 64QAM EvmRms is 0~9%, it's inadequate to calibrate VSA only near the point "EvmRms=0", which is just like only using a 1mm gauge block to calibrate a ruler whose range is 100mm. Researchers have pointed out this problem [3~5].

## 2. TECHNICAL SOLUTIONS

### 2.1 Periodical Continuity of Finite-Length Digital Modulated Baseband Waveforms

Based on the current hardware infrastructure of vector modulated signal generator (SG), we can design a finite IQ baseband waveform, and introduce the baseband part from SG. Then SG periodically extends this baseband waveform to persistently modulate the carriers and get the RF modulated signals.

The unfiltered symbol value sequence and the time-domain pulse response wave of truncated finite-length baseband filter should convolve in the time domain, to form the IQ baseband wave of finite time. However, this baseband waveform is subject to some drawbacks without special processing. The first and the last values of the

978-1-4799-4423-1/14/$31.00 ©2014 IEEE

baseband waveform are not equal to each other, i.e. the periodical waveforms extended by the SG are not continuous at the periodical connection. Such a discontinuity will bring additional errors to the signals, as shown in Fig. 1.

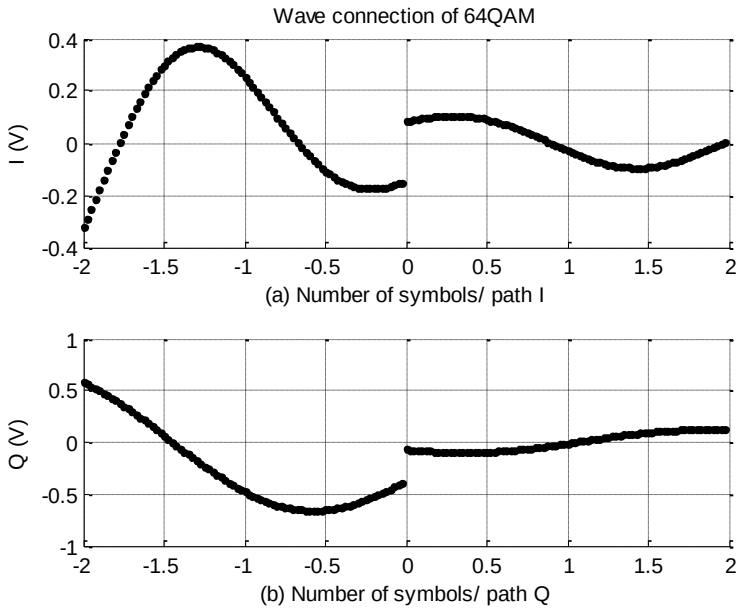


Fig 1. The periodical continuity of finite-length 16QAM wave after baseband filtering

From Fig. 1, we can see that EVM value is much larger with obvious error pulses at the periodical connection, which is due to the discontinuity of the baseband waveforms. Apparently, such a waveform is not qualified as the standard calibrating signals for VSA.

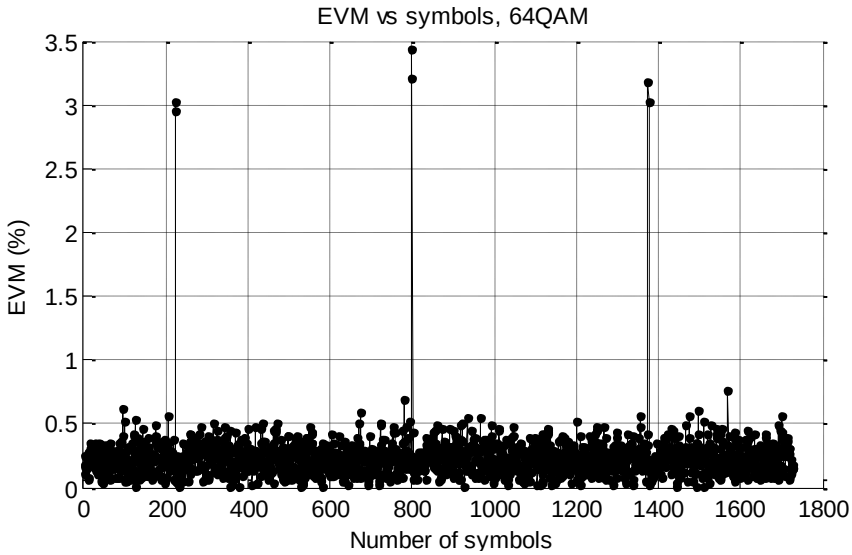


Fig. 2 –EVM corresponding to each symbol due to discontinuity of baseband waveforms

The signals can be applied to the metrology of digital modulated error parameters only when the discontinuity is solved, and we can address this problem by a variety of methods.

A. Constructing symbol sequences (CSS). As is known to all, the time domain convolution is equivalent to the frequency domain filtering. If the truncated length of time domain pulse of the baseband filter is L symbols, then the constructed symbol sequences will have symmetrical first-L and last-L symbols, just as shown in

Fig. 3.

Fig. 3 Construction of IQ symbol sequence

B. FFT and IFFT algorithm. According to the baseband wave sampling rate and symbol rate, we conduct zero inserting and filling for the unfiltered IQ symbol sequence and pulse response wave of the baseband filter, so that the time-domain sampling interval of these two waves is equal with the same sampling points N. After sampling, the resulting two sequences are processed by fast fourier transform (FFT) to get the new N-point sequences Xk1 and Xk2. Inner product is performed on Xk1 and Xk2 to get a N-point sequence Yk, which is then processed by inverse FFT to reach a time-domain wave sequence S. The sequence S is the baseband wave value sequence with the property of periodical continuity.

The methods of A and B are effective and independent to each other. By adopting either method, we show the periodical continuity effect in Fig. 4.

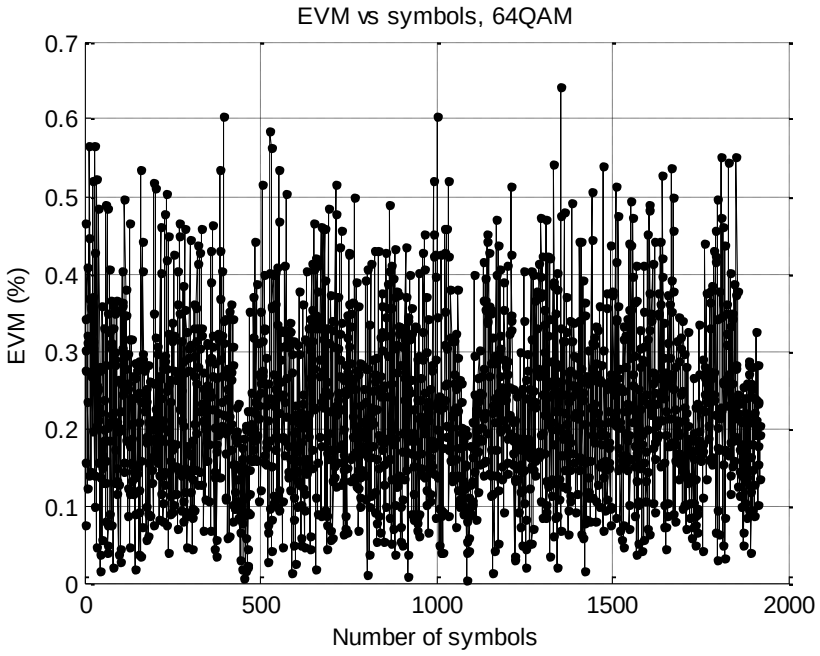


Fig. 4 The EVM of each symbol from the 64QAM baseband signal processed by periodical continuity technique

## 2.2 Fundamental Digital Modulated Error Settings Based on Error Symbol Design

For the digital modulated error settings, we design the error symbols according to the standard symbol sequences. Generally, we suppose the symbol $S_k$ is mapping into point A in the IQ domain, and according to the classical communication theory, there exists an area called decision zone of symbol $S_k$, in which we choose multiple points except A for $S_{k1}$, $S_{k2}$…$S_{kL}$. In this way, we can define and calculate such digital modulated error parameters as EVM by geometric relationship [6].

The geometric pattern of coordinate points A1、A2…AL in the IQ domain can be various, such as triangle, polygon, hexagon, etc. In this paper, we adopt one pattern called axial-symmetrical equilateral triangle, as shown in Fig. 5.

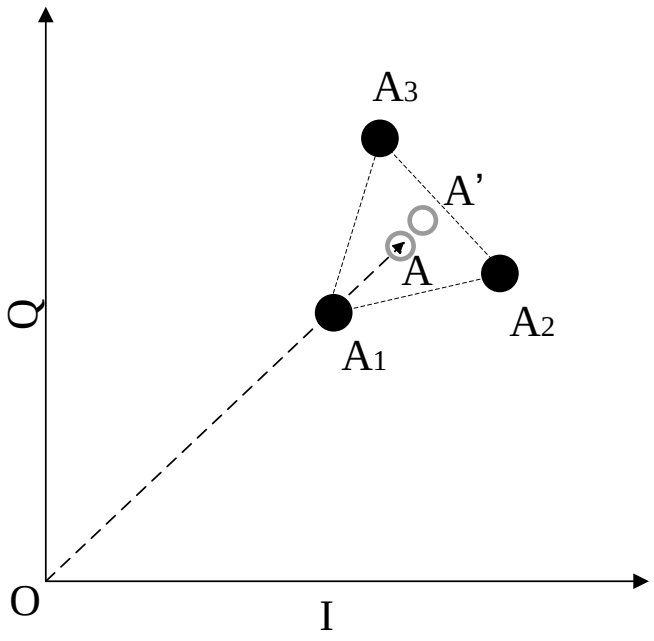


Fig. 5 axial-symmetrical equilateral triangle design in IQ domain

The point A in Fig. 5 correspond to a standard symbol, and we suppose the complex coordinates of A is I+jQ, the magnitude and phase angle of vector $OA$ is MA and $\theta_A$, respectively. Then the points $A_1$, $A_2$, $A_3$ in A's decision area have the vector coordinate as (1) to (3):

$$\overrightarrow{OA_1} = M_A\left(1-\gamma\right)\exp\left(j\theta_A\right) \quad (1)$$

$$\overrightarrow{OA_2} = \overrightarrow{OA_1} + \sqrt{3}\gamma M_A \exp\left[j\left(\theta_A - \frac{\pi}{6}\right)\right] \quad (2)$$

$$\overrightarrow{OA_3} = \overrightarrow{OA_1} + \sqrt{3}\gamma M_A \exp\left[j\left(\theta_A + \frac{\pi}{6}\right)\right] \quad (3)$$

We can call $\gamma$ in (1)~(3) as the radius of equilateral triangle. Suppose the complex coordinate of A is 1, then we have

$$\overrightarrow{OA_1} = 1-\gamma \quad (4)$$

$$\overrightarrow{OA_2} = 1+\frac{\gamma}{2}+j\frac{\sqrt{3}\gamma}{2} \quad (5)$$

$$\overrightarrow{OA_3} = 1+\frac{\gamma}{2}-j\frac{\sqrt{3}\gamma}{2} \quad (6)$$

According to the symmetry, the reference constellation point A' should be on the elongation of OA, and by mean square method:

$$\overrightarrow{OA'} = M_{A'} = \sqrt{1+\gamma^2} \quad (7)$$

$$PhaseErrPeak = \arctan\left(\frac{\frac{\sqrt{3}\gamma}{2}}{1+\frac{\gamma}{2}}\right) \quad (8)$$

$$PhaseErrRms = \sqrt{\frac{2PhaseErrPeak^2}{3}} = \sqrt{\frac{2}{3}}PhaseErrPeak \quad (9)$$

$$MagErrPeak = EvmPeak = \frac{\sqrt{1+\gamma^2}-(1-\gamma)}{\sqrt{1+\gamma^2}} \quad (10)$$

MagErrRms and EvmRms are calculated in vector by definition:

$$MagErr_i = \left|M_{A'} - \left|OA_i\right|\right| \qquad i = 1,2,3 \quad (11)$$

$$MagErrRms = \frac{\sqrt{\frac{\sum_{i=1}^{3} MagErr_i^2}{3}}}{M_{A'}} \times 100\% \quad (12)$$

$$evm_i = \left|\overrightarrow{OA_i} - \overrightarrow{OA'}\right| \qquad i = 1,2,3 \quad (13)$$

$$EvmRms = \frac{\sqrt{\frac{\sum_{i=1}^{3} evm_i^2}{3}}}{M_{A'}} \times 100\% \quad (14)$$

The equations (8) to (14) have shown the relationship of the modulated error parameter and the equilateral triangle radius γ. In the practical applications, we are given such parameter value as EvmRms, and the corresponding γ. The relationship function is given as

$$\gamma = f\left(EvmRms\right) \quad (15)$$

This function can be solved by the method of analytical inverse function, or by some highly accurate numerical method such as inserting.

### 2.3 Full Error Symbol Frame Technique

The technique guarantees that each error symbol will appear with equal probability, which will alleviate the negative effects of stochastic symbol sequences on metrology measurement, and unify the measurement model and

mathematical model.

1. Frame construction. List the complex sequence for the standard symbol of digital modulation scheme as $S_1$、$S_2$、$S_3$…$S_k$…$S_K$. For each symbol $S_k$, design the L error symbols $S_{k1}$、$S_{k2}$…$S_{kL}$ by the method given in section 2.2. In this way, we get the full error symbol frame, and call it FrameE, just as showed in Table 1.

Table 1: A complete error symbol frame: FrameE

| | | | | | | |
|---|---|---|---|---|---|---|
| $S_{11}$ | $S_{21}$ | $S_{31}$ | … | $S_{k1}$ | … | $S_{K1}$ |
| $S_{12}$ | $S_{22}$ | $S_{32}$ | … | $S_{k2}$ | … | $S_{K2}$ |
| … | … | … | … | … | … | … |
| $S_{1L}$ | $S_{2L}$ | $S_{3L}$ | … | $S_{kL}$ | … | $S_{KL}$ |

2. Frame combination. Combine multiple full error symbol frame FrameE to a new symbol matrix FrameM according to the length of our testing sequences. Reconstruct the FrameM into a complex single-row sequence, and randomly arrange the positions of its elements to form a symbol frame $S_{frame}$.
3. Wave construction. By the method of periodical continuity in section 2.1, we generate the periodically continuous baseband wave $WB_{frame}$ based on $S_{frame}$. In this way, each symbol from FrameE will be present equally in the symbol sequence of $WB_{frame}$.
4. VSA setting. Suppose that the wave $WB_{frame}$ corresponds to a sequence of P symbols, then we set the symbol analyzing length of under-testing VSA as multiples of P, and in this way, the side effects of the stochastic symbols on metrological testing are reduced, and guarantee the unify of the testing mechanism and mathematical model of digital modulated error setting.

Based on the above techniques and the hardware infrastructure of VSA, we have constructed the metrology system for the digital modulated error parameters based on periodical continuity. If the calculated value and measured value match well, and the measured values show good repeatability and reliability, this system can then be used as transfer standards or metrology standards.

# 3.SIMULATED AND MEASURED RESULTS

Building the experimental testing system based on the above techniques, we have generated digital modulated signals with set errors. Then these signals are tested by VSA as inputs, and some results are shown in Fig. 6~ Fig. 12.

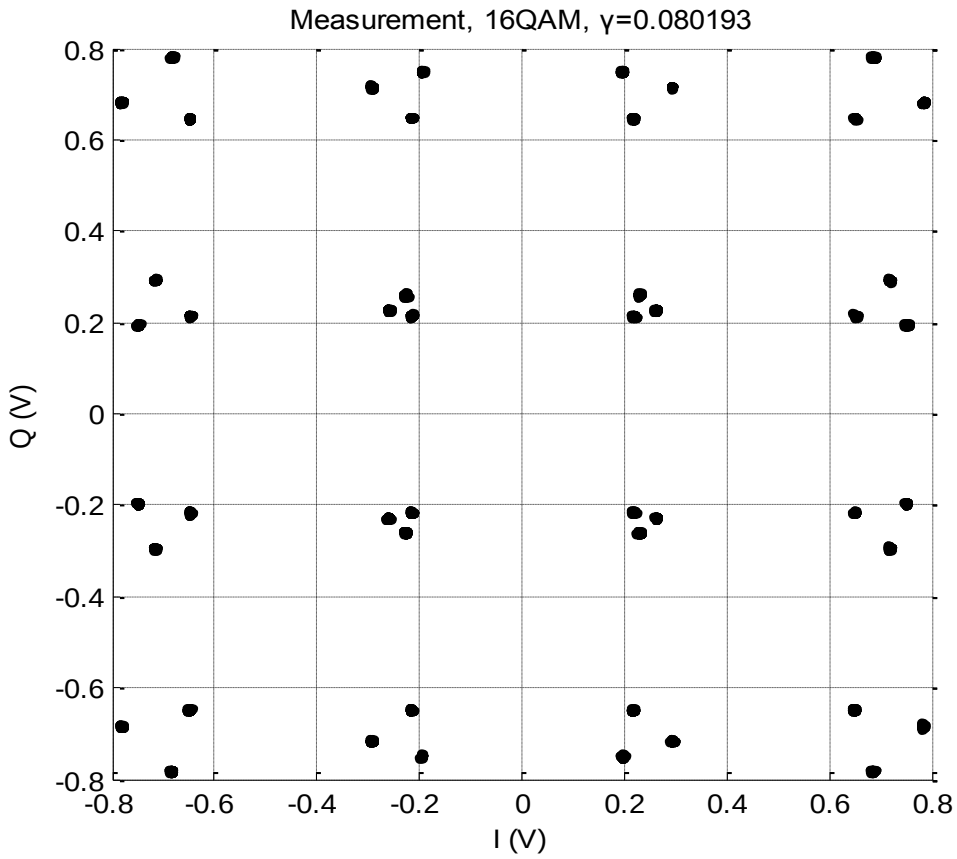


Fig 6: 16QAM, the VSA demodulation vector pattern for the digital modulated signals with set errors;

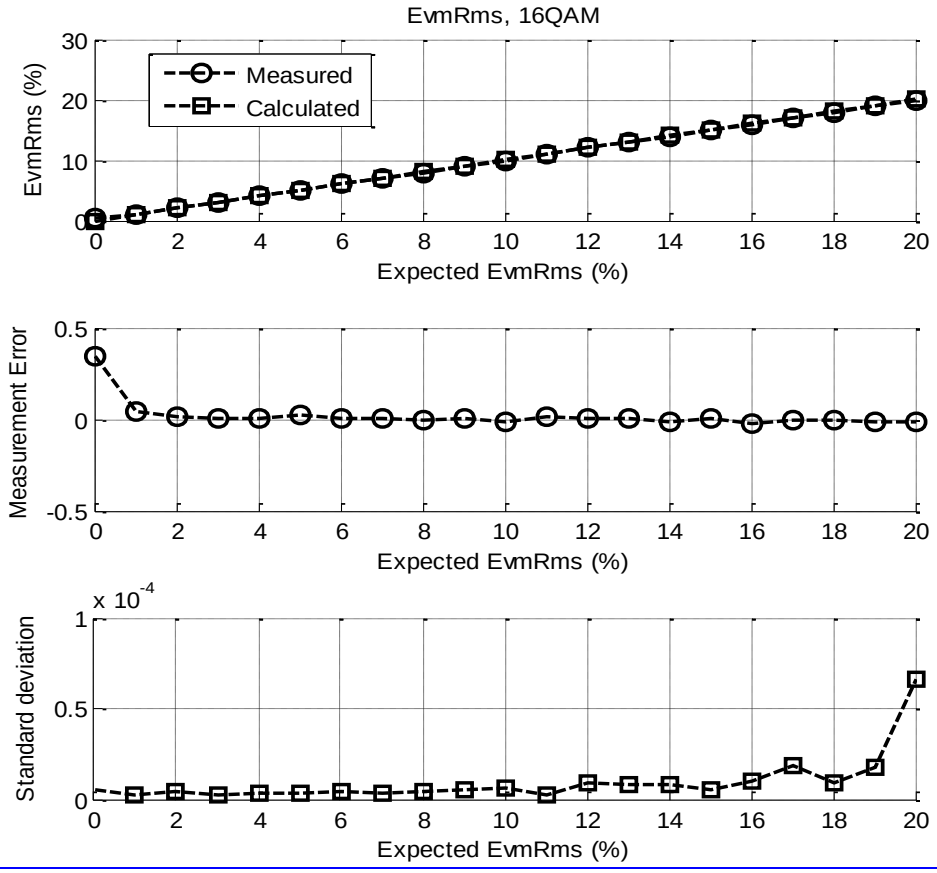


Fig. 7 The relationship of the expected EvmRms for 16QAM and our testing results. The upper figure shows MagErrRms; the middle figure shows the differences of measured and calculated MagErrRms, in terms of measurement error; the lower figure shows the standard deviation of the testing results with a value reading interval of 0.1 second.

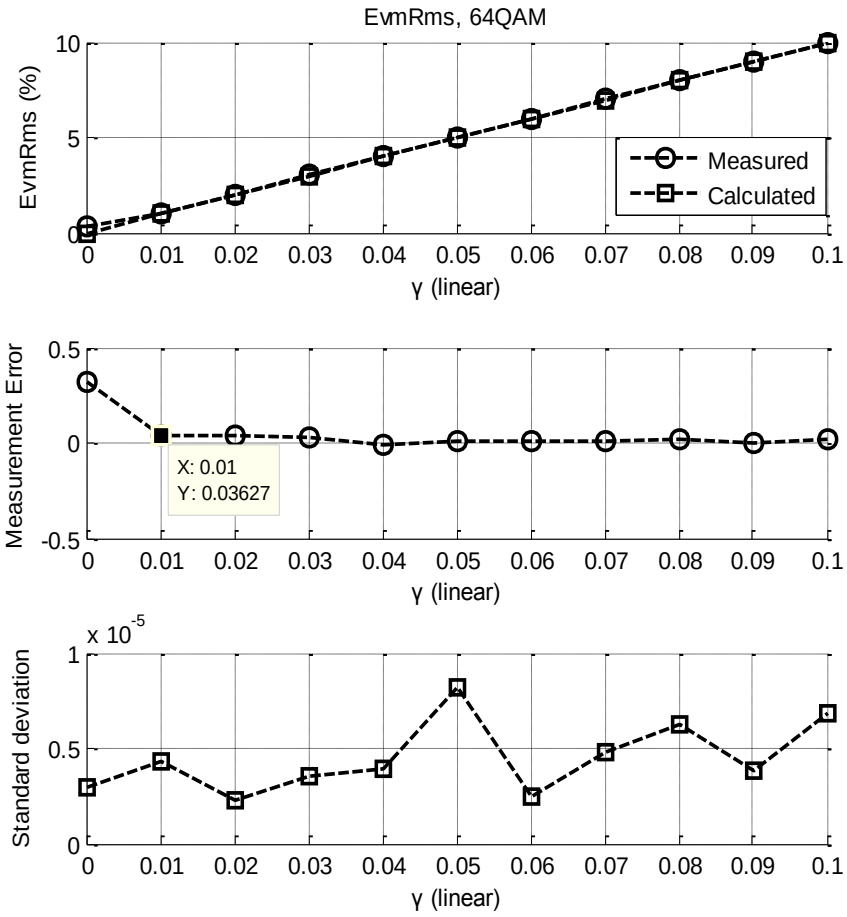


Fig. 8 The relationship of the equilateral triangle radius γ and our testing results in the error setting model for 64QAM. The upper figure shows MagErrRms; the middle figure shows the differences of measured and calculated MagErrRms, in terms of measurement error; the lower figure shows the standard deviation of the testing results with a value reading interval of 0.1 second.

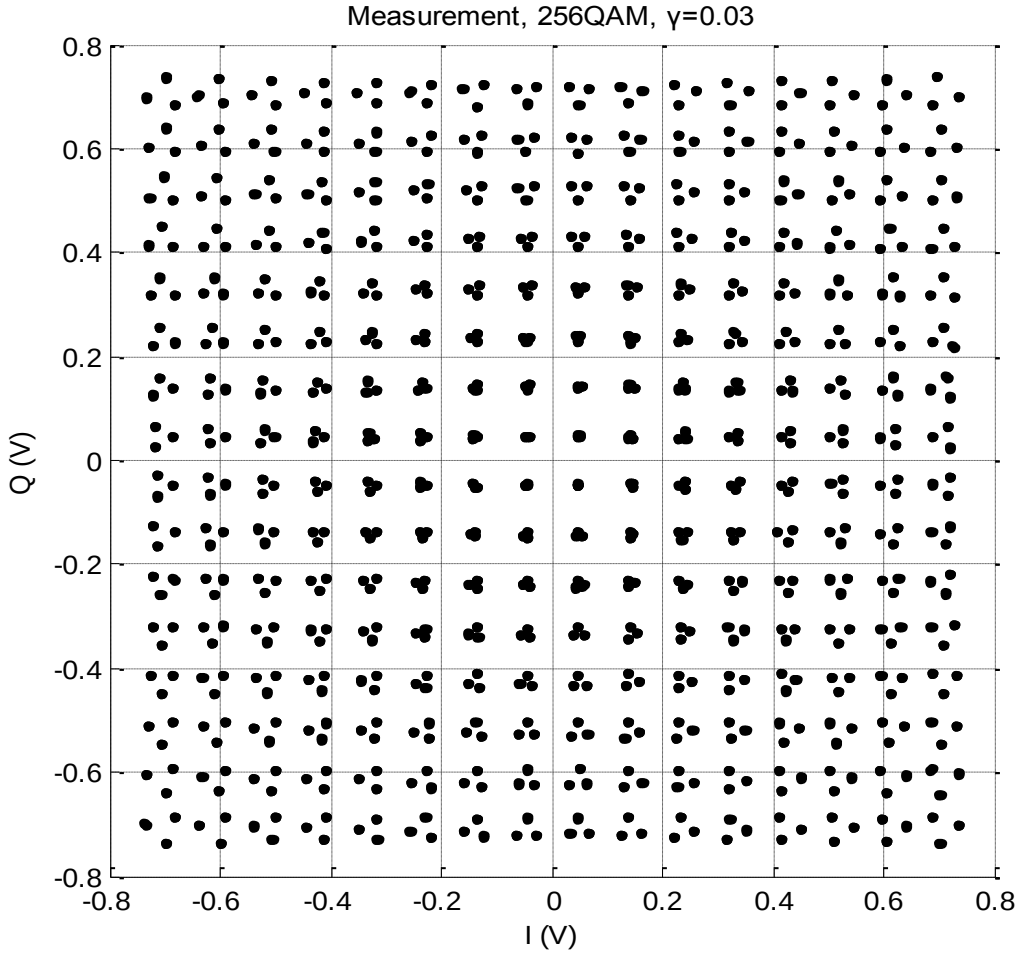


Fig. 9 Vector diagram of digital modulated signals with set standard errors, demodulated by VSA for 256QAM.

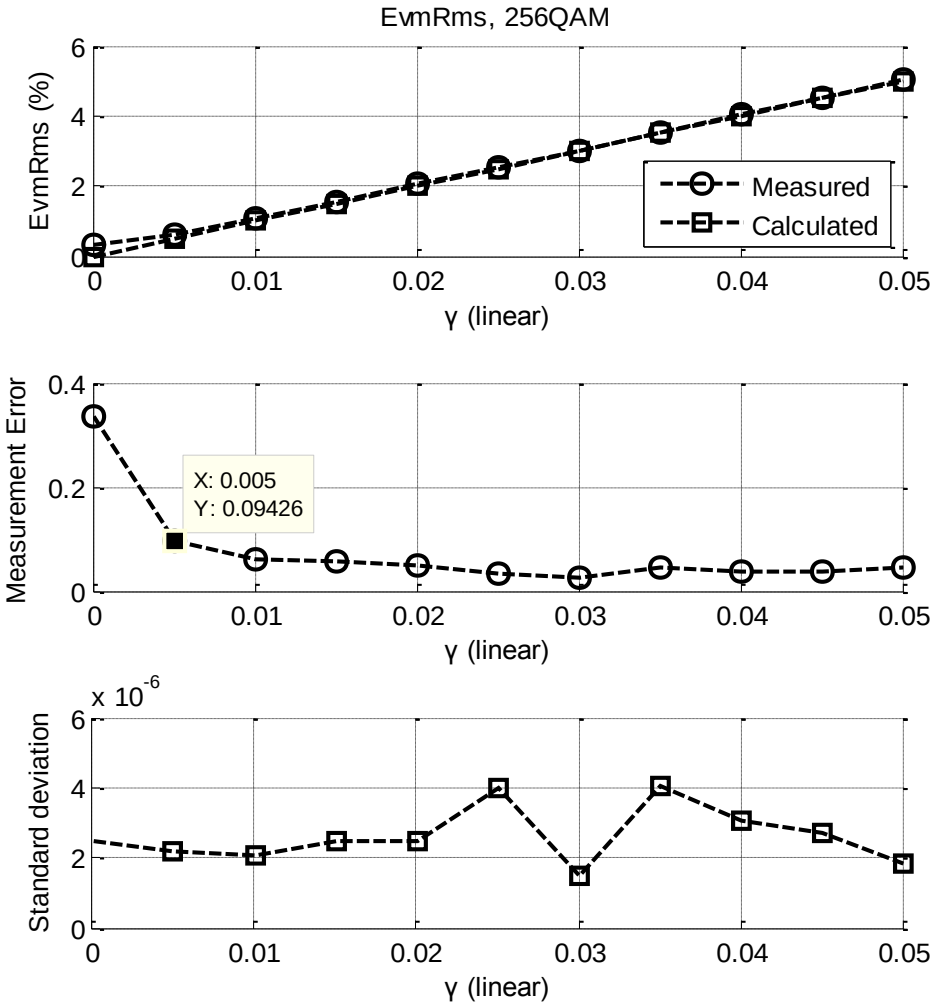


Fig. 10 The relationship of the equilateral triangle radius γ and our testing results in the error setting model for 256QAM. The upper figure shows EvmRms; the middle figure shows the differences of measured and calculated EvmRms, in terms of measurement error; the lower figure shows the standard deviation of the testing results with a value reading interval of 0.1 second.

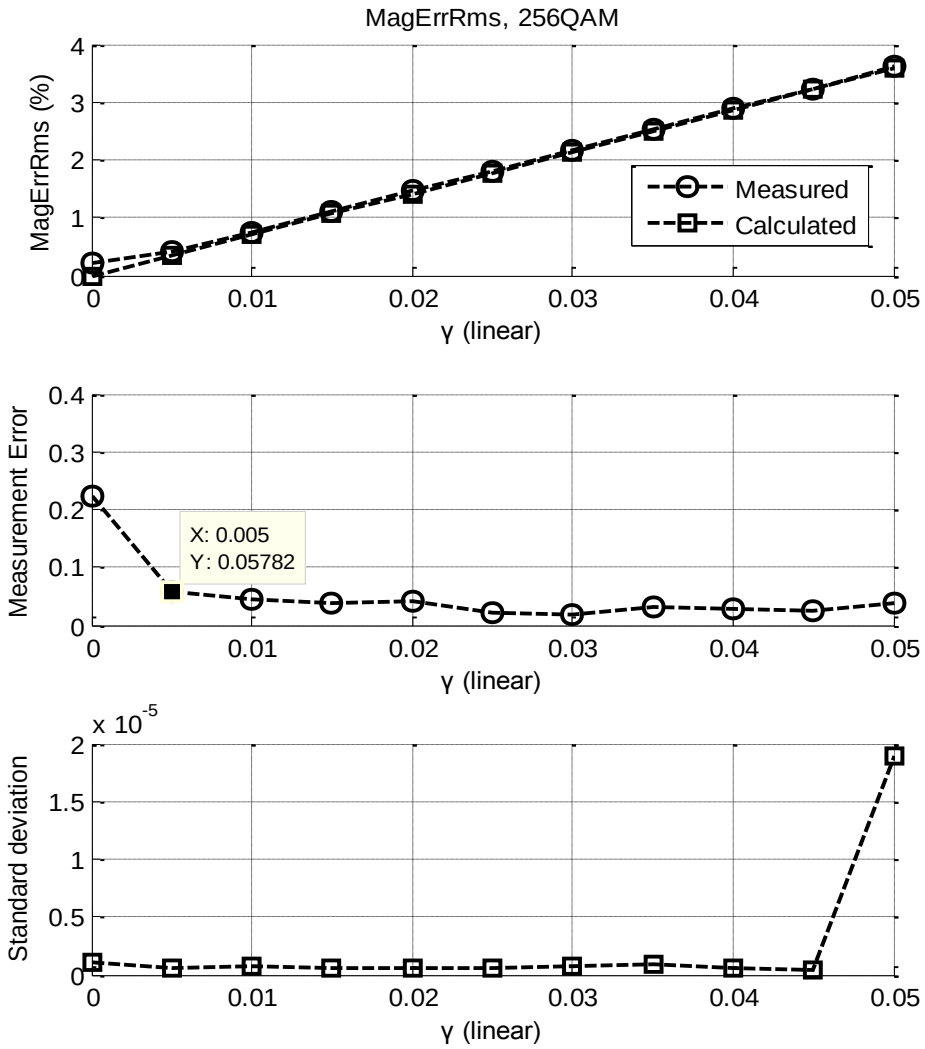


Fig. 11 The relationship of the equilateral triangle radius γ and our testing results in the error setting model for 256QAM. The upper figure shows MagErrRms; the middle figure shows the differences of measured and calculated MagErrRms, in terms of measurement error; the lower figure shows the standard deviation of the testing results with a value reading interval of 0.1 second.

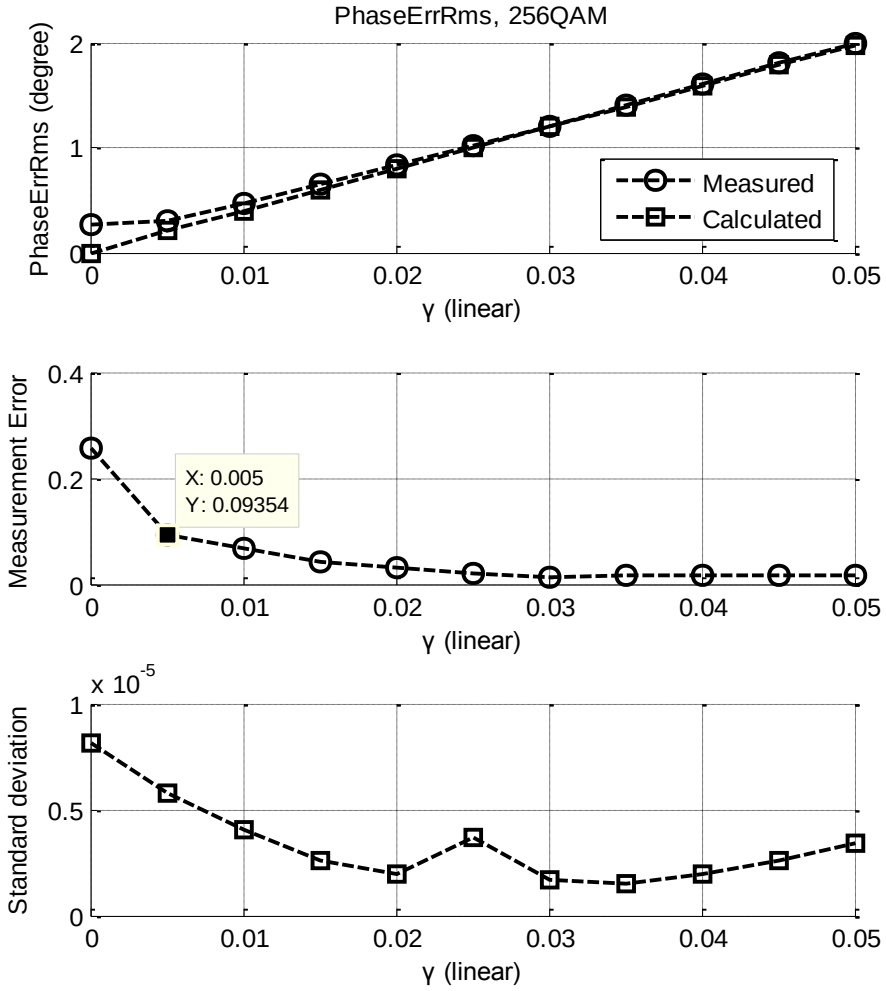


Fig. 12 The relationship of the equilateral triangle radius γ and our testing results in the error setting model for 256QAM. The upper figure shows PhaseErrRms; the middle figure shows the differences of measured and calculated PhaseErrRms, in terms of measurement error; the lower figure shows the standard deviation of the testing results with a value reading interval of 0.1 second.

# 4.CONCLUSIONS

The techniques in this paper realized the continuous adjustability of digital modulated error setting values in a large range, and gave the settings of expected error parameters, which solves the problems expressed in the introduction. Performance of the metrology standard include: the consistency of the measured value and calculated value for such digital-modulated parameters as EVM, and the repeatability on the values of digital modulated parameters. The standard deviations of EvmRms and MagErrRms have achieved the level of $10^{-5}$ %, while the standard deviation of PhaseErrRms has also reduced to a degree of $10^{-5}$. This metrology method and system for digital modulated error parameters is applicable to almost all known digital modulation scheme, such as 256QAM or higher rank modulation scheme.

ACKNOWLEDGMENT

The author wishes to thank the support of National Natural Science Foundation of China (No.61271120/F010508) for the work.

REFERENCES

[1] Michael D. McKinley, Kate A. Remley,etc. EVM Calculation for Broadband Modulated Signals. ARFTG Microwave Measurements Conference, Fall 2004. 64th, 2-3 Dec. 2004: 45 -52

[2] 3GPP TS 36．104 v8.6．0-2009．Base Station(BS)radio transmission and reception[S].2009.

[3] D. A. Humphreys, M. R. Harper, and M. Salter, “Traceable calibration of Vector Signal Analyzers,” ARFTG 75th Conf., pp 1-4, May 2010.

[4] Zhang Rui, Zhou Feng, Guo Long-qing, Wang Nan. Metrology of vector modulation error: problems and solution[C], 27th conference on precision electromagnetic measurement.p718, June 2010, Daejeon, Korean

[5] Zhou Feng, Zhang Rui, Sun Jing-lu, Shen Yuan-mao, Shi Dan, GaoYou-gang, Yin Yan. Technology for Calibrating Vector Signal Analyzer in Aspect of FSK Demodulation Error [C], IEEE 81th ARFTG Measurements Conference Digest, pp74-84. Seattle, Washington (WA) , USA, June 02-07, 2013

[6] ZHOU Feng, ZHANG Rui, etc. The metrology method and system for digital demodulation error parameter based on waveform design (Chinese patent)[P]. 201310499303.1. October 2013

[7] ZHOU Feng, ZHANG Rui, etc. Method for measuring digital demodulation error parameters based on amplitude modulation or phase modulation process and system thereof[P]. PCT patent： PCT/CN2009/075136，2009.12

[8] Martin Hudlicka. Laboratory System for a Traceable Measurement of Error Vector Magnitude[C]. Proceedings of the 39th European Microwave Conference.29 September-1 October 2009, Rome, Italy.pp.934-937

[9] David A. Humphreys and James Miall. Traceable Measurement of Source and Receiver EVM Using a Real-Time Oscilloscope[J]. IEEE TRANSACTIONS ON INSTRUMENTATION AND MEASUREMENT, VOL. 62, NO. 6, pp1413-1426.JUNE 2013

# Analyzing and Improvement of the Thermopile Output Signal Noise Ratio of a Calorimeter

Yong Li, Xiaohai Cui, Xiaoxun Gao and Weijie Sun

National Institute of Metrology of China

cuixh@nim.ac.cn

***Abstract* — At present, thermoelectric technique is a popular method to setup national RF power standards. From the measurement, the Lab's temperature stability has strong affected the thermopile's output voltage. In this paper, the reason of the influence to calorimeter's measurement from Lab's temperature change is analyzed. We use the Average Temperature Block (ATB) to eliminate the affection. The measurement results of before and after ATB used is presented.**

***Index Terms* — Calorimeter, thermoelectric, microwave power, Average Temperature Block.**

## I. INTRODUCTION

At present, calorimeter is the common technique to build national RF power standards among the NMIs. The thermistor mount calibrated in calorimeter is the most accurate and stable transfer standard than other instruments. Use RF power terminator in calorimeter is another choice when thermistor mount is not available.

Thermopile is commonly used in calorimeters to monitor the dissipated RF power in the calorimeter but not be DC substituted by power meter. Thermopile is a device inserting between the DUT and thermal reference, it can convert the temperature deviation of its two sides to voltage.

Because the temperature deviation between DUT and reference is only about hundreds micro-degrees, most thermopile output is less than 1 milli-volt. To improve the signal noise ratio, the calorimeter is put in temperature controlled equipment, such as constant temperature water bath which its stability can reach 800 micro-degrees per day. The Lab's temperature stability should be better than 1 degree per day.

Even so, the short term rapid changes of temperature in laboratory less than one degree Celsius, but still have big influence to the thermopile output.

The calorimeter of NIM (National Institute of Metrology) is put into a commercial temperature controlled water bath tank. From fig.1, the laboratory temperature waved in 24 hours is less than 0.8 degree Celsius. Its change comes from the air condition's temperature adjustment.

From fig.2, the thermopile output of calorimeter affected by Lab's wave is about 5% of the input RF power to the calorimeter that will result in about 0.5%-2% deviation of the effective efficiency of the thermistor mount. So, the room's temperature change will affect the repeatability of the measurement and large the uncertainty of the final results.

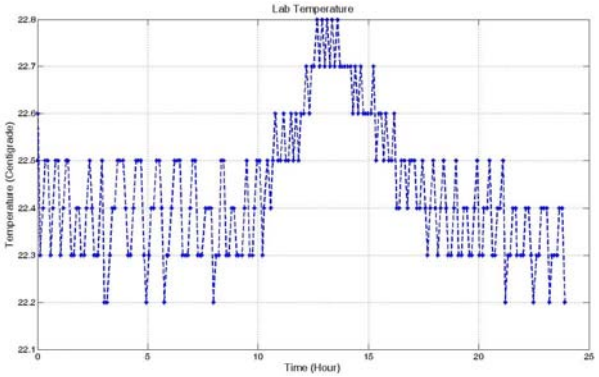


Fig. 1. Laboratory temperature change during 24 hours

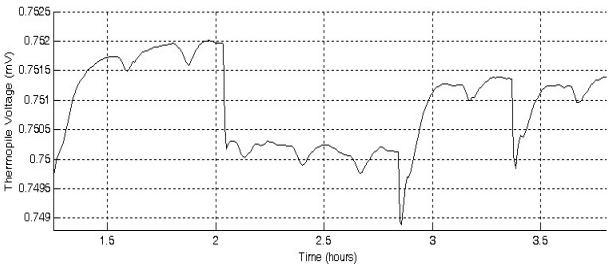


Fig. 2. Thermopile output of a WR-15 microcalorimeter

We tried to adjust the parameters of the Bath settings (such as cooling power, proportional band), but it was not enhance of the results obviously. We also sealed all the cables (DC cables, RF cables) and connectors outside of the calorimeter with cotton and foam, the big ripples still exist.

978-1-4799-4423-1/14/$31.00 ©2014 IEEE

## II. Analysis and Resolution

In order to decrease the influence of the ambient temperature to the thermopile, we analyzed the thermal conduction paths of the system. Because the leads connecting the thermopile and nano-voltmeter are directly influenced by the Lab temperature change, it should be the most sensitive section of the system. Fig.3 is the equivalent circuit of the thermopile's thermal path. $I_{TM}$ and $I_{TR}$ are the heat sources, representing the DUT and reference respectively. In theory, $I_{TR}$ is zero because it is the thermal reference. $r_1$ and $r_2$ are the thermal resistances between thermopile and DUT, dummy respectively. $r_3$ and $r_4$ are the lead's thermal resistances between thermopile and nano-voltmeter. The nano-voltmeter is a thermal source which obviously changed by the ambient temperature, so the thermopile output is added a noise signal as fig.1 shown.

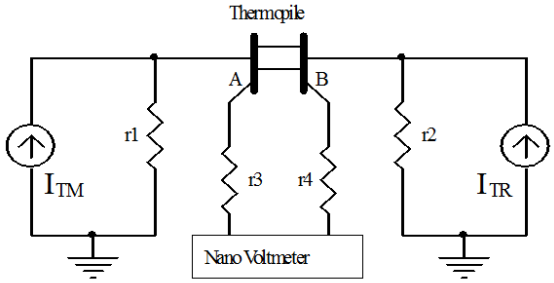


Fig.3. Equivalent Circuit of the calorimeter's thermal path

Because part of the leads connecting thermopile and digital voltage meter is put in the temperature controlled tank, the other part is exposed at outside of tank; room's temperature wave will directly affect thermopile by leads. That result in the output of thermopile unstable, equivalent circuit of the calorimeter's thermal path is shown as fig.3.

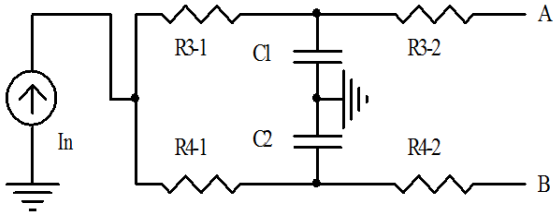


Fig.4. the Equivalent Circuit of the Average Temperature Block

To eliminate the influence from leads, we insert a copper block (Average Temperature Block) connect to the thermopile leads to average the temperature wave, shown as fig. 5. The Average Temperature Block was tightly attached to reference plate of calorimeter. The principle of the thermal conduction is shown as fig. 4. $I_n$ is the thermal noise from Lab, $C_1$ and $C_2$ are two Average Temperature Blocks, then $R_{3-1}$ and $C_1$ form a low-pass-filter which filtering the thermal noise. $R_{4-1}$ and $C_2$ form another low-pass-filter which has the similar function.

Fig.5 is a picture of a calorimeter with Average Temperature Block.

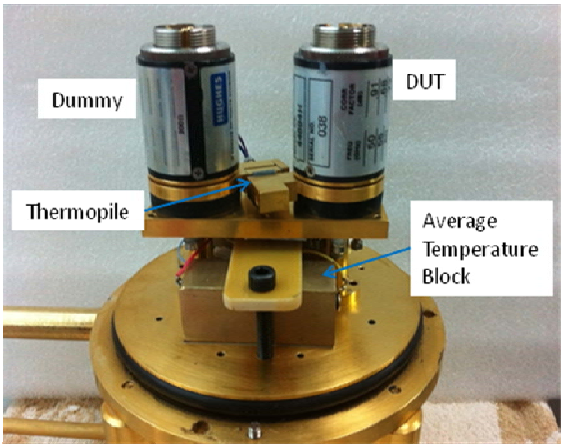


Fig. 5. WR22 (33-50GHz) calorimeter

## IV. Measurement and Results

Fig.6 shows the thermopile output of calorimeter when added the average temperature Block. The stability of the curve is obviously improved. The repeatability of effective efficiency of the thermistor mount is about 0.2%-0.3%, which is much better than before.

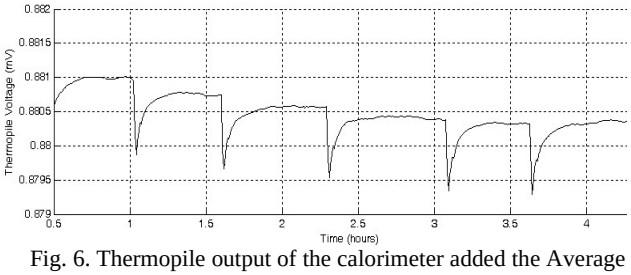


Fig. 6. Thermopile output of the calorimeter added the Average Temperature Block

## References


[1] T.P. Crowley, Xiaohai Cui, "Design and Evaluation of a WR-15(50 to 75 GHz) Microcalorimeter. CPEM 2008 Conference, June 2008

[2] J. Wayde Allen, Fred R. Clague, Neil T. Larsen, and Manly P. Weidman, "NIST Microwave Power Standards in Waveguide", NIST Technical Note 1511, Feb.1999.

[3] Xiaohai Cui and T.P. Crowley, "comparison of Experimental Techniques for Evaluating the Correction Factor of a Rectangular Waveguide Microcalorimeter" IEEE Transactions on Instrumentation and Measurement, v 60, n 7, p 2690-2695, July 2011.

# Further Investigations into Connection Repeatability of Waveguide Devices at Frequencies from 750 GHz to 1.1 THz

N M Ridler[1] and R G Clarke[2]

[1]National Physical Laboratory, UK, nick.ridler@npl.co.uk

[2]University of Leeds, UK, r.g.clarke@leeds.ac.uk

***Abstract*—This paper describes some further investigations into the connection repeatability for waveguide devices in the WM-250 (WR-01) waveguide size over the recommended frequency range of 750 GHz to 1.1 THz. This work follows previous work on this subject that was presented at the 82nd ARFTG conference in November 2013. As with the earlier investigation, three devices have been investigated – an offset short-circuit, a flush short-circuit, and a near-matched load. These devices can be used as calibration standards for Vector Network Analyzers (VNAs), and so can be found in VNA calibration kits. On this occasion, the aperture of each device was inverted (i.e. rotated through 180º) between the repeated disconnection and re-connection of the device to the VNA test port. This provides an experimental evaluation of the effect of the imperfect position of the device's flange alignment pins and holes. As before, the repeatability of the measurements is assessed using statistical techniques, in terms of the experimental standard deviation in both the real and imaginary components of the complex-valued linear reflection coefficient. The results obtained during this investigation are compared with the results obtained from the previous investigation (where flange inversion was not included as part of the disconnection and re-connection procedure for the devices).**

***Index Terms*—Measurement repeatability, Measurement standards, VNA calibration, Submillimeter-wave measurements, Measurement uncertainty**

## 1. INTRODUCTION

Vector Network Analyzers (VNAs) that can operate at high millimeter-wave and submillimeter-wave frequencies (i.e. 110 GHz to 1.1 THz) are now readily available as commercial systems. These VNAs use rectangular metallic waveguide as the test ports [1]. The dimensions of the waveguide apertures are very small at these frequencies – e.g. the nominal aperture dimensions for WM-250 waveguide (which operates from 750 GHz to 1.1 THz) is 250 μm × 125 μm [2]. Accurate alignment of the waveguide becomes critical at these frequencies in order to achieve electrical measurements that have an acceptable degree of reliability and repeatability. The inevitable misalignment of the waveguide (due to the imperfect waveguide flange/interface) induces both random and systematic errors into the electrical measurements. For example, random errors will be caused by the dimensional tolerances on the flange alignment mechanisms (i.e. the diameters of the dowel pins and holes). These dimensional tolerances will give rise to a lack of repeatability in the measurements. Systematic errors will be caused by the imperfect position, on the flange face, of the flange alignment mechanisms (i.e. the dowel pins and holes). These systematic errors will be present in all connections that are made for a given device and will typically be of a similar size (when connected to the same VNA test port).

An earlier connection repeatability exercise in WM-250 waveguide (reported in [3]), concentrated on assessing the random errors caused primarily by the dimensional tolerances on the flange alignment mechanisms (i.e. the diameters of the dowel pins and holes). The earlier investigation did not consider the systematic errors caused by imperfect location of these flange alignment mechanisms. The connection repeatability exercise reported in this paper extends the work presented in [3] by considering both the random and the systematic errors affecting the waveguide measurements that are caused by flange alignment imperfections. This is achieved by including connections of the waveguide devices during the repeatability exercise where the flange is inverted before being reconnected to the VNA test port. By inverting the waveguide flange, the imperfect position of the alignment pins and holes will, in principle, cause a systematic change in the electrical measurements made by the VNA. This systematic change will be present in the repeatability data sets along with the random changes caused by the tolerances on the diameters of the alignment pins and holes.

As with the previous repeatability exercise [3], the exercise presented here uses selected devices in the WM-250 (WR-01) waveguide size, operating from 750 GHz to 1.1 THz. These were the same devices that were used for the previous investigation – an offset short-circuit, a 'flush' short-circuit (i.e. a short-circuit containing no offset), and a low-reflecting (i.e. 'near-matched') load. Similar statistical analysis techniques to those used in the previous exercise are used here to enable meaningful comparisons to be made between the two repeatability exercises. Figure 1 shows a photograph of one of the flanges used during the investigation. The holes and pins used to align the flange are indicated in the photograph.

978-1-4799-4423-1/14/$31.00 ©2014 Crown

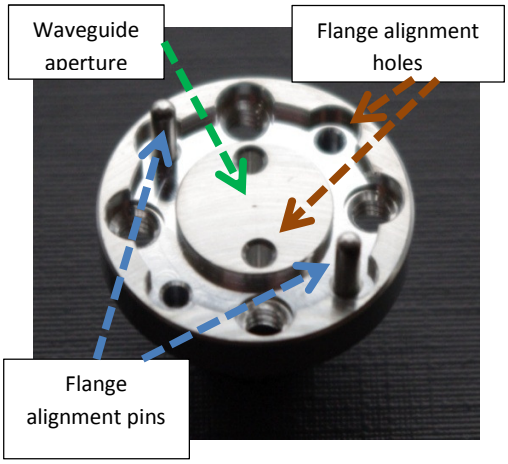


*Figure 1: One of the waveguide flanges used during the connection repeatability exercise. The rectangular waveguide aperture is 250 µm ×125 µm – barely visible to the naked eye*

## 2. METHOD

### 2.1 *Experimental Set-up*

The VNA system used for the investigation comprised an Agilent Technologies PNA-X VNA connected to WM-250 waveguide extender heads, manufactured by Virginia Diodes, Inc (VDI). This is the same system and set-up that was used for the previous repeatability investigation [3]. However, on this occasion, the extender head was arranged so that the waveguide test port pointed vertically upwards. This arrangement was chosen to minimize any effect due to gravity on the alignment of the waveguide flanges. As with the previous investigation, the power used to measure each Device Under Test (DUT) was around −35 dBm (0.3 µW) and the VNA's IF bandwidth was set to 30 Hz with no numerical averaging. This VNA system, shown in Figure 2, is situated in the Roger Pollard High Frequency Measurements Laboratory (this being a temperature-controlled laboratory) at the School of Electronic and Electrical Engineering, University of Leeds, UK. (Note: the vertical test port arrangement that was used for this investigation is not shown in this Figure.)

The VNA system was calibrated using a one-port 'three-known-loads' calibration technique. The 'known loads' (i.e. calibration standards) were an offset short-circuit, a 'flush' short-circuit and 'near-matched' load (from the VNA calibration kit). These same three standards were used subsequently as the DUTs for the repeatability investigation, these being the same DUTs that were used in [3].

For each flange connection orientation (i.e. either inverted or non-inverted), the complex-valued linear reflection coefficient of each DUT was measured 12 times, disconnecting and re-connecting the DUT between each re-measurement. This produced a set of 12 separate determinations of reflection coefficient for each DUT in each of the two orientations. Therefore, a total of 24 dis-connect / reconnect measurements were made for each of the three DUTs. All measurements were made from 750 GHz to 1.1 THz at regular intervals of 1.75 GHz across the band.

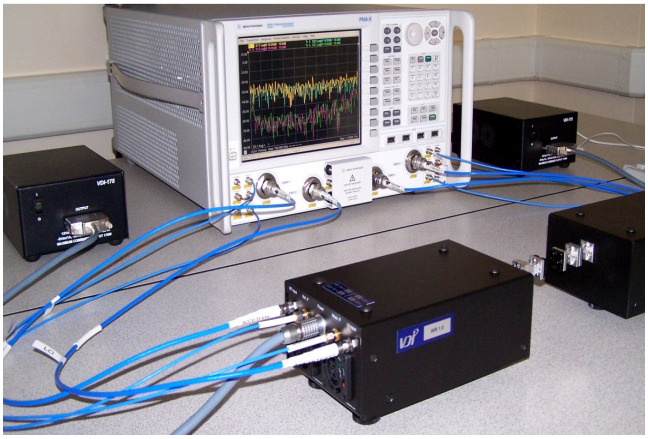

*Figure 2: The 750 GHz to 1.1 THz VNA system used for the measurements*

### 2.2 *Data Analysis*

The analysis uses calculations of the experimental standard deviation (as used previously in [3]) as the measure of variability in the observed values due to flange connection repeatability. This computation is applied separately to both the real and imaginary components of the complex-valued linear reflection coefficient. We avoid performing the analysis using the magnitude and phase components of the reflection coefficient due to problems with such calculations that have been described in [4].

Let $\Gamma$ be the complex-valued linear reflection coefficient written in terms of its real, $\Gamma_R$, and imaginary, $\Gamma_I$, components as follows (with $j^2 = -1$):

$$\Gamma = \Gamma_R + j\,\Gamma_I \tag{1}$$

For $n$ repeated determinations of $\Gamma$, the arithmetic mean of $\Gamma_R$ is given by:

$$\overline{\Gamma_R} = \frac{1}{n}\sum_{i=1}^{n}\Gamma_{R_i} \tag{2}$$

and the experimental variance is given by:

$$s^2(\Gamma_{R_i}) = \frac{1}{n-1}\sum_{k=1}^{n}(\Gamma_{R_k} - \overline{\Gamma_R})^2 \tag{3}$$

The experimental standard deviation, $s(\Gamma_{R_i})$, is equal to the positive square root of $s^2(\Gamma_{R_i})$.

Similarly, the arithmetic mean of $\Gamma_I$ is given by:

$$\overline{\Gamma}_I = \frac{1}{n}\sum_{i=1}^{n}\Gamma_{I_i} \tag{4}$$

and the experimental variance is given by:

$$s^2(\Gamma_{I_i}) = \frac{1}{n-1}\sum_{j=1}^{n}(\Gamma_{I_j} - \overline{\Gamma}_I)^2 \tag{5}$$

The experimental standard deviation, $s(\Gamma_{I_i})$, is equal to the positive square root of $s^2(\Gamma_{I_i})$.

For each DUT at each frequency, values of $s(\Gamma_{R_i})$ and $s(\Gamma_{I_i})$ are calculated for the following three situations:

(i) Using the 12 repeat measurements of the flange when connected in the non-inverted orientation. We use a superscript *N* to indicate this 'Non-inverted' situation – i.e. $\Gamma_R^N$ for the real component, and $\Gamma_I^N$ for the imaginary component;

(ii) Using the 12 repeat measurements of the flange when connected in the inverted orientation. We use a superscript *I* to indicate this 'Inverted' situation – i.e. $\Gamma_R^I$ for the real component, and $\Gamma_I^I$ for the imaginary component;

(iii) Using all 24 repeated measurements of the flange connected in both inverted and non-inverted orientations. We use a superscript *IN* to indicate this 'Inverted and Non-inverted' situation – i.e. $\Gamma_R^{IN}$ for the real component, and $\Gamma_I^{IN}$ for the imaginary component.

Since the experimental standard deviation is an *unbiased* statistical estimator, the calculated values of the experimental standard deviations for each real and imaginary component can be compared meaningfully with each other, independent of sample size, to see if the distributions for the three situations are consistent. So, we can compare the calculated values of the experimental standard deviations in the real component, $s(\Gamma_{R_i}^N)$, $s(\Gamma_{R_i}^I)$ and $s(\Gamma_{R_i}^{IN})$, and, we can compare the calculated values of the experimental standard deviations for the imaginary component $s(\Gamma_{I_i}^N)$, $s(\Gamma_{I_i}^I)$ and $s(\Gamma_{I_i}^{IN})$.

## 3. RESULTS

The results for each device – offset short-circuit, flush short-circuit and near-matched load – are presented as a pair of graphs showing:

(i) The calculated values of experimental standard deviations in the real component, $s(\Gamma_{R_i}^N)$, $s(\Gamma_{R_i}^I)$ and $s(\Gamma_{R_i}^{IN})$, as a function of frequency. Also shown are the experimental standard deviations obtained during the repeatability assessment in 2013 (from [3]).

(ii) The calculated values of experimental standard deviations for the imaginary component, $s(\Gamma_{I_i}^N)$, $s(\Gamma_{I_i}^I)$ and $s(\Gamma_{I_i}^{IN})$, as a function of frequency. Also shown are the experimental standard deviations obtained during the repeatability assessment in 2013 (from [3]).

Figures 3 and 4 show the results for the offset short-circuit; Figures 5 and 6 show the results for the flush short-circuit; and Figures 7 and 8 show the results for the near-matched load. Note that the vertical axes' sensitivies (i.e. scales) on these pairs of graphs differ: a full scale of 0.4 is used for the offset short-circuit graphs; a full scale of 0.2 is used for the flush short-circuit graphs; and, a full scale of 0.1 is used for the near-matched load graphs.

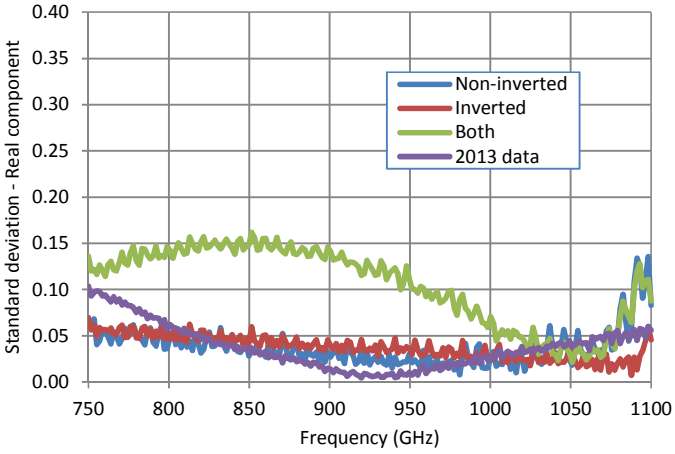


*Figure 3: $s(\Gamma_{R_i}^N)$, $s(\Gamma_{R_i}^I)$ and $s(\Gamma_{R_i}^{IN})$ for the offset short-circuit. Also shown are the results from 2013*

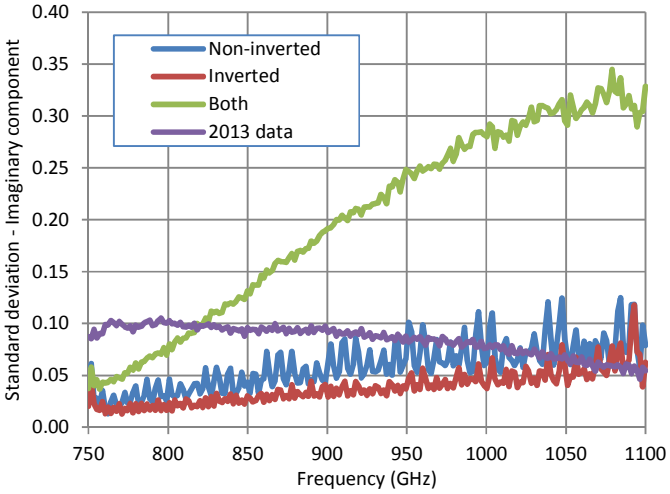


*Figure 4: $s(\Gamma_{I_i}^N)$, $s(\Gamma_{I_i}^I)$ and $s(\Gamma_{I_i}^{IN})$ for the offset short-circuit. Also shown are the results from 2013*

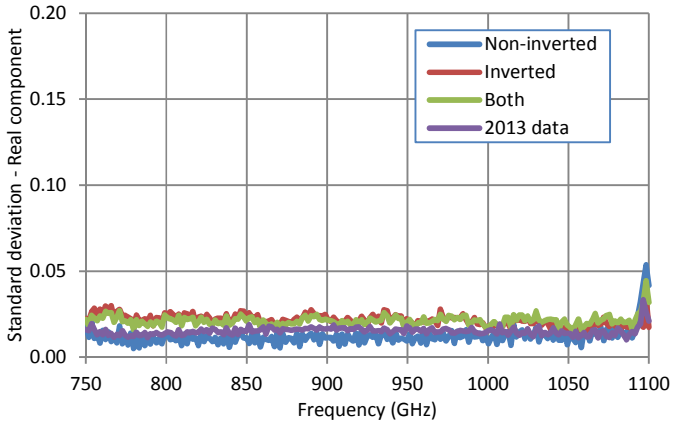


*Figure 5: $s(\Gamma_{R_i}^N)$, $s(\Gamma_{R_i}^I)$ and $s(\Gamma_{R_i}^{IN})$ for the flush short-circuit. Also shown are the results from 2013*

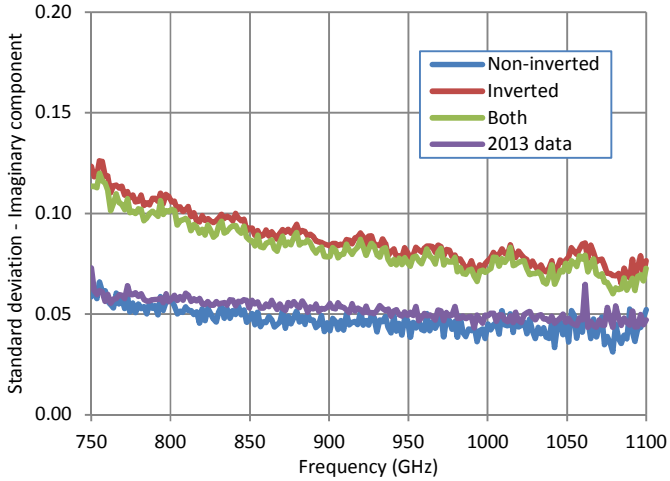


*Figure 6: $s(\Gamma_{I_i}^N)$, $s(\Gamma_{I_i}^I)$ and $s(\Gamma_{I_i}^{IN})$ for the flush short-circuit. Also shown are the results from 2013*

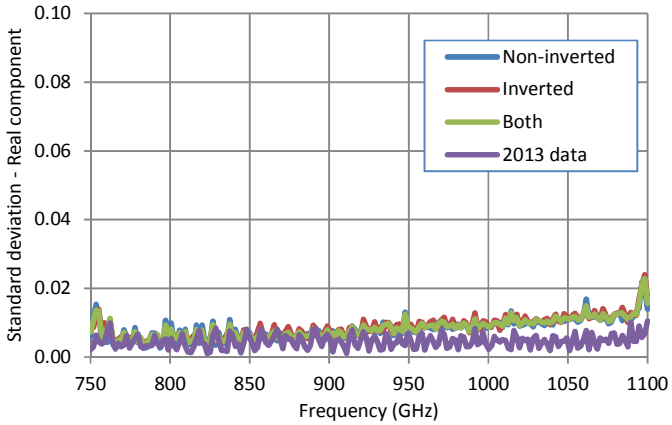


*Figure 7: $s(\Gamma_{R_i}^N)$, $s(\Gamma_{R_i}^I)$ and $s(\Gamma_{R_i}^{IN})$ for the near-matched load. Also shown are the results from 2013*

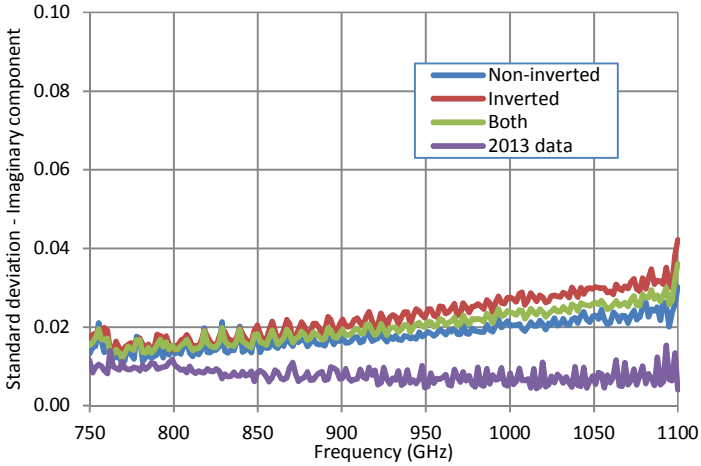


*Figure 8: $s(\Gamma_{I_i}^N)$, $s(\Gamma_{I_i}^I)$ and $s(\Gamma_{I_i}^{IN})$ for the near-matched load. Also shown are the results from 2013*

## 4. DISCUSSION

### 4.1 *Offset short-circuit*

By examining Figures 3 and 4, it is clear that, for both real and imaginary components, the experimental standard deviations for each flange connection orientation – i.e. non-inverted and inverted – are of a similar size (i.e. typically $\leq 0.10$ across the band). These standard deviation values are also of a similar size to the values obtained during the repeatability exercise in 2013. This indicates that the amount of connection variability in the two flange orientations is of similar size. This is to be expected, since we should only be observing variability due to the dimensional tolerances of the diameters of the flange alignment pins and holes.

However, Figures 3 and 4 also show that the experimental standard deviations obtained when the data from both flange orientations are analyzed together, are significantly larger (i.e. increasing to around 0.15 for the real component, and to around 0.35 for the imaginary component) than the standard deviations for each separate flange orientation – either non-inverted or inverted. This indicates that there is a significant systematic difference between the average values of the real and imaginary components of the repeatability data for each orientation. It is expected that such a systematic difference is caused by the imperfect positioning of the flange alignment pins and holes, and so the waveguide apertures of the DUT and the VNA test port will be misaligned by different amounts, depending on the orientation used for the connection of the DUT.

We can further examine this effect by calculating the averages (i.e. arithmetic means) of the repeated connections for each flange orientation – non-inverted and inverted. The arithmetic means for the real component of the repeated non-inverted and inverted flange connections ($\bar{\Gamma}_R^N$ and $\bar{\Gamma}_R^I$,

respectively) are shown in Figure 9. Similarly, the arithmetic means for the imaginary component of the repeated non-inverted and inverted flange connections ($\bar{\Gamma}_I^N$ and $\bar{\Gamma}_I^I$, respectively) are shown in Figure 10.

Figure 9 shows differences of up to 0.30 between the mean real components of the linear reflection coefficient for the two flange orientations, and Figure 10 shows differences of up to 0.66 between the mean imaginary components of the linear reflection coefficient for the two flange orientations. These are very large differences, especially when compared to the observed experimental standard deviations for the repeatability of each flange orientation (which are typically $\leq 0.10$, for both real and imaginary components, across the band).

4.2 *Flush short-circuit*

By examining Figures 5 and 6, it is clear that the experimental standard deviations for the imaginary component are significantly larger than the experimental standard deviations for the real component. This is consistent with the behavior observed during the repeatability exercise in 2013. In addition, the experimental standard deviations for inverted flange connection are larger than the experimental standard deviations for the non-inverted flange connection orientation. It is not clear why this should be, particularly as the flush short-circuit device is essentially just a flat sheet of metal and does not contain a waveguide aperture.

As with the offset short-circuit, we can calculate the arithmetic means for the real and imaginary components of the repeated non-inverted and inverted flange connections ($\bar{\Gamma}_R^N$ and $\bar{\Gamma}_R^I$, and $\bar{\Gamma}_I^N$ and $\bar{\Gamma}_I^I$, respectively). These are shown in Figures 11 and 12, respectively.

4.3 *Near-matched load*

By examining Figures 7 and 8, it is clear that the experimental standard deviations for both the real and imaginary component are of similar size (i.e. all values are less than 0.05). This is consistent with the behavior observed during the repeatability exercise in 2013. There is no clear difference between the experimental standard deviations for inverted flange connection and the non-inverted.

As with the offset and flush short-circuits, we can calculate the arithmetic means for the real and imaginary components of the repeated non-inverted and inverted flange connections ($\bar{\Gamma}_R^N$ and $\bar{\Gamma}_R^I$, and $\bar{\Gamma}_I^N$ and $\bar{\Gamma}_I^I$, respectively). These are shown in Figures 13 and 14, respectively. These Figures show that there is no significant difference between the mean real and the mean imaginary components of the linear reflection coefficient for the two flange orientations.

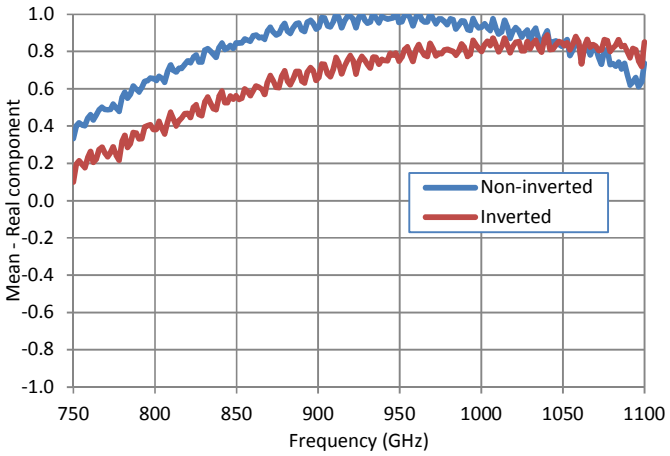


*Figure 9: $\bar{\Gamma}_R^N$ and $\bar{\Gamma}_R^I$ for the offset short-circuit*

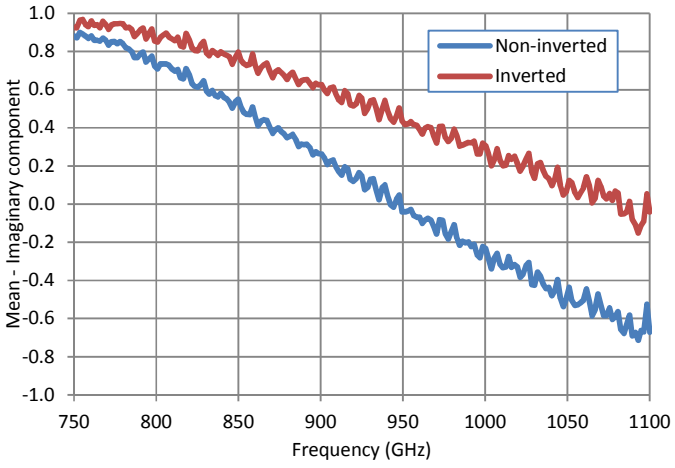


*Figure 10: $\bar{\Gamma}_I^N$ and $\bar{\Gamma}_I^I$ for the offset short-circuit*

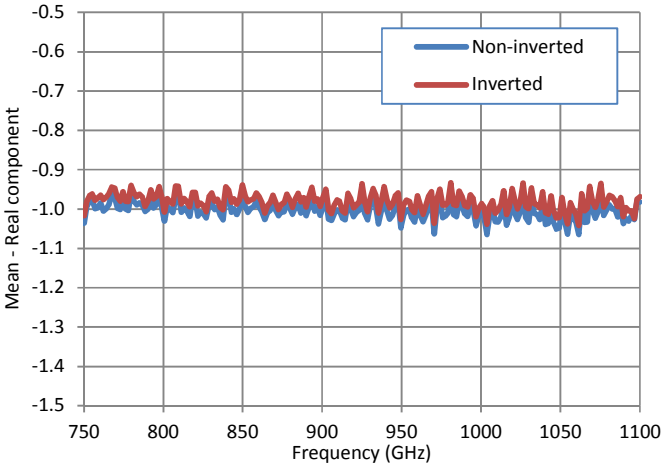


*Figure 11: $\bar{\Gamma}_R^N$ and $\bar{\Gamma}_R^I$ for the flush short-circuit*

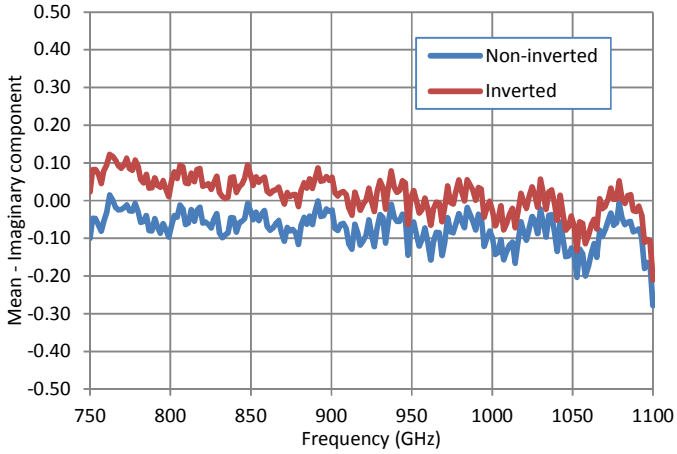


*Figure 12: $\bar{\Gamma}_I^N$ and $\bar{\Gamma}_I^I$ for the flush short-circuit*

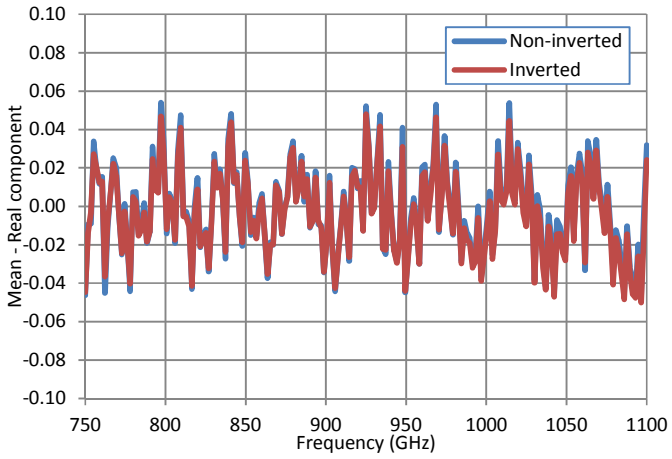


*Figure 13: $\bar{\Gamma}_R^N$ and $\bar{\Gamma}_R^I$ for the near-matched load*

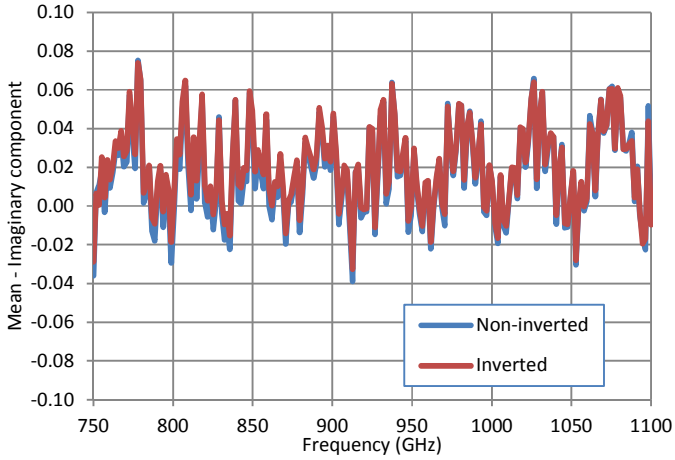


*Figure 14: $\bar{\Gamma}_I^N$ and $\bar{\Gamma}_I^I$ for the near-matched load*

## 5. SUMMARY OBSERVATIONS

We can further summarize the information for each device by recording the average observed standard deviation for each of the two flange orientations – inverted and non-inverted – for both real and imaginary components, shown in Figures 3 to 8, and compare these values with the average difference of the arithmetic means of the repeated connections for each flange orientation (shown in Figures 9 to 14), i.e. the average of $(\bar{\Gamma}_R^N - \bar{\Gamma}_R^I)$, and, the average of $(\bar{\Gamma}_I^N - \bar{\Gamma}_I^I)$. These summary values are shown in Table I (a), (b) and (c) for the offset short-circuit, flush short-circuit and near-matched load, respectively.

Table I (a) shows that, for both real and imaginary components, the average difference between the inverted and non-inverted connections for the offset short-circuit is much greater than the average standard deviations for both inverted and non-inverted connections. This suggests that, on this occasion, the errors due to the positional accuracy of the waveguide alignment pins and holes have a much greater impact on the electrical measurements compared with the errors due to the tolerance on the diameters of these alignment pins and holes.

Table I (b) shows that, for both real and imaginary components, the average difference between the inverted and non-inverted connections for the flush short-circuit is of a similar size to the average standard deviations for both the inverted and non-inverted connections. This suggests that, on this occasion, the errors due to the positional accuracy of the waveguide alignment pins and holes have a similar impact on the electrical measurements compared with the errors due to the tolerance on the diameters of these alignment pins and holes.

Table I (c) shows that, for both real and imaginary components, the average difference between the inverted and non-inverted connections for the near-matched load is significantly less than the average standard deviations for both the inverted and non-inverted connections. This suggests that, on this occasion, the errors due to the positional accuracy of the waveguide alignment pins and holes have less impact on the electrical measurements compared with the errors due to the tolerance on the diameters of these alignment pins and holes.

The information in Table I shows that dimensional errors in the waveguide flange alignment mechanisms generally have a different impact on the electrical measurements dependent on the type of device being measured. The indications are that high reflecting devices are more likely to be affected by the errors due to the positional accuracy of the waveguide alignment pins and holes; low reflecting devices are more likely to be affected by errors due to the tolerance on the diameters of these alignment pins and holes.

TABLE I

AVERAGE STANDARD DEVIATIONS, AND, AVERAGE DIFFERENCE BETWEEN MEANS OF INVERTED AND NON-INVERTED CONNECTIONS

(a) Offset short-circuit

| Component | Average standard deviation | | Average difference between inverted and non-inverted connections |
|---|---|---|---|
| | Non-inverted | Inverted | |
| Real | 0.020 | 0.013 | 0.187 |
| Imaginary | 0.059 | 0.038 | 0.380 |

(b) Flush short-circuit

| Component | Average standard deviation | | Average difference between inverted and non-inverted connections |
|---|---|---|---|
| | Non-inverted | Inverted | |
| Real | 0.012 | 0.021 | 0.023 |
| Imaginary | 0.047 | 0.088 | 0.090 |

(c) Near-matched load

| Component | Average standard deviation | | Average difference between inverted and non-inverted connections |
|---|---|---|---|
| | Non-inverted | Inverted | |
| Real | 0.008 | 0.009 | 0.003 |
| Imaginary | 0.018 | 0.023 | 0.003 |

## 6. CONCLUSIONS

This paper has presented results from a waveguide flange repeatability exercise in the WM-250 waveguide size at frequencies from 750 GHz to 1.1 THz. Three devices have been studied: an offset short-circuit; a flush short-circuit; and, a near-matched load. The primary focus with this repeatability exercise has been to evaluate the effect due to changing the orientation of the DUT's flange (i.e. by inverting the flange) between multiple disconnects and reconnects of the DUT. This is in contrast to the previous repeatability exercise [3] where this type of flange inversion was deliberately not included as part of the assessment procedure.

The results from the exercise have been analyzed by observing the variability in both the real and imaginary components of the complex-valued linear reflection coefficient. For both components, the results have been summarized in terms of observed experimental standard deviations. The analysis of the results has shown that, in general, it is important to take into account errors due to both the positional accuracy of the waveguide alignment pins and holes, and, the dimensional tolerances of the diameters of these pins and holes. The type of device being measured (e.g. whether it is high-reflecting or low-reflecting) can also have an impact on the size of the errors in the electrical measurements due to the imperfections in the flange alignment mechanisms.

These considerations need to be taken into account when evaluating the uncertainty in measurements made in this waveguide size, and similar waveguide sizes, used at these submillimeter-wave frequencies.

## ACKNOWLEDGEMENT

The work described in this paper was jointly funded by the European Metrology Research Programme (EMRP) Project SIB62 'HFCircuits', and, the National Measurement System Directorate of the UK government's Department for Business, Innovation and Skills. The EMRP is jointly funded by the EMRP participating countries within EURAMET and the European Union.

## REFERENCES

[1] J L Hesler, Y Duan, B Foley and T W Crowe, "THz Vector Network Analyzer Measurements and Calibration", 21st International Symposium on Space Terahertz Technology, Oxford, UK, April 2010.

[2] IEEE Std 1785.1-2012, "IEEE Standard for Rectangular Metallic Waveguides and Their Interfaces for Frequencies of 110 GHz and Above—Part 1: Frequency Bands and Waveguide Dimensions", March 2013.

[3] N M Ridler and R G Clarke, "Investigating Connection Repeatability of Waveguide Devices at Frequencies from 750 GHz to 1.1 THz", *Proc. 82nd ARFTG Microwave Measurement Conference*, Columbus, OH, USA, November 2013.

[4] N M Ridler and M J Salter, "Evaluating and expressing uncertainty in complex *S*-parameter measurements", *Proc. 56th ARFTG Microwave Measurement Conference,* Boulder, CO, USA, December 2000.

# An Improved Measurement Technique for Retrieval of Effective Constitutive Properties of Thin Dielectric/Magnetic and Metamaterial Samples

Himangshu Bhusan Baskey, M. J. Akhtar

Department of Electrical Engineering, Indian Institute of Technology Kanpur, Kanpur (INDIA)

himanshudmsrde@gmail.com, mjakhtar@iitk.ac.in

**Abstract— An improved partially filled waveguide based technique for the simultaneous measurement of complex permittivity and permeability of thin dielectric-magnetic and metamaterial samples is presented. The proposed approach requires placing a test specimen longitudinally at the centre of a rectangular waveguide cross section for the measurement of scattering coefficient in the specified frequency band. The constitutive properties of the specimen are determined in terms of the measured scattering coefficients using the newly derived expressions, which are based on the solution of the corresponding transcendental equation. The proposed approach is validated by measuring the permittivity and permeability of few standard samples, and comparing the results with the data available in literature. The overall procedure is non-iterative, which makes it quite versatile, and envisages the possibility of even online monitoring of certain parameters.**

**Index Terms — Constitutive properties, dielectric and magnetic properties, dielectric measurements, rectangular waveguides.**

## I. Introduction

The determination of permittivity and permeability of materials is an important aspect for the design and fabrication of a number of microwave devices and circuits. It has got immense applications in all fields of science and engineering such as the microwave material processing, bioengineering and the concrete industry [1]. The electromagnetic characterization of various type of conventional and artificial dielectrics e.g. metamaterials, becomes quite important for applications such as in the radome design, the radar cross section (RCS) reduction, the microwave imaging etc. The electromagnetic characterization of materials using the waveguide technique has certain advantages as compared to other technique such as ease of sample preparation, wide band measurement etc. The conventional waveguide technique, however, requires its cross section to be completely filled with the test specimen [2-3], which becomes difficult under certain situations.

An alternative approach to overcome the afore-mentioned problems is by filling only partially the cross section of the waveguide [4-5]. The proposed method employs this approach by inserting the test sample longitudinally across the slot in the waveguide, and thereby measuring the reflection and transmission data to compute the propagation constant of the specimen. The constitutive properties of the test specimen are then obtained in terms of the measured propagation constant by solving the simplified wave equation using the transverse resonance technique [5]. The proposed approach is validated using the measurement of material properties of standard samples, and comparing the results with other methods available in the literature.

## II. Theory Of The Proposed Technique

The basic configuration of the proposed approach is shown in Fig.1, which consists of a rectangular waveguide having a slot at the center. The test specimen having length '*l*' and

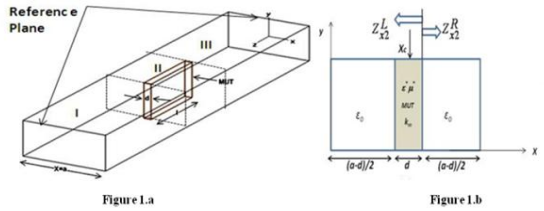


Fig.1. (a) Schematic of the partially filled waveguide (PFWG) structure (b) Cross section of the PFWG setup

thickness *'d'* is placed at the centre of the waveguide in order to make the structure symmetrical. The wave propagation in the case of partially filled waveguide arrangement shown in Fig. 1 can be assumed to be of *TE-to-x* and *TM-to-x* type usually known as hybrid modes consisting of the $LSE_x$ mode characterized by $E_x=0$, and the $LSM_x$ mode characterized by $H_x=0$ [6]. The governing equations which relate the effective constitutive properties with the measured scattering coefficients in case of partially filled waveguide structures may be summarized as follows:

$$T \equiv e^{-\gamma d} = K \pm j\sqrt{K^2 - 1}\,; \quad K = \frac{(1 + S_{21}^2 - S_{11}^2)}{(2S_{21})} \qquad (1)$$

$$z = \pm\sqrt{\frac{(1+S_{11})^2 - S_{21}^2}{(1-S_{11})^2 - S_{21}^2}} \equiv f(k_{xo}, k_{xm}, n) \qquad (2)$$

$$\gamma^2 = k_{xm}^2 - k_0^2 \; n^2 \equiv k_{xo}^2 - k_0^2 \qquad (3) \qquad \varepsilon_r^* = \frac{n}{z}, \quad \mu_r^* = n\,z \qquad (4)$$

978-1-4799-4423-1/14/$31.00 ©2014 IEEE

where, $T$ is the local transmission coefficients, $k_0$ is the free space wave number, $d$ is the sample thickness, γ is the propagation constant, $k_{x0}$ and $k_{xm}$ are the $x$-directed wave numbers in the air and material region, respectively, and '$n$' is the refractive index of the test sample. The $S_{11}$ and $S_{21}$ in the above equations represent the measured reflection and transmission coefficients, respectively at the sample interface.

## III. Experimental Setup And Validation

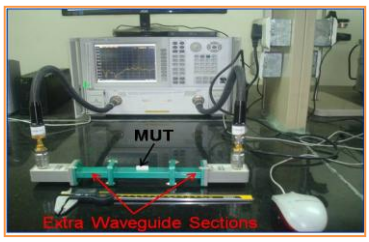


Fig. 2. Experimental arrangement for the E.M characterization

For validating the proposed approach, the scattering coefficients of few standard samples was carried out in the 'X' band using the experimental setup as shown in Fig. 2 using the calibrated VNA. The permittivity and the loss tangent values were calculated using the proposed technique, and the data were compared with other reference method [4] as shown in Fig. 3.

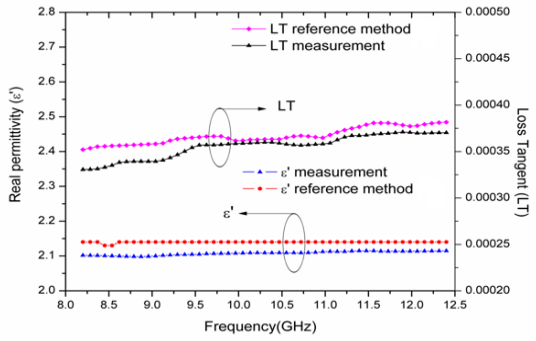


Fig.3. Comparison of the real permittivity and loss tangent of teflon using proposed approach and other reference method [4]

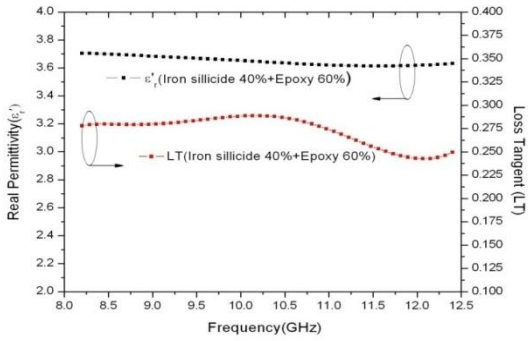


Fig.4. Measured real permittivity and loss tangent of carbonyl-iron epoxy composite

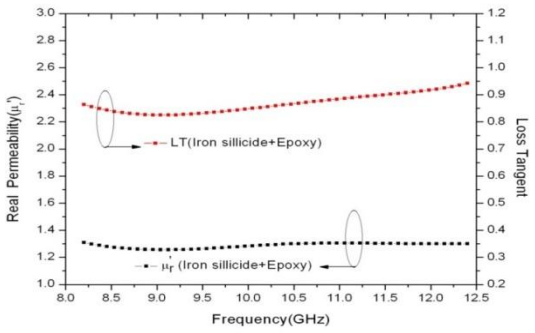


Fig.5. Measured real permeability and loss tangent of carbonyl-iron epoxy composite

It can be clearly observed from the Fig. 3 that our proposed technique agrees quite well with the other method. After validating the proposed approach, a dielectric-magnetic composite sample (carbonyl iron-40%+epoxy-60%) was fabricated and characterized using our proposed technique. The retrieved results for permittivity, permeability and their loss tangent values are shown in Fig.4 and Fig.5, respectively.

## IV. E.M Simulation Of the Metamaterial Structure in a Partially Filled Waveguide

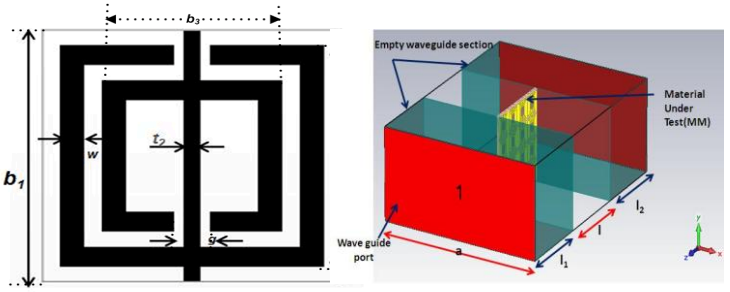


Fig. 6 a. Unit cell of the structure b. Meta material structure placed inside partially Filled Waveguide

In this section, our main aim is to verify the proposed approach for the metamaterials structure. For this purpose, we have used the standard SRR and the wire structures as a unit cell as shown in Fig. 6(a). The dimensions of the unit cell are $b_1$=2.5 mm, $b_2$=2.2 mm, $b_3$= 1.5 mm, $w$=g=0.3 mm, which is designed on the FR4 substrate (ε=4.4, loss tangent of 0.02) having thickness of 0.25 mm. The conductors are made of copper having thickness of 17 μm and electrical conductivity of $\sigma=5.8X10^7$ s/m. The copper strip of width $t_2$= 0.20 mm is printed at the opposite side of the FR-4 substrate. In order to simulate the structure in the partially filled X band waveguide, we have taken (8 X 4 unit cell) which are effectively placed inside the centre of the partially filled rectangular waveguide having dimensions $l_1$=40mm,$l_2$=40mm and $l$=20mm as shown in Fig. 6 (b).

The CST microwave Studio [7] is employed to simulate the 'S' parameters of the structure in the specified frequency band. The Simulated 'S' parameters and the retrieved permittivity and permeability of the structure over the

frequency region of 8.2-12.4 GHz are shown in the Fig. 7 and Fig.8 respectively.

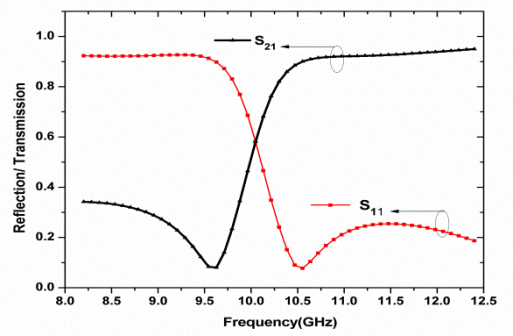


Fig.7. Simulated reflection and transmission coefficients of the metamaterial structure

Fig. 7 shows the reflection and transmission coefficients of the structure, where a dip of $S_{21}$ can be observed at 9.7 GHz which indicates the presence of the negative index band.

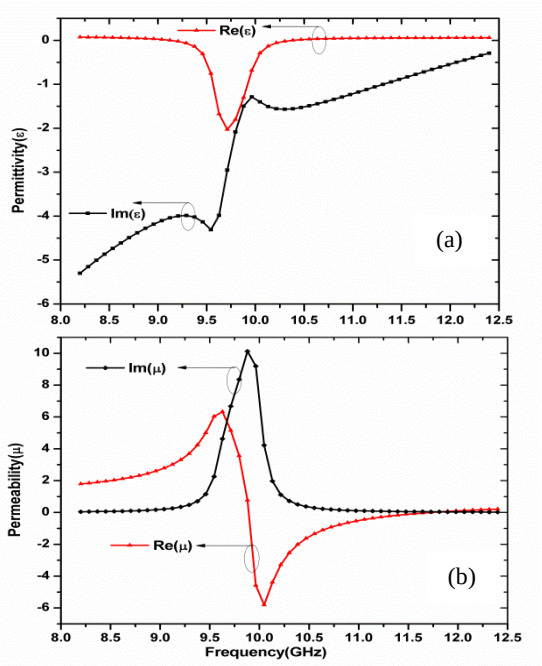


Fig. 8.Retrieved (a) complex permittivity (b) complex permeability of the metamaterial structure using proposed technique

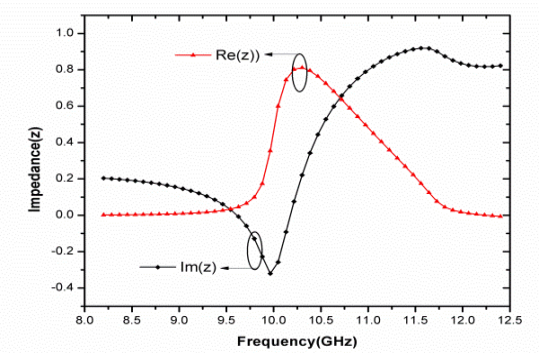


Fig.9. Retrieved complex impedance of the metamaterial structure using proposed technique

The retrieved sign of permittivity in Fig. 8 at the position of dip shows the anti-resonance, and the trends of permeability shows the resonance, which also conforms to the wave propagation in a passive medium. The retrieved value for the impedance is shown in Fig. 9, where the imaginary part of impedance having negative sign explains the negative index of refraction.

## V. Conclusion

A retrieval method has been proposed for extracting the permittivity and permeability of the conventional samples as well as the metamaterials using the partially filled waveguide. The proposed method is specially suited for thin smaples, and the the test specimen is not required to fill the complete aperature of the waveguide. The proposed approach has been validated using few standard samples, and the data have been compared with other reference methods. In this paper, our main concern was to measure the constitutive parameters of samples in the X band, but the overall method can be conveniently employed for other frequency regions in order to obtain the dielectric and magnetic properties of various types of materials.

## References


[1] L.F. Chen, C. K. Ong, C. P. Neo, V. V. Varadan, V.K. Varadan, *Microwave Electronics: Measurement and Materials Characterization*, John Wiley & Sons, West Sussex, England, 2004.

[2] A. M. Nicholson, G.F. Ross, "Measurement of the intrinsic properties of materials by time domain technique," *IEEE Trans. Instrum. Meas.*vol.19,pp. 377-382,1970.

[3] Abdel Hakim Boughriet, Legrand Christian, Alain Chapton, "Noniterative stable transmission/reflection method for low-loss material complex permittivity determination *IEEE Trans. Instrum. Meas.* Vol.45,pp. 52-57,1997.

[4] U. C. Hasar, "Accurate complex permittivity inversion from measurements of a sample partially filling a waveguide aperture," *IEEE Trans. Microw. Theory Tech.* vol.58. no. pp.451-457,2010.

[5] M.J.Akhtar, L.E Feher, M.Thumm, "A closed form solution for the reconstruction of permittivity of dielectric slabs placed at the center of a rectangular waveguide,"*IEEE Geosci.Remote Sens.Lett.*vol.4,pp.122 -126, 2007.

[6] C.A.Balanis, *Advanced Engineering Electromagnetics* John Wiley & Sons, New Jersey,N.J. 1989.

[7] CST-*Computer SimulationTechnology*,www.cst.com

# Using Electromagnetic Modeling to Evaluate Uncertainty in a Millimeter-wave Cross-guide Verification Standard

*Hui Huang[1,+] N M Ridler[2] and M J Salter[2]*

*[1]National Institute of Metrology, China; [2]National Physical Laboratory, UK;*

*[+]Visiting researcher - National Physical Laboratory, UK;*

**Abstract — This paper describes some investigations, made using electromagnetic modeling, into the uncertainty for a cross-guide verification standard of transmission loss for waveguide Vector Network Analyzers (VNAs) operating at millimeter-wave frequencies. The cross-guide is calculable and can be made traceable to the International System of units (SI) via precision dimensional measurements of the waveguide aperture and flange. The measurement errors due to dimensional tolerances of the cross-guide line (including waveguide aperture height, width, corner radii and waveguide line length) and the mechanical discontinuity between the cross-guide and the VNA test ports (including the connection angle) can be predicted from electromagnetic theory. The measurement uncertainty due to these errors can be calculated according to the Law of Propagation of Uncertainty. The paper describes these details, and compares experimental results, obtained using a VNA operating in the 140 GHz to 220 GHz band, with simulated values evaluated by electromagnetic modeling software.**

**Index Terms — Uncertainty, Traceability, Cross-guide, Transmission loss measurements, Verification standard, Electromagnetic modeling, Millimeter-wave measurements.**

## I. Introduction

In recent years, there has been a significant increase in the availability of millimeter-wave rectangular waveguide Vector Network Analyzers (VNAs). With this increase comes a need for verifying the performance of these VNAs at these operational frequencies. Traditionally, this has been done in waveguide at lower frequencies using VNA waveguide verification kits containing devices such as sections of precision waveguide (with close to zero reflection and transmission loss) and sections of reduced-height waveguide (with significant reflection and transmission loss). However, to further reduce the height of such waveguide becomes difficult to manufacture, and ensuring the accuracy is mechanically challenging in the extreme at high millimeter-wave frequencies. At the present time, NMIs do not provide attenuation standards at frequencies above 110 GHz, and the transmission loss is still not traceable to the SI. During 2013, a new form of 'calculable' device was introduced as a candidate for primary standards applications. This verification standard is simply a section of precision waveguide that is connected so that the waveguide aperture is at right-angles to the usual connection orientation of the waveguide. A diagram illustrating this connection strategy for the waveguide apertures is shown in Fig. 1. We call this type of device a 'cross-guide' standard [1]-[3].

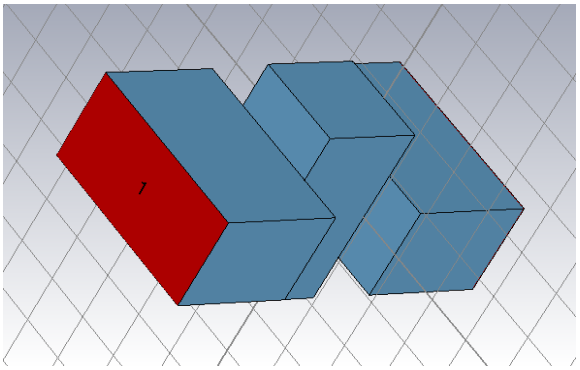

Fig. 1 Diagram to illustrate a section of cross-guide inserted between two conventionally-oriented waveguides [1] [3]

The performance of a cross-guide device as a verification standard is calculated from its waveguide aperture and flange sizes. Hence, it can be made traceable to the SI via precision dimensional measurements. This paper analyzes the impact on the measurement performance of the cross-guide device due to the imperfection in the interface between the cross-guide and the VNA test ports, including the tolerance of the aperture height and width, corner radii, line length and connection angle. These measurement errors are predicted from electromagnetic theory according to the values suggested in the IEEE std 1785.1-2012 standard [4], using electromagnetic simulation software – in particular, CST Microwave Studio [5]. The measurement uncertainty due to these errors is calculated according to the Law of Propagation of Uncertainty [6].

This paper presents experimental results obtained for a cross-guide line in the WR-05 waveguide size at frequencies from 140 GHz to 220 GHz, this being the conventional operating band for this waveguide size. These results are compared with the electrical performance predicted using electromagnetic modeling software.

## II. Dimensional Measurements on Cross-guide

Traceability for S-parameter measurements is established via precision dimensional measurements of the waveguide aperture and flange. The measurements of the cross-guide

978-1-4799-4423-1/14/$31.00 ©2014 IEEE

waveguide aperture size, e.g. width and height, are made using a coordinate measuring machine (CMM) with a 0.3 mm diameter ball tip micro-stylus. This process is used to characterize WR-05 line standards [7] [8]. The length of the cross-guide is measured by micrometer. The connection angle between the cross-guide and the VNA test ports is estimated based on the flange design. The nominal values for the aperture width and height are 1.295 mm and 0.647 5 mm. The measured values can be summarized in terms of the maximum observed deviation from the nominal dimensions of the cross-guide. The summary values are shown in TABLE I.

TABLE I
DIMENSIONAL MEASUREMENTS FOR CROSS-GUIDES

| Cross-guide Dimension | Results | Max Deviation |
|---|---|---|
| Width, $a$ | 1.295 mm | 13.8 μm |
| Height, $b$ | 0.6475 mm | 3.5 μm |
| Length, $l$ | 1.478 mm | 5 μm |
| Angle, $\Phi$ | 90° | 0.4° |

## III. ELECTROMAGNETIC SIMULATION OF CROSS-GUIDE

The electromagnetic characteristics of the cross-guide as a verification standard are calculated from its waveguide aperture and flange sizes. Hence, it can be traceable to the SI via precision dimensional measurements. These dimensions are: aperture height, width and corner radii, line length, and the mechanical discontinuity between the cross-guide and the VNA test ports due to the connection angle. For a cross-connected waveguide, the width and corner radii of the aperture are assumed to have no significant influence for transmission loss measurements and so are not included in the simulation. The other dimensions will affect the electromagnetic measurements. The summary tolerance values of the cross-guide are shown in TABLE II. In TABLE II, tolerances of height are suggested in the IEEE std 1785.1-2012 standard, tolerances of length are due to the likely dimensional measurements errors, and tolerances of angle are derived from the specification for a standard UG-387 waveguide flange.

TABLE II
TOLERANCES OF CROSS-GUIDE DIMENSIONS

| Par. | Tolerance in simulation | | | | |
|---|---|---|---|---|---|
| $b$ | ±2.6 μm | ±6.5 μm | ±13 μm | ±26 μm | |
| $l$ | ±1 μm | ±2 μm | ±3 μm | ±4 μm | ±5 μm |
| $\Phi$ | ±0.2° | ±0.4° | ±0.6° | ±0.8° | ±1.0° |

The transmission loss errors of cross-guide due to these dimensional errors are calculated from electromagnetic theory, using electromagnetic simulation software – in particular, CST Microwave Studio.

In Fig. 2, errors due to the tolerances of the cross-guide aperture height are shown, and values at selected frequencies are summarized in TABLE III. In Fig. 3, errors due to the tolerances of the cross-guide line length are shown, and values at selected frequencies are summarized in TABLE IV. In Fig. 4, errors due to the tolerances of the angle of connection are shown, and values at selected frequencies are summarized in TABLE V. From these simulation results, it can be seen that the influence on the transmission loss of the cross-guide due to the aperture height tolerance is the most significant, and the influence due to angle tolerance is the second most significant.

The influence due to length errors is much smaller than the influences due to height and angle tolerance. The simulation results also show that the effect on the achieved transmission loss due to a positive error within the tolerance interval is larger than the influence due to a negative error within the tolerance interval (assuming the positive and negative errors are of the same magnitude).

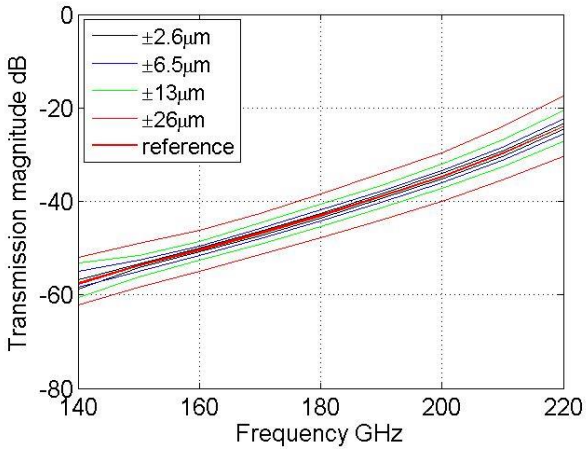

Fig. 2 Loss errors due to height tolerances

TABLE III
LOSS ERRORS DUE TO HEIGHT TOLERANCES AT SELECTED FREQUENCIES

| Freq. (GHz) | S21 (dB) | Δ S21 (dB) | | | |
|---|---|---|---|---|---|
| | | ±2.6 μm | ±6.5 μm | ±13 μm | ±26 μm |
| 140 | 57.61 | 1.17 | 2.71 | 4.40 | 5.69 |
| 160 | 50.43 | 0.41 | 1.12 | 2.16 | 4.48 |
| 180 | 43.02 | 0.49 | 1.22 | 2.41 | 4.82 |
| 200 | 34.62 | 0.51 | 1.31 | 2.62 | 5.29 |
| 220 | 24.05 | 0.67 | 1.66 | 3.31 | 6.39 |

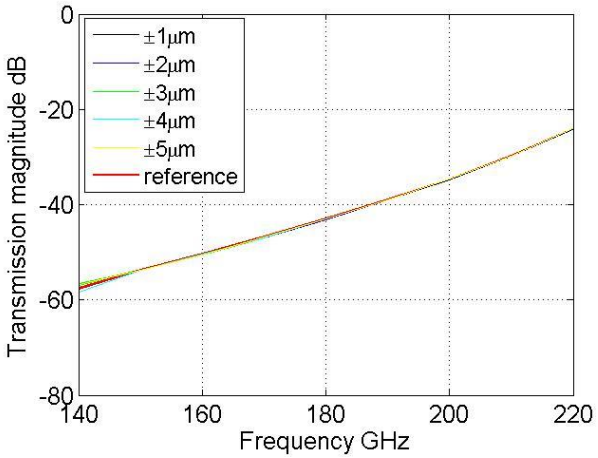

Fig. 3 Loss errors due to length tolerances

TABLE IV
LOSS ERRORS DUE TO LENGTH TOLERANCES AT SELECTED FREQUENCIES

| Freq. (GHz) | S21 (dB) | Δ S21 (dB) | | | | |
|---|---|---|---|---|---|---|
| | | ±1 μm | ±2 μm | ±3 μm | ±4 μm | ±5 μm |
| 140 | 57.61 | 0.89 | 0.69 | 0.97 | 0.75 | 0.79 |
| 160 | 50.43 | 0.10 | 0.06 | 0.17 | 0.13 | 0.16 |
| 180 | 43.02 | 0.04 | 0.07 | 0.10 | 0.11 | 0.14 |
| 200 | 34.62 | 0.03 | 0.04 | 0.08 | 0.09 | 0.11 |
| 220 | 24.05 | 0.02 | 0.06 | 0.04 | 0.08 | 0.09 |

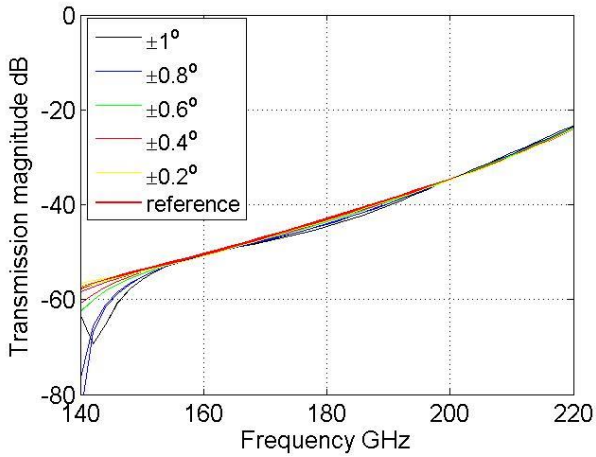

Fig. 4 Loss errors due to angle tolerances

## IV. UNCERTAINTY ESTIMATES

In order to specify the performance of the cross-guide as a transmission loss verification standard, uncertainty budgets are constructed showing the likely size of uncertainty contributions due to errors derived from cross-guide aperture, flange and line length tolerances. The approach used to establish the uncertainty in the measurements follows the procedures given in [6]. For a cross-guide transmission loss verification standard, the three uncertainty components are:

(i) Worst-case errors due to height tolerance;
(ii) Worst-case errors due to angle tolerance;
(iii) Worst-case errors due to length tolerance.

If $\Delta b$ is the worst-case errors due to the aperture height tolerance, the equivalent standard uncertainty, $u(\Delta b)$, can be established using :

$$u(\Delta b) = \frac{\Delta b}{\sqrt{3}} \quad (1)$$

If $\Delta\Phi$ is the worst-case errors due to angle, the equivalent standard uncertainty, $u(\Delta\Phi)$, can be established using :

$$u(\Delta\phi) = \frac{\Delta\phi}{\sqrt{3}} \quad (2)$$

If $\Delta l$ is the worst-case errors due to length, the equivalent standard uncertainty, $u(\Delta l)$, can be established using :

$$u(\Delta l) = \frac{\Delta l}{\sqrt{3}} \quad (3)$$

Equation (1), (2) and (3) are used to determine the overall uncertainty for transmission loss measurements, expressed in dB. The combined standard uncertainty for transmission loss measurements, $u(A)$, is given by:

$$u(A) = \sqrt{\left(u(\Delta b)\right)^2 + \left(u(\Delta\phi)\right)^2 + \left(u(\Delta l)\right)^2} \quad (4)$$

Therefore, the expanded uncertainty, $U(A)$, is given by:

$$U(A) = 2 \times u(A) \quad (5)$$

TABLE V
LOSS ERRORS DUE TO ANGLE TOLERANCES AT SELECTED FREQUENCIES

| Freq. (GHz) | S21 (dB) | Δ S21 (dB) | | | | |
|---|---|---|---|---|---|---|
| | | ±0.2° | ±0.4° | ±0.6° | ±0.8° | ±1.0° |
| 140 | 57.61 | 0.99 | 0.68 | 4.94 | 26.78 | 5.39 |
| 160 | 50.43 | 0.36 | 0.18 | 0.15 | 0.18 | 0.14 |
| 180 | 43.02 | 0.29 | 0.25 | 0.56 | 1.08 | 1.65 |
| 200 | 34.62 | 0.23 | 0.09 | 0.11 | 0.18 | 0.15 |
| 220 | 24.05 | 0.03 | 0.10 | 0.24 | 0.44 | 0.67 |

In practice, the calculation of uncertainty is performed at each frequency. For selected frequencies across the band, this leads to the values of uncertainty shown in TABLE VI.

In TABLE VI, the height tolerance is chosen to be ±6.5 μm from TABLE II, which is the tolerance for Grade 0.5 (-34 dB reflection coefficient) waveguide given in [4] and is slightly larger than the maximum observed deviation for the height of the cross-guide given in TABLE I. The length tolerance is chosen to be ±3 μm from TABLE II, which is the estimated

measurement uncertainty of the micrometer used to measure the length of the cross-guide line and is within the manufacturing tolerance for length given in TABLE I. The angle tolerance is chosen to be ±0.4° from TABLE II based on the waveguide flange design.

$\Delta Dut$, the last column in TABLE VI, is given by:

$$\Delta Dut = Mea.Dut - Mod.Dut \quad (6)$$

where, $Mea.Dut$ is the measured attenuation of the cross-guide in dB (see Section V) and $Mod.Dut$ is the corresponding modeled value.

TABLE VI
LOSS ERRORS AND EXPANDED UNCERTAINTIES DUE TO CROSS-GUIDE TOLERANCES AT SELECTED FREQUENCIES

| Freq. (GHz) | S21 (dB) | Δ S21 (dB) | | | | |
|---|---|---|---|---|---|---|
| | | $\Delta b$ = 6.5 μm | $\Delta l$ = 3 μm | $\Delta\phi$= 0.4° | $U$ ($k$=2) | $\Delta Dut$ |
| 140 | 57.61 | 2.71 | 0.97 | 0.68 | 3.42 | 1.78 |
| 160 | 50.43 | 1.12 | 0.17 | 0.18 | 1.32 | 0.09 |
| 180 | 43.02 | 1.22 | 0.10 | 0.25 | 1.44 | 0.65 |
| 200 | 34.62 | 1.31 | 0.08 | 0.09 | 1.52 | 0.91 |
| 220 | 24.05 | 1.66 | 0.04 | 0.10 | 1.92 | -0.01 |

## V. COMPARISON OF MEASURED AND MODELED VALUES

A measurement was made on one candidate cross-guide line using NPL's Primary Impedance Measurement System (PIMMS) [9]. A millimeter-wave VNA was configured with WR-05 waveguide test ports. These test ports were established as reference planes by performing a 'Thru-Reflect-Line' (TRL) calibration using: two "¾-wave" lines (as the Line standard); a flush short-circuit connected, in turn, to both test ports (as the Reflect standard); and, joining the test ports together (as the Thru standard) [10] [11]. A relatively short waveguide line, of approximate length of 1.478 mm, was connected as the cross-guide line to the VNA test port reference planes, as shown in Fig. 5.

Fig. 6 show plots of the measured transmission magnitude, as a function of frequency, for the cross-guide line. Also shown in Fig. 6 are the values predicted by the electromagnetic model. The uncertainty intervals for the modeled values can be used to verify the measured values – i.e. the measured values are verified when they fall within the range of values established by the uncertainty intervals for the modeled values.

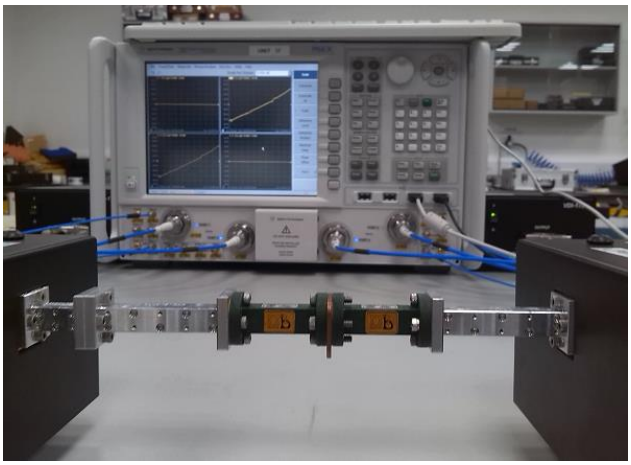

Fig.5 Transmission loss measurement of a cross-guide verification standard

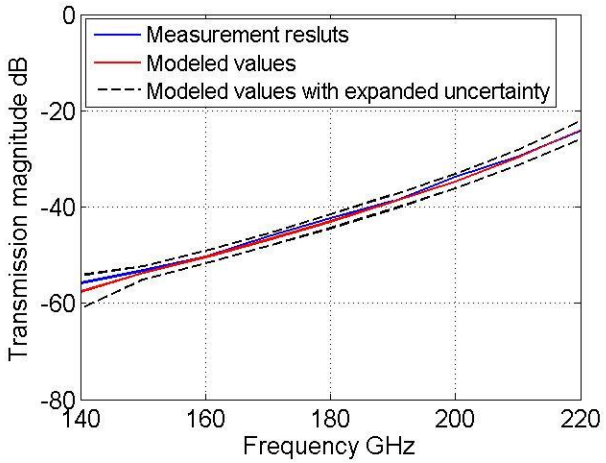


Fig.6 Transmission loss measurement results and modeled values along with the expanded uncertainty for cross-guide as verification standard

## VI. CONCLUSION

This paper has presented an analysis of the uncertainties in a cross-guide verification line used as a standard of attenuation. The analysis used electromagnetic modeling to predict the effect due to tolerances in the dimensions of the cross-guide line and the subsequent impact on the electromagnetic behavior of the line. These model-based uncertainties have been used subsequently to verify a VNA by comparing measurements of a cross-guide line with these modeled values, with uncertainties. By using a range of different cross-guide lengths, the performance of a VNA can be verified over a wide range of operating conditions. This is analogous to the use of commercial coaxial verification kits to verify VNAs that operate at frequencies below 110 GHz.

## ACKNOWLEDGEMENT

This work was part-funded through the European Metrology Research Programme (EMRP) Project SIB62 'Metrology for New Electrical Measurement Quantities in High-frequency Circuits'. The EMRP is jointly funded by the EMRP participating countries within EURAMET and the European Union.

Hui Huang's involvement with this work was funded by National Institute of Metrology, China.

## REFERENCES

[1] N M Ridler and M J Salter, "Cross-connected Waveguide Lines as Standards for Millimeter- and Sub millimeter-wave Vector Network Analyzers" Proc. 81st ARFTG Microw. Meas. Conf., Seattle, Washington, USA, 7th June 2013.

[2] T Schrader, K Kuhlmann, R Dickhoff, J Dittmer and M Hiebel, "Verification of scattering parameter measurements in waveguides up to 325 GHz including highly-reflective devices", Adv. Radio Sci., Vol 9, pp 9-17, 2011.

[3] N M Ridler, Roland Clarke, M J Salter and Alan Wilson, "The Trace is on Measurements: Developing Traceability for S-Parameter Measurements at Millimeter and Submillimeter Wavelengths", IEEE Microwave Magazine, Vol. 14, No. 7, pp. 67-74, November/December 2013.

[4] IEEE Standard 1785.1-2012, "IEEE P1785: IEEE Standard for Rectangular Metallic Waveguides and Their Interfaces for Frequencies of 110 GHz and Above—Part 1: Frequency Bands and Waveguide Dimensions"

[5] www.cst.com

[6] ISO/IEC Guide 98-3:2008, "Uncertainty of Measurement – Part 3: Guide to the expression of the Uncertainty in Measurement (GUM: 1995)", International Organization for Standardization. Available from: www.iso.org.

[7] R G Clarke, R D Pollard, N M Ridler, M J Salter and A Wilson, "Traceability to National Standards for S-parameter Measurements of Waveguide Devices from 110 GHz to 170 GHz", 73th ARFTG Microwave Measurement Conference digest, pp 127-136, Boston, MA, 12 June 2009.

[8] N M Ridler, Roland Clarke, M J Salter and A Wilson, "Traceability to National Standards for S-parameter Measurements in Waveguide at Frequencies from 140 GHz to 220 GHz", 76th ARFTG Microwave Measurement Conference digest, pp. 8-14, Marriott Suites on Sand Key, Clearwater Beach, FL, USA, 2-3 December 2010.

[9] G J French and N M Ridler, "A Primary National Standard for Millimetric Waveguide S-parameter Measurements", Microwave Engineering Europe, pp. 29-32, October 1999.

[10] N M Ridler, "Choosing line lengths for calibrating waveguide vector network analyzers at millimeter and sub-millimeter wavelengths", NPL Report TQE5, National Physical Laboratory, UK, March 2009.

[11] G F Engen and C A Hoer, "Thru-Reflect-Line: An improved technique for calibrating the dual six-port automatic network analyzers", IEEE Trans, Vol MTT-27, No 12, pp 987-993, December 1979.

# Observations on the Sensitivity of On-Wafer Cascode Cell S-parameter Measurements Due to Probing Uncertainties

*Priya Shinghal[1], Robin Sloan[1], Christopher I. Duff[1] and Steven Cochran[2]*

*[1] School of EEE, MCS Research Group, The University of Manchester, Manchester, UK*

*[2] Agilent Technologies, Santa Rosa, CA, USA*

**Abstract — On-wafer probing accuracy limitations affect measurement repeatability for potentially unstable circuits. Here we present a 2x25 µm pHEMT cascode cell on 2 mil GaAs substrate measured from 0.045–110 GHz. The S-parameter measurements carried out for the same device using two different on-wafer measurement systems, one PNA based (Sys-1) and the other a 8510XF VNA (Sys-2), differed by up to 2 dB in gain above 50 GHz. Measurements were performed using a Cascade Microtech probe station after applying on-wafer LRRM calibration on WINCAL XE using the same set of standards. Sys-1 used Cascade infinity probes; Sys-2 Cascade ACP probes. A maximum difference in measured gain of 1.1 dB at 85 GHz was observed with variation in probe position. As |S22| for the cascode configuration is > 1, measured gain is highly sensitive to the output termination. The extra pad metallization due to differing probe position was modeled as a negative shunt capacitance (-5 fF), effectively de-embedding the extra pad capacitance.**

**Index Terms — Cascode, MMIC, On-wafer, Probe, S-parameters, Ultra-broadband**

## I. Introduction

Monolithic Microwave Integrated Circuit (MMIC) cascode pHEMTs are widely used in design of mixers, travelling wave amplifiers, etc., for ultra-broadband applications. For accurate cascode circuit design it is imperative the designer has either a model or measured S-parameters across the full active range. Previous work investigated EM based [1] and bias dependent [2] cascode models up to 40 GHz and indicated a need for measurement validation for frequencies well above this. Shinghal et al., [3] suggest that the simulations based on the foundry model for FETs and EM based models for interconnects may not agree with the measured S-parameters for a cascode cell across the whole frequency range. Thus, measured cascode data is required for characterization of high frequency small signal performance. The aim of this work is to highlight the criticalities of making on-wafer S-parameter measurements of a cascode cell where $|S_{22}| > 1$.

## II. Cascode Cell

Cascode is a series connection of Common-Source FET (CSFET) and Common-Gate FET (CGFET) that exhibits ultra-broadband high gain and better reverse isolation than the common-source FET. The 2x25 µm cascode cell was fabricated on the PP-10 process of WIN Semiconductors Ltd., Taiwan [4]. Fig. 1 shows a schematic of the 2x25 µm cascode cell and Fig. 3 the fabricated circuit.

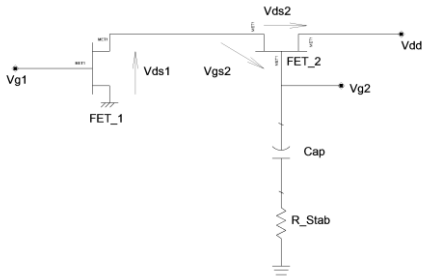


Fig. 1 Schematic of a FET cascode cell

## III. S-parameter Measurement Cases & Observations

The S-parameters of the 2x25 µm cascode cell biased at $V_d$=3.5 V, $V_{g1}$ for $I_{ds}$=3.17 mA and $V_{g2}$=0 V were measured on-wafer from 0.045-110 GHz at -15 dBm on the following two systems:

i. **Sys-1**: Agilent PNA based system and Cascade Microtech probe station with infinity probes [5] and,
ii. **Sys-2**: Agilent 8510XF VNA and Cascade Microtech probe station with ACP probes.

LRRM calibration [6] was applied using WINCAL XE with the same on-wafer calibration standards on both systems. It was observed that the gain, $S_{21}$ of the cascode was 2.0 dB lower above 50 GHz on Sys-2 than Sys-1. In order to rule out discrepancies due to a faulty device, the maximum available gain was analyzed that showed agreement between the measured data from the two systems (Fig. 2).

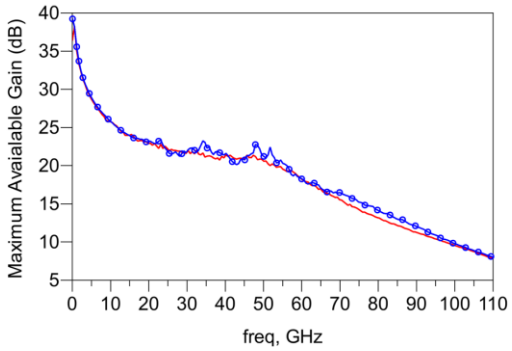


Fig. 2 Maximum Available Gain (MAG) in dB of 2x25 µm cascode cell measured on Sys-1(blue with circles) and Sys-2 (red line).

978-1-4799-4423-1/14/$31.00 ©2014 IEEE

Two cases were formed as possible explanations for the discrepancy observed:

*A. Probe Position*

The effect of variation in probe landing position on measured S-parameters was analyzed. As shown in Fig. 3, the cascode cell was probed once by landing the probe on the Outer Edge (OE), ensuring good contact, and later up to the Inner Edge (IE) of the input/output pads on Sys-2. It was observed that the difference in gain reduced to 1.1 dB (max) at 85 GHz for the measurements on the two systems (Fig. 4). Fig. 5 shows input and output return loss for measurements on Sys-1, Sys-2 with probe landed on OE and Sys-2 with probe landed on IE. It can be seen that $|S_{11}|$ is almost the same for the three measurement variations while $|S_{22}|$ varies and is sensitive to output termination that alters due to change in probe placement. Measurements with variation in probe position on Sys-1 are envisaged to be performed during future experimental work. $|S_{22}| > 1$ is a feature of the cascode configuration due to the CGFET present on the output [7]. A resonance is observed at 105 GHz in the input/output return loss measurements done on Sys-2. This is a residue from the calibration, observed in the calibration verification plot and can be ignored.

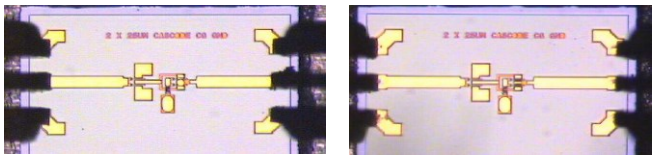

(a) (b)

Fig. 3 Fabricated 2x25 µm cascode probed at (a) inner edge and (b) outer edge of the input/output pads using ACP probes.

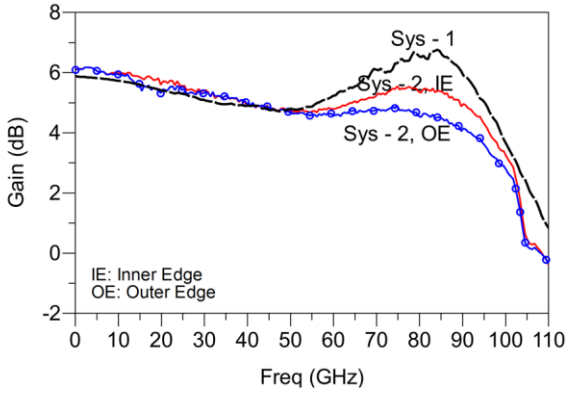


Fig. 4 Measured gain for cascode on Sys-1, Sys-2 Probe at Inner Edge (IE) and Sys-2 Probe at Outer Edge (OE).

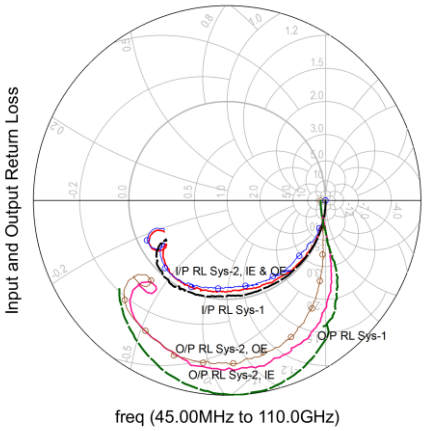


Fig. 5 Measured input and output return loss on Sys-1, Sys-2 Probes at IE and Sys-2 Probes at OE for the cascode.

*B. Pad Capacitance De-embedding*

Section A showed that probing the cascode cell up to the inner edge of the input/output pads on Sys-2 did not account for the full difference in S-parameters measured on the two systems. To account for the remaining difference, a negative shunt capacitance (-5 fF) was added on the output of the S-parameters of the device measured on Sys-2 with probes on the inner edge (Fig. 6) and simulated on Agilent Advanced Design System (ADS) [8]. This effectively de-embeds the extra pad capacitance located at the back of the probe. The size of the pads is 40 $\mu m^2$.

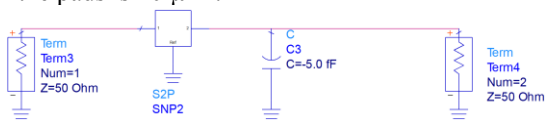


Fig. 6 Simulation setup in ADS of S-parameters measured on Sys-2 with negative shunt capacitance.

Electromagnetic (EM) simulation using ADS Momentum for the GSG probe landing pad structure resulted in an equivalent capacitance value of 16 fF. Considering a probe skate difference of up to one-third the pad length, this de-embedding value seems reasonable.

It was observed that the difference in gain reduced to < 0.5 dB up to 105 GHz (Fig. 7). Also, agreement between $|S_{22}|$ improved as shown in Fig. 8. Addition of the negative shunt capacitance on the output of the measured S-parameters better matches the equivalent impedance that the device sees at the output port, implying that the output impedance seen by the device is a function of probe position.

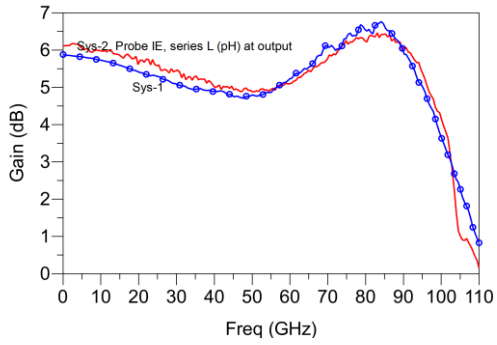


Fig. 7 Gain measured on Sys-1 and simulation of Sys-2 measurement, with device probed at Inner Edge (IE) of pad and shunt C (-5 fF) added.

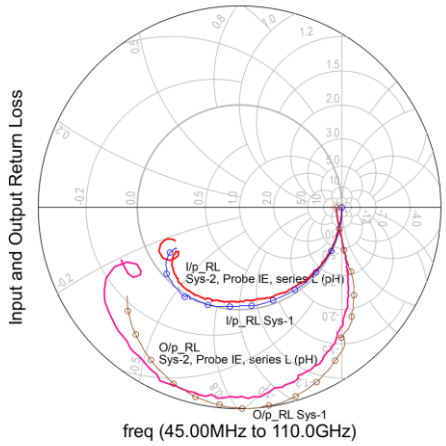


Fig. 8 Input/output return loss measured on Sys-1 and simulation of Sys-2 measurement with device probed at inner edge of pad and shunt C (-5 fF).

## IV. Conclusion

Small signal S-parameter measurements carried out in a frequency range of 0.045–110 GHz for a 2x25 µm GaAs pHEMT cascode cell on two test set-ups exhibited difference in performance above 50 GHz. To understand the difference in measurements, the device was probed at the inner and outer edge of the input/output pads and it was observed that the probe landing position could lead to a change in the output impedance seen by a device thus, changing its millimeter wave performance. Thus, accurate steps for repeatable measurements should be identified and adhered to, especially for circuits where $|S_{22}| > 1$.

## References

[1] D. Resca, J. A. Lonac, R. Cignani, A. Raffo, A. Santarelli, G. Vannini, and F. Filicori, "Accurate EM-Based Modeling of Cascode FETs," *Microwave Theory and Techniques, IEEE Transactions on,* vol. 58, pp. 719-729.

[2] P. B. Winson, L. P. Dunleavy, H. C. Gordon, Jr., M. V. Calvo, and J. Sherman, "A novel algorithm for bias-dependent cascode FET modeling," in *Microwave Symposium Digest, 1995., IEEE MTT-S International*, 1995, pp. 627-630 vol.2.

[3] P. Shinghal, C.I. Duff, R. Sloan and S. Cochran "Cascode cell analysis for ultra-broadband GaAs MMIC component design applications," in *International Microwave and RF Conference*, New Delhi, 2013.

[4] W. S. Ltd., "PP10-10 0.1µm 2 mil pHEMT Power Design Manual ver. 1.0.9."

[5] C. Microtech, "Infinity Probe - High frequency performance with low, stable contact resistance," 2008.

[6] A. Davidson, K. Jones, and E. Strid, "LRM and LRRM Calibrations with Automatic Determination of Load Inductance," in *ARFTG Conference Digest-Fall, 36th*, 1990, pp. 57-63.

[7] A. Tessmann, O. Wohlgemuth, R. Reuter, W. Haydl, H. Massler, and A. Hulsmann, "A coplanar 148 GHz cascode amplifier MMIC using 0.15 /spl mu/m GaAs PHEMTs," in *Microwave Symposium Digest. 2000 IEEE MTT-S International*, 2000, pp. 991-994 vol.2.

[8] "http://cp.literature.agilent.com/litweb/pdf/ads15/doc.html."

# Characterizing Calibration Standards Using One Airline as a Transfer Standard

T. Roberts and J. Martens
Anritsu Company, 490 Jarvis Drive, Morgan Hill, CA 95037 US
tom.roberts@anritsu.com

***Abstract*— This paper introduces methods to characterize coaxial calibration standards using one airline as transfer standard. The methods discussed lend themselves to computer optimization techniques to arrive at optimal polynomial coefficients and S-parameter model representations of calibration standards. The calibration standards characterized and data presented were from a random sample of K (2.92 mm), V (1.85 mm) and W (1.00 mm) Vector Network Analyzer calibration kits manufactured over the past decade. The focus of this paper is Open, Short and Load (OSL) characterization but can be expanded to other 1-port calibration standards or kits such as multiple offset shorts (or opens) as examples. Electrical performance comparison of characterized fixed terminations to sliding terminations is also presented.**

***Index Terms*— Vector network analysis, calibration and measurement, characterized standards, traceability to national standards, measurement uncertainty.**

## I. Introduction

Manufacturers of Open-Short-Load (OSL) coaxial calibration kits typically provide derived empirical models for calibration standards available as electronic files. Empirical models are commonly in the form of frequency dependent polynomial functions (given as polynomial coefficients) or data based S-Parameter (.s1p) files. Often, a 'common' set of calibration coefficients are assigned to a calibration kit requiring each standard to have tight mechanical tolerances. In this situation, residual port characteristics following Vector Network Analyzer calibration are not always optimal since the model parameters usually do not perfectly match the calibration standards true electrical behavior over their frequency bandwidth. Another approach is to create a 'unique' set of calibration coefficients for each calibration standard manufactured. Calibration standards with unique calibration coefficients can give optimal residual port characteristics following a calibration eliminating the need for extremely tight mechanical part tolerances. On the other hand, effort is required to create a unique set of calibration coefficients for each standard manufactured. Data-based models have increased resolution and can better represent the actual electrical response of calibration standards. The process of acquiring data-based models typically involves making measurements of the standard. This process may require a high degree of operator skill and is usually time consuming.

Various methods to estimate the parameters for the models have been discussed [1, 2] although arrived at by different means. The method discussed in this paper of estimating polynomial calibration coefficients and data based models is achieved by iteratively applying a residual error computation and reducing the residual error vector magnitude. Use of this method produces a unique set of calibration coefficients and data based model for each standard with optimal residual port characteristics of a calibrated Vector Network Analyzer. Further, this method is extremely broadband and lends itself to computer optimization.

## II. Background: Source Match Residual Error Measurement

To extract the Source Match residual error, a Source Match ripple measurement technique is performed by connecting a long airline and an offset short to the calibrated reference plane of the VNA in Fig 1.

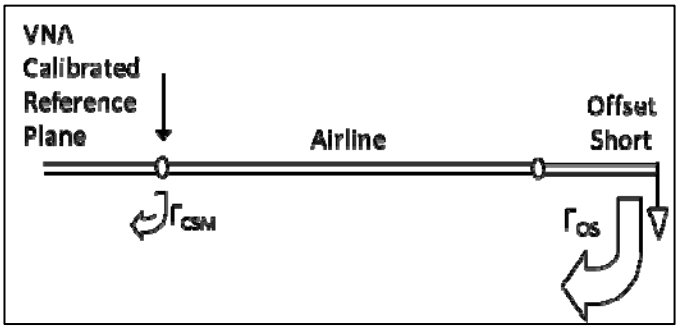


Fig. 1. Source Match ripple measurement technique

The length of the airline will cause the Offset short vector to spin around the corrected Source Match vector. The corrected Source Match is often called residual Source Match. These vectors add in the complex plan as shown in Fig. 2

978-1-4799-4423-1/14/$31.00 ©2014 IEEE

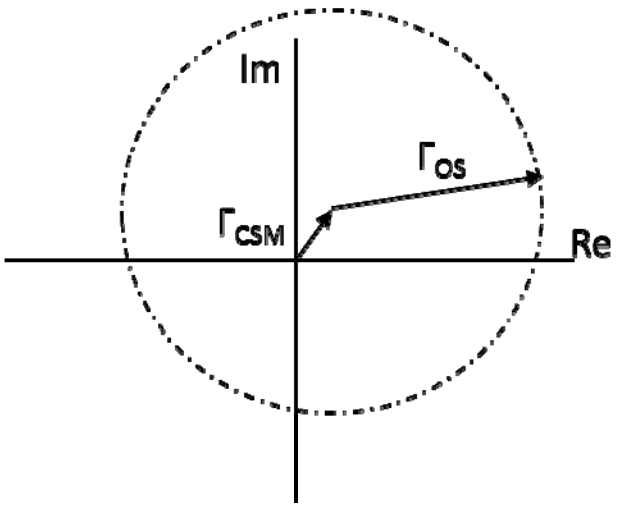


Fig. 2. Source Match vector addition in the complex plane

Since the residual Source Match vector $\Gamma_{csm}$ is non-zero, a ripple pattern is produced as shown in the top trace in Fig. 3. The Reflection coefficient $\Gamma$ is the vector sum of $\Gamma_{csm}$ and the *ideal* reflection coefficient of an airline terminated in an offset short $\Gamma_{OS}$. $\Gamma$ is computed using the Eqn. 1 below:

$$\Gamma = (\Gamma_m - ed)/[et + eps(\Gamma_m - ed)] \quad [1]$$

ed, eps and et are the Directivity, Source Match and tracking coefficients respectively. These coefficients are functions of the measured calibration standards and their models. $\Gamma_m$ is the measured reflection coefficient of the airline and offset short combination shown in Fig. 1.

## III. Error Vector Reduction Method

To evaluate the residual Source Match, the collection of data contained in approximately one cycle (each defined as the $k^{th}$ interval) is evaluated using a least squares circle fit algorithm [3]. The process of optimizing residual Source Match is to reduce the magnitude of the unwanted $\Gamma_{csm}$ error vector. This is accomplished by iteratively adjusting the capacitance correction function C(f) of the Open standard model in Eqn. 2 for each $k^{th}$ interval. This optimization process has the effect of reducing each $\Gamma_k$, $\Gamma_{k-1}$, … interval function to an equation of a line as visually shown in Fig 3.

Since the capacitance correction function is usually a slow moving function of frequency, the C(f) value obtained from the $k^{th}$ interval can be used as a seed value for the $k^{th}$ -1 interval to speed up optimization. Once the capacitance correction data points are found in each interval, a function is fitted to the data – usually a 3rd order polynomial function. From this function, the capacitance coefficients are extracted and, as a direct result of reducing the $\Gamma_{csm}$ error vector, an accurate model for the Open standard is derived. To prevent 'lumping-in' effects of the Short model into the Open model during the $\Gamma_{csm}$ error vector reduction method, an electromagnetic model for the short standard is created using [4] with knowledge of its measured mechanical and known material properties. To prevent the system of equations from being underdetermined, $L_{ind}(f)$ in Eqn. 3 is derived prior to implementing the $\Gamma_{csm}$ error vector reduction method.

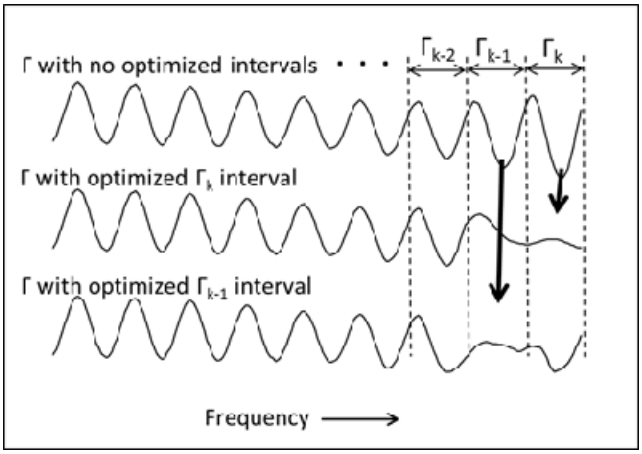


Fig. 3. Error Vector Reduction for $\Gamma_k$ and $\Gamma_{k-1}$ intervals in the Frequency Domain

$$\Gamma_{open}(f) = e^{-j2(\beta(f)L + \text{atan}(\omega(f)C(f)Zo))} \quad [2]$$

$$\Gamma_{short}(f) = -e^{-j2(\beta(f)L + \text{atan}(\omega(f)L_{ind}(f)/Zo))} \quad [3]$$

Where: $\beta(f) = \omega(f)\text{sqrt}(\varepsilon_r)/c$

$c = 2.9979 \times 10^8$ m/s, $\varepsilon_r = 1.00065$

$\omega(f) = 2\pi f$

$j = \text{sqrt}(-1)$

C(f) is the Open Standard capacitance correction function

$L_{ind}(f)$ is the Short Standard inductance correction function

The $K^{th}$ intervals can either be non-overlapping, discrete optimization bands for the case where polynomial functions are derived as shown in Fig. 3 or the interval can be a moving point-by-point window where high point density is required for .s1p model data. In either case, the $1^{st}$ and $K^{th}$ intervals do not allow evaluation of the residual at the frequency band edges and extrapolation of the model data is required. The open standard capacitance model functions were derived by minimizing the residual Source match error vector of ten, randomly chosen 3654D-1 (V) and 3652A-1 (K) and 3656C (W) calibration kits. The corrected Source Match data was averaged for each kit type and calibration standard gender as shown in Figs. 4-6.

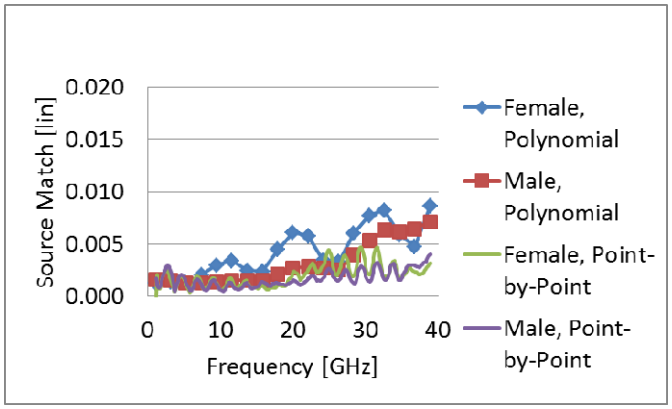


Fig. 4. Corrected Source Match vs. Frequency vs. gender and model type. K (2.92 mm) connector type.

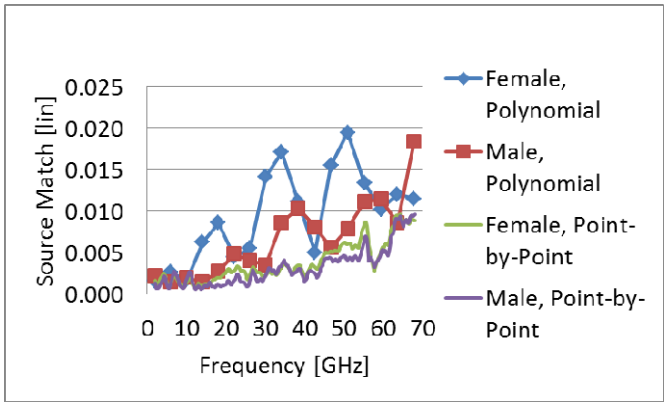


Fig. 5. Corrected Source Match vs. Frequency vs. gender and model type. V (1.85 mm) connector type.

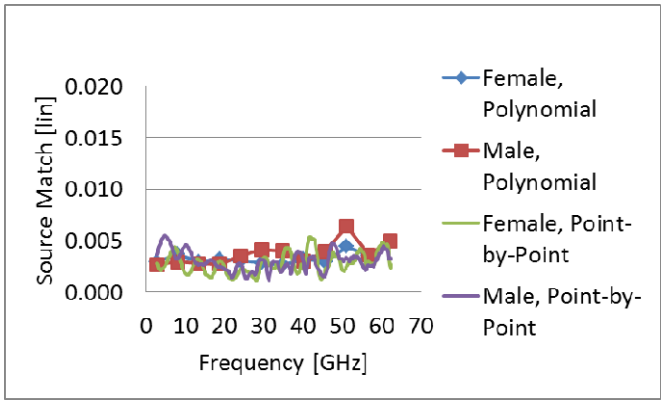


Fig. 6. Corrected Source Match vs. Frequency vs. gender and model type. W (1.00 mm) connector type.

## IV. Broadband Termination Model

The Directivity ripple measurement technique is performed similarly to the Source Match ripple technique but instead of connecting an offset short to the end of the airline, an offset termination is used. Assuming a perfect airline, the residual Directivity vector $\Gamma_{cd}$ is the result of the termination model ($\Gamma_t$) not fitting the actual electrical response of the measured termination standard ($\Gamma_{mt}$). As with the $\Gamma_{csm}$ vector, the $\Gamma_{cd}$ vector is also unwanted. To reduce the residual Directivity vector $\Gamma_{cd}$, a broadband termination model that better describes the electrical performance of the termination is needed.

An improved broadband termination model was recently introduced [5] and is an extension of the lumped element on-wafer model [6] and the lumped load transmission line model [7]. This model better approximates the physical geometry of 28K(F)50B, 28V(F)50D and 28W(F)50 series coaxial broadband terminations where a short length of coaxial transmission line extends from the connector interface to the load element. These broadband 'beadless' terminations are constructed as described in [8-10] and shown in Fig. 7. The 'beadless' structure facilitates ultra-low reflection characteristics and allows a relatively simple load model to be used. Even though these terminations have low reflection characteristics on their own, manufacturing tolerances are present and produce unwanted variability in electrical performance. The electrical model for the coaxial terminations is shown in Fig. 8.

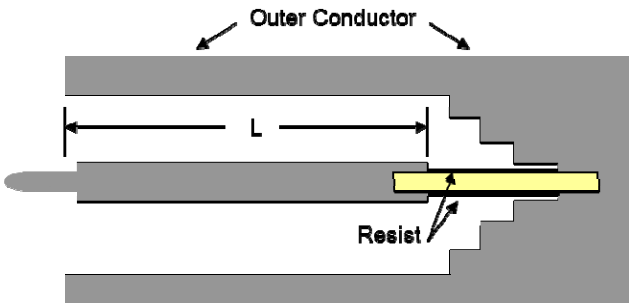


Fig. 7. Cross-sectional view of broadband coaxial termination.

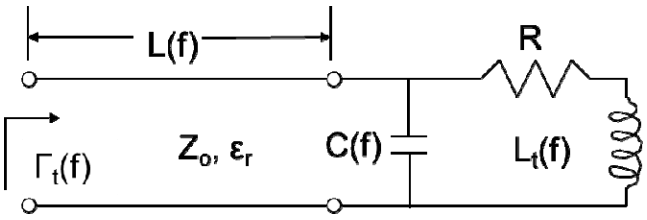


Fig. 8 Electrical model of broadband coaxial termination.

The process to reduce the residual Directivity vector $\Gamma_{cd}$ is similar to that of reducing $\Gamma_{csm}$ with the exception that now there are more optimization parameters to solve for. Like $\Gamma_{csm}$ vector reduction described earlier, $\Gamma_{cd}$ vector reduction directly leads to extraction of the termination model parameters. Forming a finite solution set and choosing the best solution for the model is the goal. Since the system is underdetermined and has an infinite solution set, imposing constraints on model parameters is necessary to reduce the solution set and computation time.

Some of these constraints are set by the physical attributes of the termination. For example, the coaxial transmission line length L(f) is approximated by the length from the terminations connector interface to the load element transition and its range of optimization values is predetermined. Another range defined is for the constant model parameter R. The thin film load termination substrate has a manufactured tolerance of 50 Ω +/- 0.1 Ω and exhibits a broadband electrical response to the model. At high frequencies where sensitivity is high, shunt capacitance C(f) and inductance Lt(f) are emphasized. These and other strategies are used to set model parameter ranges and reduced solution set for the termination model. Table 1 lists termination model parameter ranges for each connector type. The Lt and C entries on the load model are not very independent and the cross-coupling affects the values.

| | Termination | | |
|---|---|---|---|
| Range | 28K(F)50A | 28V(F)50C | 28W(F)50 |
| L [m] min./max. | 0.0/3.8e-3 | 0.0/2.4e-3 | 0.0/2.4e-3 |
| C [pF] min./max. | -5.0e-3/5.0e-3 | -3.6e-3/3.6e-3 | -3.6e-3/3.6e-3 |
| Lt [nH] min./max. | -5.0e-3/5.0e-3 | -3.0e-3/3.0e-3 | -3.0e-3/3.0e-3 |
| R [Ω] min./max. | 49.9/50.1 | 49.9/50.1 | 49.9/50.1 |

Table 1. Broadband Termination Model Parameter Ranges

Load model parameters were derived by minimizing the residual Directivity error vector using fixed terminations in ten, randomly chosen 3654D-1 (V) and 3652A-1 (K) and 3656C (W) calibration kits. For each kit type and calibration standard gender, the Directivity data was averaged. Models for the reflect standards were set to their default values during the reduction process. Directivity data using un-modeled ($\Gamma_t = 0$) and modeled ($\Gamma_t \neq 0$) fixed loads are plotted against sliding load data. See Figs. 9-19. On average, the achieved corrected Directivity using the Polynomial modeled termination is similar to the sliding termination, whereas corrected Directivity using the data modeled termination is significantly improved.

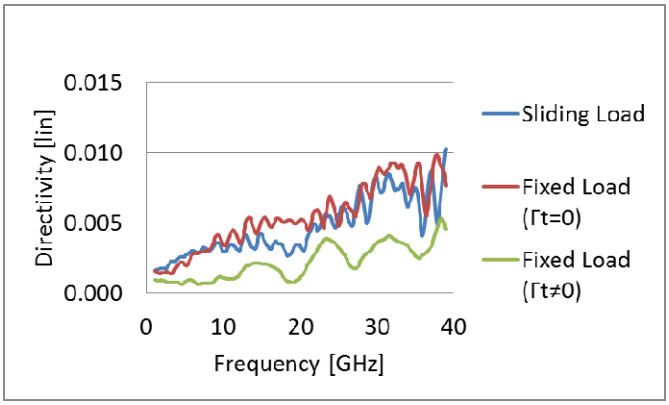


Fig. 9. Corrected Directivity vs. Frequency vs. Termination, Female K (2.92 mm), Fixed Load Point-by-Point model and Sliding Load.

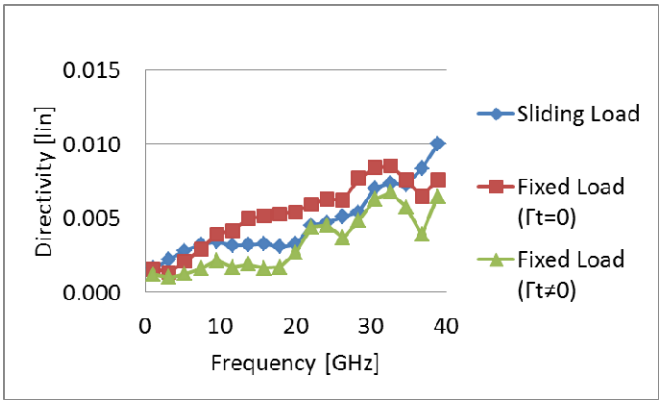


Fig. 10. Corrected Directivity vs. Frequency vs. Termination, Female K (2.92 mm), Fixed Load Polynomial model and Sliding Load.

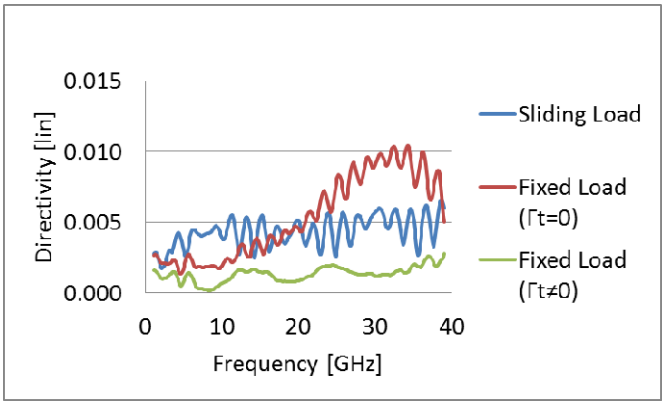


Fig. 11. Corrected Directivity vs. Frequency vs. Termination, Male K (2.92 mm), Fixed Load Point-by-Point model and Sliding Load.

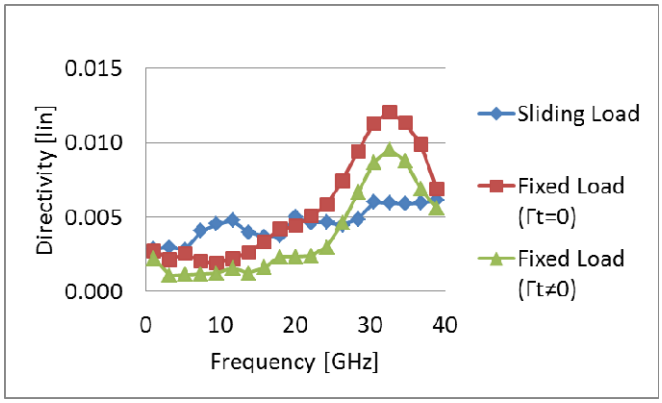


Fig. 12. Corrected Directivity vs. Frequency vs. Termination, Male K (2.92 mm), Fixed Load Polynomial model and Sliding Load.

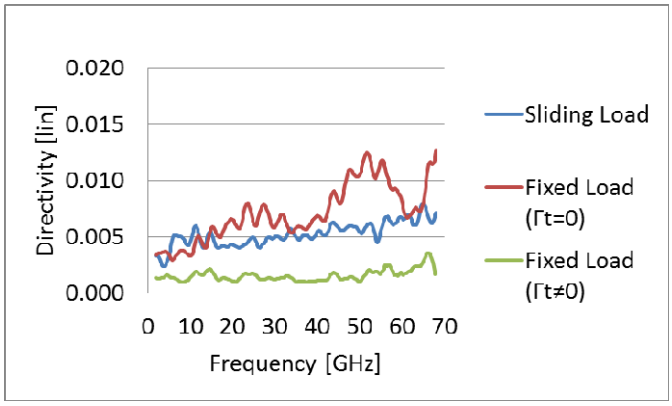


Fig. 13. Corrected Directivity vs. Frequency vs. Termination, Female V (1.85 mm), Fixed Load Point-by-Point model and Sliding Load.

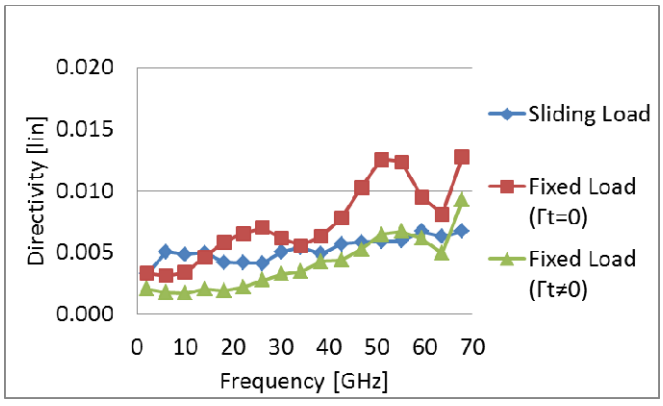


Fig. 14. Corrected Directivity vs. Frequency vs. Termination, Female V (1.85 mm), Fixed Load Polynomial model and Sliding Load.

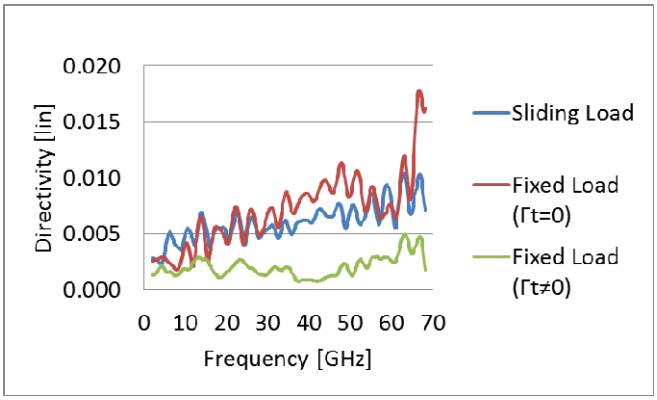


Fig. 15. Corrected Directivity vs. Frequency vs. Termination, Male V (1.85 mm), Fixed Load Point-by-Point model and Sliding Load.

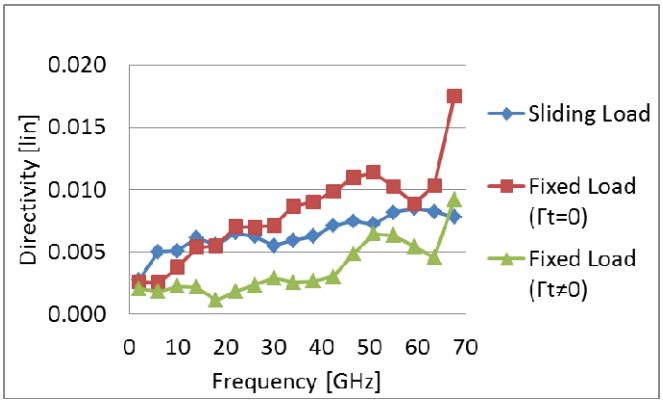


Fig. 16. Corrected Directivity vs. Frequency vs. Termination, Male V (1.85 mm), Fixed Load Polynomial model and Sliding Load.

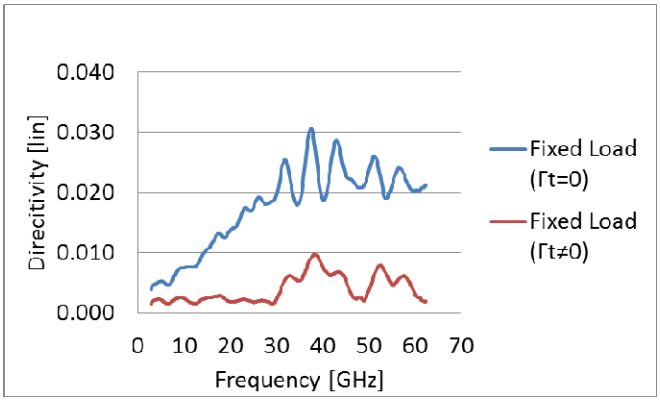


Fig. 17. Corrected Directivity vs. Frequency vs. Termination, Female W (1.00 mm), Fixed Load Point-by-Point model.

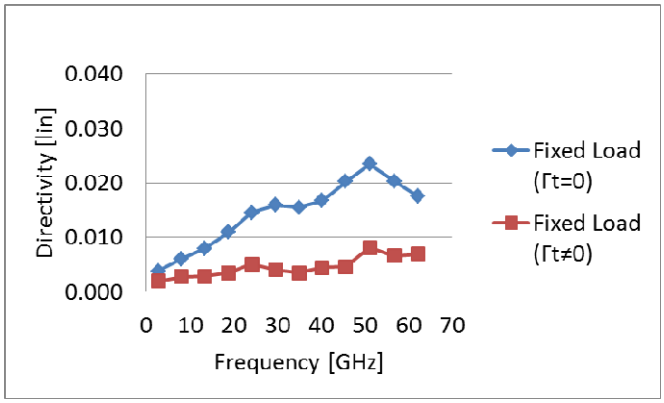


Fig. 17. Corrected Directivity vs. Frequency vs. Termination, Female W (1.00 mm), Fixed Load Polynomial model.

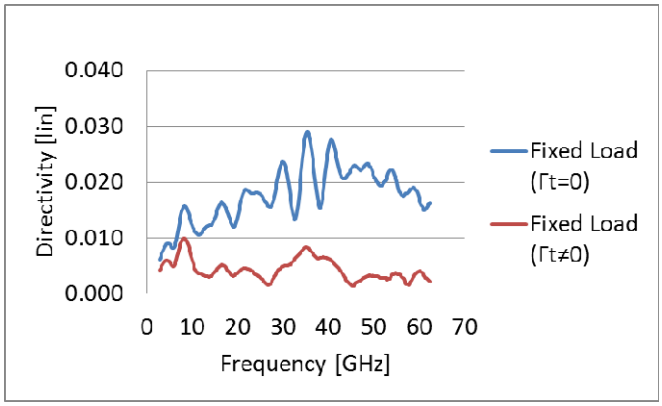


Fig. 18. Corrected Directivity vs. Frequency vs. Termination, Male W (1.00 mm), Fixed Load Point-by-Point model.

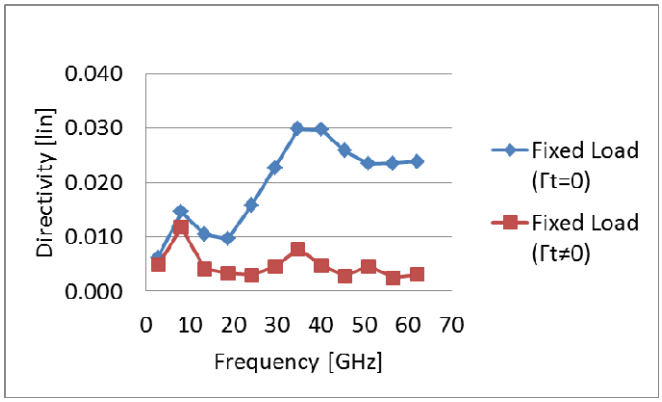


Fig. 19. Corrected Directivity vs. Frequency vs. Termination, Male W (1.00 mm), Fixed Load Polynomial model.

## V. Error Vector Coupling

Although the corrected Source Match and Directivity Ripple measurements attempt to separate the $\Gamma_{csm}$ and $\Gamma_{cd}$ error vectors from one another, the presence of non-zero error vectors can have a small influence on the vector reduction process and the model data. This is referred to as Error Vector Coupling. For example, termination model parameters were derived by reduction of the corrected Directivity error vector $\Gamma_{cd}$. These termination model parameters are then applied to the equation set used to reduce the $\Gamma_{csm}$ error vector and arrive at model parameters for the Open standard. Now, suppose the termination model parameters are set to zero forcing $\Gamma_t = 0$. This change in the termination model will have a negative impact on corrected Source Match. On the other hand, if an unmodeled termination (i.e. $\Gamma_t = 0$) was applied to the equation set used to reduce the $\Gamma_{csm}$ error vector arriving at model parameters for the Open standard, corrected Source Match would also be negatively impacted as the complex termination model is applied.

Source Match Coupling is the change in corrected Source Match with and without the termination model function applied as expressed in Eqn. 5. Conversely, Directivity Coupling is the change in corrected Directivity with and without the Open and Short standard model functions applied as expressed in Eqn. 6. Plots for Source Match and Directivity Coupling are shown in Figs. 20-25

$$\Delta CSM=abs[CSM(\Gamma_t\neq 0)-CSM(\Gamma_t=0)] \quad [5]$$

$$\Delta CD=abs[CD(C(f)\neq 0,L_{ind}(f)\neq 0)-CD(C(f)=0,L_{ind}(f)=0)] \quad [6]$$

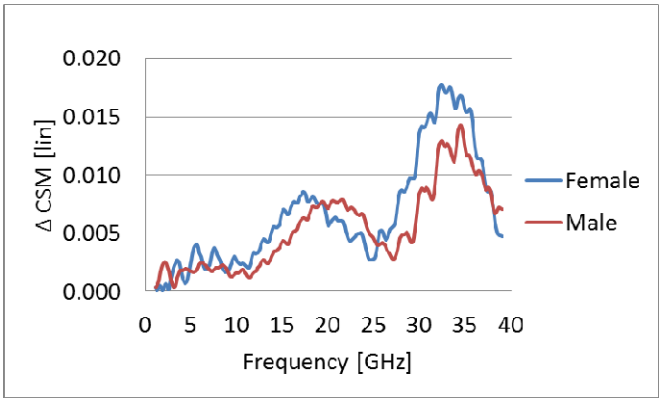


Fig. 20. Source Match Coupling vs. Frequency vs. gender, K (2.92 mm)

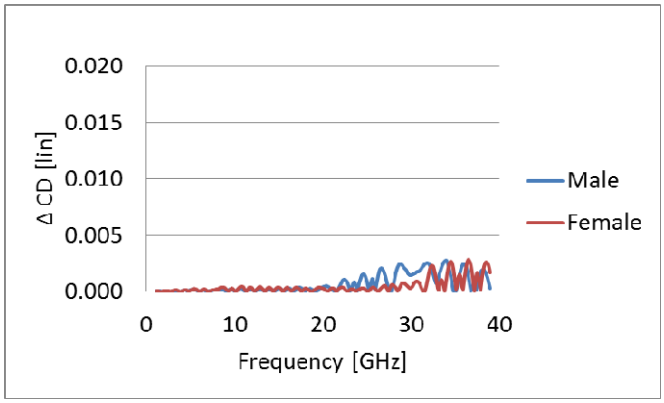


Fig. 21. Directivity Coupling vs. Frequency vs. gender, K (2.92 mm)

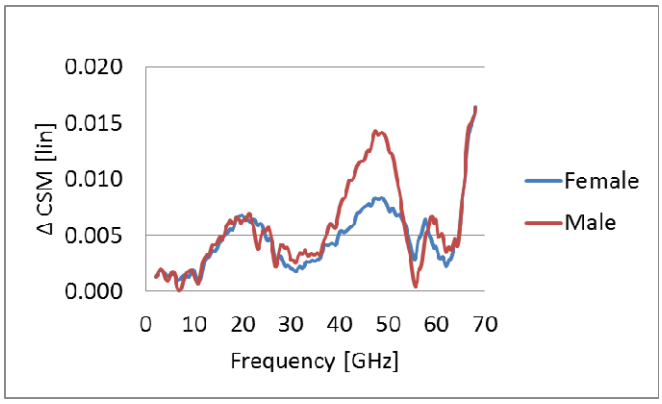


Fig. 22. Source Match Coupling vs. Frequency vs. gender, V (1.85 mm)

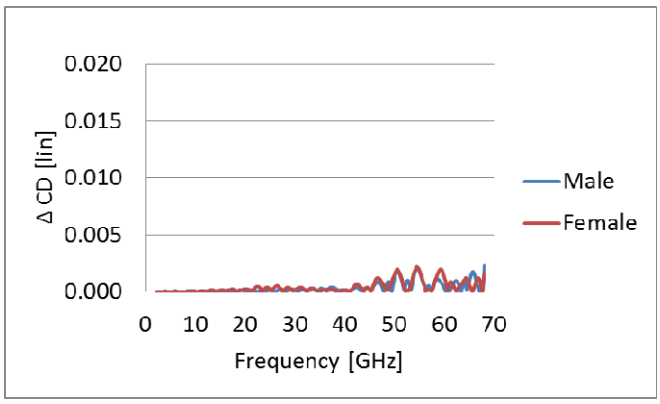


Fig. 23. Directivity Coupling vs. Frequency vs. gender, V (1.85 mm)

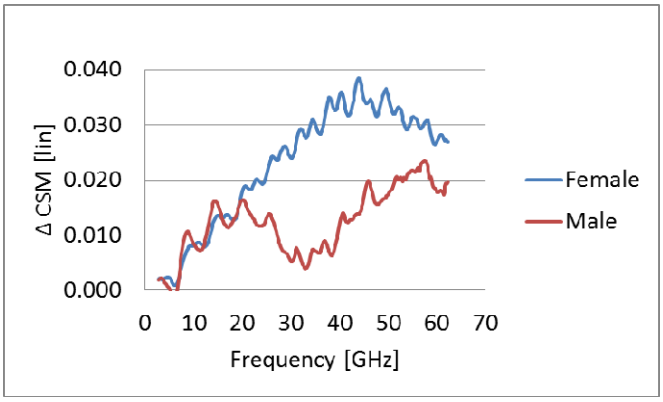


Fig. 24. Source Match Coupling vs. Frequency vs. gender, W (1.00 mm)

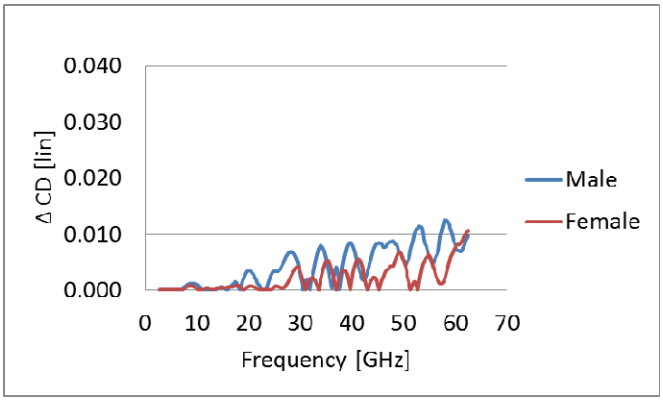


Fig. 25. Directivity Coupling vs. Frequency vs. gender, K (1.00 mm)

From Figs 20-25, Directivity Coupling only has a small influence with the applied reflect standard correction models. Source Match Coupling has a relatively large influence with the applied termination standard correction model. This gives an indication the termination standard model parameters should be derived before the open standard model since Directivity is weakly influenced by the applied reflect standard correction models. It is assumed the Source Match impact on the termination is a lot greater since it has a multiplicative impact on the measurement as shown in the denominator term in Eqn. 1. The Directivity impact on Source Match is a lot less since it is mainly additive and small relative to the Source Match measurement itself.

## VI. Corrected Source Match and Directivity Uncertainty

The process of reducing the corrected Source Match and Directivity error vectors required an assumption: The airline used for the ripple measurement was assumed to be perfect and its ideal transmission characteristics transferred to the models representing the Termination and Open standards though error vector reduction. These airlines used are reference impedance standards and their mechanical

dimensions are measured using gages whose mechanical transfer standards are traceable to national standards. Through traceable mechanical measurements, the computed impedance and reflection characteristics are known. Based on nominal mechanical part measurements, SWR and corresponding Return Loss of the airlines used are given in table 2. As corrected Source Match and Directivity values approach that of the reflection characteristics of the airline, the worst case uncertainty can be as high as 6 dB. The increased uncertainty is a consequence of the error vector reduction process.

| Connector Type | Airline SWR | Airline Return Loss (lin) |
|---|---|---|
| K (2.92 mm) | 1.002 | 1.00E-03 |
| V (1.85 mm) | 1.004 | 1.78E-03 |
| W (1.00 mm) | 1.006 | 3.16E-03 |

Table 2. Nominal Measured Airline SWR and Return Loss

The precision airlines used in this paper were "beaded" types. These precision airlines have their center conductors supported using a bead at the end of the airline assembly ensuring good concentricity, known pin gap spacing when mated and repeatable connection accuracy [11]. Unsupported, or bead-less airlines can be used although it is recommended to use dielectric rings [12] to ensure a known spacing between mating center conductors.

## VII. Conclusion

Through the process of corrected Source Match and Directivity measurements commonly used to check the quality or measurement uncertainty of a calibration, polynomial and .s1p data models for 1-port calibration standards can be derived by reducing unwanted residual error vectors. Based on very low residual levels obtained, high quality OSL calibrations with low uncertainty can be achieved using empirically derived models. It has been shown corrected Directivity using modeled Terminations, on average, meets or exceeds that of Sliding Loads. The concept of Error Vector Coupling was introduced which describes the change in Source Match with applied termination standard model and the change in Directivity with applied reflect standard models. The strong impact to Source Match from the applied termination model indicates the termination model should be derived before reflect standard models.

## References

[1] D. Shelton, M. Salter, N. Ridler, M. Hirobe, "Characterizing Artefact Standards for Use with Coaxial Vector Network Analyzers at Millimeter-wave Frequencies," 80th ARFTG Conf. Dig., Nov. 2012

[2] N. Ridler, N. Nazoa, "Using Simple Calibration Load Models to Improve Accuracy of Vector Network Analyzer Measurements," 67th ARFTG Conf. Dig., Jun. 2006

[3] P. Persson "An Algorithm for the Evaluation of the Residual Directivity 'Ripple' Trace", ANAMET May 2002

[4] CST Microwave Studio Suite, Version 2013 Service Pack 8, www.cst.com

[5] J. Martens, T. Roberts, K. Noujeim, and S. Reyes, "70 kHz-145 GHz broadband S-parameter measurements: Calibration and verification possibilities," Asia Pacific Microwave Conference (AMPC) 2012, pp. 433-435

[6] D. Walker, R. Kaiser, D. Williams, K. Coakley, "Planar Resistors for Probe Station Calibration," 40th ARFTG Conf. Dig., Dec. 1992

[7] P. Kirby, L. Dunleavy, and T. Weller, "Load Models for CPW and Microstrip SOLT Standards on GaAs," 56th ARFTG Conf. Dig., Dec. 2000, pp. 1-11.

[8] US Pat. 5047737 "Directional Coupler and Termination for Stripline and Coaxial Conductors," W. Oldfield, Sept. 10th 1991

[9] W. Oldfield, "Connector and termination construction above 50 GHz" Applied Microwave & Wireless," April 2001, pp. 56-66.

[10] W. Oldfield, "Development of Broadband Coaxial Components for a 0.04 to 110 GHz Measurement System," IEEE MTT-S International Microwave Symposium Digest, Orlando, FL, May 1995, pp. 1471-1473.

[11] T. Roberts, B. Y.S. Lee, "A Superior Solution to Control the Connection Repeatability of Coaxial Airline Impedance Standards used for Network Analyzer Verification," 77th ARFTG Digest, Spring 2011.

[12] J. Hoffmann, J. Ruefenacht, M. Wollensack, and M. Zeier, "Comparison of 1.85 mm Line Reflect Line and Offset Short Calibration," 76th ARFTG Digest, Fall 2010.

# Global Dynamic FET Model for GaN Transistors: *DynaFET* Model validation and comparison to locally tuned models

Jianjun Xu[1], Subrata Halder[2], Faramarz Kharabi[2], John McMacken[2], Joseph Gering[2], and David E. Root[1]
[1]Agilent Technologies, Inc., Santa Rosa, CA 95403 USA
[2]RFMD, Greensboro, NC 27409 USA

***Abstract* — Extensive results are presented validating a recently enhanced large signal FET model, *DynaFET*, applied to an advanced 6x75um periphery, 0.5um gate-length GaN HFET transistor, manufactured by RFMD. Excellent results are achieved for DC (including leakage current), S-parameters versus frequency and temperature, harmonic and intermodulation distortion, as well as load-pull figures of merit, over a very wide range of bias conditions, complex loads, powers, and frequencies. The DynaFET model features detailed dynamic trapping and de-trapping mechanisms for gate and drain lag, and dynamic self-heating. The multi-variate constitutive relations are represented by artificial neural networks (ANNs) trained from large-signal waveform data obtained using an active source injection NVNA-based characterization procedure. The new model is compared with two empirical models, each independently extracted from pulsed I-V data from different quiescent bias points and tuned for specific applications. The DynaFET model is demonstrated to have a much better fit than each of the individually tuned models, even at the tuned conditions. The new global model is sufficiently accurate over the entire operating range of the device that no tuning of model parameters is required for different operating points or amplifier classes of operation. The model runs in transient, harmonic balance, envelope, and all other simulation modes.**

***Index Terms* — Semiconductor device modeling, GaN, Compact models, power transistors, Microwave FETs, Neural networks, Nonlinear Vector Network Analyzer.**

## I. Introduction

GaN semiconductor technology has been developing very rapidly over the past few years. More and more foundries around the world are providing this technology for a very wide range of applications. GaN technology offers power densities (e.g. 7W/mm at microwave frequencies) much higher than GaAs, for example. Applications include high-power high-efficiency amplifiers (e.g. Doherty), efficient power generation (e.g. envelope tracking), radar, and more. GaN is pushing into the mm-wave region as well, and will eventually be widely available for generic circuit and MMIC design.

An accurate nonlinear transistor model (compact model) is a key requirement for efficient, flexible, first-pass PA and MMIC design in GaN technology. The wide range of GaN processes for various applications from low MHz to mm-wave, means the model should be very generic and flexible. The GaN FET model validated extensively in this work was introduced in [1]. The model is an extension and generalization of the approach first presented in [2] that had, until recently, been validated only for GaAs transistors. The modeling flow includes an enhanced, natively compiled (in Agilent ADS) dynamical model with trapping and self-heating effects, a new nonlinear device characterization system based on an NVNA with automated and adaptive active injection excitations incident simultaneously at input and output ports (synthetic load-dependence), and an enhanced ANN training procedure.

The present work reports extensive and detailed DynaFET nonlinear model validation results for a wide range of DC, small-signal, and large-signal performance conditions, including harmonics, load-pull, and intermodulation characteristics measured on an advanced GaN HFET device from RFMD. It also compares the global DynaFET model to two locally extracted empirical models based on pulsed IV data, each model tuned for optimal performance at distinct operating conditions. This treatment is the first to compare models constructed from large-signal CW data with those based instead on more conventional pulsed I-V data.

The characterization and hardware configuration is summarized in Section II. The model and its key features are summarized in section III. The training of the model from the waveform data is described in Section IV. Extensive validation results for the new modeling flow are presented in section V(A). Comparisons to independently extracted (to pulsed I-V data) empirical models is presented in section V(B). A discussion of the results, with implications, is provided in section VI. A Conclusions section ends the paper.

## II. Device Characterization

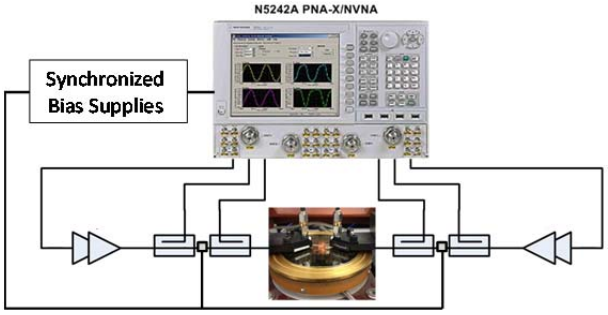


Fig. 1: Typical hardware configuration for active source injection characterization. The wafer chuck is temperature controlled. Power amplifiers boost the signal from the two internal NVNA sources. The NVNA synchronizes the bias supplies.

The hardware configuration is shown in Fig.1. An automated, adaptive, large-signal data acquisition software application was implemented on top of the NVNA nonlinear measurement system [6]. This data acquisition system controls

978-1-4799-4423-1/14/$31.00 ©2014 IEEE

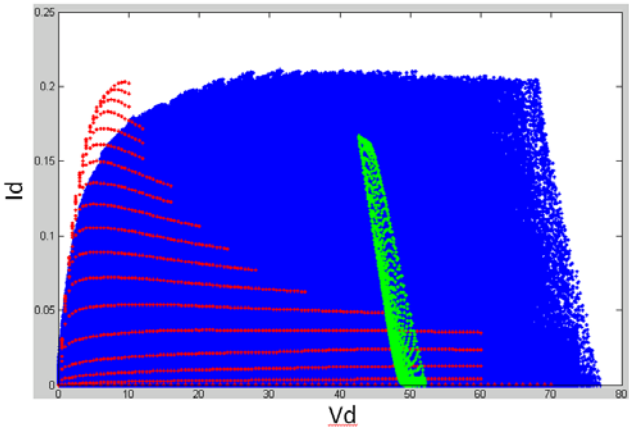


Fig. 2: Data domain in Id-Vd space of the 6x75um GaN transistor. DC I-V data (red), Id(t) vs Vd(t) from single-tone CW data versus power at 3.5GHz at quiescent point QVd=48V, QId=10mA into 50 ohms (green), and the complete set of Id(t) vs Vd(t) data (blue) from the active source injection measurements used to identify the global model.

the incident waveform excitations at both device ports, enforces device compliances for such quantities as the instantaneous gate-drain voltage, $V_{gd}(t)$ - related to breakdown - and enables large-signal coverage of the entire operating space of the device. The extent of this data is shown in blue in Fig. 2. The waveform data covers the entire region of device operation, to about 20W/mm instantaneous power, well beyond the limit of about 5W/mm for the DC measurements shown in red. These waveforms capture the transistor response at 1-10 nanosecond timescales, considerably faster than the 100-1000 nanosecond scales associated with typical pulsed bias windows.

The set of waveform data, blue in Fig. 2, does not reach up to the knee of the DC I-V curves. This is evidence of "drain-lag", or localized knee walk-out, typically seen in GaN HFET devices. Both the shape and position of the observed knee depend on the dynamical large-signal condition of the device operation. The DynaFET model provides a unique dynamical mechanism to account for this phenomenon.

## III. Model Topology and Features

The intrinsic model equivalent circuit topology is given in Fig. 3. The trapping and de-trapping circuits are based on [3] but the nonlinear coupling of the trap states and other state variables to the drain current generator is modeled by much more comprehensive functional relationships using artificial neural networks (ANNs) [1], [2].

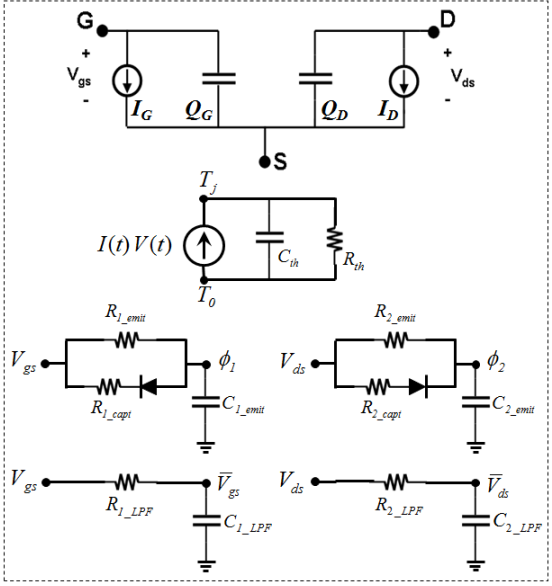


Fig. 3. Dynamic model intrinsic equivalent circuit, showing the electrical (top), thermal (middle), trapping circuits & average circuits (bottom).

The default measurement and training scheme [1] is modified from that of [2]. In the present approach, NVNA waveforms are measured at 100MHz, under large-signal active injection stimuli applied simultaneously at the input and output ports. For each waveform, trap state values, junction temperature, and other state variable values are computed. The result of the training, for example, is the explicit nonlinear dependence of Ids on the instantaneous intrinsic terminal voltages, $V_{gs}(t)$, $V_{ds}(t)$, junction temperature, $T_j(t)$ , trap states, $\phi_1(t)$ and $\phi_2(t)$ , and auxiliary dynamical variables [1]. The new model adds more functionals of the intrinsic voltage waveforms to create additional dynamical variables, beyond those reported in [2].

## IV. Model Identification From Waveform Data

The objective of the training procedure is to identify the functions $I_D$, $Q_D$, $I_G$, and $Q_G$ in Fig. 3 from the ensemble of DC, S-parameter, and large-signal data. The NVNA captures large-signal waveforms, calibrated to the device planes. For characterization and model generation, the nonlinear measurements are taken at several input power levels from small-signal to large signal, up to and often beyond 10dB of compression, at a single fundamental frequency, typically around 100MHz, for several different power levels at the output port using a second synthesizer at various relative phases compared to the signal on the input port. An adaptive algorithm automatically and adaptively controls both incident signals, and their relative phase, and the DC biases. These measurements are repeated at one or more ambient temperatures. DC and single-frequency (in the GHz range) S-parameter data, at two temperatures, are also taken collected. The lower frequency waveform measurement simplifies the

training compared to [2] where displacement current effects had to be simultaneously accounted for. Relative phase control of the large injected signals is critical to cover the full operating range while preventing the device from entering dangerous operating regions (e.g. breakdown). There is no need for an iterative convergence to effective complex loads on a grid; all that is necessary is a complete coverage of the device operating space. The ANNs are trained on the scattered multi-variate data – one of the major advantages of neural networks [5].

## V. Results

### (A) Comparison to measured data

The device chosen for the model extraction and verification is an on-wafer, 6x75um (450um total) gate-width, 0.5um gate-length GaN HFET, utilizing RFMD's GaN2C process. This technology is optimized for high linearity applications such as PMR and CATV in the 500MHz – 4GHz range. The transistor technology has a power density up to 4W/mm with a breakdown voltage over 300V [7].

DC validation results are shown in Fig. 4, in this case representing the device behavior at 55°C. A key feature of the model is the detailed and accurate simulation of the nonlinear gate leakage current, as well as its turn-on characteristics.

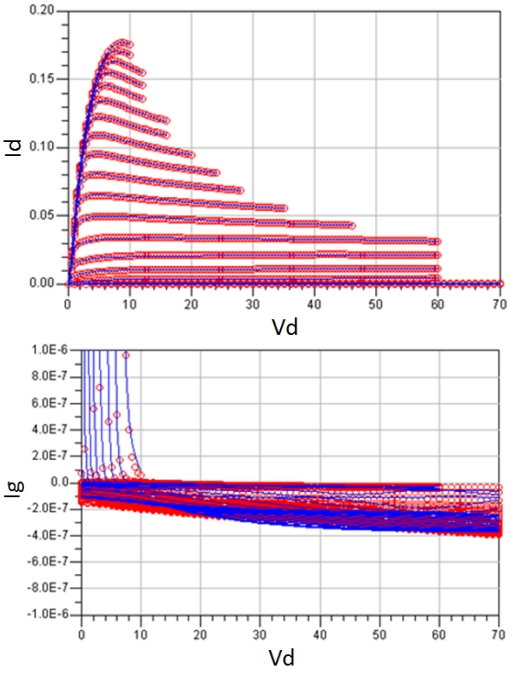


Fig. 4: Drain current (top) and gate current (bottom) versus bias at an ambient temperature of 55°C. Modeled (blue) and measured (red).

Broad-band S-parameter simulations, from 0.1GHz to 10.9GHz, are validated by independent measurements at many bias points. Examples are shown in Fig. 5. The model is generated from data only at 100MHz (large-signal), and 1.9GHz (S-parameters), yet the validation proves the model predicts very accurate broad-band S-parameters over all the device active operating range.

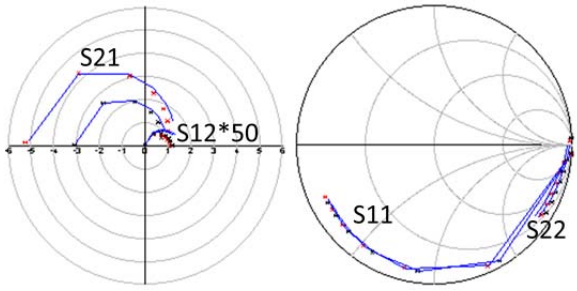


Fig. 5: S-parameters simulated from 0.1GHz – 10.9GHz (blue lines) at bias points of Vd=48Vand Id=12mA (red symbols), and 28V, 3.9mA (black symbols). The model was generated from data at only 100MHz and 1.9GHz.

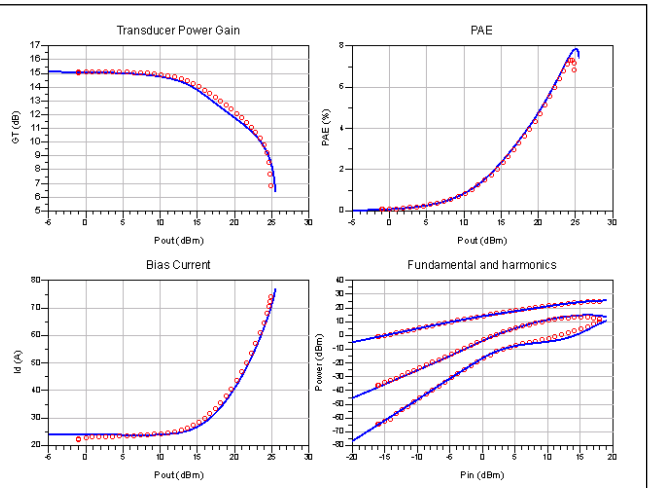


Fig. 6: Gain compression (upper left), bias current (lower left), power added efficiency (upper right), and fundamental and first two harmonics versus input power (lower right), modeled (blue) and measured (red). Freq=1GHz, V=48V, Id=20mA, Source & Load=50Ω.

A comparison of the model large-signal predictions with respect to measured gain compression, bias current, power added efficiency (PAE) and harmonic distortion is presented in Fig. 6. The model agrees to a very high level (9dB) of compression and does a very good job modeling the detailed shape of the compression and harmonic distortion curves. Similar accuracy was observed at other operating points and other fundamental frequencies.

Two-tone intermodulation simulations and validation data are presented in Fig. 7. Fig. 8 compares simulated and measured load-pull data for both delivered power and power added efficiency.

### (B) Comparison to locally extracted empirical models

The local models used in the subsequent comparison are based on the well-known EEHEMT model [8] extended to include dynamic self-heating and localized knee walkout

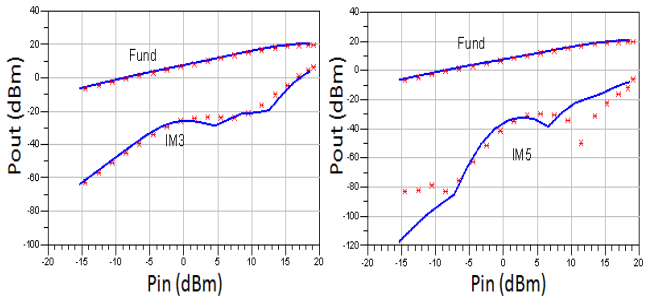


Fig. 7: Two-tone intermodulation distortion (upper sidebands) versus input power per tone for f1=3.5 GHz and f2=3.505GHz, for Vd=48V, Id=10mA. Simulation (blue) & measurements (red). The noise floor of the measurements is about -80dBm.

based on extraction to pulsed IV data, as reported in [9]. In particular, localized knee walk out is modeled by changing the empirical expression of [8] for the drain current, in order to fit the shape and position of the knee of pulsed IV data. Since this is a static approach, the model is essentially parameterized by the particular quiescent point (initial condition) of the pulsed IV measurements. Even with the addition of dynamic self-heating and localized knee walkout however, such models do not have sufficiently detailed *dynamic* trapping and de-trapping mechanisms to *simultaneously* predict DC, pulsed, and large-signal CW performance. Typically, for high-power circuit design, pulsed IV data are used to characterize the device over a large region of current and voltage. However, pulsed I-V data depend very sensitively on the quiescent point chosen for the initial condition [3], [9]. Typically, the initial condition of the pulse is associated with the quiescent bias of the subsequent application. This means the resulting extracted model must have some *a priori* knowledge of its later application, a significant restriction on its transportability.

For this work, the empirical models were extracted from two sets of pulsed I-V data, one starting from quiescent point [QVgs=-1V, QVds=28V] and the other from [QVgs=-1V, QVds=48V]. The data was acquired using an AMCAD PIV system, with pulse-widths of 650 ns. The pulsed I-V characteristics for each case are shown in Fig. 9. The devices used for these models are 6x370um, and the resulting models are then scaled down to 6x75um for comparison to the DynaFET model. It should be noted that the nearly 1/5 scaling of the empirical models is beyond the normally recommended model scaling range. Uncertainties in the parasitic element

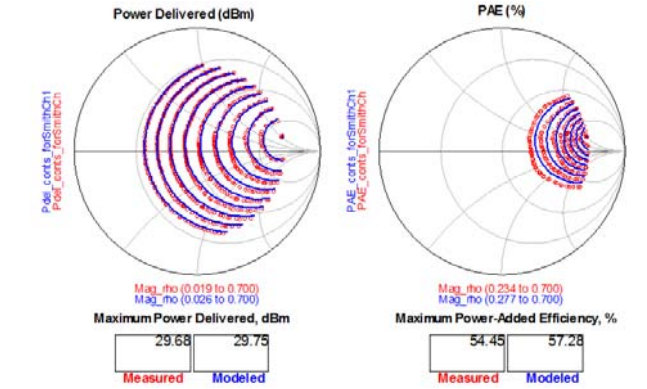


Fig. 8: Contours of measured (red) and modeled (blue) power delivered to the load and power added efficiency, at Vd=28V, Id=10mA, Pin=17dBm, at 1GHz. Contours in 1dB & 5% steps, respectively.

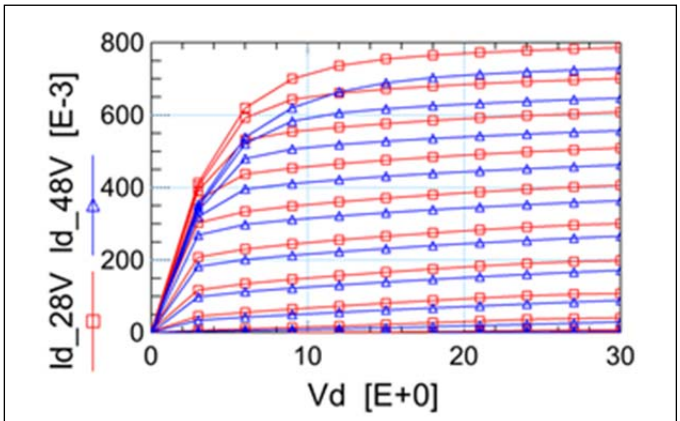


Fig. 9: Pulsed I-V characteristics from two different quiescent bias points [QVgs=-1, QVds = 28V] (red) and [QVgs=-1V , QVds=48V] (blue) used to extract and tune the empirical models [9] used for comparison to DynaFET. The curves correspond to (pulsed) gate voltages from Vgs = -2.5V to 1V, with 0.25V step.

scaling rules are accounted for, approximately, by correcting fixed capacitance values on the GS, GD, and DS branches of the equivalent circuit, until the gain from the models matched the measurements of the 6x75um device.

The parameter values of the empirical models are extracted to match a variety of performance conditions corresponding to the quiescent bias point of the pulsed I-V characteristics, as well as load-pull data around optimum PAE with the device biased at the quiescent point. The resulting local models, referred to as the RF28V and RF48V empirical models, for simplicity, are provided to designers who select between them based on the particular design application in mind.

The measured and simulated DC I-V curves for DynaFET and one of the local models is shown in Fig. 10. Both models fit well in the saturated region of operation, most important for large-signal RF operation. The DynaFET model also fits

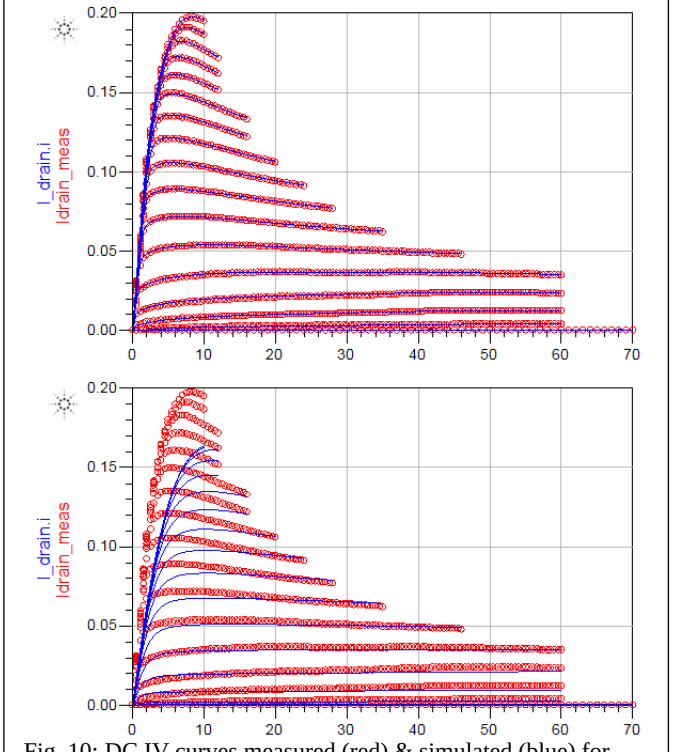


Fig. 10: DC IV curves measured (red) & simulated (blue) for DynaFET (top) & localized RF28V model (bottom). The discrepancy at the knee of the curves for the RF28V DC simulation demonstrates the inherent limitation of static localized knee walkout models: they can fit some RF large-signal characteristics and pulsed IV curves, but not also the measured DC characteristics with a single set of parameters.

nearly perfectly to the actual DC measured knee voltage, which is quite different from the effective knee voltage under either pulsed IV or CW large-signal stimulus. The discrepancy of the RF28V model in the knee area is due to the inherent compromise of the static modeling of knee walkout, which was tuned to the pulsed IV data, and therefore cannot also fit the true DC characteristics.

Measured and modeled large-signal performance is compared among the three models in Figs. 11 and 12. In Fig. 11, the models are compared with data at 48V, corresponding to the conditions under which the RF48V model was tuned, where the impedance was selected for optimum large-signal performance. In Fig. 12, comparisons are shown for the bias condition for which the RF28V model was tuned, but this time using a 50 ohm termination that was not the same as that used for tuning either of the empirical models. It can be concluded that the DynaFET model fits as well or better, over all tested conditions, than the empirical models, even when comparing

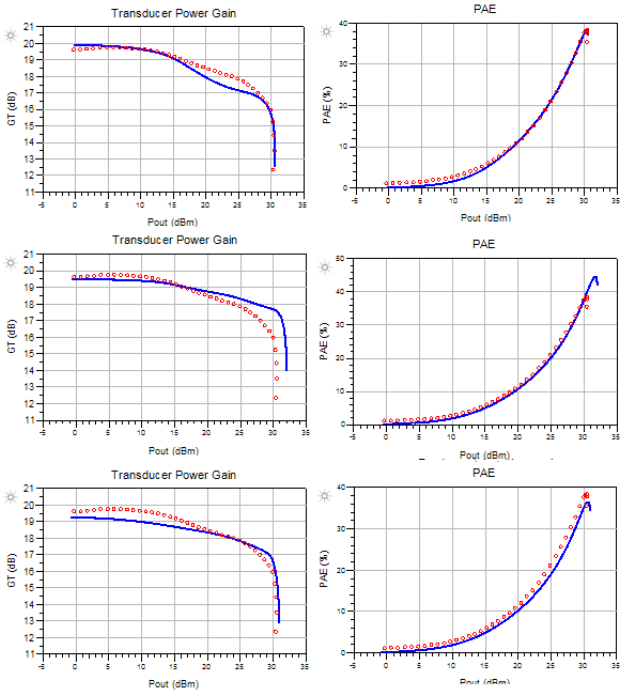


Fig. 11 Gain versus power and power added efficiency at optimum load at 1GHz measured (red symbols) versus simulation (blue lines) for DynaFET (top row), RF28V model (middle row) and RF48V model (bottom row). The measured quiescent bias conditions for this test corresponds to Id=10mA,Vds=48.

at the specific regions of performance around which the local models were tuned. This conclusion holds also for harmonic and intermodulation distortion comparisons.

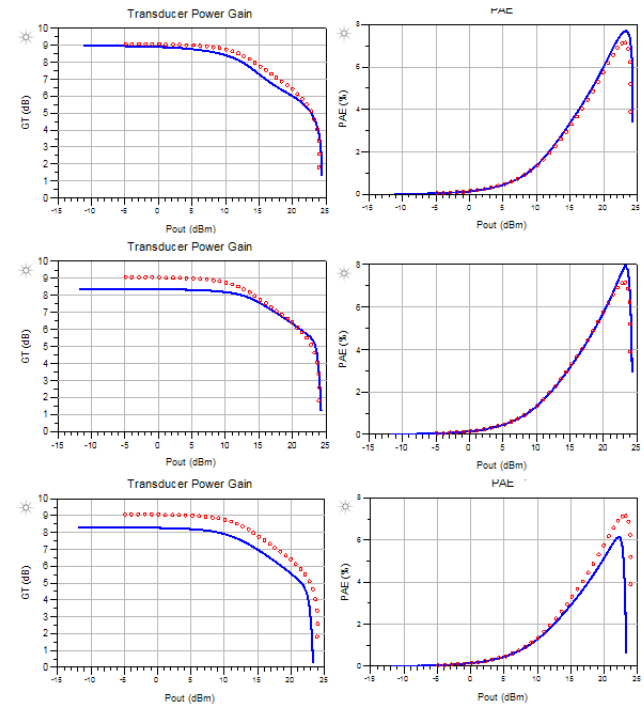


Fig. 12 Gain versus power and power added efficiency into 50 ohms at 3.5 GHz measured (red symbols) versus simulation (blue lines) for DynaFET (top row), RF28V model (middle row) and RF48V model (bottom row). The measured quiescent bias conditions for this test corresponds to Id=20mA,Vds=28V

## VI. Discussion

Parameter value tuning can enable simpler models to be used to achieve reasonable fits to performance data. However, depending on the sophistication of the empirical models, the range of validity of the resulting model is restricted to the environment around which its parameter values are optimized. This can mean extensive searching in the characterization space for optimal performance, prior to model extraction, and then independent optimization to these subsets of data. It also means providing multiple parameter sets, or multiple “bins,” for models of the same device that don’t agree with one another.

The advantage of the new DynaFET characterization and modeling flow is that it results in a single, global model, based on automatically characterized data. This means the optimal device performance region, which can vary greatly according to bias, frequency, and load, can be determined in simulation, rather than on the bench. This is only possible if the model is sufficiently general and accurate over the entire accessible range of device operation, where the DC, high-frequency, and large-signal RF responses can all be predicted from the same model.

The DynaFET model uses the large-signal waveforms, as well as DC and S-parameter data, to separate dynamical mechanisms of trapping, de-trapping, and self-heating. The

model then re-combines the independently identified mechanisms into a predictive nonlinear simulation model of the conventional "compact" time-domain form, unlike that of, for example, an X-parameter model [4] that is restricted to the frequency or envelope domains. That is, the DynaFET compact model works in all modes of simulation (e.g. transient (TA), harmonic balance (HB), circuit envelope (CE), AC, SP, and more. The ANN-based constitutive relations can model the very general and detailed nonlinear coupling of the trap states and other dynamical variable without additional simplifications, such as assuming the traps modulate the pinch-off voltage, as postulated in [3]. Additionally, the ANNs' straightforward mathematical form doesn't impact convergence, where empirical models typically trade off complexity for convergence. The DynaFET model includes fully two-dimensional nonlinear intrinsic device capacitances, providing more accuracy for high-frequency simulation than the one-dimensional simplifications of [3]. It is scalable with geometry in the same way as conventional empirical compact transistor models and has an external thermal node for mutual thermal coupling of multiple devices and/or coupling to the local thermal environment.

## CONCLUSIONS

An enhanced large-signal dynamic FET model – *DynaFET* - with self-heating and detailed trapping effects, has been identified using an active source injection large-signal NVNA waveform characterization application, and extensively validated experimentally on an advanced microwave GaN transistor manufactured by RFMD. The DynaFET model has also been compared to two extractions of an established empirical model tuned for applications at specific quiescent bias points. The model has been systematically identified from large-signal waveform data obtained from automatically controlled NVNA active-source injection large-signal measurements, as well as single frequency S-parameter and DC data. The model is natively implemented in a commercial nonlinear circuit simulator (Agilent ADS). The DynaFET model predicts the DC, broad-band, linear and high power nonlinear behavior of the DUT, including harmonic and intermodulation distortion and load-pull performance over the full active range of device operation. Even for the range around the localized empirical model extractions, the global DynaFET model achieves comparable or better performance than the empirical models. This demonstrates that DynaFET presents a single, global model that can predict the range of device performance indicative of the technology, without the need for any tuning of empirical model parameters. This should simplify the foundry process design kits, and offer designers both more confidence and also more degrees of design freedom with the GaN technology.

Extensive independent large and small-signal measurements, not used in the model fitting, were used to validate the model. The model incorporates frequency dispersion, very accurately accounts for leakage current, distortion effects from small-signal conditions to very large levels of compression at low and high frequencies, accounts for "knee walkout," and other large-signal dynamical effects common to GaN FETs. This paper presented the detailed results from an advance microwave GaN semiconductor process manufactured by RFMD. The model has been similarly validated for a range of other GaN and GaAs devices, with quite different characteristics, from several different manufacturers, with similar results. The modeling flow is therefore expected to be of great utility for accurate and general nonlinear modeling of GaN and GaAs transistors.

## REFERENCES


[1] J. Xu, R. Jones, S. A. Harris, T. Nielsen, and D. E. Root, "Dynamic FET Model – *DynaFET* - for GaN Transistors from NVNA Active Source Injection Measurements," *IEEE International Microwave Symposium Digest*, Tampa, FL. June, 2014

[2] J. Xu, J. Horn, M. Iwamoto, D. E. Root, "Large-signal FET model with multiple time scale dynamics from nonlinear vector network analyzer data," *IEEE MTT-S International Microwave Symposium Digest*, May, 2010

[3] O. Jardel, F.D. Groote, T. Reveyrand, J.C. Jacquet, C. Charbonniaud, J.P. Teyssier, D. Floriot, and R. Quéré, "An Electrothermal Model for AlGaN/GaN Power HEMTs Including Trapping Effects to Improve Large-Signal Simulation Results on High VSWR," *IEEE Trans. MTT.*, vol. 55, pp. 2660-2669, 2007.

[4] D.E. Root, J. Verspecht, J. Horn and M. Marcu, *X-Parameters: Characterization, Modeling, and Design of Nonlinear RF and Microwave Components*,Cambridge University Press, 2013.

[5] Q.J. Zhang and K.C Gupta, Neural Networks for RF and Micrwoave Desgin, Normawar, MA: Artech House, 2000.

[6] http://www.agilent.com/find/nvna

[7] http://www.rfmd.com/openfoundry

[8] Agilent ADS Documentation: nonlinear component manual

[9] Kharabi, F.; McMacken, J.R.F.; Gering, J.M.,"A Verilog-A Large-Signal GaN HEMT Model for High Power Amplifier Design" Compound Semiconductor Integrated Circuit Symposium (CSICS), 2010

# A Digital, PXI-Based Active Load-Pull Tuner to Maximize Throughput of a Load-Pull Test Bench

*Tudor Williams, **Brian Wee, *Randeep Saini, *Simon Mathias, **Marc Vanden Bossche

*Mesuro Ltd. Pencoed Technology Park, Pencoed, CF35 5HZ

** National Instruments Belgium NV/SA, Network Analyzer Centre of Excellence, Belgium

**Abstract — This paper presents a cost effective, digital, PXI-based active load-pull tuner architecture. This allows for significant reduction in test time, without compromising measurement quality or control. We will demonstrate for the first time, ability to compensate for the non-linear behavior of the loop amplifier within the active loop, thus moving from a proof of concept architecture to one that is applicable to real-world applications. The calibration process required for accurate reflection coefficient setting is presented, as well as analysis of the long-term reflection coefficient stability. It is shown how the RF bandwidth of the architecture can be increased through the use of up/down convertors directly in the feedback loop, with testing completed at 17GHz. A direct comparison in measurement time between passive, active open-loop and the digital architecture is also presented, showing the digital tuner as much as 14 times faster than a passive tuner for a fixed power impedance grid, using the same measurement receiver and setup.**

**Index Terms — Load-Pull, Active Load-Pull, Non-linear measurements, non-linear modeling, behavioral modeling, power amplifiers.**

## I. Introduction

Traditionally, load-pull, has been achieved using passive tuners [1], indeed such tuners are still dominant in the market, and have become an integral part of semiconductor device test process from initial device understanding through to final application in design or modeling. Limitations of passive tuners are well documented, most notably issues with presenting very high reflects, vibrations, physical size etc. These do not however, prevent the large-scale use of such tuners. By far the largest issue faced by the industry is measurement throughput, as changing impedance state is a mechanical operation, it is inevitably slow.

The solution presented in this paper is an active load-pull architecture; whereby emulation of load impedance is achieved by injecting an amplified signal of specific magnitude and phase into the output of the DUT. Such systems are not without issue, and this has hindered their application to date. Active systems can be configured as "open loop" or "closed loop" architecture. In a "closed loop" system; first presented by Bava [2], the injected signal is a modified version (direct function) of the DUT output signal. This ensures that the emulated load impedance (matching circuit) is independent of drive level, however this architecture is prone to oscillations. Most modern commercial solutions are therefore "open loop" systems, first introduced by Takayama [3], in which the injected signal is generated independently. This avoids the oscillation problems, however in order to maintain constant load impedance under changing drive conditions, a number of magnitude and phase adjustments of the injected signal are required. This results in a potentially slow, iterative process to maintain the target reflection coefficient. In addition, such systems are typically packaged as full measurement systems including state of the art test and measurement equipment, making them very expensive.

The solution presented overcomes the aforementioned issues, firstly; the digital tuner is a self contained PXI module, which can be used as a drop-in replacement for a passive tuner. This means that the rest of the load-pull test bench can remain unchanged, leading to a cost effective solution. Based on the patented envelope load-pull technique, first presented in [4], the 'quasi' closed loop nature of this active load-pull architecture maintains all of the benefits of the closed-loop load-pull in terms of speed - no iterations are required to set or maintain an impedance. However, inherent stability issues are avoided, as the feedback loop is no longer closed at the RF frequency of operation, in addition the use of an FPGA directly in the loop allows limits to be set preventing uncontrolled power ramping.

## II. Digital Load-Pull Tuner Description

The system containing the digital tuner is shown in Figure 1, and is the schematic illustrated in Figure 2.

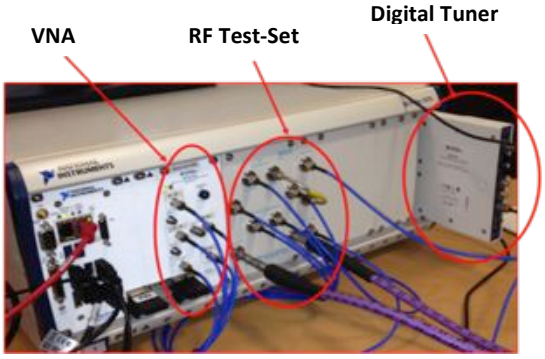


*Figure 1. Digital Tuner within a PXI based Measurement System*

The output port of the DUT is fed via a circulator through an attenuation stage to a PXI based transceiver card, which includes the down convertor module, an FPGA module and an up convertor module.

978-1-4799-4423-1/14/$31.00 ©2014 IEEE

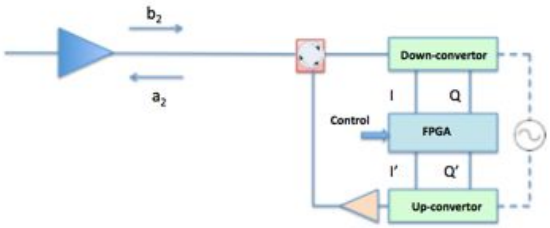


*Figure 2. Digital Tuner Schematic*

The signal is down-converted to I and Q signals that fully represent the signal at the device output. These I and Q signals are then processed based on the reflection coefficient set by the user to give a modified version I' and Q'. If the required reflection coefficient set by the user is represented by x+jy, then the required transfer function is the transfer function shown in (1).

$$F(x,y) = I' + jQ' = (xI - yQ) + j(xQ + yI) \qquad (1)$$

This formulation will ensure a drive-level independent emulated load, quantified by the user defined values of x and y. Conversion to RF frequency to provide the output-injected signal is achieved using the up-convertor module of the transceiver card.

Note that the up and down conversion process share a common local oscillator (LO) thus relaxing the requirement for the drive signal of the device and the active loop to be phase locked. This also means that there is no drift in phase over time – a problem inherent in most open-loop architectures.

The digital tuner also benefits from the ability to present constant load impedance over a wide bandwidth. Although not the topic of this paper, initial tests have shown that a constant load-impedance can be maintained and controlled for a signal spanning 10MHz, note here that latency in the loop leads to a requirement for a repetitive signal envelope. Further work is underway that should extended this to the full 100MHz instantaneous bandwidth of the FPGA.

## III. Loop Calibration and Effect of Non-Linear Elements

The first step in the calibration process is to define a linear error flow model for the load-pull loop as shown in Figure 3.

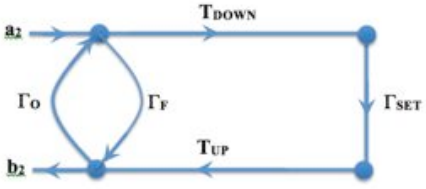


*Figure 3. Error Flow Model of the Digital Tuner*

Where $\Gamma_O$ is the system impedance (defined with zero gain set) $\Gamma_F$ is the feedback due to the limited isolation of the loop, $T_{DOWN}$ is the transfer function of the down-convertor and $T_{UP}$ is the transfer function of the up-convertor and $\Gamma_{SET}$ is the set impedance. From the error model it is clear that the set impedance, given by $a_2$ divided by $b_2$ is governed by (2) –

$$\frac{a_2}{b_2} = \frac{\Gamma_{SET} T_{DOWN} T_{UP}}{1-\Gamma_F(\Gamma_{SET} T_{DOWN} T_{UP})} + \Gamma_O \qquad (2)$$

We now introduce a new variable $\Gamma_{CORR}$, which is the corrected value sent to $\Gamma_{SET}$ to correct a given impedance setting to give (3)

$$\Gamma_{MEAS} = \left(\frac{\Gamma_{CORR} T_{DOWN} T_{UP}}{1-\Gamma_F(\Gamma_{CORR} T_{DOWN} T_{UP})}\right) + \Gamma_O \qquad (3)$$

Combining the effect of the down-conversion and up-conversion yields a new variable; the gain of the loop (G).
G is therefore given by (4)

$$G = T_{DOWN} T_{UP} \qquad (4)$$

Giving (5), which can be re-written as (6) –

$$\Gamma_{MEAS} = \Gamma_O + \Gamma_{MEAS}\Gamma_{CORR}(\Gamma_F G) + \Gamma_{CORR}\big(G(1 - \Gamma_O\Gamma_F)\big) \qquad (5)$$

$$\Gamma_{MEAS} = A + B(\Gamma_{MEAS}\Gamma_{CORR}) + C(\Gamma_{CORR}) \qquad (6)$$

Where –

$$A = \Gamma_O \qquad (7)$$
$$B = \Gamma_F G \qquad (8)$$
$$C = G(1 - \Gamma_O\Gamma_F) \qquad (9)$$

Only 3 independent measurements are required to fully characterise the loop. In reality more measurements are conducted to provide redundancy and improve overall accuracy (typically 100). The calibration process is extremely fast (around 20 seconds), a significant advantage over a passive tuner.

Figure 4 shows the target and achieved reflection coefficients for a grid of 50 load impedances where the maximum error is less than 1.3%.

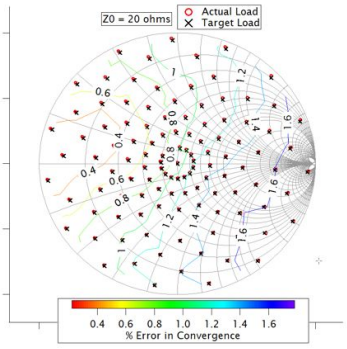


*Figure 4. Achieved calibration accuracy*

Once the linear calibration is complete, the user-defined impedance is maintained until the system amplifier becomes non-linear. To overcome this undesired variation in set impedance, an algorithm has been written allowing the user to set a tolerance for load convergence. As soon as the amplifier begins to compress and the load fails to converge the value of G is updated from the last measurement taken using the relationship shown in (10).

$$G = \frac{\Gamma_{MEAS} - \Gamma_0}{\Gamma_{CORR}(\Gamma_F(\Gamma_{MEAS} - \Gamma_0) + 1)} \qquad (10)$$

## IV. Long Term Reflection Coefficient Stability – Removing the Vector Receiver

There are two main reasons why the long-term stability of the presented reflection coefficient is important. Firstly even if measuring the impedance, we would like to be consistently setting the desired impedance grids as the measurements are run; secondly and more importantly as the architecture is framed as a passive load tuner replacement, there may well be a requirement for the VNA to be used for calibration then removed from the system. In this case it is necessary that there is no drift in the set impedance over the measurement time (as we will no longer measure the presented impedance). Clearly for this to be an option, the non-linearity of the loop power amplifier needs to be compensated within the FPGA, rather than on the fly (on the product roadmap).

Figure 5 shows the stability of a set reflection coefficient over a 24-hour period, with measurements taken every hour. As shown by the data, the digital tuner presents very consistent impedance over the 24 hours, with variation in magnitude and phase of 0.0089 and 1.2 degrees respectively. The final test was to define a grid of 100 load points; this grid is then run every hour for 24 hours. The results are shown in Figure 6, with target impedance is shown by a blue square with measured points shown by red X's. It can be seen from the data that excellent agreement is maintained throughout the duration of the sweep.

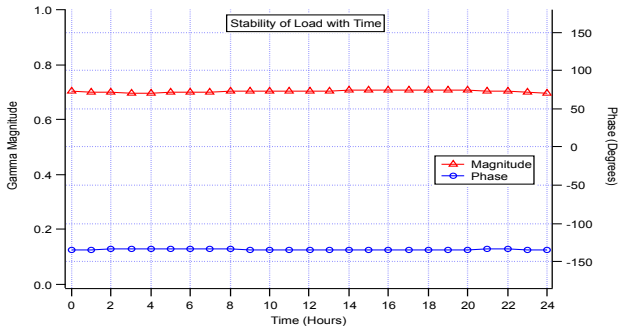


*Figure 5. Stability of a set reflection coefficient over a 24 hour period*

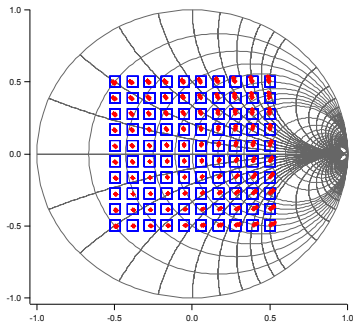

*Figure 6. Stability of a measured impedance grid over a 24-hour period*

## V. Frequency Extension

One potential limitation of the digital tuner presented thus far is the current upper operating frequency of the transceiver module, which is limited from 200MHz to 4.4GHz [5]. This becomes an issue for higher frequency applications which place higher requirements on fundamental frequencies, for example military applications. It would also limit the use of the tuner at harmonic frequencies for many of the traditional communications bands. In order to overcome this issue, the architecture of the load-pull loop was modified to as shown in Figure 7.

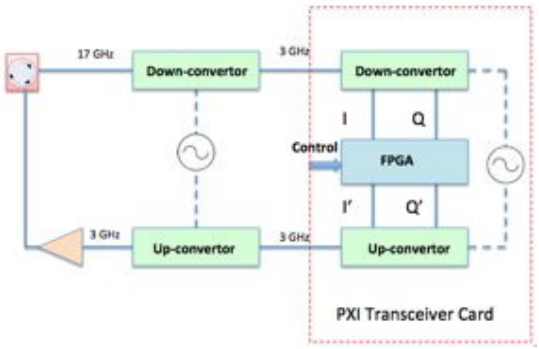


*Figure 7. Modified Architecture including up/down convertor*

In Figure 7, a further up/down convertor was employed within the loop, in this case allowing us to extend the operational frequency to 17GHz with a 1GHz bandwidth [6]. The calibration process is identical to the one presented in Section III since the properties of the up/down convertor are captured by the same error terms.

Testing showed the same accuracy and speed could be obtained with the new high frequency of operation, extending its functionality to a variety of applications.

## VI. System Comparisons

For the system comparisons; an identical vector receiver measurement system and measurement condition was used, all

controlled through the same software interface, with only the load-pull tuner architecture changing in each case. In all cases the measurement system was based around a Rohde and Schwarz ZVA-67 with control software from Mesuro Limited. The measurement IF bandwidth of the VNA was set to 100Hz. The system was calibrated for power, allowing power contours to be plotted. Note that DC bias and measurement can also be added to the system, however this is omitted for the basic speed test. The target grid used is shown in figure 8.

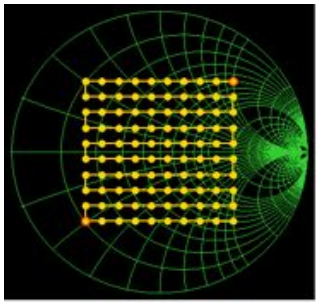

*Figure 8. Test grid for speed comparisons*

The resulting speed of each of the load-pull architectures is shown in Table 1; note that this test was created for a single drive level and just impedance was swept in each case.

| | **Sweep Plan (S)** | **Per point (S)** | **Relative to passive** |
|---|---|---|---|
| Passive LP | 278.70 | 2.79 | - |
| Active LP | 40.69 | 0.41 | - 85.41% |
| Digital LP | 18.52 | 0.19 | - 93.4% |

*Table 1. Comparison of load-pull time Impedance Only*

This was perhaps a little hard on the passive system, which is faster when it comes to swept power measurements, as once the load is set it is maintained over drive. However if we repeat the analysis for a 25dB power sweep with 1dB step for 50-point load-pull grid, the reduction in measurement time is still significant, see Table 2.

| | **Sweep Plan (Mins)** | **Per point (S)** | **Relative to passive** |
|---|---|---|---|
| Passive LP | 12 | 0.576 | - |
| Active LP | 8.0 | 0.384 | - 33.33% |
| Digital LP | 3.95 | 0.19 | - 67% |

*Table 2. Comparison of load-pull time with sweep plan*

The final step in the comparison was to compare the measured load-pull contours to ensure that the quality of the measurements is not affected by the speed. For this test the DUT was a 10W GaN packaged part running at 28V. The contours of output power for the passive architecture and the digital tuner at 1 dB compression point is shown in figure 9. As shown excellent agreement is obtained.

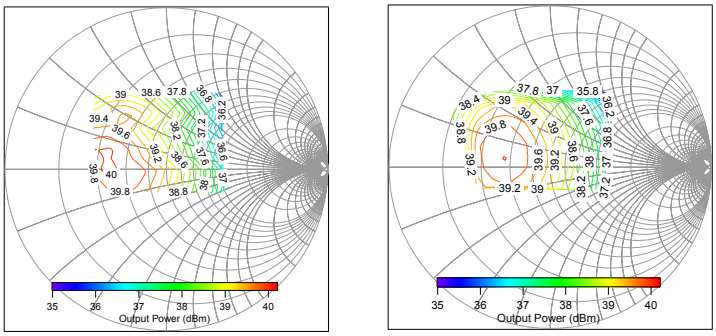


*Figure 9. Comparison of 1dB compression contours of power*

## VII. Conclusions

A new cost effective, digital, PXI based active load-pull tuner architecture has been presented; it has been shown that the architecture allows for significant reduction in test time, without compromising measurement quality or control. It has been shown that the digital tuner can be scaled to higher operating frequencies allowing for high frequency and harmonic application. The long-term stability of the architecture has been investigated with, showing excellent repeatability over a 24-hour period. Direct comparisons of the architecture were presented showing that the new digital tuner is as much as 14 times faster compared to incumbent technologies.

## Acknowledgements

This project has received funding from the ERDF under the SMARTCymru RD&I Scheme. The authors would also like to thank National Instruments, and in particular NI System Engineering Budapest for their helpful support with this project.

## References

[1] J.Sevic, "Introduction to Tuner Based Measurement and Characterization" Maury Microwave Corporation application note: 5C-054 Feb. 2004.

[2] J.P.Bava, U. Pisani, V. Pozzolo, "Active Load Technique for Load-Pull Characterization at Microwave Frequencies'" Maury Microwave Corporation application note: 5C-054 Feb. 2004. Electronic Letters 18th February 1982, Vol. 18, No. 4, pp. 178-180.

[3] Y. Takayama, " A New Load-Pull Characterization Method for Microwave Power Transistors" IEEE MTT-S Internatioanl Microwave Symposium Digest 1976, pp. 218-220.

[4] T. Williams, J. Benedikt, P. J. Tasker, "Novel Base-Band Envelope Load-Pull Architecture", Proceedings 9th IEEE High Frequency Postgraduate Colloquium, Manchester. Sept. 2004.

[5] National Instruments "NI 5791R User Manual and Specifications" User Manual May 2013.

[6] SenarioTek, "Wideband Frequency Convertors" Product Datasheet. May 2013.

# A Novel Half Space Time-Domain Measurement Technique for One-Dimensional Microwave Imaging

Sonu Lal Gupta[#1], Zubair Akhter[#2], Manoj Bhaskar[#3] and M. Jaleel Akhtar

Department of Electrical Engineering, Indian Institute of Technology Kanpur

Kanpur U.P.-208016 INDIA

[1]sonulal@iitk.ac.in , [2]zuakhter@iitk.ac.in, [3]bhaskar@iitk.ac.in

**Abstract — In this paper, the moisture content for cement based materials having different water to cement (w/c) ratios is measured using the microwave free space technique. The overall process is non-destructive and employs the time-domain measurement data. The measurement system consists of a vector network analyzer, a wide-band lens horn antenna, cement based material of having different water to cement (w/c) ratio and associated microwave components. The main focus here is to determine the permittivity, the effective conductivity and the thickness of test specimens under the situation, where only reflection measurements can be carried out due to the restricted access of the object from the other side. It is observed that the effective conductivity is directly proportional with the moisture content or the w/c ratios of these test samples.**

**Index Terms — Microwave NDT, moisture determination, water to cement ratio measurement.**

## I. Introduction

In the present scenario, most of the commonly used building materials are cement based. It is desired to inspect the quality, especially the strength of buildings on a regular basis for safety purpose. A number of techniques have been proposed in past to monitor conditions of the cement based buildings. These methods can be broadly categorized as the destructive and the non-destructive techniques. It is preferable to monitor the buildings or structures using a non-destructive approach so that they do not get damaged during the monitoring process. The non-destructive technique is also advantageous because no special sample preparation is required for the testing. It is mainly due to these advantages that the microwave non-destructive testing (NDT) is being used here for monitoring various concrete structures [1]-[3]. The microwave time domain method has recently been employed to determine the real part of complex permittivity of various samples [4]. However, it is equally important to determine the imaginary part of the complex permittivity in order to find the moisture content or the w/c ratios of cement based samples.

In this paper, both the real and imaginary parts of the complex permittivity of test specimens are measured using the proposed microwave free-space time domain approach. The thickness of the specimen is also determined during the process, which is advantageous under situations where the test sample or object cannot be accessed from the other side. It is observed that the imaginary part of the complex permittivity can be directly related with the moisture content, which helps in monitoring the quality, stability and aging of cement based structures. It may be mentioned here that various components of the structure such as the metal bar, air crack or porosity, can also be estimated using this procedure due to their difference in permittivity values and loss factors.

## II. Basic Procedure

The complex permittivity of material under test (MUT) is usually determined in the RF and microwave frequency range using the reflection and transmission coefficients data measured in the spectral domain. In the proposed method, only the reflection coefficient of test sample measured using the vector network analyser (VNA) is employed to estimate the complex permittivity of various structures. The measured reflection coefficient in the spectral domain is converted into time domain using the inverse FFT algorithm, which is observed on the time domain reflectometer (TDR) of the VNA. The proposed method utilizes the time domain reflected signal to calculate the dielectric constant, the thickness and the electrical conductivity various cement based samples. In order to accomplish this, a series of measurements have been carried out as shown in Fig. 1 and Fig. 2. In the first case, when a metal plate is placed in front of the sample, the EM wave is completely reflected from the metal surface. Thus only one high peak is observed on the TDR screen, which is approximately equal to the power available at that surface as denoted by $P_0$ in Fig. 1. In second case, when the metal plate

978-1-4799-4423-1/14/$31.00 ©2014 IEEE

is removed from the front side of the test sample, two peaks have been observed on TDR screen as shown in Fig. 2. The first peak here is due to the impedance mismatch between the air and front side of the MUT represented by $P_1$, while the second peak is due to the impedance mismatch between the back side of MUT and air represented by $P_2$.

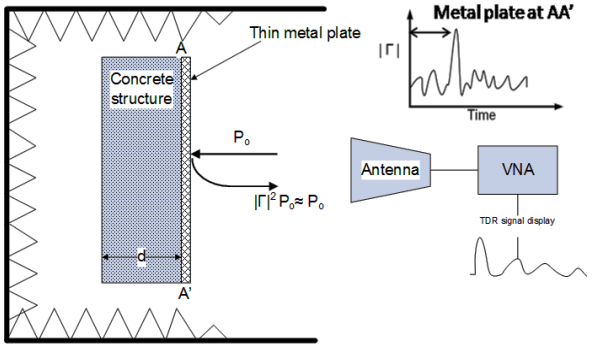


Fig. 1. Measurement System Configuration (first case)

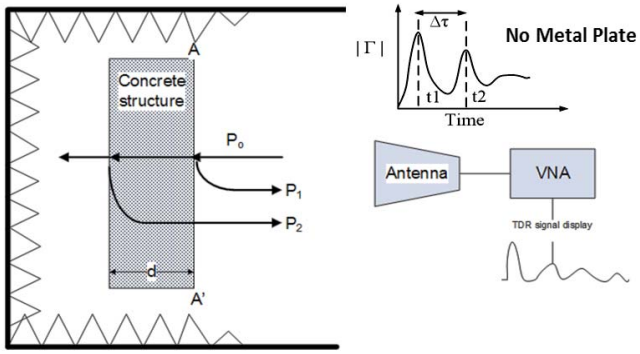


Fig. 2. Measurement System Configuration (second case)

These peaks shown in Figs. 1 and 2 are directly measurable, and can be observed on the TDR screen. The next task is to relate these reflection coefficient peaks with the desired parameters viz. the relative permittivity, the electrical conductivity, and the thickness of test samples. The relationship between the incident power ($P_0$) and the reflected power ($P_1$).can be given as follows

$$\left|\Gamma\right|^2 = \frac{P_1}{P_0} \tag{1}$$

where, Γ is defined as the local reflection coefficient of the test sample, which can be determined in terms of measured powers $P_0$ and $P_1$. The relative dielectric constant and the thickness of test samples can be determined as follows.

$$\varepsilon_r = \left(\frac{1+\left|\Gamma\right|}{1-\left|\Gamma\right|}\right)^2 \tag{2}$$

$$d = \frac{c\,\Delta\tau}{2\sqrt{\varepsilon_r}} \tag{3}$$

where, $c = 3\times10^8\, m/\sec$, $\Delta\tau = t_2 - t_1$ is the time difference between two peaks of reflection coefficient shown in Fig. 2. In order to calculate the effective conductivity of test samples, the following relationship between the incident power ($P_0$) and the reflected power from the second TDR peak ($P_2$) is utilized

$$P_2 = \left|\Gamma\right|^2 (1-\left|\Gamma\right|^2)^2\ P_0\ e^{-4\alpha d} \tag{4}$$

where, $\alpha$ is the attenuation constant. The propagation constant $\gamma$ and attenuation constant are defined as follows [5].

$$\gamma = \alpha + j\beta = \sqrt{j\omega\mu(\sigma + j\omega\varepsilon)} \tag{5}$$

$$\alpha = \omega\sqrt{\frac{\mu\varepsilon}{2}\left\{\sqrt{1+\left(\frac{\sigma}{\omega\varepsilon}\right)^2} - 1\right\}} \tag{6}$$

In limiting case, when $\left(\frac{\sigma}{\omega\varepsilon}\right) \le 0.1$, (6) can be simplified for the non-magnetic medium to obtain the following relationship

$$\sigma = \frac{2\alpha\sqrt{\varepsilon_r}}{\eta_0} \tag{7}$$

where, $\eta_0$ is the free space intrinsic wave impedance.

## III. MEASUREMENT SETUP

The actual measurement system shown in Fig.5 consists of a horn antenna with dielectric lens from Q-par Angus Ltd, the metallic plate and the vector network analyzer. The wide band horn antenna with the dielectric lens has bandwidth over 1 to 18 GHz. It is used in order to have high directivity and low beam width. The measurement is carried out over wide frequency range from 1 to 15 GHz. The typical gain of the antenna is 11.6 dB and beam width is 43 degree at the central frequency of 8 GHz. It is assumed here that the size of test sample is sufficiently large as compared to the antenna's aperture. The sample is kept in the far field region so that the TEM wave can be assumed to be incident normally over the

test sample. The summary of employed cement based samples can be seen in Table I.

TABLE I. SUMMARY OF CEMENT BASED MATERIAL.

| Sample (w/c) | Material Used | Material Ratio | Width (cm) |
|---|---|---|---|
| SS 4 (0.4) | Cement & Standard Sand | 1 : 3 | 6.5 |
| SS 6 (0.6) | | 1 : 3 | 6.5 |
| C 5 (0.5) | Cement & Sand & Agg. (20 -10) mm. | 1 : 1.58 : 3.12 | 7.0 |

Agg. (Concrete)

These samples have been tested, and the time-domain reflection coefficient has been measured for both the cases (when metal plate is present and when there is no metal plate). The recorded traces of time domain reflection coefficients for C-5 and Teflon have been shown in Fig. 3 and Fig. 4 respectively

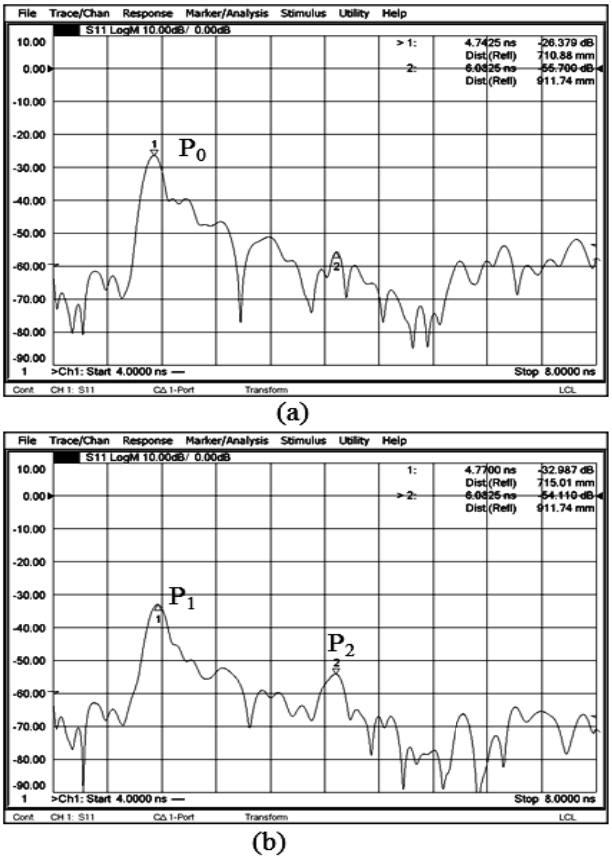


Fig. 3 Time-domain reflection coefficient trace for C-5, (**a).** With metal plate at interface, **(b).** without metal plate

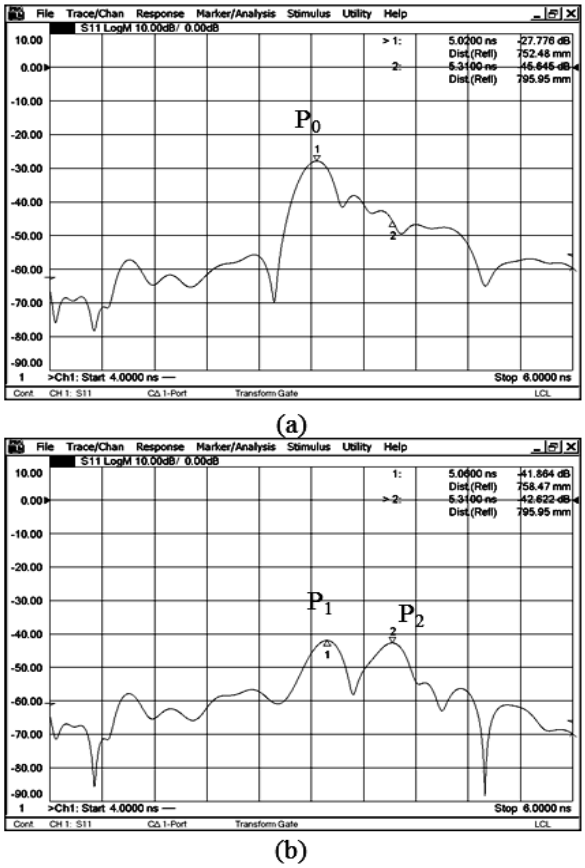


Fig. 4 Time-domain reflection coefficient trace for Teflon, (**a).** With metal plate at interface, **(b).** without metal plate

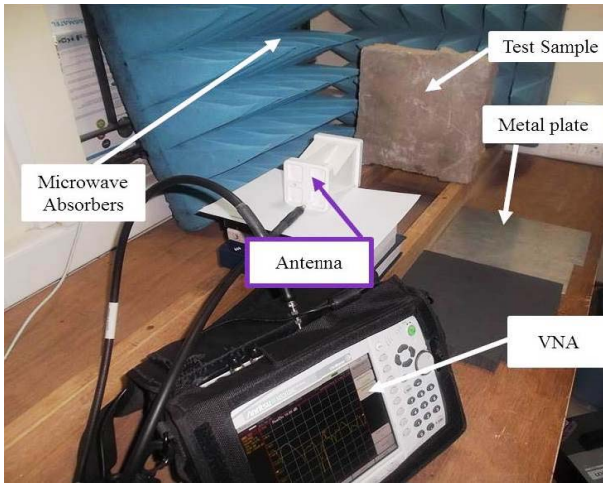


Fig.5 Measurement setup for testing test sample.

The values of incident and reflected powers along with respective time difference in peaks for test specimens are shown in Table II. The results of relative permittivity, effective conductivity and the thickness of cement based test samples are shown in Table III. In order to validate this scheme, some standard samples have first been measured, and the results are compared with the data available in literature as shown in Table IV

TABLE II. MEASURED INCIDENT AND REFLECTED POWERS FOR DIFFERENT TEST SAMPLES.

| Sample | $P_0$ (dB) | $P_1$ (dB) | $P_2$ (dB) | $\Delta\tau$ (ns) |
|---|---|---|---|---|
| Teflon | -27.776 | -41.864 | -42.622 | 0.2500 |
| PVC | -26.296 | -38.465 | -41.491 | 0.2625 |
| PMMC | -27.470 | -39.777 | -42.518 | 0.2563 |
| SS4 | -26.857 | -34.307 | -50.982 | 1.0969 |
| SS6 | -26.728 | -33.888 | -58.710 | 1.0975 |
| C5 | -26.379 | -32.987 | -54.110 | 1.3125 |

TABLE III. MEASURED PERMITTIVITY, CONDUCTIVITY AND THICKNESS OF CEMENT BASED SAMPLES

| Test Sample | Permittivity $\varepsilon_r$ | Width d (cm) | Conductivity $\sigma$ (S/m) |
|---|---|---|---|
| SS4 | 6.116 | 6.65 | 0.1697 |
| SS6 | 6.564 | 6.43 | 0.2796 |
| C5 | 7.587 | 7.15 | 0.2234 |

TABLE IV. MEASURED PERMITTIVITY, CONDUCTIVITY AND THICKNESS OF STANDARD SAMPLES

| Sample | | Teflon | PVC | PMMA |
|---|---|---|---|---|
| $\varepsilon_r$ | Standard [6] | 2.10 | 2.57 | 2.34 |
| | Calculated | 2.22 | 2.73 | 2.69 |
| $\sigma$ (S/m) | Standard [6] | 0.0065 | 0.0319 | 0.0826 |
| | Calculated | 0.0075 | 0.0530 | 0.0473 |
| d (cm) | Actual | 2.50 | 2.50 | 2.50 |
| | Calculated | 2.51 | 2.38 | 2.34 |

## IV. CONCLUSION

In this work, the dielectric constant, the effective conductivity and the thickness of various concrete and mortar samples having different compositions as well as different water to cement ratio have been measured using the microwave non-destructive testing procedure. It has been observed that by increasing the w/c ratio, the effective dielectric conductivity of the sample usually increases. The technique would be applied in future to study some actual building structures.


## ACKNOWLEDGEMENT

The authors would like to thank Prof. Sudhir Misra and his team from Department of Civil Engineering, IIT Kanpur for providing the cement based samples.


## REFERENCES


[1] Baker-Jarvis, J.; Vanzura, E.J.; Kissick, W.A., "Improved technique for determining complex permittivity with the transmission/reflection method," Microwave Theory and Techniques, IEEE Transactions on , vol.38, no.8, pp.1096,1103, Aug. 1990.

[2] U. C. Hasar, "Unique permittivity determination of low-loss dielectric materials from transmission measurements at microwave frequencies," *Progress In Electromagnetics Research*, Vol. 107, 31-46, 2010.

[3] K. Mubarak, K. J. Bois, R. Zoughi, "A simple, robust, and on-site microwave technique for determining water-to-cement ratio (w/c) of fresh Portland cement-based materials," *Instrumentation and Measurement, IEEE Transactions on*, vol. 50, no. 5, pp. 1255-1263, Oct 2001.

[4] B.Barman,Z.Akhter and M.J.Akhtar, "Microwave testing of cement based material," *International Microwave and RF conference*, Dec-14-16, India 2013.

[5] C. A. Balanis, *Advanced Engineering Electromagnetics*, John Wiley & Sons, New Jersey, NJ, 1989.

[6] B. Riddle, J. Baker-Jarvis and J. Krupka, "Complex permittivity measurements of common plastics over variable temperatures," *Microwave Theory and Techniques, IEEE Transactions on* , vol. 51, no. 3, pp. 727-733, Mar 2003.

# A Method for De-Embedding Cable Flexure Errors in S-parameter Measurements

Faisal Mubarak*, *member IEEE*, Gert Rietveld*, *senior member IEEE*, and Marco Spirito†, *member IEEE*

*Van Swinden Laboratorium (VSL), Thijsseweg 11, 2629 JA Delft, The Netherlands; fmubarak@vsl.nl

† Delft University of Technology, Faculty of Electrical Engineering, Delft, The Netherlands

***Abstract*—Errors due to inevitable cable flexure are one of the major error and uncertainty sources in high-precision S-parameter measurements. Recently developed two-port electronic calibration units allow for determination and correction of these errors. A method is presented where such a unit is applied to de-embed cable flexure errors in S-parameter measurements. In a series of steps, the effects of the cable as well as from the electronic calibration unit itself are determined and subsequently corrected for. First results show that using this method, cable flexure errors can be decreased with a factor of 5 to 10, with the most significant gain at the higher frequencies.**

***Index Terms* — S-parameters, cable errors, VNA, PNA, cable flexure, impedance, de-embedding, measurement techniques, RF.**

## I. Introduction

The accuracy of vector network analysers (VNAs) is continuously increasing, driven by high-demanding applications in for example aerospace and semiconductor device industries. Industrial measurements of S-parameters are now approaching uncertainties so far only achievable by national metrology institutes (NMIs). With the improved uncertainties in S-parameter measurements, effects that previously were relatively small are now becoming more important.

One of these effects is errors due to flexing of the cable connecting the device under test (DUT) to the VNA. They presently have become a dominant uncertainty source in high-precision transmission measurements. Recent published work has focused on characterization and subsequent minimization of such errors [1-2]. While this work has been successful in significantly improving uncertainties in S-parameter measurements, still a non-negligible effect of cable flexure remains.

In this paper, a method is proposed for de-embedding cable flexing errors in S-parameter measurements. The method exploits a two-port electronic calibration unit, but traceability in the measurements is still realized via coaxial reference standards. After a description of the proposed method, the first experimental results exploiting the method are presented and discussed.

This work was funded through the European Metrology Research Program (EMRP) Project SIB62 'Metrology for New Electrical Measurement Quantities in High-frequency Circuits' and the Dutch Ministry of Economic Affairs. The EMRP is jointly funded by the EMRP participating countries within EURAMET and the European Union.

## II. Proposed Analysis Method

The S-parameter measurement system for two-port devices used in this study consists of a two-port VNA (PNA 5225A Metrology grade) and a pair of 1.85 mm high-precision flexible test-port cables. The cable connected to Port-1 of the VNA is kept in a fixed position and is not moved during the measurements. The cable connected to Port-2 is moved in order to enable the calibration and device under test measurements. Both test-port cables are terminated with high-precision test-port adapters.

The proposed method utilizes a two-port electronic calibration unit (ECU) as integral part of the S-parameter measurement system as shown in Figure 1. One port (port B) of the ECU is connected to the movable flexible cable of the VNA and the other port (port A) of the ECU serves as the new test-port of the VNA.

The concept on the new method relies on the possibility of realizing an automated one-port calibration after each movement of the cable without the need of disconnecting the device under test. Through this one-port calibration any discrepancy due to flexing of the test-port cable is detected and subsequently can also be corrected for. The method assesses the error through reflection coefficient measurements, and hence can also be used to correct one-port reflection coefficient measurements.

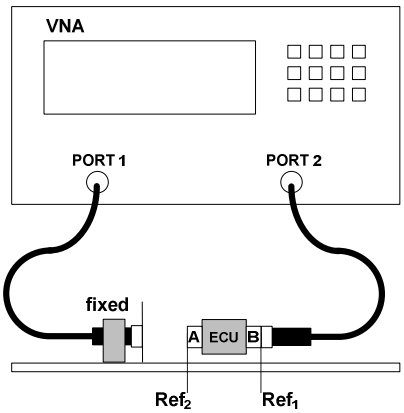


*Figure 1. Schematic diagram of the new S-parameter measurement system including an electronic calibration unit to de-embed errors due to flexing of the cable connected to Port-2 of the VNA. $Ref_1$ and $Ref_2$ indicate the reference planes in the measurements (see text).*

978-1-4799-4423-1/14/$31.00 ©2014 IEEE

Port-2 of the VNA, including an ECU in the measurement path, is calibrated through a three-tier calibration process. Each step uses a short-open-load (SOL) based calibration method [3] at a different reference plane to characterize error-terms for individual parts of the measurement system. Figure 2 shows a graph of the signal flow of VNA Port-2.

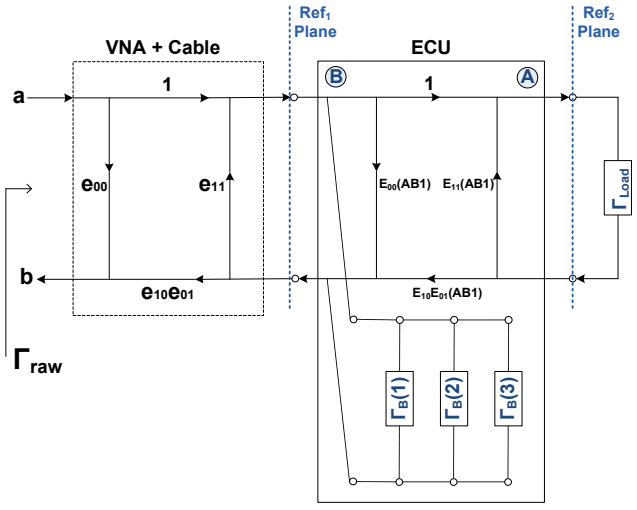


*Figure 2. Signal flow graph of Port-2 of the S-parameter measurement system, having an electronic calibration unit (ECU) as integral part of the system. The active switches inside the ECU are omitted for clarity.*

The calibration process starts with positioning the Port-2 cable at the starting position. Subsequently, waiting time is included in the process to allow for the cable to stabilize. Before connecting the ECU, a set of SOL-based calibration measurements $\Gamma_n(raw)$ are performed at the test-port connector of the flexible cable. This serves as the first reference plane $Ref_1$ in the three-tier calibration process, see figures 1 and 2. Using available reference data $\Gamma_n$ for each of the three calibration devices used in the SOL calibration, the three error-terms $VNA_0$ related to the VNA and the test-port cable are calculated at the starting position using the following equation:

$$\begin{bmatrix} 1 & \Gamma_1 \cdot \Gamma_1(raw) & -\Gamma_1 \\ 1 & \Gamma_2 \cdot \Gamma_2(raw) & -\Gamma_2 \\ 1 & \Gamma_3 \cdot \Gamma_3(raw) & -\Gamma_3 \end{bmatrix} \cdot \begin{bmatrix} e_{00} \\ e_{11} \\ \Delta \end{bmatrix} = \begin{bmatrix} \Gamma_1(raw) \\ \Gamma_2(raw) \\ \Gamma_3(raw) \end{bmatrix} \quad (1)$$

$$e_{10}e_{01} = e_{00} \cdot e_{11} - \Delta$$

Here, the error terms $e_{00}$, $e_{11}$ and $e_{10}e_{01}$ represent directivity, source match, and reflection tracking of the calibrated VNA respectively and $\Gamma_{corr,ref1}$ denotes the reflection coefficient seen at reference plane $Ref_1$, the test-port connector of a calibrated VNA.

Having calibrated the system up to the $Ref_1$ reference plane, port B of the ECU is connected to the test-port connector. A second set of measurements is performed by measuring the three internal impedance states $\Gamma_B(1,2,3)$ associated to port B of the ECU, as shown in Figure 2. Using previously calculated error-terms $VNA_0$ of the VNA, calibrated data for each impedance state is determined using:

$$\Gamma_{corr,ref1}(i) = \frac{\Gamma_{raw}(i) - e_{00}}{e_{10}e_{01} + e_{11} \cdot (\Gamma_{raw}(i) - e_{00})} \quad (2)$$

This calibrated data serves as reference for each state in the following *n* measurements and is used to recalibrate the VNA $VNA_n$ up to reference plane $Ref_1$ after each movement of the test-port cable.

The ECU is part of the measurement system and port A is the new reference plane $Ref_2$ of the VNA, see Figure 2. A third and final set of SOL-based calibration measurements are performed at the reference plane $Ref_2$. These measurements are used to determine error-terms related to the port A and port B through-state of the ECU and are needed to propagate measurement results from reference plane $Ref_1$ to $Ref_2$. The ECU error-terms $ECU_0(AB)$ are calculated using the following equation:

$$\begin{bmatrix} 1 & \Gamma_1 \cdot \Gamma_{corr,ref1}(1) & -\Gamma_1 \\ 1 & \Gamma_2 \cdot \Gamma_{corr,ref1}(2) & -\Gamma_2 \\ 1 & \Gamma_3 \cdot \Gamma_{corr,ref1}(3) & -\Gamma_3 \end{bmatrix} \cdot \begin{bmatrix} E_{00}(AB1) \\ E_{11}(AB1) \\ \Delta 1 \end{bmatrix} = \begin{bmatrix} \Gamma_{corr,ref1}(1) \\ \Gamma_{corr,ref1}(2) \\ \Gamma_{corr,ref1}(3) \end{bmatrix} \quad (3)$$

$$E_{10}E_{01}(AB1) = E_{00}(AB1) \cdot E_{11}(AB1) - \Delta 1$$

Here, the error terms $E_{00}(AB1)$, $E_{11}(AB1)$ and $E_{10}E_{01}(AB1)$ are calculated. The error-terms represent the directivity, source match, and reflection tracking of the through state between port A and port B of the ECU. The SOL measurements performed at reference plane $Ref_2$ are first corrected using equation 2, resulting in $\Gamma_{corr,ref1}(m)$. This de-embeds the errors up to reference plane $Ref_1$ from the measurement data and this data serves as input for equation 3.

In the following device under test calibration, the cable flexure error is assessed by recalibrating the VNA up to reference plane $Ref_1$. The recalibration is performed by measurement of the ECU internal port B impedance states. The reference data of these states is determined earlier using equation 2. With the new set of VNA error-terms $VNA_n$, the measurement system is calibrated up to reference plane $Ref_1$. The same set of ECU error-terms $ECU_0(AB)$ is then used to transfer the measurement results from reference plane $Ref_1$ to $Ref_2$ using the following equation:

$$\Gamma_{corr,ref2}(j) = \frac{\Gamma_{corr,ref1}(j) - E_{00}(AB1)}{E_{10}E_{01}(AB1) + E_{11}(AB1) \cdot (\Gamma_{corr,ref1}(j) - E_{00}(AB1))} \quad (4)$$

## III. Experimental Approach

A series of experiments are conducted to study stability of individual parts of the measurement system used for the proposed method outlined above, see Figure 1. First the VNA stability is investigated, followed by a study of the stability of the ECU impedance states as calibration devices.

The stability of the VNA is investigated using a set of mechanical SOL devices as reference (see Figure 3a). Each SOL device is connected directly at Port-2 of the VNA and subsequently reflection coefficient measurements are performed every 15 minutes for a full day, resulting in 96 measurements for each device. The error-terms of the VNA are calculated using this data, resulting in 96 sets of VNA error-terms. The standard deviation for each VNA error-term serves as a figure of merit for assessment of VNA stability. These error-terms include 3-day drift, noise, and non-linearity effects, resulting in a worst-case stability analysis of the VNA.

In the second experiment the VNA stability is investigated using the different ECU impedance states as calibration devices for SOL-based calibration of the VNA. Port B of the ECU is connected directly to Port-2 of the VNA (see Figure 3b), and the three ECU impedance states seen from Port B of ECU are used as calibration devices, whereas Port A is terminated with a high-reflect short device. The three ECU impedance states are measured, together with the through state between Port A and Port B of the ECU. So, four ECU states are measured, again with 15 minutes interval during a full day, resulting in 96 measurements for each impedance state. Again, the error terms of the system are calculated, resulting in 96 sets of worst-case error terms, that now not only include VNA imperfections but also ECU imperfections, such as impedance state stability, switch stability, noise, and non-linearity effects.

Finally, the applicability of the new proposed method is studied using the setup depicted in Figure 3c. For the actual measurement of cable flexure effects up to 50 GHz, a high-precision flexible coaxial cable with 1.85 mm male connector was selected. The cable is moved between two predefined ends, 80 mm apart, using a special-purpose horizontal translation stage [2]. After reaching the outer end, the movement in opposite direction is initiated. In this way, two sets of data are obtained, one for each movement direction. In addition, after each movement, three port B impedance states of the ECU are measured together with through (AB) state. Port A of the ECU is terminated with a high reflect short device. Reflection coefficient measurements are performed with fifteen minutes delay between the movements. A total of 18 sets of measurements are performed at each measurement position.

## IV. Measurement Results and Discussion

The first two experiments give results for the VNA error-term stability, measured using mechanical SOL devices and ECU impedance states as calibration devices. The three error-terms of the VNA Port-2 are determined up to an identical reference plane in both experiments. In Figure 4 the standard deviation of VNA $E_{10}E_{01}$-term is depicted for both experiments. Each standard deviation value is determined from a set of 96 measurement values. The (red) data points are results corrected using mechanical SOL calibration devices. The (blue) data points are results corrected using ECU impedance states as SOL calibration devices. The other two error-terms, $E_{00}$ and $E_{11}$, are similar for both experiments such as the transmission/tracking term shown in Figure 4.

From the data in Figure 4 it can be seen that the standard deviations of the two first experiments essentially are equal. Only for the real part the second experiment, with the ECU, shows a slightly larger noise in the measurements in the frequency range from 25 GHz to 41 GHz. We thus can conclude that over the time scale needed to perform the measurements, the ECU Port B impedance states hardly add any noise and/or instabilities to the VNA measurements.

The following presents the experimental results conducted to investigate the stability of measured reflection coefficient via the through state, between Port A and B, of the ECU. The investigation focuses on studying the impact of an active device such as the ECU on S-parameter measurement and is investigated as described in experiment 2.

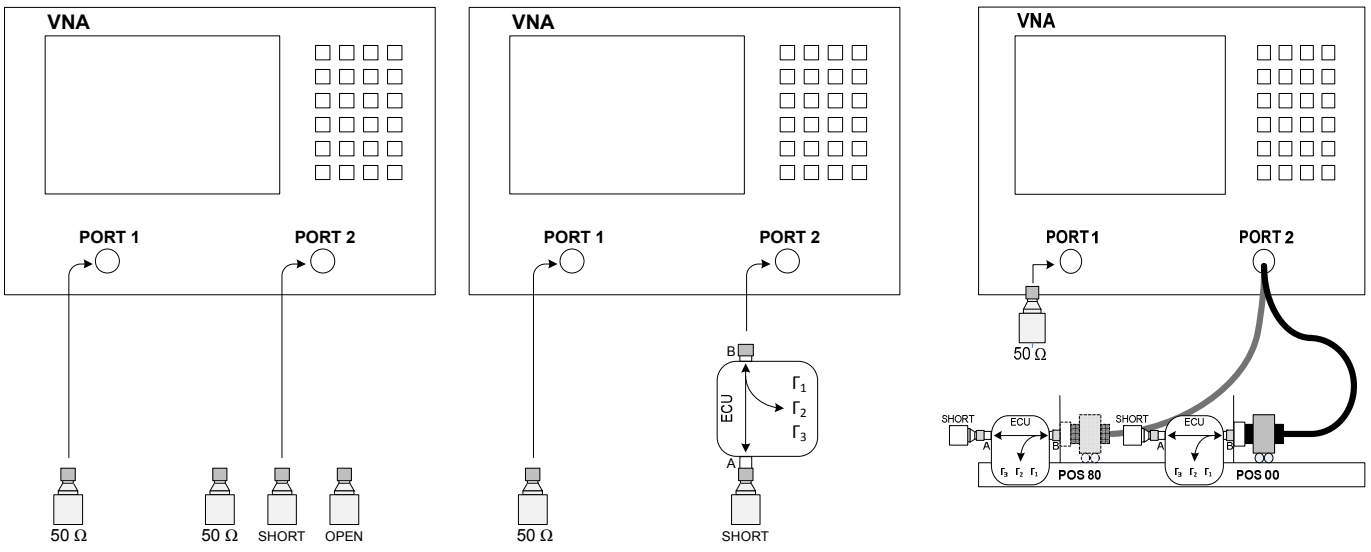


Figure 3. Measurement system used for the three subsequent stages of the experiment (a – c, from left to right).

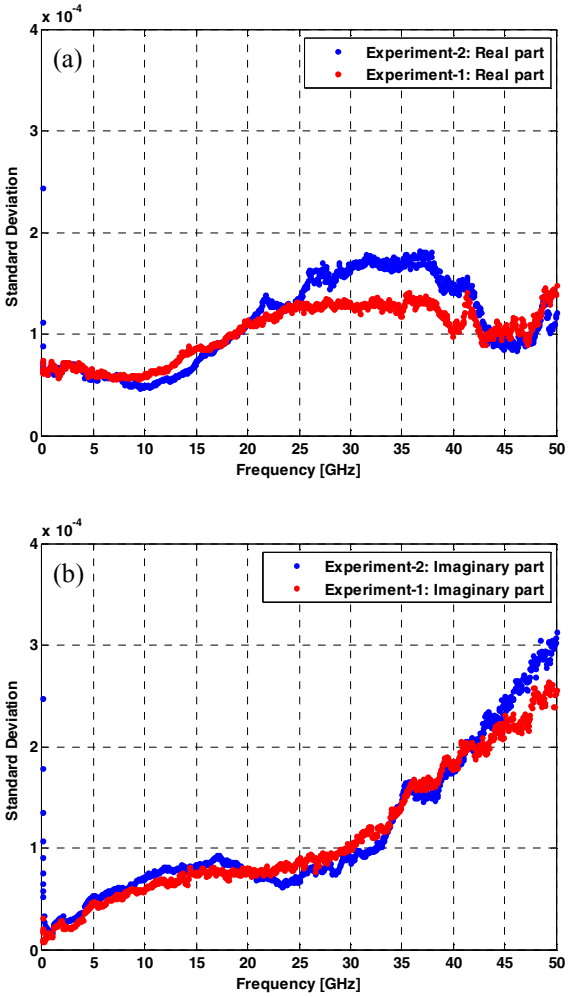


*Figure 4. Measurement results for the VNA $E_{10}E_{01}$-term. The standard deviation for real (top graph) and imaginary (bottom graph) component of $E_{10}E_{01}$. The (red) data points are results for $E_{10}E_{01}$ determined using mechanical SOL standards at VNA test-port. The (blue) data points are results for $E_{10}E_{01}$ determined using three ECU impedance standards at VNA test-port.*

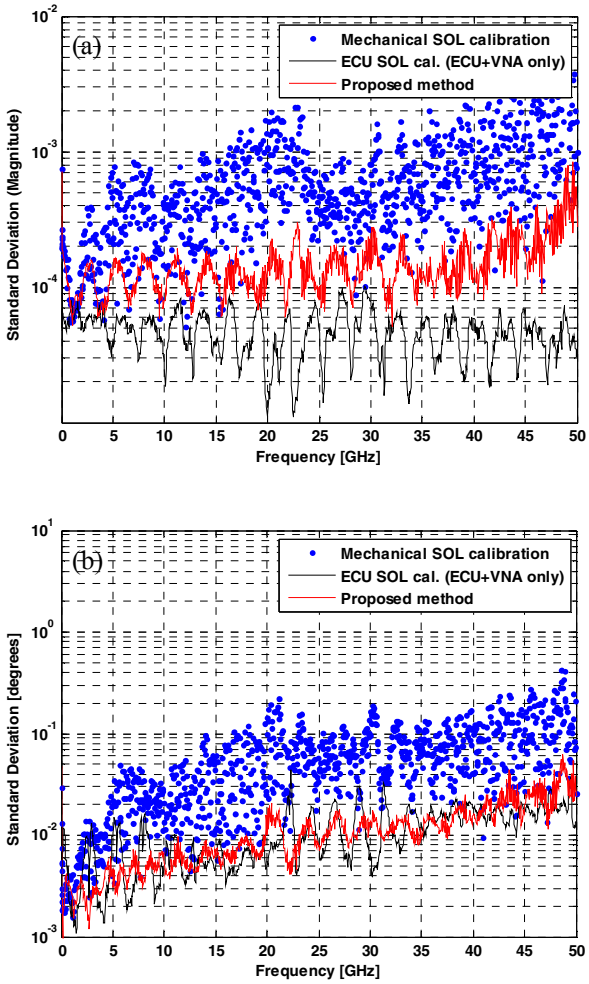


*Figure 5. Measurement results for a high-reflect short termination, showing the standard deviation for magnitude (top) and phase (bottom). The (blue) data points are data corrected according to the classical SOL calibration using mechanical standards at the start of the measurements. The (red) line is data corrected according to the proposed method. The (black) line is data corrected using ECU based calibration method without using the flexible cable.*

In Figure 5 the standard deviation of calibrated reflection coefficient of high-reflect short device is depicted for experiments 2 and 3. Each standard deviation value is determined from a set of 96 measurement values. The (black) data points are results corrected using ECU impedance states as SOL calibration devices without using the flexible cable, see experiment 2 details. In this experiment the reflection coefficient is determined up to Port B of the ECU. The (blue) data points are results corrected up to Port A of the ECU using classical SOL calibration performed once at the start of the experiment 3, using mechanical calibration devices. The (red) data are results corrected also up to Port A of the ECU as proposed in the new method. For data in (blue) and (red), measurement results from same experiment 3 are used as input.

From the data in Figure 5 two main conclusions can be drawn. First of all, the proposed method for de-embedding cable flexure noise and errors using an ECU unit gives a largely improved standard deviation in the measurement data, both for magnitude and phase, with respect to the conventional method using just SOL calibration with mechanical calibration devices at the start of the measurements. Secondly, the standard deviation in the measurements using a cable that is achieved with the new method using the ECU is close to (magnitude) or even essentially equal to (phase) the standard deviation achieved for the 'bare' VNA and ECU itself. This indicates that the new method is quite effective in reducing cable flexure noise in VNA measurements.

This finding is confirmed in the final experiment where a high-reflect short device connected to port B of the ECU is measured for two cable positions (see Figure 3c). Figure 6 shows the measured magnitude and phase error between the two measurements positions, 80 mm apart. The (blue) data points are data achieved as in a traditional SOL calibration performed at the beginning of the measurements using mechanical calibration devices. The (red) line gives the data after re-calibrating the VNA according to the proposed method, described in the previous section.

It can be seen that the results achieved with the new method have a significantly reduced error that is approaching the standard deviation levels shown in Figure 5. In other words: the new method seems to be able to correct for cable flexure errors to almost within the noise.

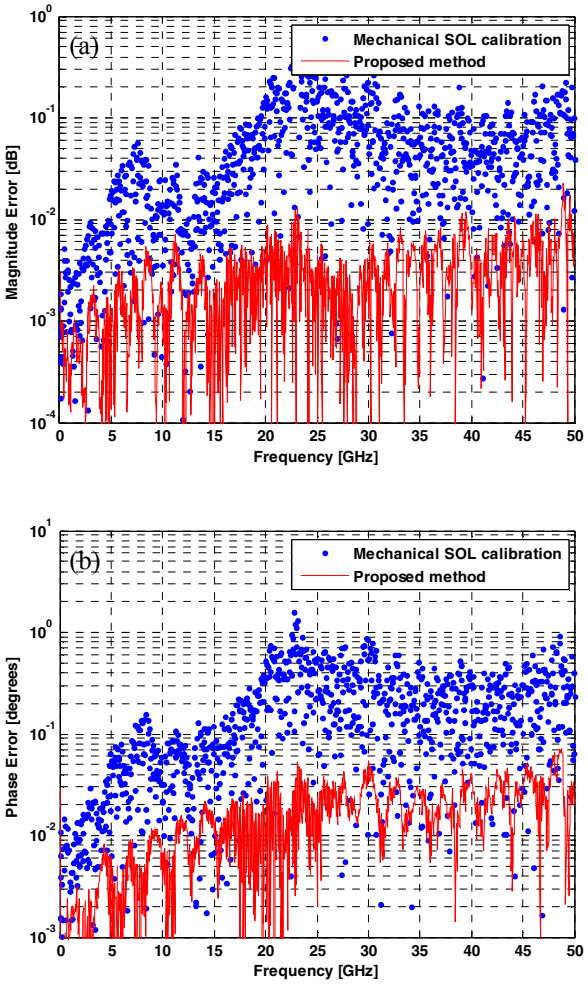


*Figure 6. Measurement results for a high-reflect short termination. The magnitude and phase difference between two measurement positions (80 mm apart) is plotted for a high precision 1.85 mm flexible cable tested up to 50 GHz. The (blue) data points are uncorrected data; the (led) line is data corrected according to the proposed method.*

## V. DISCUSSION & CONCLUSIONS

We have evaluated the possibility of improving the noise and errors in S-parameter measurements by use of an electronic calibration unit (ECU). The measurement results show a significant improvement comparing the results of the proposed method with respect to those using only a standard SOL calibration with mechanical reference standards. In general, the noise in S-parameter measurements caused by cable flexure is reduced to almost the level of the VNA itself. A factor of 5 to 10 reduction in size of the cable flexing error is achieved.

There are some limitations of the new method. For example, the stability does decrease when propagating calibration results via the through state (ports A and B) of the ECU. Also, it is not possible to distinct cable errors from errors arising from the electronic calibration unit. Hence, the stability of this unit becomes an important remaining source of uncertainty after de-embedding of the cable flexure errors. The results presented in this paper already show a quite good stability of the ECU. This likely will further improve with continuous development and performance enhancement, so it may be expected that the next generation of electronic calibration units will become a permanent part of S-parameter measurement systems.

The current method is tested on a one-port device, but it should also be applicable to transmission measurements as well. Therefore, in our future work, this method will also be extended to correction of cable flexure errors in transmission measurements.

## ACKNOWLEDGEMENT

The authors wish to acknowledge the assistance and support of Agilent Technologies in providing the measurement equipment needed to perform the measurements described in this paper. The authors furthermore acknowledge Nick Ridler (National Physical Laboratory) for many useful discussions and support.

## REFERENCES

[1] Liu, J.C., Wong, K., "Test Port Cable Instability and VNA Measurement Errors", in Proc. of the 81st Microwave Measurement Conference (ARFTG), pp. 1 – 8, June 2013.

[2] Faisal Mubarak, Gert Rietveld, Dennis Hoogenboom, Marco Spirito, "Characterizing Cable Flexure Effects in S-parameter Measurements", in Proc. of the 82nd Microwave Measurement Conference (ARFTG), December 2013.

[3] Gerd Wubbeler, Clemens Elster, Thomas Reichel, and Rolf Judaschke, "Determination of the Complex Residual Error Parameters of a Calibrated One-Port Vector Network Analyzer", IEEE Trans. on Instrumentation and Measurement, Vol 58, No.9, pp. 3238 – 3244, September 2009.

# Calibration of EM Simulator on Substrate Complex Permittivity

*Vratislav Sokol[1], Jan Eichler[1,2] and Marc Rütschlin[1]*

*[1]Computer Simulation Technology, 64289 Darmstadt, Germany*
*[2]Czech Technical University in Prague, 16627, Czech Republic*

**Abstract — A novel broadband non-resonant Thru-Line (TL) technique is proposed for the extraction of substrate complex permittivity, while the influence of the end-launch connectors is fully suppressed. The main difference to the traditional TRL techniques is that only two calibration standards are needed and the length difference between Thru and Line is much larger than a quarter of a wavelength at the central frequency of the band. The larger effective line length increases sensitivity to the substrate losses, and allows accurate measurement at lower frequencies. The technique uses the measured propagation constant in a 3D EM field simulator for the complex permittivity extraction. This TL technique has been verified experimentally for microstrip and grounded coplanar waveguide transmission lines using RO4350B substrate in the frequency range 45 MHz – 26 GHz. A ring resonator coupled to microstrip line was used as the verification DUT.**

**Index Terms — Calibration, complex permittivity, EM simulator, propagation constant, TRL, two-tier calibration.**

## I. Introduction

Over the last decade many papers have been published on the extraction of substrate complex permittivity using various techniques. Two of the most commonly used techniques are the permittivity extraction using a weakly coupled resonator that is printed on PCB [1], [2], or a rectangular closed resonator made from PCB exploiting the volumetric modes [3].

A common drawback of the above mentioned techniques is the influence of the probes that are used for the coupling to the resonator [4]. They either influence the accuracy of the dielectric loss estimation or they limit the usable frequency range. Therefore we focus in this paper on the TRL-like techniques that allow a full correction of the probes [5], [6]. In contrast to the resonator techniques, a transmission line approach provides output data evenly distributed across the whole frequency range (not just at the discrete points of the resonances).

It has been shown in [7] that the propagation constant of a transmission line can be determined by solving the eigenvalue problem. Then the propagation constant can be used for the complex permittivity extraction as has been shown in [8] for waveguide in X-band. In other work, wideband extraction has been applied to a low-loss CPW line in the frequency range 1 - 110 GHz [9]. The related error analysis has been performed in [10].

We show in this paper that the TL technique can be used to extract properties over a wide frequency range and that an electromagnetic (EM) field simulator can form part of an efficient extraction algorithm that requires just a few full-wave EM simulations.

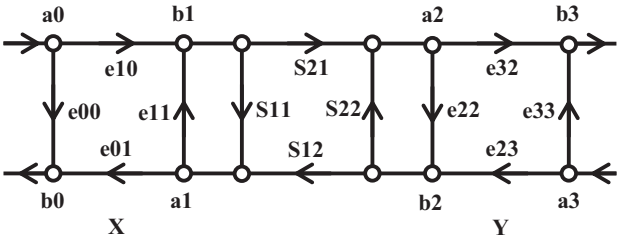


Fig. 1. 8-term error model.

## II. Thru-Line Calibration Technique

The Thru-Line technique uses the 8-term error model that is depicted at Fig. 1. In the following sections we assume that the VNA is pre-calibrated using an OSML calibration kit. Thus the error model corresponds just to the test fixture including the connectors. The goal is first to derive the propagation constant of the transmission line based on measured S-parameters, then to use this propagation constant for the extraction of complex permittivity using the 3D EM field simulator.

### *A. Propagation constant*

The measured S-parameters in the forward direction are expressed as follows

$$S_{21M} = \frac{e_{10}S_{21}e_{32}}{1-e_{11}S_{11}-e_{22}S_{22}-e_{11}S_{21}e_{22}S_{12}+e_{11}S_{11}e_{22}S_{22}}, \quad (1)$$

$$S_{11M} = e_{00} + \frac{e_{10}S_{11}e_{01}(1-e_{22}S_{22})+e_{10}S_{21}e_{22}S_{12}e_{01}}{1-e_{11}S_{11}-e_{22}S_{22}-e_{11}S_{21}e_{22}S_{12}+e_{11}S_{11}e_{22}S_{22}}. \quad (2)$$

Assuming that the error model is symmetrical and reciprocal, which means $S_{11}=S_{22}$, $S_{21}=S_{12}$, $e_{00}=e_{33}$, $e_{11}=e_{22}$ and $e_{10}=e_{01}=e_{32}=e_{23}$, the equations for the transmission and reflection coefficient are further simplified

$$S_{21M} = \frac{e_{10}^2 S_{21}}{1-2e_{11}S_{11}-e_{11}^2S_{21}^2+e_{11}^2S_{11}^2}, \quad (3)$$

$$S_{11M} = e_{00} + \frac{e_{10}^2S_{11}(1-e_{11}S_{11})+e_{10}^2S_{21}^2e_{11}}{1-2e_{11}S_{11}-e_{11}^2S_{21}^2+e_{11}^2S_{11}^2}. \quad (4)$$

978-1-4799-4423-1/14/$31.00 ©2014 IEEE

The measured S-parameters for the Thru calibration standard ($S_{11}=0$, $S_{21}=1$) can be written as

$$S_{21T} = \frac{e_{10}^2}{1-e_{11}^2}; \tag{5}$$

$$S_{11T} = e_{00} + \frac{e_{10}^2 e_{11}}{1-e_{11}^2} = e_{00} + S_{21T} e_{11}, \tag{6}$$

and the measured S-parameters for the Line calibration standard ($S_{11}=0$, $S_{21}= e^{-\gamma L}$) can be written as

$$S_{21L} = \frac{e_{10}^2 e^{-\gamma L}}{1-e_{11}^2 e^{-2\gamma L}}; \tag{7}$$

$$S_{11L} = e_{00} + \frac{e_{10}^2 e_{11} e^{-2\gamma L}}{1-e_{11}^2 e^{-2\gamma L}} = e_{00} + S_{21L} e_{11} e^{-\gamma L}, \tag{8}$$

where $\gamma$ is the propagation constant of the transmission line and $L$ is the physical length difference between the Thru and Line standards. By substitution of $e_{00}$ from (6) to (8) we get

$$e^{-\gamma L} = \frac{S_{11L} - S_{11T} + S_{21T} e_{11}}{S_{21L} e_{11}}. \tag{9}$$

Then by further substitutions of $e^{-\gamma L}$ from (9) to (7) and $e_{10}^2$ from (5) to (7) we get a quadratic equation for $e_{11}$

$$e_{11}^2 S_{21T} \Delta_{11} + e_{11}\left(S_{21T}^2 - S_{21L}^2 + \Delta_{11}^2\right) + S_{21T} \Delta_{11} = 0, \tag{10}$$

where $\Delta_{11}=S_{11L}-S_{11T}$. Then by solving this equation and substitution of the roots for $e_{11}$ back to (9) we can write the final equation for the term including the transmission line propagation constant, which depends only on the measured S-parameters

$$e^{-\gamma L} = \frac{S_{21L}}{S_{21T}}\left(1 + \frac{2\Delta_{11}^2}{S_{21T}^2 - S_{21L}^2 - \Delta_{11}^2 \pm \sqrt{\left(S_{21L}^2 - S_{21T}^2 + \Delta_{11}^2\right)^2 - 4S_{21L}\Delta_{11}^2}}\right). \tag{11}$$

Since we get two roots of the equation (10) the resulting transmission coefficient $e^{-\gamma L}$ has two solutions too. However the selection of the right root is easy thanks to the first-tier OSML calibration. We know that the transmission line is a passive 2-port network and therefore the absolute value of its transmission coefficient must be below one.

The transmission coefficient $e^{-\gamma L}$ is calculated in (11) just from the subset of S-parameters that represent the forward direction. However the coefficient $e^{-\gamma L}$ can be calculated from the S-parameters of the reverse direction too. Since the test-fixture is not perfectly symmetrical the transmission coefficients will be different and slightly rippled. This ripple can be minimized by using the average value of those two coefficients for the complex permittivity extraction procedure.

The transmission coefficient $e^{-\gamma L}$ could alternatively be calculated from the full set of measured S-parameters considering a general asymmetrical error model as described in [7] and [8]. The two eigenvalues can be expressed as follows

$$\lambda_1, \lambda_2 = \frac{M_{11}^{TL} + M_{22}^{TL} \pm \sqrt{\left(M_{11}^{TL} - M_{22}^{TL}\right)^2 + 4M_{12}^{TL} M_{21}^{TL}}}{2}, \tag{12}$$

where

$$\mathbf{M}^{TL} = \mathbf{M}^{L}\left[\mathbf{M}^{T}\right]^{-1}, \tag{13}$$

where $\mathbf{M}^{\mathrm{L}}$ and $\mathbf{M}^{\mathrm{T}}$ are measured cascade matrices of Line and Thru respectively. They are calculated from measured S-parameters using the conversion formula

$$\mathbf{M}^{i} = \frac{1}{S_{21}^{i}}\begin{pmatrix} S_{12}^{i}S_{21}^{i} - S_{11}^{i}S_{22}^{i} & S_{11}^{i} \\ -S_{22}^{i} & 1 \end{pmatrix}. \tag{14}$$

Finally the transmission coefficient can be written as

$$e^{-\gamma L} = \frac{1}{2}\left(\lambda_1 + \frac{1}{\lambda_2}\right), \tag{15}$$

where $L$ is the length difference between Line and Thru and $\gamma$ is the propagation constant of the transmission line.

*B. DUT S-parameters*

In order to get DUT S-parameters an additional Reflect calibration standard would be required for the full VNA calibration [11]. Nevertheless it has been shown in [12] that the error terms can be obtained using just two lines with a different length in the case of the symmetrical error model. We use a similar approach and thus the terms can be estimated as follows

$$e_{11} = \frac{S_{11L} - S_{11T}}{S_{21L} e^{-\gamma L} - S_{21T}}, \tag{16}$$

$$e_{00} = S_{11T} - S_{21T} e_{11}, \tag{17}$$

$$\begin{aligned} &e_{10}^2 = S_{21T}\left(1 - e_{11}\right) \Rightarrow \\ &e_{10} = \sqrt{\left|S_{21T}\left(1 - e_{11}\right)\right|}\exp\left(\tfrac{1}{2}\arg\left(S_{21T}\left(1 - e_{11}\right)\right)\right). \end{aligned} \tag{18}$$

where $S_{xyT}$ and $S_{xyL}$ are measured S-parameters of the Thru and Line respectively. The S-parameters of the DUT can be calculated using the matrix equation for cascaded t-parameters

$$\mathbf{T} = \mathbf{T}_X^{-1}\mathbf{T}_M\mathbf{T}_Y^{-1}, \tag{19}$$

where $\mathbf{T}$ is the cascade matrix of the DUT, $\mathbf{T_M}$ is the matrix of the measured t-parameters, and $\mathbf{T_X}$, $\mathbf{T_Y}$ are matrices of the

symmetrical error model that are calculated from the error terms

$$\mathbf{T}_X = \frac{1}{e_{10}}\begin{pmatrix} 1 & -e_{11} \\ e_{00} & e_{10}^2 - e_{00}e_{11} \end{pmatrix}, \quad \mathbf{T}_Y = \frac{1}{e_{10}}\begin{pmatrix} 1 & -e_{00} \\ e_{11} & e_{10}^2 - e_{00}e_{11} \end{pmatrix}. \quad (20)$$

Finally the DUT S-parameters are converted from the cascade **T** matrix

$$\mathbf{S}_{DUT} = \frac{1}{t_{11}}\begin{pmatrix} t_{21} & t_{11}t_{22} - t_{12}t_{21} \\ 1 & t_{12} \end{pmatrix}. \quad (21)$$

Please note that in contrast to [12] the TL technique does not require knowledge of the line characteristic impedance. The propagation constant results automatically from the self-calibrating process given by the equation (11).

*C. Bandwidth, singularities*

If the length difference between the Line and Thru measurements corresponds to a multiple of a half-wavelength then the difference between the reflection coefficients, $\Delta_{11}$, is equal to zero for an ideal loss-free transmission line. This is a problem for the TRL technique that practically limits the relative bandwidth to an 8:1 ratio. This limitation does not apply when extracting the transmission line coefficient $e^{-\gamma L}$ using the TL technique. It can be shown that

$$\lim_{\Delta_{11}\to 0} e^{-\gamma L} = \frac{S_{21L}}{S_{21T}}. \quad (22)$$

Therefore the solution doesn't suffer from the singularities and the curve of $e^{-\gamma L}$ is smooth across a wide frequency range.

## III. Extraction of Complex Permittivity

Extraction of the complex permittivity is performed using the workflow described by the flowchart in Fig. 2, in which the EM simulation plays a central role. In the first step we calculate $e^{-\gamma L}$ from the measured data using (4). Since the material properties are defined in the EM simulator as a table the discrete frequency points where the phase of $e^{-\gamma L}$ is ± 90 deg are determined. They correspond to multiples of the quarter-wavelength length difference between Thru and Line. In the third step the initial table for the real part of the relative permittivity $\varepsilon_r$ and the loss tangent tg $\delta$ is created based on the material property values from a datasheet. Then we perform two EM simulations (we used CST MICROWAVE STUDIO [13]) of the transmission line, first using the initial complex permittivity, and then again for slightly different values of dielectric constant and loss tangent in order to calculate how sensitive $S_{21}$ is to those properties. In the next step the tabular material properties are corrected in the sense of inverse gradient that is estimated by the differences in the previous step. Finally the EM simulation is performed with the corrected table values. The loop is terminated as soon as the error between the measured and simulated $S_{21}$ parameter is smaller than the required accuracy $\xi_M$ and $\xi_P$ for the magnitude and phase respectively.

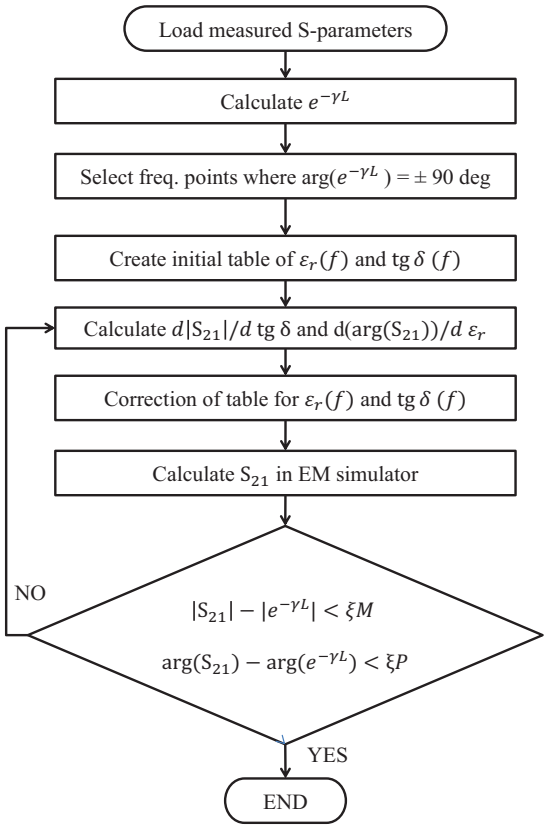


Fig. 2. Flowchart for the complex permittivity extraction.

It is important that the transmission line model used in the 3D EM field simulator accurately takes into account the effects of the manufacturing process. Therefore we considered the so called etch-factor, which describes the chamfer angle of the trapezoidal metal strip cross-section that is used instead of the rectangular shape, and the over-etching effect that makes strips narrower and gaps wider. The surface roughness of the metallization as well as the effect of nickel/gold plating are also considered.

## IV. Experimental Results

The extraction procedure described above was applied to a microstrip and grounded coplanar waveguide (CPWG) line with a length difference between Thru and Line of $L$ = 50 mm. The four transmission lines were manufactured on RO4350B substrate together with a parallel-coupled ring resonator, which is used as a verification DUT. The manufactured set-up is shown in Fig. 3. The substrate thickness is 0.508 mm and the microstrip line width is 1.08 mm. The CPWG has a gap of 0.25 mm and a strip width of 0.707 mm. The vias of the

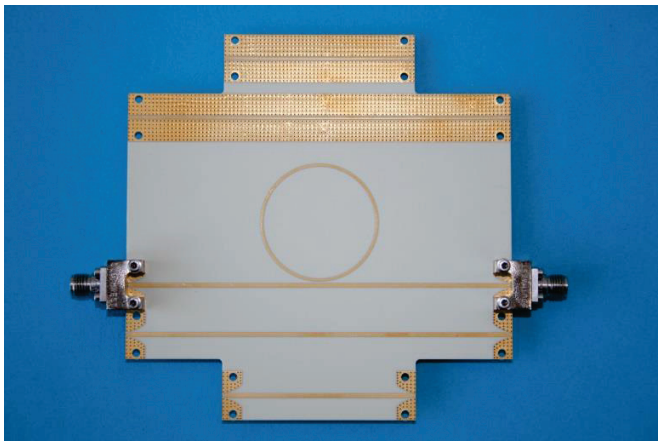

Fig. 3. Manufactured sample on RO4350B. From the top: CPWG Thru, CPWG Line, parallel-coupled ring resonator DUT, microstrip Line, microstrip Thru.

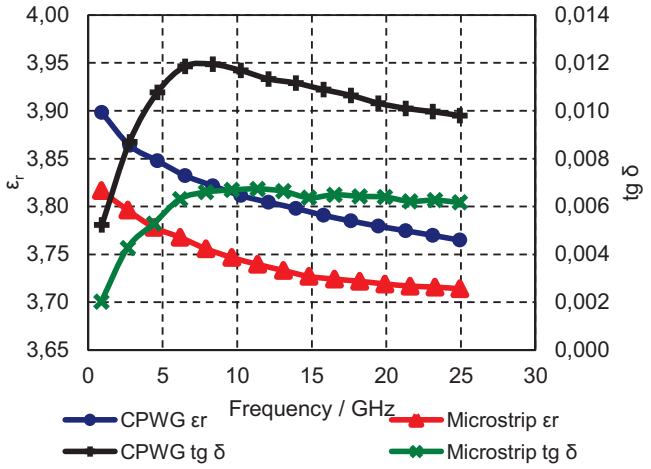


Fig. 4. Dielectric constant and loss tangent.

CPWG had a diameter of 0.3 mm and placed every 1 mm along the line. The copper metallization (43 µm thickness) was plated with nickel/gold layers (4 µm and 0.09 µm thickness respectively). The etch factor was calculated from microscopic measurements of the microstrip line dimensions to have an average value of 62 degrees. The over-etching was measured to be 33 µm on average. Southwest Microwave SWMI 1092-02A5 end-launch connectors have been used for the connection to a ZVA 67 Rohde & Schwarz vector network analyzer.

The extraction algorithm converged in just three iterations, yielding the dielectric constant and the loss tangent shown in Fig. 4. The complex permittivity extracted using the microstrip line was subsequently used in the EM simulator to calculate the response of the ring resonator. The resulting S-parameters are compared to measurement in Fig. 5. The measured S-parameters have been estimated by using the symmetrical error model as described above. There is an excellent agreement between simulated and measured $S_{21}$ in terms of resonance positions and the insertion loss. The largest

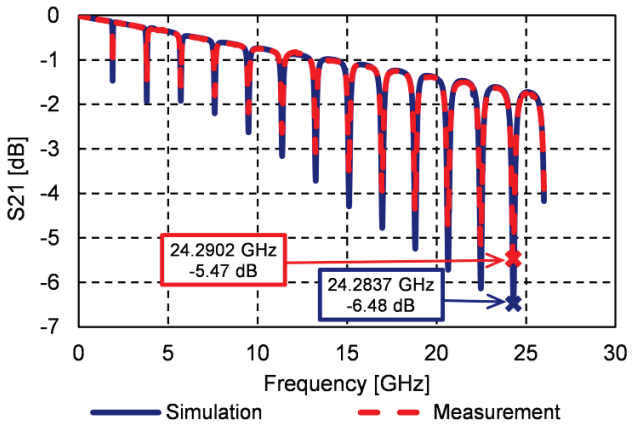


Fig. 5. Comparison of the simulation and measurement for the microstrip ring resonator.

difference between measured and simulated resonance positions is marked in Fig. 5. The magnitude at the resonances is slightly different, indicating that the coupling to the ring resonator seems to have been overestimated by the simulation.

We believe that the reason of the reduced coupling between the microstrip line and the ring resonator can be explained by the anisotropic permittivity as described in [2]. The microstrip line that is used for the extraction corresponds to vertical permittivity, while the coupling between the microstrip and the ring resonator is rather related to the horizontal permittivity, which is slightly smaller than the vertical one for the RO4350 substrate [2].

The difference between the loss tangent calculated using the microstrip line and grounded coplanar waveguide deserves further research. We suspect that the reason for such a big discrepancy might be the underestimated losses at the sharp edges of the metallization in the 3D EM model.

A comprehensive uncertainty analysis was beyond the scope of this short paper, but this would form an important part of future work. The influence on the extracted results of differences in the dielectric properties of different batches of substrate, as well as differences in the etching and plating processes, should be taken into account.

## V. Conclusion

We have shown that an EM field simulator can be accurately calibrated in terms of the substrate complex permittivity using a TL technique, and verified the extraction process using the ring resonator as an independent DUT. The advantage of this method is that we need only two transmission line samples. In addition, the data processing is easy and straightforward. On the other hand an OSML pre-calibration of the VNA is required. Since the assumption of the error model symmetry is not fully satisfied, DUT S-parameters accuracy could be further improved if a multiline TRL calibration technique were used.

## ACKNOWLEDGEMENT

We would like to thank the Department of Electromagnetic Field at the Czech Technical University in Prague, Faculty of Electrical Engineering for access to a VNA, and to Milan Příhoda for his valuable comments on the TRL calibration technique.

## REFERENCES

[1] J.M. Heinola and K. Tolsa "Dielectric characterization of printed wiring board material using ring resonator techniques: A comparison of calculation models," *IEEE Trans. on Dielectrics and Electrical Insulation,* vol. 13, No. 4, pp. 717-726, August 2006.

[2] J. C. Rautio, R. L. Carlson, B. J. Rautio and S. Arvas, "Shielded dual-mode microstrip resonator measurement of uniaxial anisotropy," *IEEE Trans. On Microwave Theory and Techniques.,* vol. 59, no. 3, pp. 748-754, March 2011.

[3] A. E. Engin, "Extraction of dielectric constant and loss tangent using new rapid plane solver and analytical Debye modeling for printed circuit boards," *IEEE Trans. On Microwave Theory and Techniques.,* vol. 58, no. 1, pp. 211-219, January 2010.

[4] E. L. Holzman, "Wideband measurement of the dielectric constant of an FR4 substrate using a parallel-coupled microstrip resonator," *IEEE Trans. On Microwave Theory and Techniques.,* vol. 54, no. 7, pp. 3127-3130, July 2006.

[5] Z. Abbas, R. D. Pollard and R. W. Kelsall "Complex permittivity measurement at Ka-band using rectangular dielectric waveguide," *IEEE Trans. On Instrumentation and Measurement.,* vol. 50, no. 5, pp. 1334-1342, October 2001.

[6] L. S. Rocha, C. C. Junquiera, E. Gambin, A. N. Vincente, A. E. Culhaoglu and E. Kemptner, "A free space approach for dielectric material characterization," *IEEE IMOC 2013 conference Proceedings,* Rio de Janeiro, August 2013.

[7] R. B. Marks, "A multiline method of network analyzer calibration," *IEEE Trans. On Microwave Theory and Techniques.,* vol. 39, no. 7, pp. 1205-1215, July 1991.

[8] M. D. Janezic, "Complex permittivity determination from propagation constant measurement," *IEEE Microwave and Guide Wave Letters.,* vol. 9, no. 2, pp. 76-78, February 1999.

[9] U. Arz, M. D. Janezic and W. Heinrich, "Wideband relative permittivity extraction based on CPW phase constant measurement," *Microwave Measurement Conference (ARFTG), 2011 77th ARFTG*, On page(s): 1 - 3.

[10] U. Arz, D. F. Williams, "Uncertainties in complex permittivity extraction from coplanar waveguide scattering-parameter data," *Microwave Measurement Conference (ARFTG), 2013 81st ARFTG*, On page(s): 1 - 6.

[11] M. Hiebel, *Fundamentals of Vector Network Analysis,* pp. 116 Rohde & Schwarz GmbH, 2005.

[12] J. E. Zúñiga-Juárez, J. A. Reynoso-Hernández and J. R. Loo-Yau, "Two-tier L-L De-embedding Method for S-Parameters Measurements of Devices Mounted in Test Fixture," *Microwave Measurement Conference (ARFTG), 2009 73rd ARFTG*, On page(s): 1 - 5.

[13] CST STUDIO SUITE®, CST AG, Germany, www.cst.com.

# HFTools - An open source python package for microwave engineering

J. Stenarson*†
*SP Technical Research Institute of Sweden, jorgen.stenarson@sp.se
†GHz Centre, Chalmers University of Technology

***Abstract*—This paper presents HFTools an open source python package for microwave engineering. The focus of the development of the package at this time is fundamental tools, e.g. file IO, dataset object, array object, and multiport object. The basic HFTools package contains tools for reading data files in several common formats, e.g. touchstone, mdif, and citi. The package also contains tools for conversion of multi-port parameters. The paper presents the capabilities of the package by a series of short examples.**

## I. Introduction

When analyzing measurement data it is inevitable that you need to use a computer to plot results, compute new results from measurements, or convert results into another form e.g. by converting between file formats.

If you choose to use matlab, excel or mathematica you will also need other toolkits that support microwave problems. If they exist they tend to have expensive license fees, especially if you are not part of an academic institute.

To simplify future collaboration we have decided to improve on the scientific python stack commonly known as scipy [1] by developing a new library, HFTools [2], of routines that support common microwave file formats, classes for multi-ports, and simplified plotting. A description of some of the python tools already available to the microwave engineer was given in [3]

There are other toolkits available one noteable example is scikit-rf [4] which contains quite a lot of useful functionality described in part in [5]. The HFTools is at this time more focused on the fundamental datatypes, e.g. array objects and dataset objects. We hope that once the development of our fundamental datatypes stabilizes we can increase collaboration between the projects.

We hope open source projects like these [2], [4] will promote sharing of ideas and that they will become another means of disseminating research results not just in papers but also in software tools that the user can adapt to their own problems.

## II. Examples

In this section we will give a number of examples to show what the hftools package can do at this time. The examples are given as they would be typed in an interactive python environment. User input is shown >>>, output is shown in italics. All examples assume that the following imports have been made

```
import numpy as np
import hftools.plotting as hfplot
import matplotlib.pyplot as plt
from hftools.file_formats import read_data
from hftools.dataset import hfarray, DimSweep,
    DimRep
from hftools.networks.multiports import SArray,
    ZArray, YArray
np.set_printoptions(precision=3, threshold=5)
```

### A. Example 1. numpy array

The first example will briefly describe the standard numpy array object. A numpy array is an n-dimensional array where every element is of the same type, e.g. float or complex number. The standard array can have up to 32 dimensions. Operations on the array object is usually performed elementwise. Adding to arrays requires the dimensions to match in size. A dimension that is of length 1 in array a can be broadcasted over the same dimension in array b with length n.

Examples:

```
>>> np.array([1]) + np.array([1, 2, 3])
array([2, 3, 4])
>>> np.array([[10],
              [20]]) + np.array([[1, 2, 3]])
array([[11, 12, 13],
       [21, 22, 23]])
```

If the number of dimensions don't match the smaller array gets new dimensions of length 1 added:

```
>>> np.array([[10],
              [20]]) + np.array([1, 2, 3])
array([[11, 12, 13],
       [21, 22, 23]])
```

### B. Example 2. hftools hfarray

The hftools package contains a modified array that is extended by having named dimension instead of anonymous dimensions. This enables automatic matching of dimensions when broadcasting.

```
>>> a = hfarray([1., 2.],
                dims=(DimSweep("Vds", 2),)) +
        hfarray([1, 2, 3],
                dims=(DimSweep("Vgs", 3),))
>>> a
hfarray([[11., 12., 13.],
         [21., 22., 23.]])
>>> a.info
```

978-1-4799-4423-1/14/$31.00 ©2014 IEEE

```
(DimSweep('Vds', shape=(2,)),
 DimSweep('Vgs', shape=(2,)))
```

The drawback is more verbose code when defining arrays, this is usually not a big problem when most arrays are created by reading data from disk. The DimSweep object is used to name dimensions it also contains properties that about the unit or data associated with the dimenasion.

```
>>> fi = DimSweep("freq", 3)
>>> fi.data
array([0, 1, 2])
>>> fj = DimSweep("freq", [1e9, 2e9, 3e9],
                  unit="Hz")
>>> fj.unit
'Hz'
>>> fj.data
array([1.000e+09, 2.000e+09, 3.000e+09])
```

### C. Example 3. hftools read_data

The hftools package can read a number of file formats. The file io functions return a DataBlock object that contains all data in the file. Variable names in the files are normalized such that a number of spellings of frequency is transformed into freq, units are also detected. Matrix indices are usually named i, and j.

```
>>> d = read_data("transistor.s2p")
>>> d
Blockname: transistor.s2p

sweep vars:
freq      [Hz] <101> min: 1.0 GHz  max: 50.0 GHz
i         []   <2>   min: 0.0      max: 1.0
j         []   <2>   min: 0.0      max: 1.0
FILEINDEX []   <1>   min: 0.0      max: 0.0

Dependent vars:
S         []     <101x2x2>
Z0        [Ohm]  <>
Vds       [V]    <>
Id        [A]    <>
Ig        [A]    <>
Vgs       [V]    <>
FILENAME  []     <>

#S-parameters at first frequency
>>> d.S[0]
hfarray([[ 9.926e-01-0.053j,  1.109e-03+0.008j],
         [-2.460e+00+0.119j,  6.223e-01-0.03j ]])

#Matrix elements can also be accessed by
>>> d.S11[0]
hfarray([ 0.993-0.053j,  0.990-0.078j,
          0.985-0.104j, ..., -0.240-0.728j,
         -0.243-0.709j, -0.256-0.694j])
#The unit of the variable can be accessed
>>> d.Z0.unit
'Ohm'
>>> d.freq.unit
'Hz'
>>> d.S.unit
None
```

### D. Example 4. Plotting

HFTools extends matplotlib (a python plotting library) [6] to simplify plotting. The first dimension of the variable to be plotted is used as x-axis and is automatically extracted and used. By importing `hftools.plotting` some extensions to matplotlib are available e.g. the default when plotting a complex variable is to plot in the complex plane, or by giving a projection argument to the subplot command we can choose a function to apply before plotting (e.g. db, mag, deg, groupdelay, real, imag ...). The `xlabel_fmt` or `ylabel_fmt` commands can be used to set the axis labels. Use an empty pair of brackets ([]) as a place holder for where the unit should be placed in the label, if possible the x-values will be scaled by an appropriate si-prefix, see Fig. 1 where the x-axis data is scaled to GHz.

```
>>> d = read_data("transistor.s2p")
>>> plt.subplot(111, projection="db")
>>> plt.plot(d.S11)
>>> plt.plot(d.S22)
>>> hfplot.ylabel_fmt("Sii []")
```

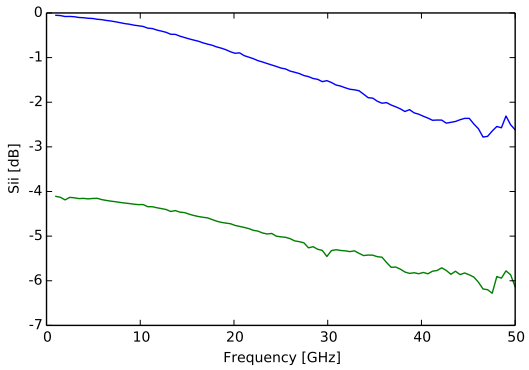


Fig. 1. Example 4. Transistor S-parameters

### E. Example 5. Network conversions

It is also possible to convert an hfarray to a network object, the network object can be easily converted between forms. Below we can see how to convert S-parameters into Z- and Y-parameters, Fig. 2.

```
>>> d = read_data("transistor.s2p")
>>> d.S = SArray(d.S)
>>> d.Z = ZArray(d.S)
>>> d.Z.unit = "Ohm"
>>> d.Y = YArray(d.S)
>>> d.Y.unit = "S"
>>> plt.subplot(211, projection="real")
>>> plt.plot(d.Z11)
>>> hfplt.ylabel_fmt("real(Z11) []")
>>> plt.subplot(212, projection="real")
>>> plt.plot(d.Y11)
>>> hfplt.ylabel_fmt("real(Y11) []")
```

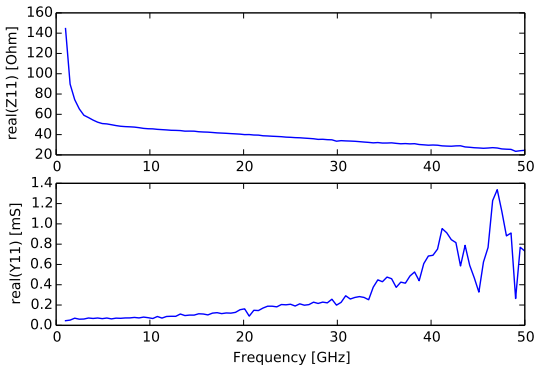


Fig. 2. Example 5. Transistor Z-parameters

### F. Example 6. Bias sweep

We have a dataset containing measured S-parameters at different bias points.

```
>>> dGaN = read_data("data/GaN_data.hdf5")
>>> dGaN
Blockname: None

sweep vars:
INDEX1 []     <310>  min:   0.0      max: 309.0
freq   [Hz]   <201>  min: 100.0 MHz max:  40.0 GHz
i      []     <2>    min:   0.0      max:   1.0
j      []     <2>    min:   0.0      max:   1.0

Dependent vars:
Date            []     <310>
IDS             []     <310>
IGS             []     <310>
Index           []     <310>
MeasType        []     <310>
S               []     <201x310x2x2>
VDS             []     <310>
VDS_SET         []     <310>
VGS             []     <310>
VGS_SET         []     <310>
Z0              [Ohm]  <310>
```

As we can see from the information of the dataset object above the different bias points are indexed by the the INDEX1 variable and not by VGS_SET, and VDS_SET that contained the settings used on the bias supply at each bias point.

In order to plot an IV-curve we need to extract data for constant Vgs this can be done by looping and indexing the data, Fig. 3.

```
>>> dGaN
>>> ax1 = subplot(211, projection="real")
>>> for vgs in sorted(set(dGaN.VGS_SET)):
        ax1.plot(dGaN.VDS[dGaN.VGS_SET==vgs],
                 dGaN.IDS[dGaN.VGS_SET==vgs], "b")
>>> ax1.axis(xmin=0, ymin=0)
>>> ax1.set_xlabel_fmt("Vds []")
>>> ax1.set_ylabel_fmt("Id []")
```

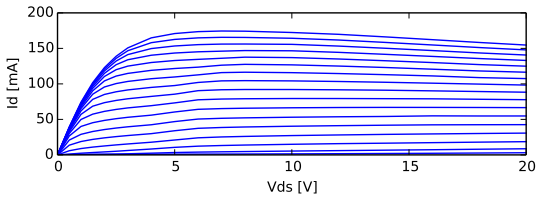


Fig. 3. Example 6. IV-Curve

If the data was taken on a hypercube grid we can reshape the data. By plotting VDS_SET vs. VGS_SET each other we can see that the bias points are not on a rectangular grid, Fig 4.

```
>>> ax1 = subplot(211, projection="real")
>>> ax1.plot(dGaN.VDS_SET, dGaN.VGS_SET, "b.")
>>> ax1.axis(xmin=-0.5, xmax=21, ymin=-5, ymax=1)
>>> ax1.set_xlabel_fmt("Vds []")
>>> ax1.set_ylabel_fmt("Vgs []")
```

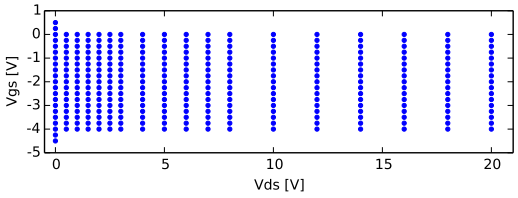


Fig. 4. Example 6. Non-rectangular Vgs-Vds grid

We can remove the extra points not on the hypercube grid by filtering the dataset, see Fig. 5 for the resulting grid.

```
>>> dGaN_sub = dGaN.filter((dGaN.VGS_SET<=0.) &
    (dGaN.VGS_SET>=-4.0))
>>> ax1 = subplot(211, projection="real")
>>> ax1.plot(dGaN_sub.VDS_SET, dGaN_sub.VGS_SET,
    "b.")
>>> ax1.set_xlabel_fmt("Vds []")
>>> ax1.set_ylabel_fmt("Vgs []")
>>> ax1.axis(xmin=-0.5, xmax=21, ymin=-5, ymax=1)
```

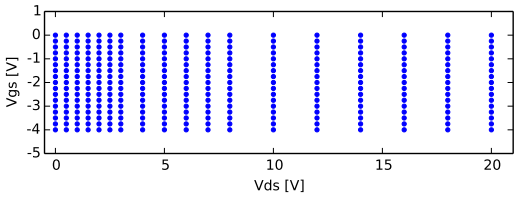


Fig. 5. Example 6. Rectangular Vgs-Vds grid

Now we can reshape the dataset and get the data indexed by VGS_SET and VDS_SET

```
>>> dGaN_cube = dGaN_sub.hyper(["VGS_SET",
                               "VDS_SET"],
                                   "INDEX1")
```

```
>>> dGaN_cube
Blockname: None

sweep vars:
VGS_SET [V]    <17>   min:  -4.0 V   max:  0.0 V
VDS_SET [V]    <18>   min:   0.0 V   max: 20.0 V
freq    [Hz]   <201>  min: 100.0 MHz max: 40.0 GHz
i       []     <2>    min:   0.0     max:  1.0
j       []     <2>    min:   0.0     max:  1.0

Dependent vars:
Date            []     <17x18>
IDS             [A]    <17x18>
IGS             [A]    <17x18>
Index           []     <17x18>
MeasType        []     <17x18>
S               []     <201x17x18x2x2>
VDS             [V]    <17x18>
VGS             [V]    <17x18>
Z0              [Ohm]  <17x18>
```

As we can see now we have index variables `VGS_SET` and `VDS_SET` instead of the INDEX1 variable we had before. The S-parameter array now has 5 indices: frequency, `VGS_SET`, `VDS_SET`, i, and j.

With the data in a hypercube format we can more easily do the IV-plot.

```
>>> ax1 = subplot(211, projection="real")
>>> ax1.plot(dGaN_cube.IDS.T, "b");
>>> ax1.axis(xmin=0, ymin=0)
>>> ax1.set_xlabel_fmt("Vds []")
>>> ax1.set_ylabel_fmt("Id []")
```

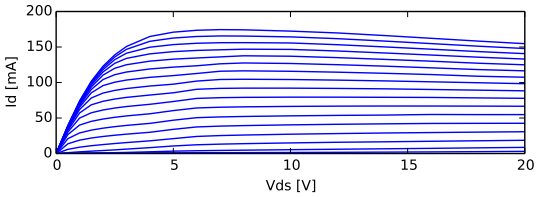


Fig. 6. Example 7. Simplified plot of I-V curve

## III. Conclusion

We have presented a new open source toolkit for simplifying processing of microwave measurement data. There are other toolkits using python available e.g. scikit-rf [4], [7], [8]. We have focused on more low level tools, e.g. an improved array type. It is hoped we can collaborate more in the future to provide a more comprehensive toolkit.

By releasing this code as open source we want to promote the future sharing of research results in the form of source codes.

## IV. Acknowledgment

This research has been partly carried out in GigaHertz Centre in a joint project financed by Swedish Governmental Agency of Innovation Systems (VINNOVA), Chalmers University of Technology, Comheat Microwave AB, Ericsson AB, Infineon Technologies Austria AG, Mitsubishi Electric Corporation, NXP Semiconductors BV, Saab AB, SP Technical Research Institute of Sweden, and United Monolithic Semiconductors.

## References

[1] E. Jones, T. Oliphant, and P. Peterson, "Scipy: Open source scientific tools for Python." http://www.scipy.org/, 2001–.
[2] J. Stenarson, "HFTools." github.com/hftools/hftools, 2014.
[3] N. Kinayman, "Python for microwave and RF engineers [application notes]," *Microwave Magazine, IEEE*, vol. 12, no. 7, pp. 113–122, 2011.
[4] A. Arsenovic, "Scikit-RF." www.scikit-rf.org, 2010.
[5] A. Arsenovic, C. Lihan, M. F. Bauwens, L. Huilin, N. S. Barker, and R. M. Weikle, "An experimental technique for calibration uncertainty analysis," *Microwave Theory and Techniques, IEEE Transactions on*, vol. 61, no. 1, pp. 263–269, 2013.
[6] J. D. Hunter, "Matplotlib: A 2D graphics environment," *Computing In Science & Engineering*, vol. 9, pp. 90–95, May-Jun 2007.
[7] "hycohanz." http://mradway.github.io/hycohanz/, 2010.
[8] "Python IVI." http://github.com/alexforencich/python-ivi, 2010.

# Microwave Substrate Loss Tangent Extraction from Coplanar Waveguide Measurements up to 125 GHz

Uwe Arz
Physikalisch-Technische Bundesanstalt (PTB), 38116 Braunschweig, Germany

***Abstract*— We present a semi-numerical method to extract the loss tangent of a low-loss microwave substrate material from on-wafer scattering-parameter measurements of coplanar waveguides of different lengths. We demonstrate the method using test structures built on a $SiO_2$ wafer for frequencies up to 125 GHz.**

## I. Introduction

In this paper we propose a method for determining the loss tangent of low-loss dielectric substrates in a wide frequency range from coplanar waveguide (CPW) measurements. The method applies a combination of analytic CPW models to extract the loss tangent of the substrate material from the CPW propagation constant, which is derived from uncorrected S-parameter measurements of different line lengths.

When characterizing the permittivity of dielectric materials several resonator measurement methods like the cylindrical cavity resonator, the dielectric post resonator or the split-post resonator are commonly used. Typical of all traditional resonator methods is a very limited frequency range. In contrast to resonator measurement methods, where samples of the bulk dielectric material are used, transmission-line based methods require the fabrication of test structures on the substrate one wishes to examine.

The new approach we present in this paper builds on the methods introduced in [1] and [2] and allows for the wideband extraction of the imaginary part of the complex permittivity for low-loss microwave substrates from CPW measurements.

The method presented in [1] extracts both the relative permittivity and the loss tangent from broadband measurements of the propagation constant $\gamma$ with the aid of the quasi-static CPW model of [3]. For low-loss substrates, however, the method of [1] is quite limited, as will be shown in Section II. In [2], the extraction of the real part of the complex permittivity is greatly enhanced when using the CPW model of [4], which extends the quasi-static model of [3] and accounts for all relevant effects from conductor loss to high-frequency dispersion.

In the following sections we investigate the performance of the methods of [1] and [2] when applied to fused silica, describe the new loss tangent extraction procedure, and compare the results against different resonator measurements.

## II. Test structures and results from [1]

The extraction of material properties in the methods of [1] and [2] relies on the accuracy of the two different CPW models

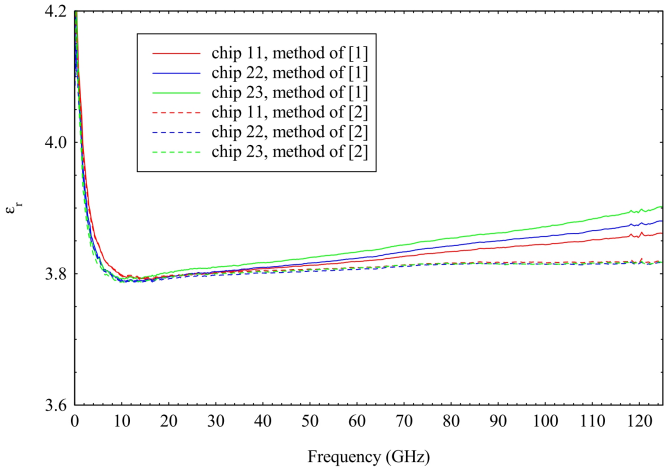


Fig. 1. Relative permittivity of fused silica substrate measured with the methods of [1] and [2].

[3] and [4], which both need the parameters of the CPW cross-section as input. The input quantities of the CPW model of [3] are the width of the ground planes $w_g$, the center conductor width $w$, the width $s$ of the slot between center line and ground planes, the relative permittivity $\varepsilon_r$, the dielectric loss tangent of the substrate $\tan\delta$, the thickness $t$ and the conductivity $\kappa$ of the metal layer, respectively. In the CPW model of [4], also the substrate height $h_s$ is considered.

The CPW test structures were built in three different cross-sections according to Table I. The cross-section dimensions were measured with an optical multi-sensor coordinate measuring machine at PTB. The chips corresponding to these geometries were fabricated on the same $SiO_2$ wafer, and are labeled 'chip 11', 'chip 22', and 'chip 23' in the following.

| Parameter | Unit | chip 11 | chip 22 | chip 23 |
|---|---|---|---|---|
| $w$ | $\mu$m | 87.8 | 105 | 119.1 |
| $s$ | $\mu$m | 9.2 | 11 | 12.1 |
| $w_g$ | $\mu$m | 436 | 521 | 591 |
| $t$ | $\mu$m | 0.5 | 0.5 | 0.5 |
| $h_s$ | $\mu$m | 584.8 | 584.8 | 584.8 |
| $\kappa$ | MS/m | 35 | 35 | 35 |
| $\tan\delta$ | - | $2.2\cdot10^{-4}$ | $2.2\cdot10^{-4}$ | $2.2\cdot10^{-4}$ |

TABLE I
*Parameters of CPW test structures on fused silica substrate.*

978-1-4799-4423-1/14/$31.00 ©2014 IEEE

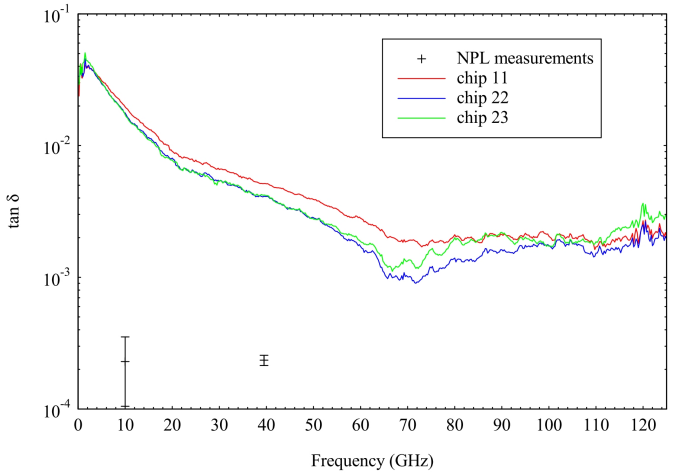


Fig. 2. Loss tangent of fused silica substrate measured with the method of [1] and with different resonator techniques at NPL.

We used the multiline TRL algorithm described in [5] to determine $\gamma$ from uncorrected S-parameter measurements of CPW lines of different lengths. The 4 available line lengths varied between 1030 $\mu$m and 13300 $\mu$m. All on-wafer measurements were performed on a ceramic chuck.

Figure 1 shows the relative permittivity extracted by the methods of [1] and [2] for the three available cross sections. Up to intermediate frequencies of about 50 GHz the two methods give similar results. For higher frequencies, the method of [2] is superior due to the better CPW model of [4].

While for low-loss substrates, the method of [1] can be used in a limited frequency range for determining the relative permittivity for the given cross sections, the extracted loss tangent, however, is wrong by several orders of magnitude. This is shown in Fig. 2. For verification purposes, we included measurements performed at the National Physical Laboratory (NPL) at 10 GHz with a split-post dielectric resonator and at 39.5 GHz using an open resonator. The uncertainties are given with a coverage factor k=2.

As stated in [1], the method is only recommended for medium-loss substrates such as e.g. AF45, it is not meant to be used for low-loss substrates. Furthermore, an accurate determination of the CPW conductors' conductivity is mandatory for obtaining reasonable estimates of the loss tangent.

## III. New measurement procedure

Figure 2 demonstrates that using a constant value for the conductivity $\kappa$ of the CPW lines does not lead to satisfactory results. Instead, a frequency-dependent conductivity value is required, which better describes the relationship between transverse and longitudinal losses in the coplanar waveguide.

To address this problem, we employ a new procedure to determine a quantity we name equivalent conductivity, which is determined from the measured CPW propagation constant. The procedure, which is described in detail in [6], only needs an accurate estimate of the loss tangent at low frequencies, together with the CPW cross-section dimensions and the measured CPW propagation constant.

One advantage of this approach is that it does not need any information about the metal conductivity $\kappa$, besides a generous estimate of the minimum and maximum values $\kappa_{\min}, \kappa_{\max}$. This is replaced by the loss tangent estimate at low frequencies. The most important input quantity, the CPW propagation constant, is determined by measurement, and contains all the relevant physical effects.

As described in [6], the equivalent conductivity is extracted from a numerical inversion of the CPW model of [3]. Even though this inversion cannot capture all relevant effects because of the limitations of the CPW model of [3], we still expect it to provide us with reasonable results up to intermediate frequencies. In [6], this technique is applied to GaAs and $Al_2O_3$ substrates.

Figure 3 shows the equivalent conductivity for the fused silica substrate used in this study. Fig. 3 also contains the DC value of the conductivity, which was determined from resistance measurements of the CPW conductors of different lengths. From a physical point of view, we would expect the effective metal conductivity to decrease with frequency. The equivalent conductivity curves of Fig. 3 vary around a mean value of roughly 32 MS/m, which is lower than the measured DC value. The differences between the results for the three different cross-sections are small.

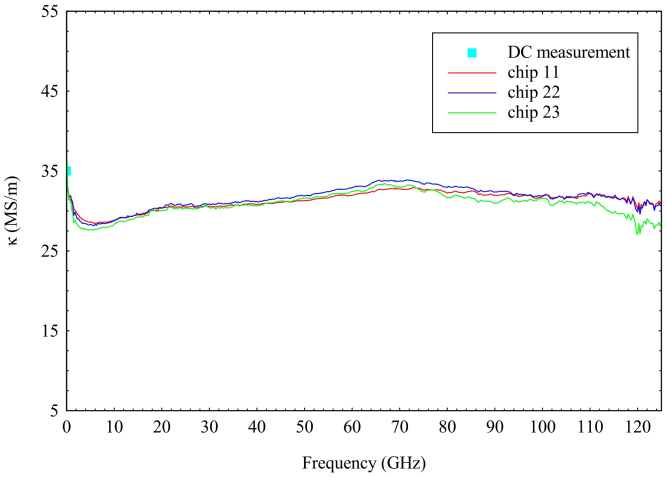


Fig. 3. Equivalent conductivity for $SiO_2$ substrate.

As an intermediate step, we determine the relative permittivity $\varepsilon_r$ of the substrate material used for the CPW fabrication. To this end, we employ the method described in [2], which makes use of the more advanced CPW model introduced in [4]. Since the method of [4] requires an estimate of the loss tangent, we use the low-frequency value given in Tab. I.

In addition to the method of [4], we now apply the frequency-dependent equivalent conductivity value (see Fig. 3). However, the differences in the extracted relative permittivity are negligibly small compared to the case when

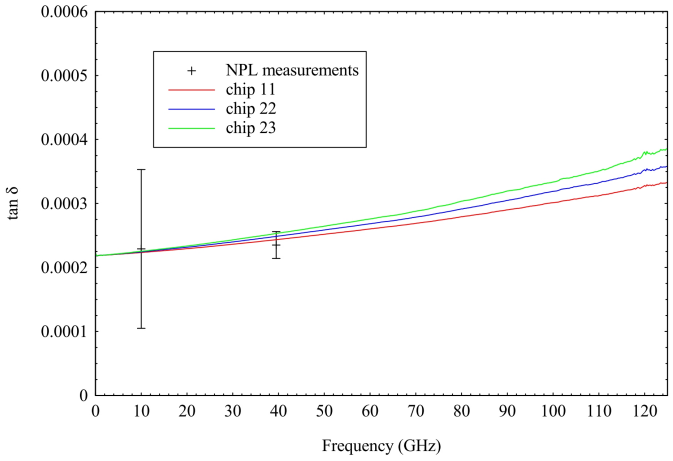


Fig. 4. Measured loss tangent for $SiO_2$ substrate.

the DC conductivity value is applied.

To finally extract the loss tangent, we also use the more advanced CPW model of [4] together with the equivalent conductivity determined in the first step and the relative permittivity from the intermediate step. Our new procedure applies a one-dimensional minimization to the scalar error function defined by the square of the difference between measured and modeled values of the normalized conductance per unit length.

The conductance per unit length is normalized by the capacitance per unit length multiplied by the angular frequency. The algorithm we use is based on golden section search and parabolic interpolation in a given interval for the loss tangent $\tan\delta$. In our investigations, we used the interval $10^{-5} < \tan\delta < 10^{-1}$. The minimization is performed for each frequency point individually.

## IV. Measurement Results and Verification

Figure 4 shows the loss tangent $\tan\delta$ extracted using the new measurement procedure over a frequency range from 0.1 to 125 GHz together with the resonator measurements performed at NPL, which we already discussed in Fig. 2. The S-parameter measurements of the CPW lines of different lengths were performed with an Anritsu VectorStar vector network analyzer. The total processing time for the 506 frequency points was below 1 minute on an average desktop PC. We did not encounter any convergence problems in our study.

In comparison to Fig. 2, the new approach demonstrates a significant progress compared to the method of [1]. Even though there is a dependence on the CPW geometry, the results from the three chips still fall within the uncertainties stated in the NPL measurements up to 39.5 GHz. Since we do not have independent loss tangent measurements with sufficient accuracy above 39.5 GHz, we cannot state the correctness of our higher-frequency results with absolute certainty.

## V. Conclusion

We investigated a new broadband method to extract the loss tangent of low-loss dielectric substrates from on-wafer S-parameter measurements of coplanar waveguides of different lengths. The method uses a combination of both the quasi-TEM CPW model of [3] and the more advanced model of [4]. It consists of three steps, which subsequently determine estimates for the metal conductivity $\kappa(f)$, the relative permittivity $\varepsilon_{\mathrm{r}}(f)$, and, finally, the loss tangent $\tan\delta(f)$.

We applied the method successfully to a fused silica substrate and verified the results independently with resonator measurements.

## Acknowledgment

The author would like to thank Dr. D. Allal from LNE, France, for providing the test structures on $SiO_2$, and Dr. K. Lees from NPL, U.K., for providing the resonator-based measurement data. The author also thanks Dipl.-Ing. D. Schulz and Dipl.-Ing. D. Schubert from PTB, Braunschweig, Germany, for performing the dimensional CPW measurements and the on-wafer scattering-parameter measurements, respectively.

This work was funded by the European Metrology Research Programme (EMRP) under Grant Agreement No. 217257. The EMRP is jointly funded by the EMRP participating countries within EURAMET and the European Union.

## References

[1] U. Arz and J. Leinhos, "Broadband Permittivity Extraction from On-Wafer Scattering-Parameter Measurements," in *12th IEEE Workshop on Signal Propagation on Interconnects SPI 2008*, May 2008.

[2] U. Arz, M. D. Janezic, and W. Heinrich, "Wideband Relative Permittivity Extraction Based on CPW Phase Constant Measurements," in *77th ARFTG Microwave Measurement Conference*, 2011, pp. 37–39.

[3] W. Heinrich, "Quasi-TEM description of MMIC coplanar lines including conductor-loss effects," *IEEE Trans. Microwave Theory Tech.*, vol. 41, no. 1, pp. 45–52, Jan. 1993.

[4] F. Schnieder, T. Tischler, and W. Heinrich, "Modeling Dispersion and Radiation Characteristics of Conductor-Backed CPW With Finite Ground Width," *IEEE Trans. Microwave Theory Tech.*, vol. 51, no. 1, pp. 137–143, Jan. 2003.

[5] R. B. Marks, "A multiline-method of network analyzer calibration," *IEEE Trans. Microwave Theory Tech.*, vol. 39, no. 7, pp. 1205–1215, July 1991.

[6] U. Arz, "Loss Tangent Extraction Based on Equivalent Conductivity Derived from CPW Measurements," in *18th IEEE Workshop on Signal and Power Integrity SPI 2014*, May 2014.

# Noise Diode Calibration Using Receiver Noise Parameters

Richard Aarons and Mark H. Weatherspoon

Department of Electrical and Computer Engineering
Florida A&M University-Florida State University College of Engineering, Tallahassee, FL 32310

**Abstract — An alternate method for solid state noise diode calibration is explored as an application of a noise parameter-based measurement method. A microwave noise diode is characterized over 4-18 GHz using the noise parameters of a commercial noise measurement system, and the results are compared to those provided by the manufacturer. The excess noise ratio (ENR) obtained across the measurement band has a mean difference of 0.102 dB with a worse case of 0.195 dB. This represents a mean error of 0.7% in the ENR over the band. The mean difference in effective noise temperature is 206 K which corresponds to a mean error of 2.4% over the measurement band. These results suggest that the noise parameter-based measurement method can be used for commercial laboratory grade calibrations of noise diodes.**

**Index Terms — Excess noise ratio, microwave noise diode, radiometer, noise, noise parameters, noise receiver, noise source calibration, noise temperature, noise temperature measurement, solid state noise diode, thermal noise.**

## I. Introduction

Noise diodes calibrated from reference standards with traceable history to national standards laboratories such as the National Institute of Standards and Technology (NIST), Boulder, CO, are an integral part of noise measurement systems utilizing commercial instrumentation. NIST and other national laboratories have traditionally used custom designed radiometers with isolators to accurately measure thermal noise temperature and calibrate microwave noise sources [1]-[3]. In recent years, many new measurement and calibration techniques have been developed at national laboratories while not exclusively using traditional radiometers [4]-[6]. However, calibration and certification by such national laboratories can be expensive if only commercial laboratory grade calibrations are needed. It is desired to explore an alternate method for commercial laboratory grade noise diode calibration that is less expensive but with minimal and acceptable reduction in accuracy. This work investigates the first step in establishing this alternate method through the characterization of a microwave noise source using commercial instrumentation.

## II. Measurement Method and Set-up

A noise parameter-based noise temperature measurement method utilizing commercial instrumentation to determine the effective noise temperature of a one-port DUT as illustrated in Fig. 1 is used in this work to characterize a microwave noise diode device under test (DUT) with measurement method details further described below and in [7]. (In fact, another

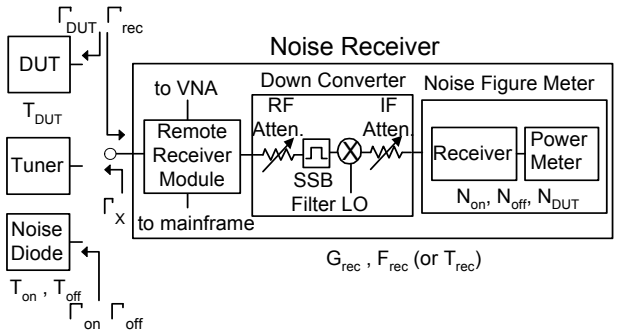


Fig. 1 One-port noise parameter-based measurement system with tuner and noise diode standard for noise receiver calibration.

noise parameter-based noise temperature measurement method for calibration has been reported in [8], but results were only presented for low excess noise ratio (ENR) noise sources around 2 GHz.)

The noise receiver of Fig. 1 consists of a remote receiver module with a low noise amplifier path, down converter, and a noise figure meter. Before a DUT is measured, the noise receiver is calibrated. Calibration includes the characterization of the noise receiver (i.e. determination of the receiver noise parameters $F_{min,rec}$, $\Gamma_{opt,rec}$, $R_{n,rec}$, $k_BBG_0$, and $\Gamma_{rec}$.) using a tuner and noise diode standard as part of a commercial noise parameter measurement system as in Fig. 1 and described in [7]. After calibration, the detected noise power, $N_X$, at the power meter can be written as

$$N_X = k_B \cdot B \cdot G_{rec}(\Gamma_X) \cdot \left[T_X + T_{rec}(\Gamma_X)\right] \text{ (W)} \quad (1)$$

where $k_B$ and $B$ are respectively Boltzmann's constant and the noise measurement bandwidth with the receiver gain, $G_{rec}(\Gamma_X)$, given in terms of the receiver matched gain, $G_0$, and source mismatch factor, $M_s(\Gamma_X)$, as

$$G_{rec}(\Gamma_X) = G_0 \cdot M_s(\Gamma_X) \quad (2)$$

with

$$M_s(\Gamma_X) = \frac{1-|\Gamma_X|^2}{|1-\Gamma_{rec}\Gamma_X|^2} \quad . \quad (3)$$

By substituting DUT for X in (1) and solving for $T_{DUT}$, the available vector noise temperature $T_{DUT}^V$ can be expressed as

$$T_{DUT}^V = \frac{N_{DUT}}{k_BBG_0 \cdot M_s(\Gamma_{DUT})} - T_{rec}(\Gamma_{DUT}) \text{ (K)} \quad (4)$$

978-1-4799-4423-1/14/$31.00 ©2014 IEEE

where $N_{DUT}$ and $\Gamma_{DUT}$ are respectively the measured system noise power with the DUT connected to the receiver of Fig. 1 and the measured DUT reflection coefficient. These values are measured by the noise parameter measurement system when a DUT is connected to the receiver and a noise measurement is performed. The last term of (4) represents the noise temperature of the receiver when connected to the DUT and is a function of the receiver noise parameters with noise temperature calculated from noise figure as in [7]. The uncertainty of this method for noise temperature measurement of hot loads is 3.2% [9].

## III. Measurement Results

A coaxial solid state microwave noise diode was connected as a DUT to the receiver of Fig. 1 for noise characterization. This DUT diode was a different noise diode than the one that was used for system calibration. Additionally, the reflection coefficient of the DUT was measured using a vector network analyzer. All measurements were made in the frequency range from 4-18 GHz with steps of 1 GHz.

The magnitude of the reflection coefficient of the DUT is plotted in Fig. 2. This measured data is used to convert the measured available noise temperature of the DUT to an effective noise temperature that can be properly compared to the noise temperature which is calculated from the ENR provided by the manufacturer.

In Fig. 3, the measured and manufacturer effective noise temperatures of the DUT are compared. Error bars are placed around the manufacturer mean values to reflect the uncertainties in the noise temperatures. These noise temperature uncertainties are calculated from the ±0.2 dB ENR uncertainty provided by the manufacturer. Fig. 4 shows the magnitude of the difference between the measured and manufacturer effective noise temperature for the DUT. In most instances, the measured data tracks the manufacturer data reasonably well, and in all but one case, the measured data falls within the margin of error. The worst-case disagreement was found to be only 6.6% at 6 GHz. The largest absolute difference of 612 K occurred at 6 GHz. This data point appears to be an outlier, especially relative to adjacent frequencies and could truly represent a worst-case scenario due to an error in the reported manufacturer's mean ENR in conjunction with a bad measured data point associated with the underlying receiver noise parameters. Nevertheless, the mean difference over the measurement band was 206 K.

In Fig. 5, the measured and manufacturer ENR of the DUT are compared. Error bars also are included in the plot and are placed around the manufacturer values to reflect ±0.2 dB ENR uncertainty provided by the manufacturer. The measured data generally tracks the manufacturer data and never falls outside the provided margins. The worst-case disagreement was found to be only 1.3% at 7 GHz.

Fig. 6 shows the magnitude of the difference between the measured and manufacturer ENR for the DUT. The largest absolute difference of 0.195 dB occurred at 7 GHz, and 80% of the data points had an absolute difference of less than 0.15 dB between measured and manufacturer ENR. Additionally,

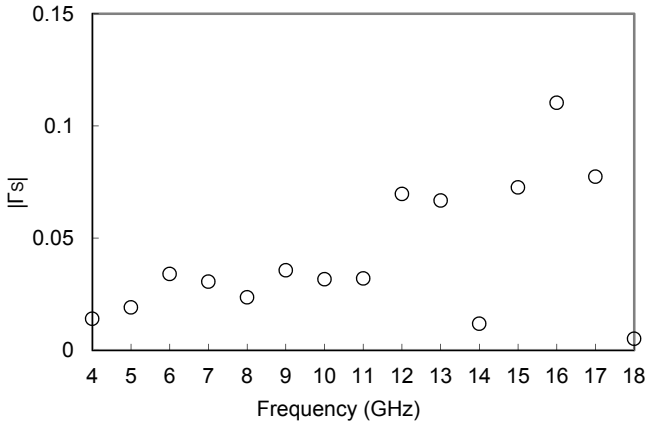


Fig. 2 Plot of the magnitude of the reflection coefficient $|\Gamma_S|$ of a solid state noise diode DUT versus frequency.

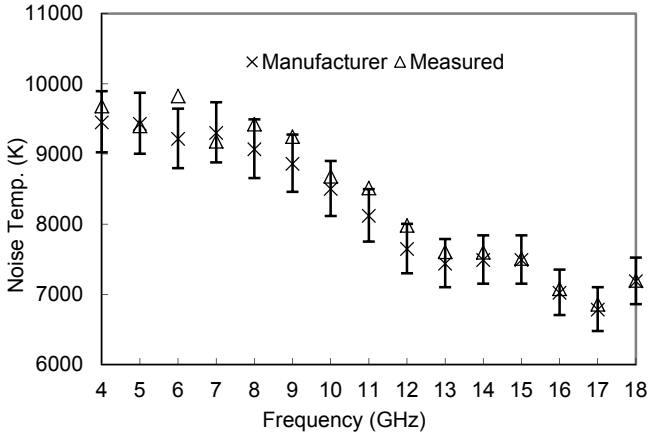


Fig. 3 Comparison of measured and manufacturer effective noise temperatures for the solid state noise diode. Error bars around the manufacturer mean values are calculated for a ±0.2 dB ENR uncertainty of the DUT.

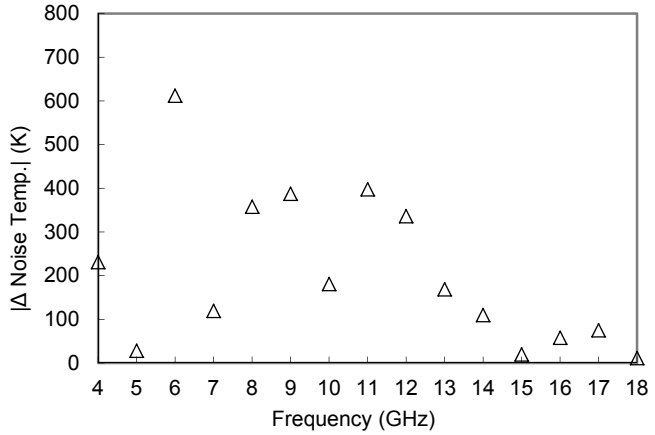


Fig. 4 Plot of the magnitude of the difference between the measured and manufacturer mean effective noise temperatures for a solid state noise diode DUT.

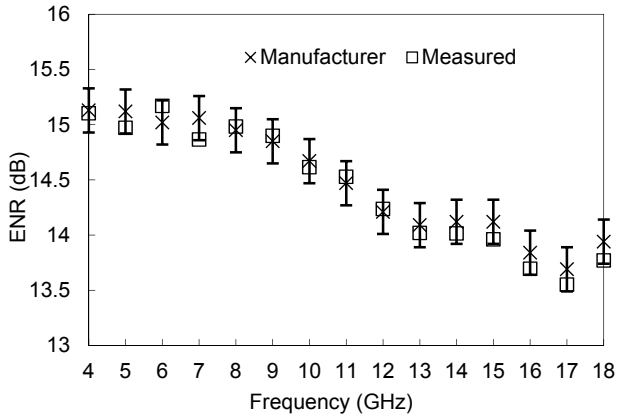


Fig. 5 Comparison of measured and manufacturer ENRs for a solid state noise diode DUT. Error bars are around the manufacturer mean values for a ±0.2 dB ENR uncertainty.

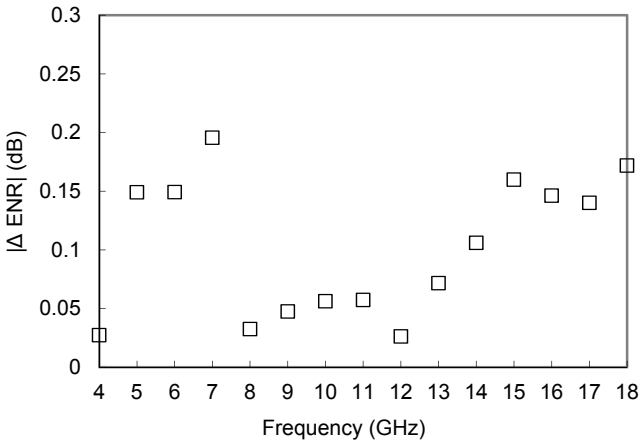


Fig. 6 Plot of the magnitude of the difference between the measured and manufacturer ENRs for a solid state noise diode DUT.

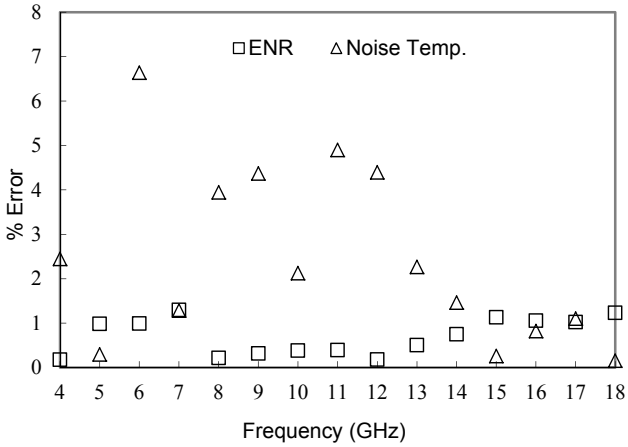


Fig. 7 Plots of the percent error in the measured ENR and effective noise temperature with respect to the manufacturer data for a solid state noise diode DUT.

the mean difference from the manufacturer's data across the measurement band was 0.102 dB.

Finally, plots of the percent error in measured DUT effective noise temperature and ENR with respect to the manufacturer data are presented in Fig. 7. The ENR percent error versus frequency is generally steady and caps out at 1.3% with a mean of 0.7%. In contrast, the effective noise temperature percent error versus frequency is quite erratic with a maximum of 6.6% error. However, 93.3% of the effective noise temperature data points (all but one data point) have an error that is below 5.0%. This results in a mean effective noise temperature error of 2.4%.

## IV. Conclusion

A microwave solid state noise diode was characterized using commercial instrumentation. A mean difference of 0.102 dB (0.195 dB maximum) in ENR was obtained across the band with a corresponding 0.7% mean error. A mean error of 2.4% (206 K mean difference) in effective noise temperature was measured across the band. These results suggest that the noise parameter-based measurement method employed would be acceptable for commercial laboratory grade calibrations of microwave solid state noise diodes since a ±0.2 dB ENR uncertainty is generally specified by commercial manufacturers [10].

## References


[1] D. F. Wait and T. Nemoto, "Measurement of the noise temperature of a mismatched noise source," *IEEE Trans. Microw. Theory Tech,* vol. MTT-16, no. 9, pp. 670-675, Sep. 1968.

[2] G. L. Williams, "A broadband radiometer for calibrating mismatched noise sources," *IEEE Trans. Instrum. Meas.,* vol. 40, no. 2, pp. 443-445, Apr. 1991.

[3] J. Randa, J. Achkar, et al. "International comparison of thermal noise-temperature measurements at 2, 4, and 12 GHz," *IEEE Trans. Instrum. Meas.,* vol. 48, no. 2, pp. 174-177, Apr. 1999.

[4] C. A. Grosvenor, J. Randa, and R. L. Billinger, "Design and testing of NFRad-A new noise measurement system," NIST Tech. Note 1518, Mar. 2000.

[5] T.-W. Kang, J-H. Kim, et al., "Determining noise temperature of a noise source using calibrated noise sources and an RF attenuator," *IEEE Trans. Instrum. Meas.,* vol. 60, no. 7, pp. 2558-2563, Jul. 2011.

[6] H. Iida, Y. Shimada, and K. Komiyama, "Auxiliary-transmission-line method for calibrating noise temperature of a microwave noise source," *IEEE Trans. Instrum. Meas.,* vol. 60, no. 7, pp. 2308-2313, Jul. 2011.

[7] M. H. Weatherspoon and L. P. Dunleavy, "Vector corrected on-wafer measurements of noise temperature," *IEEE Trans. Instrum. Meas.,* vol. 54, no. 3, pp. 1327-1332, Jun. 2005.

[8] L. Belostotski, "A calibration method for RF and microwave noise sources," *IEEE Trans. Instrum. Meas.,* vol. 59, no. 1, pp. 178-187, Jan. 2011.

[9] Mark H. Weatherspoon and R. Joe Smith, "Noise temperature measurement uncertainty analysis using Monte Carlo simulations," *69th ARFTG Conference,* pp.1-7, Honolulu, HI, June 2007.

[10] *Operation and Service Manual Agilent 346A/B/C Noise Source,* Agilent Technologies, Jun. 2009.

# *A Novel CPW- Fed Polarization Reconfigurable Microstrip Antenna*

[1]Vahid Zarei, [2]Mohammadnaghi Azarmanesh, [3]Hamid Boudaghi
Microelectronics Research Laboratory, Urmia University
Urmia, Iran
[1] vahidzprp@gmail.com, [2] m.azarmanesh@urmia.ac.ir, [3] st_h.boudaghi@urmia.ac.ir

Sajjad Abazari Aghdam
CEECS Dept., Florida Atlantic University
FL, USA
Sabazariaghd2012@fau.edu

***Abstract*—A novel CPW-Fed reconfigurable circular polarization microstrip antenna is presented. Two PIN diodes are attached to achieve polarization diversity. By switching the diodes ON or OFF, the proposed antenna can be operated either RHCP (Right Hand Circular Polarization) mode or LHCP (Left Hand Circular Polarization) mode. The experimental result shows that the proposed antenna has a circular polarization bandwidth (AR ≤ 3dB) of about 415MHz at the center frequency of 2.4GHz for both RHCP and LHCP mode. Measured results show good agreement with simulated ones.**

***Keywords-CPW-Fed, Circular Polarization, Microstrip Antenna, PIN diode, Reconfigurable.***

## I. Introduction

Microstrip antennas with reconfigurable polarization can realize frequency reuse, which expands the capability of communication systems and is meaningful in an epoch of frequency shortage. Polarization diversity antennas can also alleviate the harmful influence caused by multipath effects, which has been used in modern wireless communication systems [1].

In general a polarization reconfigurable antenna can be designed to switch between different linear polarizations, two circular polarizations (right hand and left hand circular polarization) and any number of elliptical polarizations (with different axial ratios and tilt angles). In most investigations the point refers to the switch between RHCP and LHCP in a desired frequency [3, 4]. In some papers, antenna could switch to linear polarization in addition of RHCP and LHCP too [5-8]. In some cases the polarization is switched between vertical and horizontal linear polarization [9,10].

There are some switches like MEMS (Micro electromechanical switch), PIN diodes and Varactors which are used to produce reconfiguration property. MEMS have some advantages such as lower resistance and parasitic capacitance, low insertion loss, high isolation in off state and small size. Although all of these advantages, PIN diodes are used in most cases because of low cost, fast switching capability, high power bearing and lower threshold voltage [11-12].

In this paper a novel CPW-Fed microstrip antenna which uses two PIN diodes to switch between RHCP and LHCP, is introduced. This antenna is designed to work in center frequency of 2.4 GHz which is applicable in WLAN system.

## II. Antenna Configuration

Fig. 1 shows the geometry of the proposed Antenna, which consists of a rectangular ground plane with dimension of L and W and a square slot in the center of ground. Four inverted-L-shape grounded strips around the corners, and an inverse vertical T-shape strip between two upper inverted-L-shape strips are embedded in the square slot.

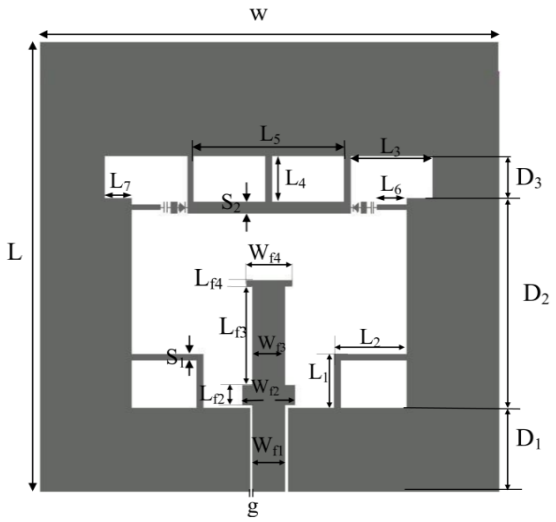


Fig. 1. Geometry of the proposed antenna.

The proposed antenna is designed on an FR4 substrate with a loss tangent of 0.02, permittivity of 4.4, and a thickness of 1mm. The antenna is fed by a 50- ohm CPW having a single strip of width $W_{f1}$ =5mm and two identical gaps of width g=0.4mm. The single strip of the CPW is protruded into the slot by a length of $W_{f1}$, $W_{f2}$, $W_{f3}$ and $W_{f4}$. Two parameters, $W_{f1}$ and g are adjusted to produce 50 Ω impedance for feeding of the antenna. Other parameters of feeding strip such as $W_{f2}$, $W_{f3}$, $W_{f4}$ and the width of them are embedded and adjusted for impedance matching and resonance bandwidth improvement.

The CP operation of the proposed antenna is chiefly related to the four grounded inverted-L strips inserted around the corners of the square slot.

The dimensions of proposed antenna in Fig. 1 are listed in Table I.

In Fig. 1 the path of current in upper strips can be controlled by use of two PIN diodes. To feed PIN diodes by DC supply two stubs with dimension of 1×1.5 mm are used. Each stub has one 100pF capacitor in one side and other side is connected to PIN diode. To make diodes ON we can use these stubs for giving positive DC voltage to diodes [13].

When diode is in the OFF-state, it works like a small capacitor which can be considered as an open circuit. When diode is in ON-state it works like a small resistance. In an ideal state this resistance can be considered as a short circuit.

978-1-4799-4423-1/14/$31.00 ©2014 IEEE

TABLE I. Dimensions of the proposed antenna (unit: mm)

| **Parameter** | $L_1$ | $L_2$ | $L_3$ | $L_4$ | $L_5$ |
|---|---|---|---|---|---|
| **dimension** | 9 | 11 | 12.5 | 7.5 | 23 |
| **Parameter** | $L_6$ | $L_7$ | $S_1$ | $S_2$ | $D_1$ |
| **dimension** | 5.5 | 4 | 1 | 2 | 14 |
| **Parameter** | $D_2$ | $D_3$ | $W_{f1}$ | $W_{f2}$ | $W_{f3}$ |
| **dimension** | 35 | 7 | 5 | 8 | 5 |
| **Parameter** | $W_{f4}$ | $L_{f2}$ | $L_{f3}$ | $L_{f4}$ | **g** |
| **dimension** | 7 | 3.3 | 16.5 | 1 | 0.4 |

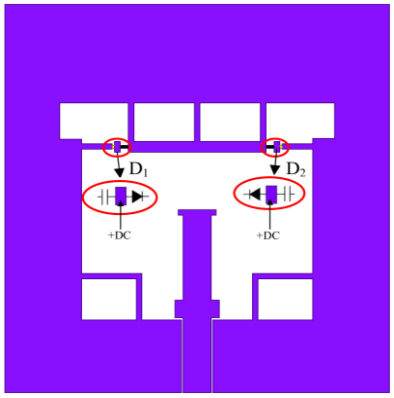


Fi g. 2. Switching structure of the antenna including diodes and capacitors.

PIN diodes used in the proposed antenna are BAR64-02W diodes. According to datasheet of this diode, in ON-state it has 2.1Ω resistance and in OFF-state it equals to 0.17pF capacitance. The switching structure of the proposed antenna is demonstrated in Fig. 2.

## III. Experimental Results and Discussion

In each step of the design procedure, the full-wave analyses of the proposed antenna were performed using Ansoft HFSS (ver.13). For simulation of the diodes in on state we model them by a resistance of 2.1Ω. We also model the diodes in off state with a capacitance of 0.17pF.

The proposed antenna with dimensions in Table I has been fabricated on an FR4 substrate with a loss tangent of 0.02, permittivity of 4.4, rectangular dimensions of 75×70mm, and thickness of 1mm. The photograph of fabricated antenna is shown in Fig. 3. An Agilent E8363C vector network analyzer has been used to measure antenna parameters.

In Fig. 4 the measurement and simulated results of $S_{11}$ in RHCP and LHCP state are shown. The antenna has an impedance bandwidth ( $S_{11} \leq$ -10dB) of 935MHz (1.995~2.930GHz) at RHCP mode, an impedance bandwidth ($S_{11} \leq$ -10) of 965MHz (1.935~2.960 GHz) at LHCP mode.

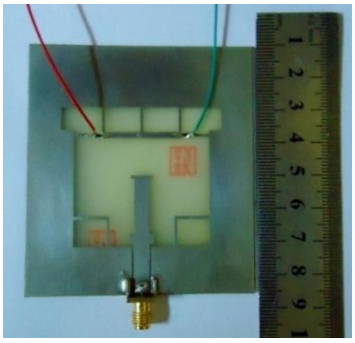

Fig. 3. Photograph of the fabricated antenna.

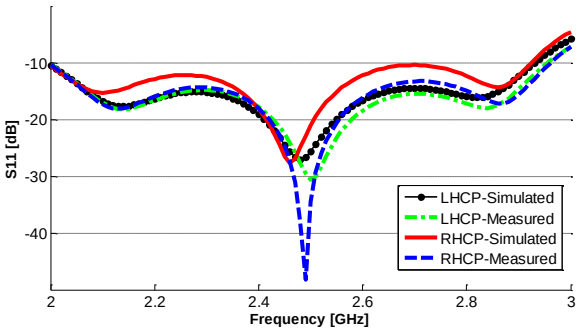


Fig. 4. Simulated and measured reflection coefficient of the antenna for RHCP and LHCP.

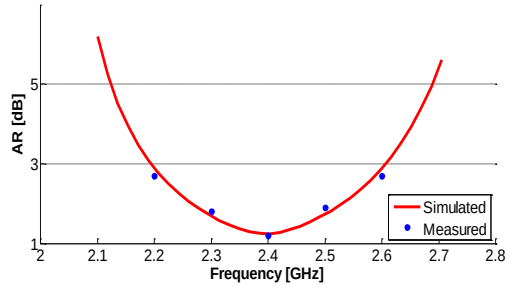


(a)

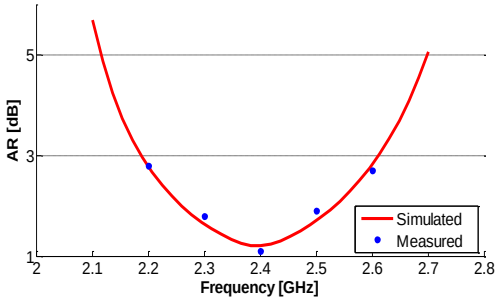


(b)

Fig. 5. Measured and simulated AR for (a) RHCP and (b) LHCP.

Embedding inverted-L-shape grounded strips at the upper corner of square slots make the CP polarization possible. This strips are separated by two PIN diodes. When D1 is ON and D2 is OFF, the polarization of the antenna will be RHCP and

When D2 is ON and D1 is OFF, the polarization of the antenna will be LHCP. So by making the diodes ON or OFF different polarization will be obtained.

The simulated and measured Axial Ratio (AR) results in RHCP and LHCP states is shown in Fig. 5. As it is seen, the AR for RHCP and LHCP states is the same and in frequency range of 2.180～2.595, the AR is lower than -3dB. In this bandwidth, it can be considered a circular polarization for proposed antenna.

The L-shape strips at the lower corners are for AR improvement and increasing of the antenna bandwidth. Center frequency of AR are affected by length of L6. This length is chosen to have minimum axial ratio at frequency of 2.4 GHz . As we can see in Fig. 6, by increasing the length L6 the axial ratio bandwidth shifts to lower frequencies.

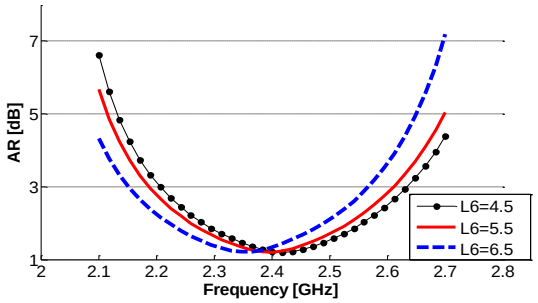


Fig. 6. Simulated AR values for different values of L6.

The inversed T-shape strip embedded between upper L-shape strips will increase the gain of the antenna and make it smoother in the bandwidth. The simulated results for the gain of the proposed antenna in RHCP and LHCP state are shown in Fig.7. In this figure the measured results of the gain in LHCP state is shown too.

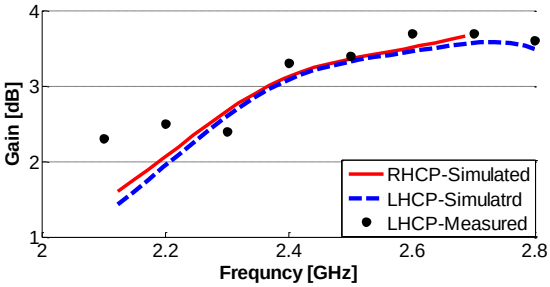


Fig. 7. Measured and simulated results for antenna gain in RHCP and LHCP.

The gain of proposed antenna is upper than 2dB in the desired bandwidth and in center frequency 2.4 GHz it is 3.2dB. In Fig. 7, it can be seen that as the operation frequency increases, the antenna gain is increased too. The antenna gain in the AR bandwidth in the best mood is 3.6 dB. The gain of the antenna has a direct relationship with the length of the antenna. Fig. 8, shows the gain of the antenna for different values of L. Increasing the length of the antenna will increase the gain of the antenna and it has a negligible effect on the AR and return loss. In Fig. 9 the radiation pattern of the proposed antenna is demonstrated.

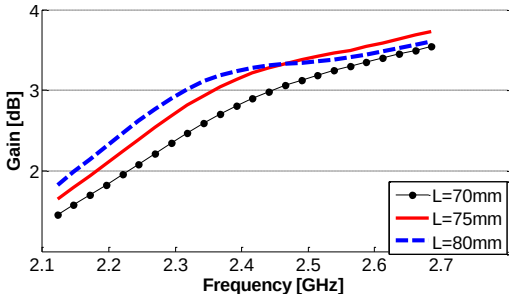


Fig. 8. Gain of the proposed antenna for various values of L.

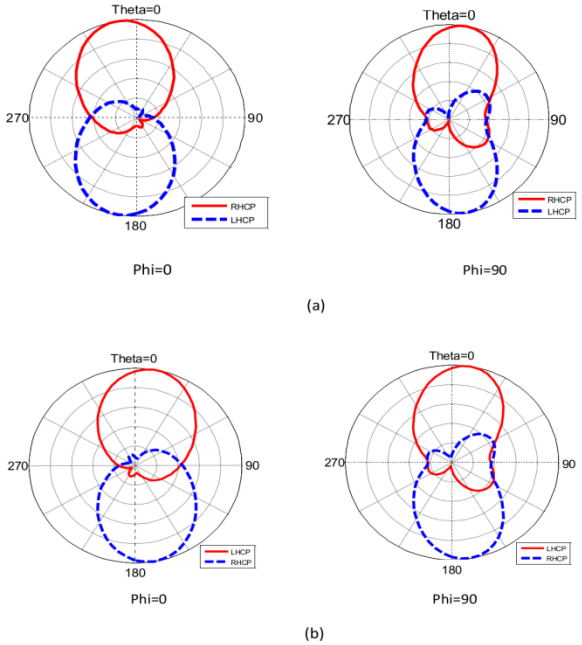


Fig. 9. Radiation pattern of antenna: (a) RHCP antenna; (b) LHCP antenna.

## IV. Conclusion

A novel polarization reconfigurable antenna has been presented. The antenna is simple to design and fabricate and exploits PIN diode switches to deliver reconfigurable capability. This antenna uses four inverted-L grounded strips for the excitation of two orthogonal resonant modes for CP radiation. Measured results have good agreement with simulated ones. The proposed antenna is suitable for Bluetooth/WLAN (2400– 2484 MHz) frequencies.

## References

[1] C. S-Xiong, Y. X-Xia, G. Bo, and S. B-Cheng, “A Reconfigurable Microstrip Antenna with Agile Polarization Using Diode Switches,”

[2] A. Kim, Jung-han Kim and Hong-min Lee “Reconfigurable Annular Ri ng Slot Antenna with Circular Polarization Diversity” Proceedings of Asia-Pacific Microwave Conference, 2007, IEEE.

[3] S. Pyo, J.-W. Baik and Y.-S. Kim, “Slot-perturbed microstrip antenna for switchable circular polarization,” Electronics letters. Vol. 47, No. 10, May. 2011.

[4] Y-jin Kim, J-kwan Kim, J-han Kim and H-min Lee, “Reconfigurable Annular Ring Slot Antenna with Circular Polarization Diversity,” Proceedings of Asia-Pacific Microwave Conference, pp. 815-818, 2007 IEEE.

[5] Y. Sung, “Investigation In to the Polarization of Asymmetrical-Feed Triangular Microstrip Antennas and its Application to Reconfigurable Antennas,” IEEE trans. Antennas propag., vol. 58, no. 4, April. 2010.

[6] P-Yuan Qin, A. R. Weily, Y. J. Guo, and C-Hong Liang, “Polarization Reconfigurable U-Slot Patch Antenna,” IEEE trans. Antennas propag., vol. 58, no. 10,pp. 3384-3388, October. 2010.

[7] M. S. Nishamol, V. P. Sarin, D. Tony, C. K. Aanandan, P. Mohanan, and K. Vasudevan, “An Electronically Reconfigurable Microstrip Antenna With Switchable Slots for Polarization Diversity,” IEEE trans. Antennas propag., vol. 59, no. 9, pp. 3424-3427, September. 2011.

[8] X.-X. Yang, B.-C. Shao, F. Yang, A. Z. Elsherbeni, and B. Gong, “A Polarization Reconfigurable Patch Antenna With Loop Slots on the Ground Plane,” IEEE trans. Antennas propag., vol. 11,pp. 69-72, 2012.

[9] Y. Li, Z. Zhang, W. Chen, and Z. Feng, “Polarization Reconfigurable Slot Antenna with a Novel Compact CPW-to-Slotline Transition for WLAN Application,” IEEE antennas and wireless propaga. Lett., VOL. 9, pp. 252-255, 2010.

[10] Y. Li, Z. Zhang , W. Chen, Z. Feng, and M. F. Iskander, “Dual-Polarization Slot Antenna Using a Compact CPW Feeding Structure,” IEEE antennas and wireless propaga. Lett., vol. 9, pp. 191-194, 2010.

[11] H. Boudaghi, M. Azarmanesh, and M. Mehranpour, “A Frequency-Reconfigurable Monopole Antenna Using Switchable Slotted Ground Structure,” IEEE antennas and wireless propaga. Lett., vol. 11, pp. 655-658, 2012.

[12] Sajjad Abazari Aghdam” Reconfigurable Antenna with Diversity Filtering band Feature Using Active Devices for Communication Systems," *IEEE Trans*. Antennas Propag.,vol.61,No. 10, 2013.

[13] H. Boudaghi, J. Pourahmadazar, and S. Abazariaghdam, “Compact UWB monopole antenna with reconfigurable band notches using PIN diode switches” 14th Annual Wireless and Microwave Technology Conference, WAMICON 2013, pp. 1-4.

# Correlation Analysis between a VNA-based Passive Load Pull System and an Oscilloscope-based Active Load Pull System: A Case Study

*Z. Mokhti, P. Tasker and J. Lees*

*Centre of High Frequency Engineering, Cardiff University, UK*

**Abstract — This paper presents a case study of performance comparison between a passive load pull system that uses a vector network analyzer (VNA) as its receiver, and an active load pull system that uses a sampling oscilloscope. The objective of the comparison was to enable parallel research activities between two sites. The two systems are independently used to measure the same device under test, a packaged high-voltage laterally diffused metal oxide semiconductor (HVLDMOS) device at a fundamental frequency of 900MHz and under the same bias and drive settings. A simulation of the device performance is also performed using Agilent ADS to accompany the measurement results and to verify the accuracy of the device model. Results show that both load pull systems are well correlated within two times the measurement uncertainty and that the device model gives a good performance prediction. A further investigation is performed by manipulating the harmonic loads using the active load pull system to demonstrate its advantages over the passive system in discovering the true capability of the device under test in terms of drain efficiency.**

**Index Terms — Harmonic terminations, load pull systems, power amplifiers, waveform measurements.**

## I. Introduction

A load pull system used to characterize the device behavior under different load conditions and is a critical resource in the design process of power amplifiers. It does so by presenting a specific load in any location on the Smith chart to the output of the device under test (DUT). Similarly a source pull system presents a specific impedance on the Smith chart to the input side of the device, for example to enable a matching condition. There are two ways to implement a load pull system architecture, namely through a passive method or active. A passive load pull system uses a passive impedance tuner at the output of the DUT to change the load conditions. This method in general has a lower setup cost compared to the active system, but due to the limitations of the tuner it is almost impossible to present a load along the perimeter of the Smith chart [1].

An active load pull system on the other hand uses signal generators to inject signals back into the device output emulating the reflected waves. Therefore it does not have the limitation of going to the edge of the Smith chart, and in fact it can also be used to present a load outside the Smith chart if needed such as the case demonstrated in [2].

A receiver is used in a load pull system to measure the incident and reflected waves at both ports of the DUT. This receiver can be a vector network analyzer (VNA) or a time-domain acquisition equipment such as a sampling oscilloscope. A calibration step is performed to transfer the reference plane from the receiver ports to the device plane. The information about the absolute power of the DUT is determined by including a receiver power calibration step in the calibration sequence. The path from the DUT to the receiver is considered as the calibrated path and it may exclude other paths and components in the overall system such as the bias tee path, driver amplifiers, and power combiners.

## II. Load Pull System Architectures & Measurement Settings

### *A. Passive load pull system*

The passive load pull system discussed in this paper uses a vector network analyzer (VNA) a receiver together with passive source and load tuners from Maury. To characterize a packaged device under test that typically has low output impedances, a test fixture with a 7:1 impedance transformer is used. This effectively scales down the Smith chart reducing the original coverage area, but at the same time enables a much lower impedance to be presented to the DUT.

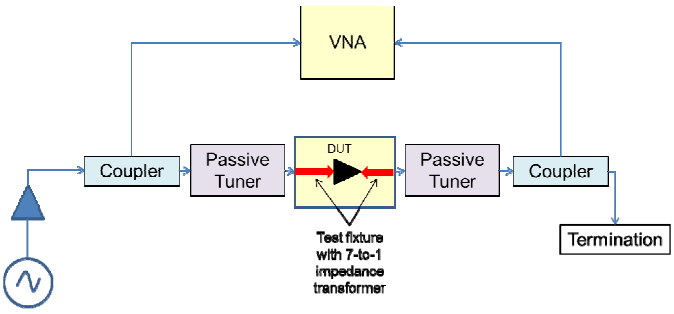


Fig. 1. Passive load pull system with a VNA as receiver.

A thru-reflect-line (TRL) calibration using a customized calibration kit is performed to shift the reference plane to the DUT package plane. This system also has an impedance tuner located on the source side of the DUT to perform source pull and enabling a source matching procedure. The measurement uncertainty of this system is +/-0.125 dB for power and 2%-point for drain efficiency.

978-1-4799-4423-1/14/$31.00 ©2014 IEEE

### B. Active load pull system

The active load pull system discussed in this paper is the system used in Cardiff University Centre of High Frequency Engineering, UK. It consists of a Tektronix sampling oscilloscope as its receiver, a signal generator at its input side, and three signal generators at the output side of the DUT to emulate the reflected waves up to the third harmonic. A triplexer is used to combine the output of these three signal generators and their power amplifiers. Circulators are used to isolate the output signal of the DUT from the injected signals that come from the three signal generators.

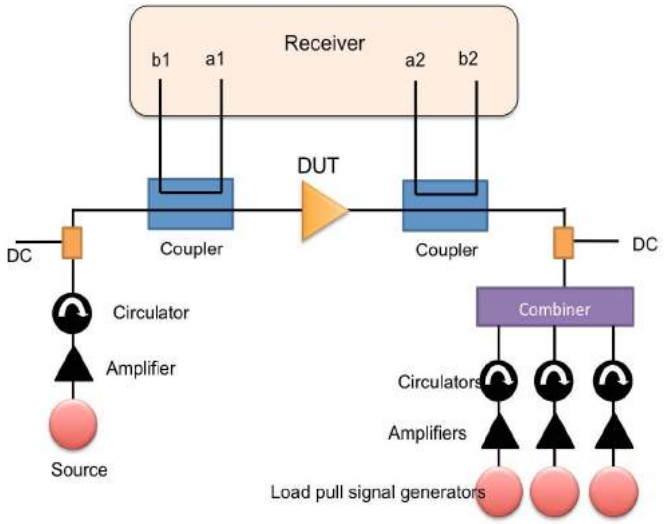


Fig. 2. Active harmonic load pull system with a sampling oscilloscope as receiver.

A different test fixture is used for this system and it does not contain any impedance transformers. A short-open-load-thru (SOLT) calibration is performed to shift the reference plane to the device package.

### C. Device & Measurement Settings

The device under test used in this paper is a 10W high-voltage laterally diffused metal oxide semiconductor (HVLDMOS) device in a packaged form. The drain voltage is set to 48V, which is the maximum drain bias condition under normal operations. The device is set to a class-AB bias condition with the gate biased such that the quiescent current is at about 5% of maximum drain current. The input signal is a continuous wave at 900MHz. When characterizing the output power and drain efficiency, the device is driven into 3dB compression.

The measurement procedures are setup to achieve two objectives: to obtain load pull contours of drain efficiency and output power, and to obtain a gain compression plot by performing a power sweep at the optimum load for output power.

In parallel, a simulation is also performed in Agilent ADS using the device model where the same setup conditions above are emulated.

## III. Measurement Steps & Results

### A. Measurements using passive load pull system.

Initially the device is measured using the passive load pull system according to the setups previously discussed. This will yield the optimum load location on the Smith chart for maximum power and drain efficiency, as well as the maximum power and efficiency that can be achieved.

In order to replicate the exact same impedance environment at the active load pull system later on, the harmonic impedances that the device sees needs to be characterized. There are two stages of impedances after the device package plane that need to be characterized: the customized test fixture with a 7:1 impedance transformer, and the Maury tuners. For the tuners, a standalone VNA is used to measure the impedances looking into each tuner when the optimum fundamental load is found. As for the test fixture, a thru, a reflect, and a line standard of the customized calibration kit are measured with a VNA. This information is then used to construct the s2p files of the test fixture in ADS. Finally the s2p files of the test fixture and tuners are cascaded together to produce a known impedance combination of fundamental and harmonic loads that can be reproduced using the active load pull system in Cardiff. Fig. 3 shows the combination of these impedances. For a good data comparison, the load location as recorded by the passive load pull system is also plotted to verify the characterization process.

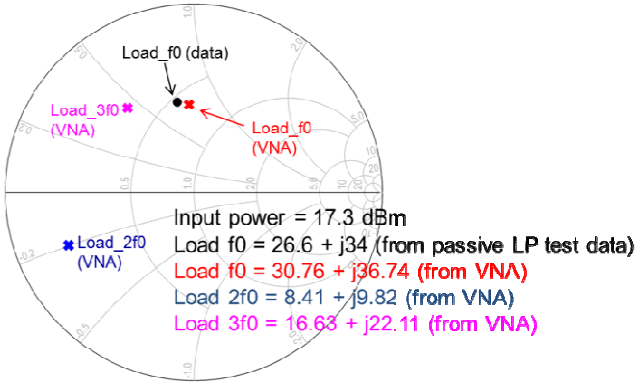


Fig. 3. The resulting impedance combination that the device sees at the fundamental frequency of 900MHz (red), second harmonic (blue) and third harmonic (purple), as measured by the VNA in the passive load pull system. The black dot shows the fundamental load as read by the user interface which shows a slightly different value as measured by the VNA.

### B. Measurements using active load pull system

With the information about the device settings and the impedance combination that the device sees is known, the active load pull system in Cardiff University is used to reproduce the same settings. The active load pull system does not have a source pull capability so the input power is gradually increased to overcome the mismatch loss. Table I shows the comparison in performance between the two load

pull systems in measuring the same HVLDMOS device. The simulation results are included as reference. The drain efficiency results from the Cardiff active load pull system is about 5 percentage-points lower than the passive load pull results. The differences in output power and in gain although less obvious are still greater than the two times the uncertainty. Another observation that can be made is that the simulation results, although yield higher numbers, are well correlated with the results from the passive load pull results.

TABLE I
PERFORMANCE COMPARISON AT THE OPTIMUM LOADS SET BY THE PASSIVE LP SYSTEM

| | Passive LP | Active LP | Simulation |
|---|---|---|---|
| Output power (dBm) | 40.2 | 39.5 | 40.4 |
| Drain efficiency (%) | 60.2 | 55.5 | 64.4 |
| Gain (dB) | 22.9 | 22.0 | 23.2 |
| Input power (dBm) | 17.3 | 17.5 | 17.3 |

### *C. Independent Search for Optimum Load Using the Active Load Pull System*

The differences in the results between the two load pull systems can be investigated by running an independent search for optimum loads using the active load pull system in Cardiff University. By fixing the second and third harmonic loads according to those found from the passive tuners, the fundamental load is swept around the target load to generate the output power and drain efficiency contours using the active load pull system and to locate the optimum loads for maximum output power and drain efficiency. Fig.4 shows the outcome of this exercise.

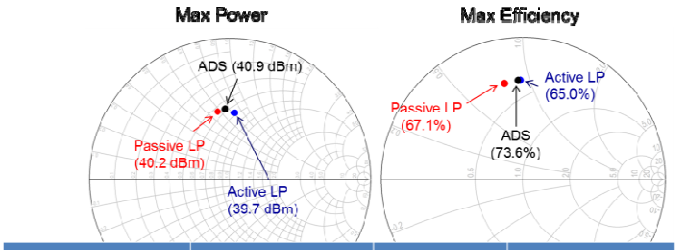


| | Passive LP (reference) | Active LP | ADS Simulation |
|---|---|---|---|
| Max Pout | 40.2 dBm | 39.7dBm | 40.9 dBm |
| ZL for Max Pout | 26.6 + j34.0 | 23.0 + j43.1 | 28.4 + j37.9 |
| Max Efficiency | 67.1% | 65.0% | 73.6% |
| ZL for Max Efficiency | 15.0 + j39.0 | 16.8 + j46.0 | 16.3 + j44.9 |

Fig. 4. Comparison of optimum load ($Z_L$)locations for maximum output power ($P_{OUT}$) and drain efficiency as well their values, when searched independently by sweeping the fundamental load. The harmonic loads are fixed according to those of the passive tuners.

The difference in drain efficiency between the two load pull systems is now about 2%, and the residual difference could be attributed to the uncertainty of the harmonic load locations. The maximum output power between the two load pull systems are also within two times the uncertainty. The simulated drain efficiency is now 73.6%, 6.5%-point higher than the measured drain efficiency from the load pull contour using the passive system. This difference could also be attributed to the uncertainty of the harmonic load terminations, as well as possible limitations in the model accuracy.

## IV. MANIPULATING THE HARMONIC LOADS

The main advantage of using an active load pull system is the ability to set the harmonic loads and potentially uncovering the true device performance. To demonstrate the significance of this advantage, the harmonic loads are swept around the Smith chart one at a time and the change in drain efficiency is monitored. This exercise is not performed to engineer any specific high-efficiency mode (e.g. Class-F, class $F^{-1}$), rather it is a quick verification on the device package plane to get a preliminary results of drain efficiency improvements. Fig. 5 shows the trend in drain efficiency as the second and third harmonic loads are swept around the Smith chart. A final drain efficiency number of 72% is achievable from this exercise. It is worth noting that with a proper engineering of class-F mode of operation, a drain efficiency of 75% is achievable with this device.

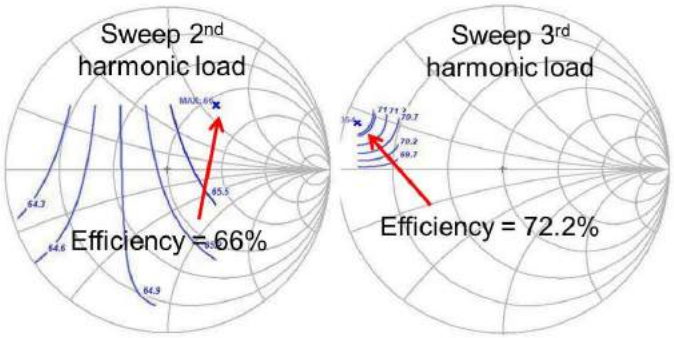


Fig. 5. The effect of sweeping the second and third harmonic loads to uncover the true performance of the device. An increase of 7%-point was observed.

To further verify the effect of harmonic load terminations, the same fundamental and harmonic load combinations are then simulated in ADS. Table II shows that the measured results are well correlated with the simulation results for this device at these settings.

## V. CONCLUSION

A correlation analysis of a VNA-based passive load pull system and an oscilloscope-based active load pull system has been presented. Both systems produce results that are within two times of the measurement uncertainty. The active load pull system does provide an added advantage in discovering

the DUT's true performance by means of manipulating the harmonic loads. In this example an increase of 7%-point was observed after sweeping the second and third harmonic loads.

Another advantage of an active load pull system is that, with proper de-embedding of the device package it has the capability to engineer certain current and voltage waveforms at the device current generator plane, enabling the analysis of a highly efficient mode of operation.

This analysis was done to enable parallel research activities between two locations, and the positive outcome of the analysis provide a high amount of confidence level of the results obtained from harmonic load manipulations where the feature is not available on the passive load pull system.

TABLE II
EFFECTS OF HARMONIC LOAD MANIPULATIONS

| | Active LP | Simulation |
|---|---|---|
| Output power (dBm) | 39.5 | 39.6 |
| Drain efficiency (%) | 72.2 | 74.5 |
| Gain (dB) | 25.2 | 25.4 |
| Input power (dBm) | 14.3 | 14.3 |

## ACKNOWLEDGMENT

This research is part of the Celtic Eureka OPERA-Net 2 project initiatives to reduce the environmental impact of radio networks.

## REFERENCES

[1] Z. Aboush, J. Lees, J. Benedikt, and P.J. Tasker, "Active harmonic load pull system for characterizing highly mismatched high powe transistors," *IEEE MTT-S Int. Microwave Symp. Dig.*, pp. 1311-1315, June 12-17 2005.

[2] M. Akmal, V. Carrubba, J. Lees, S. Bensmida, J. Benedikt, K. Morris, M. Beach, J. McGeehan, and P.J. Tasker, "Linearity enhancement of GaN HEMTs under complex modulated excitation by optimizing the baseband impedance environment," *IEEE MTT-S Int. Microwave Symp. Dig.*, pp. 1-4, June 5-10 2011.

# A New Method for the Determination of the Reflection and Transmission Characteristics of Dielectric Materials

*Jeong-Hwan Kim, Jin-Seob Kang, Jeong-Il Park, and Tae-Weon Kang*

*Center for Electromagnetic Wave*

*Korea Research Institute of Standards and Science (KRISS)*

*267 Gajeong-ro, Yuseong-gu, Daejeon 305-340, Korea*

*Tel:+82-42-868-5170/E-mail:kimjh@kriss.re.kr*

**Abstract — This paper presents a new method for the determination of the reflection and transmission characteristics of dielectric materials that are the parameters for the calculation of the complex permittivity using the Nicolson–Ross–Weir (NRW) method. In transmission line methods, most widely used methods for broadband permittivity measurements, the NRW method gives a stability problem for low-loss dielectric materials near the thickness resonance frequencies. The proposed method successfully removes the problem using a relationship between the reflection and transmission characteristics. The proposed method is a new iterative transmission/reflection method applicable to permittivity measurements using arbitrary sample lengths in wide-band frequencies.**

**Index Terms — Dielectric materials, complex permittivity, reflection and transmission characteristics, transmission line methods, NRW method.**

## I. INTRODUCTION

Measurements of material properties in RF and microwave frequency regions have been getting more important, especially in the research fields, such as material science, microwave circuit design, absorber development, biological research, etc., as the frequency of the applications goes up to sub-millimeter wave range and the areas of the applications are being wider. Dielectric measurement is important because it can provide the electrical or magnetic characteristics of the materials, which proved useful in many research and development fields. The most widely used techniques in the microwave region are: cavity resonators, free space, open-ended coaxial probe, and transmission-line [1]–[4]. Among these techniques transmission-line techniques are the simplest methods for electromagnetic characterization in wideband frequencies for the growing number of wideband applications of various RF and microwave materials.

For the transmission/reflection method (TR), the measuring holder is made up of a section of coaxial line or rectangular wave guide filled with the sample to be characterized. The sample electromagnetic parameters are deduced from the scattering parameters defined at the sample planes. The Nicolson–Ross–Weir (NRW) procedure [5], [6] is the most commonly used method for performing this calculation. This method has the advantage of being non-iterative and applicable to coaxial line and rectangular waveguide holders. However, it is well known that this method diverges for low-loss materials at frequencies corresponding to integer multiples of one half wavelength in the sample. To eliminate these instabilities an iterative procedure applicable to permittivity measurements [7] was proposed and a simplified version of the well-known Nicolson–Ross–Weir (NRW) method applicable for dielectric materials was also proposed [8].

## II. FORMULATION

A When a sample is inserted inside a measurement holder (transmission line) as shown in Fig. 1 we can formulate the following equations which are applicable for the coaxial line holder (TEM mode) and the rectangular waveguide holder with TE10 mode [7]:

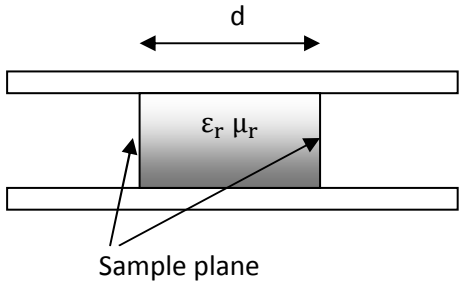


Fig. 1. A sample in the transmission line.

$$S_{11} = \frac{\Gamma\,(1-T^2)}{1-\Gamma^2T^2} \tag{1}$$

$$S_{21} = \frac{T\,(1-\Gamma^2)}{1-\Gamma^2T^2} \tag{2}$$

$$\Gamma = \frac{Z-Z_0}{Z+Z_0} = \frac{\gamma_0\mu_r-\gamma}{\gamma_0\mu_r+\gamma} \tag{3}$$

$$T = e^{-\gamma d} \tag{4}$$

978-1-4799-4423-1/14/$31.00 ©2014 IEEE

$$\gamma = j\frac{2\pi}{\lambda_0}\sqrt{\epsilon_r\mu_r - (\frac{\lambda_0}{\lambda_c})^2} \quad (5)$$

$$\gamma_0 = j\frac{2\pi}{\lambda_0}\sqrt{\frac{c_{vac}^2}{c_{lab}^2} - (\frac{\lambda_0}{\lambda_c})^2} \quad (6)$$

$$Z = \frac{j\omega\mu_0\mu_r}{\gamma} \quad (7)$$

$$Z_0 = \frac{j\omega\mu_0}{\gamma_0} \quad (8)$$

, where $S_{11}$ and $S_{22}$ are the reflection and transmission scattering parameters; Γ and T are the reflection coefficient at the sample plane, when the sample length is infinite, and the transmission coefficient; $\gamma_0, Z_0$ and $\gamma, Z$ represent respectively, the propagation constants and the impedances of the empty and filled holders; $\lambda_0$ and $\lambda_c$ are the free-space wavelength and the cutoff wavelength, which becomes infinite for TEM mode; d is the sample length; $\epsilon_r$ and $\mu_r$ and are the relative permittivity and permeability of the sample; $c_{vac}$ and $c_{lab}$ are the speed of the light in vacuum and in the air respectively.

The NRW method uses (9) ~ (11) to calculate the reflection and transmission characteristics from the measured scattering parameters. From them the permittivity and permeability of the sample can be obtained.

$$K = \frac{S_{11}^2 - S_{21}^2 + 1}{2S_{11}} \quad (9)$$

$$\Gamma = K \pm \sqrt{K^2 - 1} \quad (10)$$

$$T = \frac{S_{11} + S_{21} - \Gamma}{1 - (S_{11} + S_{21})\Gamma} \quad (11)$$

From (3) we can get the propagation constant in the sample from the reflection characteristics and by putting it into (4) we get the following equation. This can be a constraint equation to be used in the iterative method.

$$T = \exp(-\gamma_0\mu_r\frac{1-\Gamma}{1+\Gamma}\, d) \quad (12)$$

In the proposed method the initial values for the reflection and transmission characteristics are from the initial step of the NRW method and with them an iterative OLS (Ordinary Least Squares) procedure is carried out using (1), (2), and (12) for the reflection and transmission characteristics of a dielectric material ( $\mu_r$ =1). To fully use the measured scattering parameters four equations for the scattering parameters and (12) are used in the procedure.

Baker-Jarvis *et al*. [7] proposed an iterative procedure to bypass the inaccuracy peaks applicable to dielectric materials. The permittivity is calculated numerically using (3)–(6) and

$$S_{21} + \beta S_{11} = \frac{T(1-\Gamma^2)}{1-\Gamma^2T^2} + \beta\frac{\Gamma(1-T^2)}{1-\Gamma^2T^2} \quad (13)$$

Compared to the iterative procedure the proposed method does not need to adjust a parameter depending on the properties of the dielectric material under test, so it is more versatile.

As for the case of the coaxial transmission line with a low loss the characteristic impedance and propagation constant are given respectively by [9]

$$Z = Z_{0,vac,pec}.\alpha_c\sqrt{\frac{\mu_r}{\epsilon_r}} = Z_{0,pec}\cdot\alpha_c, \quad (14)$$

$$\gamma = \alpha + j\beta = jk\alpha_c \quad (15)$$

, where $\alpha_c = \sqrt{1 - h^2/k^2}$, $k = k_{0,vac}\sqrt{\epsilon_r\mu_r}$, and $h$ is the transverse wavenumber due to a loss in the transmission line (Quasi-TEM mode), $\epsilon_r$ and $\mu_r$ are the relative permittivity and permeability of the medium of the transmission line, and $k_{0,vac}$ is the wavenumber in vacuum. So the reflection coefficient Γ of the sample for the TM (Quasi-TEM) mode is

$$\Gamma = \frac{Z-Z_0}{Z+Z_0} = \frac{\frac{\gamma}{\epsilon} - \frac{\gamma_0}{\epsilon_{air}}}{\frac{\gamma}{\epsilon} + \frac{\gamma_0}{\epsilon_{air}}} = \frac{\gamma - \gamma_0\epsilon_r/\epsilon_{r,air}}{\gamma + \gamma_0\epsilon_r/\epsilon_{r,air}} \quad (16)$$

, where

$$Z_0 = Z_{0,vac,pec}.\alpha_{c0}\sqrt{\frac{1}{\epsilon_{r,air}}} = Z_{0,air,pec}.\alpha_{c0},$$

$$\gamma_0 = jk_{0,air}\,\alpha_{c0} = jk_{0,vac}\sqrt{\epsilon_{r,air}}\alpha_{c0}.$$

In (14) ~ (16) subscript 'pec' is used to represent the perfect conductor of the transmission line, subscripts 'vac' and 'air' represent the medium of the transmission line, vacuum and air, respectively, and subscript '0' to represent the symbols for the air medium.

From (14) and (15) we get

$$Z\cdot\gamma = Z_{0,vac,pec}\mu_r\, jk_{0,vac}\,\alpha_c^2 = Z_{0,air,pec}\mu_r\, jk_{0,air}\,\alpha_c^2 \quad (17)$$

$$\gamma = \frac{Z_{0,vac,pec}}{Z}\mu_r\, jk_{0,vac}\,\alpha_c^2 = \frac{Z_{0,air,pec}}{Z}\mu_r\, jk_{0,air}\,\alpha_c^2 \quad (18)$$

Putting (18) into (4) gives

$$T = \exp(-j\,k_{0,air}\,\alpha_c^2\,\mu_r\frac{1-\Gamma_m}{1+\Gamma_m}\, d) \quad (19)$$

In (19) the reflection coefficient $\Gamma_m = \frac{Z-Z_{0,air,pec}}{Z+Z_{0,air,pec}}$ and the reference impedance of the VNA, usually 50 Ω, is set to $Z_{0,air,pec}$. If $\Gamma_m$ is set to $\frac{Z-Z_0}{Z+Z_0}$, (19) can be written as

$$T = \exp\left(-\gamma_0 \left({}^{\alpha_c}/_{\alpha_{c0}}\right)^2 \mu_r \frac{1-\Gamma_m}{1+\Gamma_m} d\right). \quad (20)$$

The propagation constant is also expressed from (16) as $\gamma = \gamma_0 \frac{\epsilon_r}{\epsilon_{r,air}} \frac{1+\Gamma}{1-\Gamma}$. So it seems that for the magnetic material ($\epsilon_r = 1$) coaxial transmission line (jig) can be used even when it has a loss.

As for the case of the low-loss waveguide transmission line made of a non-magnetic metal, the characteristic impedance and the propagation constant are respectively given by

$$Z_{TE} = \frac{jk}{\gamma}\sqrt{\frac{\mu}{\epsilon}} = \frac{jw\mu}{\gamma} = \frac{jw\mu}{\alpha+j\beta} \quad (21)$$

$$\alpha = \frac{\sqrt{\pi f \mu_0 \rho}}{b}\sqrt{\frac{\epsilon}{\mu}}\left\{\frac{1+\frac{2b}{w_e}\left({}^{f_c}/_{f}\right)^2}{\sqrt{1-\left({}^{f_c}/_{f}\right)^2}}\right\} \quad (22)$$

$$\beta = 2\pi f\sqrt{1-\left({}^{f_c}/_{f}\right)^2}\sqrt{\epsilon_r\mu_r}/c_{vac} = 2\pi f\sqrt{1-\left({}^{f_c}/_{f}\right)^2}\sqrt{\epsilon\mu} \quad (23)$$

, where fc is the cutoff frequency given by $f_c = \frac{1}{2w_e}\frac{1}{\sqrt{\epsilon\mu}} = f_{c,vac}\frac{1}{\sqrt{\epsilon_r\mu_r}} = f_{c,air}\frac{\sqrt{\epsilon_{r,air}}}{\sqrt{\epsilon_r\mu_r}}$, and $b$ is the height and $w_e$ is the effective width of the waveguide aperture and ρ is the resistivity of the conductor. If we set the reflection coefficient as

$$\Gamma_{TE} = \frac{Z_{TE}-Z_{TE,air}}{Z_{TE}+Z_{TE,air}}, \quad (24)$$

transmission characteristics can be expressed by

$$T = \exp\left(\frac{-jw\mu_0}{Z_{TE,air}}\mu_r\frac{1-\Gamma_{TE}}{1+\Gamma_{TE}}d\right) = \exp\left(-\gamma_0\mu_r\frac{1-\Gamma_{TE}}{1+\Gamma_{TE}}d\right) \quad (25)$$

, which is the same as (12).

So for the TE mode waveguide transmission line (12) can be used even for the lossy waveguide. However for the low-loss coaxial transmission line with ${}^{\alpha_c}/_{\alpha_{c0}} \approx 1$, as can be seen from (20), (12) can be also used with a small error.

## III. Experiments

To show the validity of the proposed method a dielectric sample of 5.18 mm length was measured using a P-band waveguide holder from 12.4 GHz to 18 GHz. Fig. 2 shows the results, reflection and transmission characteristics and the permittivity/permeability using the NRW method and the proposed one. And a dielectric sample of 6.677 mm length was measured using a 30 mm long 7-mm air line from 50 MHz to 18 GHz. Fig. 3 shows the results, reflection and transmission characteristics.

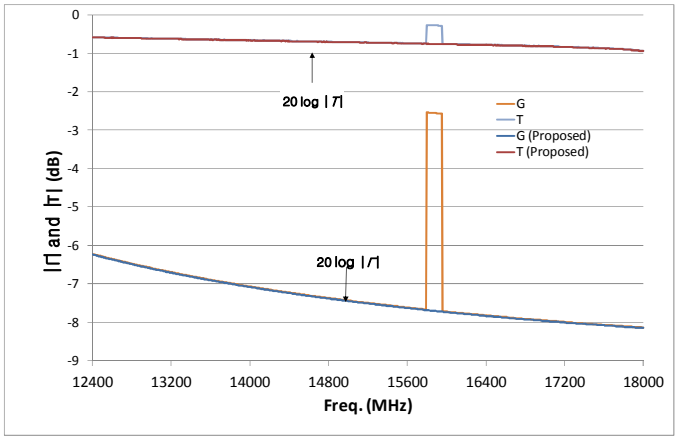


(a)

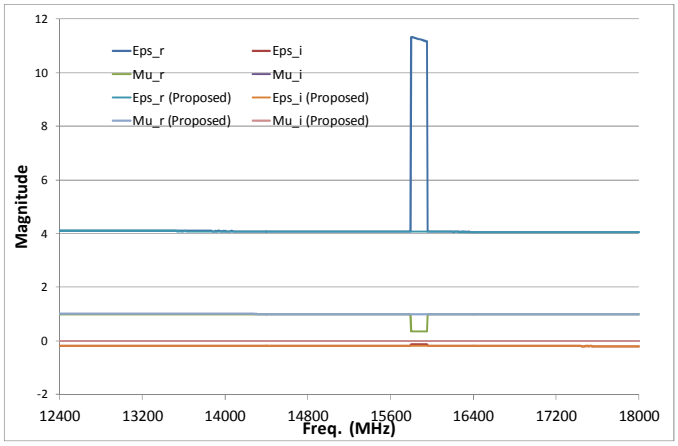


(b)

Fig. 2. Results of the proposed method. (a) Reflection and transmission. (b) Permittivity and permeability.

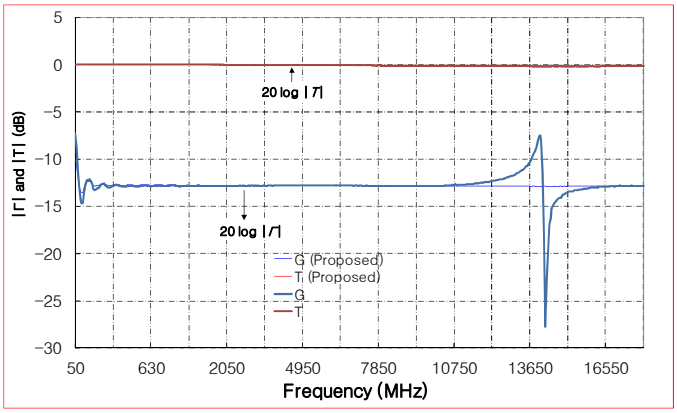


Fig. 3. Results of the proposed method for coaxial transmission line.

## IV. Conclusion

For the determination of the reflection and transmission characteristics of dielectric materials we proposed a new method that, using a relationship between the reflection and transmission characteristics, successfully removes the stability problem for low-loss dielectric materials near the thickness resonance frequencies. It is a new iterative transmission/reflection method applicable to permittivity measurements using arbitrary sample lengths in wide-band frequencies.

As the frequency goes up, most materials are dielectric and the sample thickness can be integer multiples of one half wavelength in the sample. So the proposed method is expected to be useful.

## References


[1] M. N. Afsar, J. R. Birch, and R. N. Clarke, "The measurement of the properties of materials," *Proc. IEEE*, vol. 74, pp. 183–199, Jan. 1986.

[2] R. J. Cook, "Microwave cavity methods," in *High Frequency Dielectric Measurement*, J. Chamberlain and G. W. Chantry, Eds. Guildford, U.K.: IPC Science and Technology, 1973, pp 12–17.

[3] M. A. Stuchly and S. S. Stuchly, "Coaxial line reflection method for measuring dielectric properties of biological substances at radio and microwave frequencies—A review," *IEEE Trans. Instrum. Meas.*, vol. 29, pp 176–183, Sept. 1980.

[4] D. K. Godgaonkar, V. V. Varadan, and V. K. Varadan, "Free-space measurement of complex permittivity and complex permeability of magnetic materials at microwave frequencies," *IEEE Trans. Microwave Theory Tech.*, vol. 39, pp. 387–394, Apr. 1990.

[5] A. M. Nicolson and G. Ross, "Measurement of intrinsic properties of materials by time domain techniques," *IEEE Trans. Instrum. Meas.*, vol. 19, pp. 377–382, Nov. 1970.

[6] W. B. Weir, "Automatic measurement of complex dielectric constant and permeability at microwave frequencies," *Proc. IEEE*, vol. 62, pp 33–36, Jan. 1974.

[7] J. Baker-Jarvis, E. J. Vanzura, and W. A. Kissick, "Improved technique for determining complex permittivity with the Transmission/Reflection method," *IEEE Trans. Microwave Theory Tech.*, vol. 38, pp. 1096–1103, Aug. 1990.

[8] Abdel HakimBoughrie, Christian Legrand, Alain Chapoton, "Non-iterative stable transmission/reflection method for lowloss material complex permittivity determination," *IEEE Trans. Microwave Theory Tech.*, *vol 45, no.1, January 1997*.

[9] W. C. Daywitt, "Exact principal mode field for a lossy coaxial line," *IEEE Trans. Microwave. Theory Tech.*, vol. 39, no. 8, pp.1313 -1322, 1991.